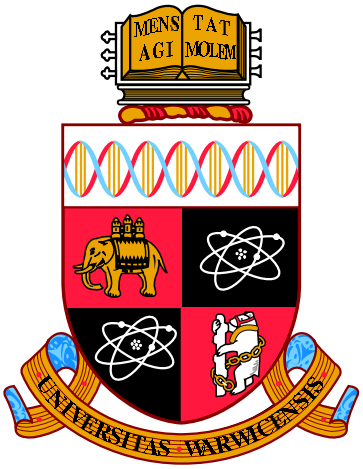

Characterisation of Non-crystalline Pharmaceuticals (Ionic Liquids/Liquid Crystals) by NMR Spectroscopy

by

Sarah Kate Mann

Thesis

Submitted to the University of Warwick

for the degree of

Doctor of Philosophy

Department of Physics

June 2020

Contents

List of Tables

List of Figures

Acknowledgments

Firstly, I would like to thank my supervisor, Professor Steven Brown, for all of his help, guidance and encouragement during the course of this work, including giving me the opportunity to work on this project and supporting me to attend and present at conferences and meetings in many locations. I would also like to thank my second supervisor, Dr. Józef Lewandowski, whose door was always open for advice, valuable discussions, and coffee.

Next, I would like to thank the people who provided assistance with NMR experiments. Particularly Trent Franks, who assisted numerous times when the spectrometers or my pulse sequence didn't do as I wanted them to, and Angelo Gallo and Anjali Menakath, who were always happy to help.

I would also like to acknowledge the many people at GSK who have contributed to this collaboration. Tran Pham, Lisa McQueen, Bernie O'Hare, Dewey Barich, Andy Tatton, Lindsay Knight and Andrew Edwards, thank you for taking an interest in my work and providing useful insights and feedback. I am grateful to have had the opportunity to spend time working at GSK in both Stevenage and Collegeville, PA, where I had the privilege of working closely with Tran and Bernie. Financial support from GSK is also gratefully acknowledged.

I am thankful to Tom Welton, Jay Griffith, David Pugh and Patricia Hunt, from Imperial College, for involving me in the CAGE project and sharing their knowledge on ionic liquids, and to Doug MacFarlane, for allowing me to undertake a project in his lab at Monash University.

Special thanks go to the members of the Warwick solid-state NMR group. Their friendship, the constant supply of cake, and hours spent climbing made my time spent at Warwick University enjoyable. Finally, I wish to thank my parents for their support throughout my years at university.

Declarations

The work in this thesis is original, and was conducted by the author, unless otherwise stated, under the supervision of Prof. Steven Brown (Department of Physics) and Dr. Józef R. Lewandowski (Department of Chemistry). An exception is the work in Chapter 4, which was carried out by the author under the supervision of Prof. Douglas Macfarlane in the School of Chemistry, Monash University, Australia. This thesis has not been submitted for a degree or diploma or other qualification at any other University.

Some of the results presented have been published. Specifically, results from Chapter 4:

S. K. Mann, S. P. Brown and D. R. MacFarlane. Structure Effects on the Ionicity of Protic Ionic Liquids, *ChemPhysChem* **2020** (Accepted Article)

Results from Chapter 5:

S. K. Mann, T. N. Pham, L. L. McQueen, J. R. Lewandowski and S. P. Brown. Revealing Intermolecular Hydrogen Bonding Structure and Dynamics in a Deep Eutectic Pharmaceutical by Magic-Angle Spinning NMR Spectroscopy. *Molecular Pharmaceutics*, **2020** *17*(2), 622-631[1]

Results from Chapters 6 and 7:

S. K. Mann, M. K. Devgan, W. T. Franks, S. Huband, C. L. Chan, J. Griffith, D. Pugh, N. J. Brooks, T. Welton, T. N. Pham, L. L. McQueen, J. R.

Lewandowski and S. P. Brown. MAS NMR Investigation of Molecular Order in an Ionic Liquid Crystal, *The Journal of Physical Chemistry B*, **2020** *doi: 10.1021/acs.jpcb.0c02328*[2]

Abstract

Non-crystalline forms of pharmaceuticals (ionic liquids/liquid crystals) offer tremendous scope for alteration of the physicochemical and pharmacokinetic properties of drugs with otherwise non-ideal properties. The pharmaceutical industry currently relies predominantly on solid-state crystalline therapeutics, for which a standard set of characterisation methods is available. However, such methods (e.g., X-ray crystallography) are not applicable to liquid therapeutics. In order to facilitate the transition of non-crystalline forms of pharmaceuticals from laboratory to the market, routine methods for their characterisation are required. The overall aim of the work presented in this thesis is to develop such methodology and build on the knowledge of the microscopic/molecular structures and dynamics of ionic liquid (IL), deep eutectic solvent (DES) and liquid crystal (LC) materials used in pharmaceutical applications.

Nuclear magnetic resonance (NMR) is a powerful probe of the local atomic environment and intermolecular interactions (e.g., hydrogen bonding) and can also provide detailed information on molecular dynamics. Thus, NMR is the primary technique utilised in this thesis. Specifically, ^{1}H solution-state and ^{1}H and ^{13}C magic angle spinning (MAS) NMR experiments have been employed to provide insight into the diffusivity, intermolecular interactions between active pharmaceutical ingredients (APIs), exchange processes and reorientational dynamics in a range of pharmaceuticals and model systems.

It is demonstrated that for a series of protic ILs, small changes in structure (hydrogen bonding ability, alkyl chain length and degree of branching) strongly influence the bulk properties (proton transfer, ionicity, viscosity and conductivity). Such properties are dependent on the molecular structure of the constituents and nature of the the inter-ionic interactions. Key hydrogen bonding interactions are directly detected for a model DES composed of two APIs, lidocaine and ibuprofen, by two-dimensional ^{1}H-^{1}H NOESY and ROESY MAS NMR experiments. The hydrogen-bonding dynamics are qualitatively determined by following the chemical exchange between the labile protons by means of variable temperature ^{1}H MAS NMR linewidth analysis. Insight into the nature and strength and dynamics of hydrogen bonding is also obtained for an IL composed of choline and geranate (CAGE) and a series of six structural analogues from the 1D ^{1}H MAS NMR spectra. Fast proton exchange is revealed by a single resonance for the carboxylic acid and hydroxyl protons, while the temperature dependence of the ^{1}H chemical shift of $-[6-7]\times10^{-3}$ ppm K^{-1} is indicative of strong intermolecular hydrogen bonding for all analogues. Further evidence

from hydrogen bonded clusters is provided by mass spectroscopy for a CAGE octanoic acid analogue, with $[(\text{choline})(\text{geranate})(\text{octanoate})]^-$, $[(\text{choline})(\text{octanoate})_2]^-$ and $[(\text{choline})(\text{geranate})_2]^-$ species at intensities significantly higher than expected of electrostatic ion clusters and compared to those for $[(\text{anion})_2(\text{H})]^-$ species, suggesting strong association of the choline cation with the anions.

CAGE and CAGE-octanoic acid were observed to undergo phase transitions by differential scanning calorimetry (DSC), which small-angle X-ray scattering (SAXS) revealed to be an isotropic to LC transition. Polarising optical micrographs of CAGE octanoic acid show a smectic (i.e, layered) phase. In LCs, the anisotropic interactions are partially averaged by fast molecular motions which modulate the orientation of the interaction tensor. The motionally averaged value can be compared to the rigid-limit value to obtain an order parameter, S^2, which describes the spatial restriction of the motion. It is shown, for the CAGE and CAGE octanoic acid ILCs, that order parameters S^2_{CH} and S^2_{HH} can be obtained from the measurement of ^{1}H-^{13}C and ^{1}H-^{1}H residual dipolar couplings by cross-polarisation (CP) and double-quantum (DQ) build-up curves, respectively. The obtained order parameters, S^2, ranging from 0 to 0.05, are considerably lower than those typically observed for conventional non-ionic LCs, revealing highly dynamic LC phases. The order parameters further provide site-specific information, showing a mobility gradient along the alkyl chains and a greater amplitude of motion of the choline cation compared to the carboxylate anions. In addition, further characterisation of the dynamics of the CAGE octanoic acid ILC is provided by nuclear spin relaxation measurements. Specifically, site-specific variable temperature relaxation measurements of ^{1}H R_1, ^{13}C R_1, ^{13}C $R_{1\rho}$, ^{1}H-^{13}C NOE, and ^{13}C $R_{1\rho}$ relaxation dispersion (RD) are measured. Fitting of ^{13}C relaxation rates at two magnetic fields to a model for overall anisotropic molecular reorientation superimposed with internal motions provides estimates for the diffusion coefficients, on the order of 10^6 and 10^8 s^{-1} for rotation around the short and long molecular axis, respectively, and activation energies ranging from $\sim$20-40 kJ mol^{-1}. Local internal motions were also detected, with S^2 ranging from 0.17-1, on a timescale of 10^{-11} to 10^{-12} s with activation energies < 19 kJ mol^{-1}.

Abbreviations

API Active Pharmaceutical Ingredient 4
AIL Aprotic Ionic Liquid 56
CAGE Choline and Geranate 3
CP Cross Polarisation 8
CSA Chemical Shift Anisotropy 23
DES Deep Eutectic Solvent 2
DIPSHIFT Dipolar Chemical Shift Correlation 47
DOSY Diffusion Ordered NMR Spectroscopy 7
DP Direct Polarisation 42
DSC Differential Scanning Calorimetry 10
DQ Double Quantum 41
EMF Extended Model-Free 33
FID Free Induction Decay 39
FSLG Frequency-Switched Lee-Goldburg 48
FT Fourier Transform 40
HETCOR Heteronuclear Correlation 43
HBA Hydrogen Bond Acceptor 2
HBD Hydrogen Bond Donor 2
IL Ionic Liquid 1
ILC Ionic Liquid Crystal 3
INEPT Insensitive Nuclei Enhanced by Polarisation Transfer 42
IR Infrared 56
LC Liquid Crystal 3
MAS Magic-Angle Spinning 7
NE Nernst-Einstein 57

Chapter 1

Introduction

The focus of this thesis is on the characterisation of liquid formulations of active pharmaceuticals. In Section 1.1, various subsets of liquids are introduced, including ionic liquids, deep eutectic solvents and liquid crystals, and their properties and applications are discussed. The use of these classes of materials in the pharmaceutical industry is then outlined in Section 1.2, highlighting the potential advantages that they offer over conventional solid-state pharmaceuticals. The primary experimental technique utilised in this thesis, nuclear magnetic resonance (NMR) spectroscopy, is introduced in Section 1.3, demonstrating its suitability for the characterisation of the molecular-level structure and dynamics in such systems.

1.1 Ionic Liquids, Deep Eutectic Solvents, and Liquid Crystals

The term *ionic liquid* (IL) simply means a liquid composed of ions. Frequently, yet arbitrarily, ILs have been defined as salts that have melting points below 100 °C; this appears to have the purpose only of distinguishing them from classical inorganic molten salts, which melt at higher temperatures.[3] Since the first IL (ethylammonium nitrate) was reported by Walden in 1914,[4] the field has continued to expand, receiving attention across numerous scientific areas, particularly over the past two decades. Considering the low vapour pressure of some ILs, they have been heavily utilised for the application of 'green' solvents.[5,6] However, many other areas have also benefitted from the use of ILs, including energy technologies (e.g., as advanced batteries,[7,8] dye-sensitised solar cells[9] and fuel cells[10]), engineering (e.g., coatings[11] and lubricants[12]), biotechnology (e.g., biocatalysts[13,14] and protein purification[15]) and the focus of this thesis, in the pharmaceutical industry[16–19] (to be discussed in more detail in Section 1.2). The numerous applications of ILs can be attributed to the 'designer solvent' concept: the idea that there are millions of cation-anion

combinations that can be selected to form an IL with the desired properties for specific applications.[20] Some of the most frequently encountered ILs in the literature are based on four types of cations: alkylammonium, phosphonium, imidazolium and pyridinium, paired with inorganic or organic anions (e.g. halides, $[BF_4]^-$, $[PF_6]^-$, $[NTf_2]^-$, $[OTf]^-$) (Figure 1.1).

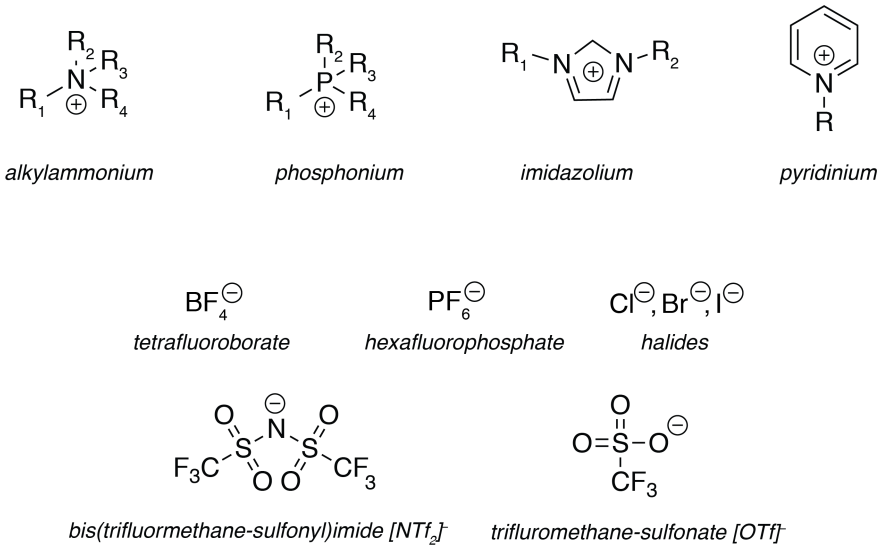

Figure 1.1: Structures of common cations and anions of ILs.

In addition to liquids composed solely of ions, i.e., with no molecular species present, a number of closely related systems have found similar interest and applications. The most well-known are the *deep eutectic solvents* (DESs), introduced by Abbott *et al.* in 2003.[21] DESs are formed from mixtures of Lewis or Brønsted acids and bases, and can contain a variety of anionic, cationic and neutral species. In DESs, it is hydrogen bonding between donor (HBD) and acceptor (HBA) molecules, rather than ionisation, that results in a lower melting point than the constituent components (see Figure 1.2a for a typical phase diagram). The first DES was formed by mixing choline chloride and urea in a 1:2 molar ratio (Figure 1.2b).[21] Numerous other DESs have been formed from choline chloride and various HBDs, including amides, carboxylic acids and alcohols. When the DES precursors originate from natural sources, such as urea, organic acids, amino acids, carbohydrates or even water, the compounds can be called natural deep eutectic solvents (NADES).[22] In some cases, the distinction between ILs and DESs is unclear, with the terms often used interchangeably. For example, in mixtures of Brønsted acids and bases, proton transfer may be complete, leading to the formation of a fully ionised protic IL (PIL), or the proton transfer equilibrium may lie anywhere on the continuum toward the neutral forms.[23] Two of the systems studied in this thesis, lidocaine ibuprofen

(Chapter 5) and choline geranate (CAGE; Chapters 6-7), have been labelled as both DESs and ILs in various publications.[24–29]

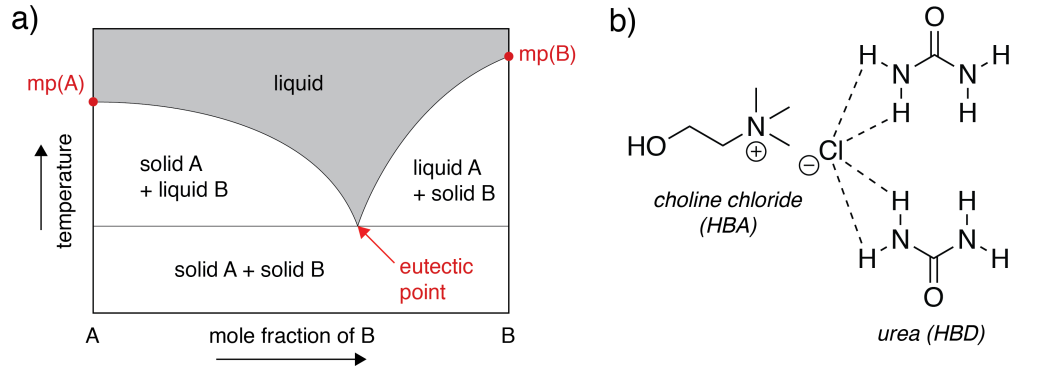

Figure 1.2: (a) Schematic representation of a phase diagram for a two-component eutectic system where mp refers to melting point. Figure adapted from ref.[30] (b) The structure of the DES, choline chloride urea (1:2), showing the interaction of choline chloride (HBA) with urea (HBD).

The final class of materials that are relevant to this thesis are liquid crystals (LCs). As the name suggests, LCs exhibit properties of both liquids and crystals (Figure 1.3), and are therefore defined as a *mesophase* (from the ancient Greek word "mesos", meaning "intermediate"). LCs display positional and/or orientational long-range order in at least one direction, and some degree of mobility (translational and rotational diffusion), i.e., the molecules have no fixed position. Conventional LCs are often rod-shaped molecules with a rigid core (commonly composed of aromatic rings) and one or more flexible alkyl chains. Many different LC phases exist, including *smectic* (or lamellar) phases, exhibiting positional order in addition to orientational order in the form of layers, and *nematic* LCs which show only orientational order (Figure 1.3). The formation of LC phases may be induced by either changes in temperature or concentration of the mesogens in a solvent, for *thermotropic* and *lyotropic* LCs, respectively.

Ionic liquid crystals (ILCs) combine the properties of LCs with those of ILs.[31] At this point, it should be mentioned that even the "isotropic liquid" state of many ILs (typically those with alkyl chains of $n > 4$) display some degree of local anisotropy, in the form of segregation of polar and non-polar domains, as shown by small and wide angle X-ray scattering (SAXS/WAXS), neutron scattering, and molecular dynamics simulations.[32–37] This intermediate-range order does not occur on the same length scale as for ILCs, which exhibit long-range positional and/or orientational order. ILCs are almost exclusively of the smectic type, stabilised by the formation of strongly bonded 'ion-rich' layers and hydrophobic layers.[31]

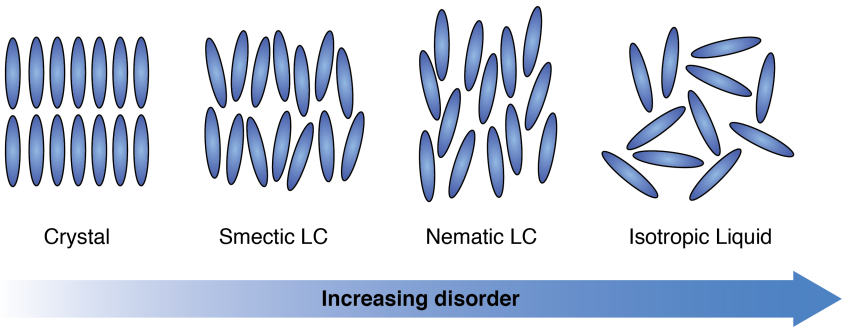

Figure 1.3: Schematic illustration of crystalline solids, smectic and nematic liquid crystals, and isotropic liquids.

1.2 Non-crystalline Pharmaceuticals

The pharmaceutical industry currently relies predominantly on solid active pharmaceutical ingredients (APIs), which exist in various forms.[38,39] However, significant problems of solid-state drugs exist, including (but not limited to) polymorphism (the existence, and sometimes interconversion, between multiple crystalline forms), poor solubility and a variety of other factors. The use of non-crystalline pharmaceuticals (ILs/DESs/ILCs) can overcome many of the problems associated with solid APIs (Figure 1.4). These include the elimination of polymorphism, improved solubility and membrane permeability, improved bioavailability and the potential for alternative methods of delivery such as transdermal delivery (through the skin).

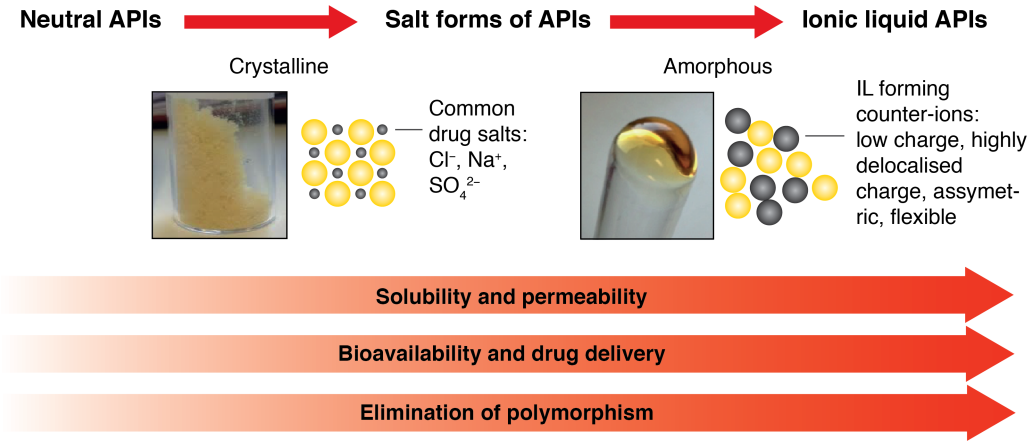

Figure 1.4: Schematic diagram of API-IL perspectives. Adapted from ref.[17]

Whilst ionic liquids have been the focus of research for electrochemical applications and their use as 'green' solvents for some time, the concept of API-ILs is relatively recent. In 2007 Rogers and co-workers reported two of the first API-ILs, ranitidine docusate and lidocaine docusate (see structures in Figure 1.5).[19]

Ranitidine hydrochloride is an anti-ulcer drug that was removed from the market due to polymorphic conversion. However, reformulation of ranitidine in combination with the hydrophobic anion, docusate (an emollient which aids absorption) produced a room temperature ionic liquid, eliminating the possibility of polymorphism. Lidocaine docusate combines the topical anaesthetic lidocaine cation with docusate to produce a hydrophobic room temperature IL, displaying increased analgesic ability of longer duration.[18] After the initial report of API-ILs, many different formulations started to appear in the literature. Rogers demonstrated that room temperature ILs could be formed from the benzalkonium cation with anions of ibuprofenate (an anti-inflammatory), sulfacetamide (an anti-bacterial) and Colawet MA-80 (a wetting agent).[19] This study showed that various combinations of cations and anions may be used in IL formulations to specifically select desired biological functions. MacFarlane and collaborators demonstrated that ions from the GRAS list (a list of substances Generally Recognised as Safe by the FDA) may be deliberately selected to inhibit crystallisation using an 'anti-crystal engineering' approach.[40] In this study, a range of quaternary ammonium compounds were paired with the artificial sweetener anions, saccharinate and acesulfamate.

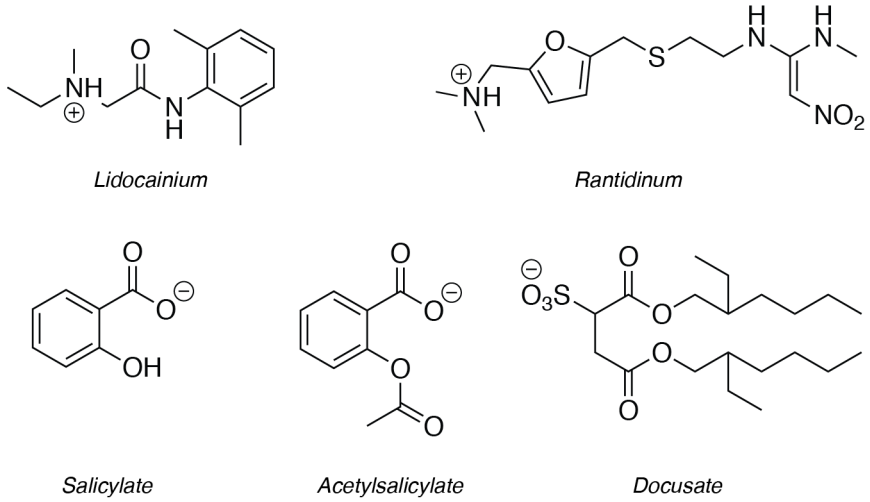

Figure 1.5: Examples of API cations and anions used in the formulation of ILs.

Further developments in API-ILs include formulations which are not purely stoichiometric or fully ionised liquid salts.[41] Whilst not technically fitting some definitions of ILs, these approaches utilise 'liquefaction' to improve the properties of APIs. In 2010, Rogers and Bica introduced the concept of *oligomeric API-ILs*, formulations containing ions and non-ionised compounds in a hydrogen-bonded network-type structure.[42] Oligomeric API-ILs are formed as a result of excess acid or base, resulting in an equilibrium between the ionised and molecular species. A

stoichiometric combination of tetrabutylphosponium salicylate produced a solid compound, however increased amounts of salicylic acid beyond one equivalent, lead to the formation of an 'oligomeric' liquid. In 2011, Rogers *et al.* demonstrated the concept of API-DESs, also termed *liquid co-crystals*, compounds with similarities to pharmaceutical co-crystals.[43] In this study of mixtures of lidocaine with various fatty acids, Rogers demonstrated that not only salt formation, but also hydrogen bonding may be the driving force for the liquefaction of solid APIs. In contrast to traditional API-ILs, liquid co-crystals can be formed from pharmaceuticals already in clinical use where the toxicity profiles are known, and can be prepared with variable stoichiometry. The role of hydrogen bonding between the components of API-ILs/DESs has been studied. MacFarlane showed that protic API-ILs with strong hydrogen-bonding, such as butylammonium acetate and tuammoniumheptane salicylate, are more rapidly transported through a model membrane compared to those that are dissociated.[44] Additionally, Rogers *et al.* studied the membrane transport of lidocaine and ibuprofen in different forms.[26] They demonstrated that hydrogen bonding within liquid co-crystals may be strong enough to remain intact in solution, thereby affecting membrane transport.

In addition to the preparation of APIs as liquid formulations, biocompatible ILs and DESs have been utilised as alternative reaction media for the preparation of pharmaceutical drugs and as drug delivery systems. The replacement of organic toxic solvents by ILs has been shown to improve reaction conditions (i.e., produce higher yields without the need for catalysts), as well as facilitate the purification of the desired product.[45] IL-based drug delivery systems have been reported in various forms, from solvation media for oral and transdermal delivery of poorly water-soluble APIs, to IL-containing vesicles, micelles and micro-emulsions as carriers for larger therapeutic biomolecules.[46–50] For example, choline geranate has shown to be an effective transdermal and oral delivery agent, facilitating the delivery of both small molecule drugs and large proteins into deep layers of the skin, and through the intestinal wall.[27,51,52] For all of the aforementioned applications, the use of ILs/DES is enhanced by the ability to selectively tune their physicochemical and biological properties by changing the anion/cation combinations, for example, to obtain high API solubility, low toxicity and biodegradability.

1.3 NMR Spectroscopy

The structural characterisation of new pharmaceuticals is a crucial part of the drug development process. The molecular structure may have an impact on drug performance, such as physical stability, solubility and absorption. In ILs, interactions between APIs and counter-ions and the arrangement of molecules into supramolecular

structures are key features. NMR spectroscopy is an ideal analytical technique for studying these systems.

Since its discovery by Bloch and Purcell in 1946,[53,54] NMR has become one of the major tools for examining the structure of molecules. NMR spectroscopy has been applied to a wide range of fields including organic chemistry, inorganic chemistry, materials science, polymer research and the study of proteins. Many significant developments have expanded the applications of NMR beyond simple structural characterisation, enabling the study of processes such as molecular dynamics, chemical exchange and molecular binding. NMR can provide information on intermolecular interactions that determine molecular arrangements. For example, ^{1}H chemical shifts are extremely sensitive to the local environment, and may be used to probe the strength of hydrogen bonds and $\pi - \pi$ stacking, the non-covalent interactions between aromatic rings. Additionally, spin-spin interactions enable the determination of through-space proximities between atoms.

Both solution- and solid-state NMR spectroscopy are used in this thesis to characterise IL/DES/ILC systems, both as neat formulations and as aqueous solutions. A solution-state NMR experiment typically produces a high-resolution spectrum with narrow linewidths due to random molecular motion inherent to liquids, which results in an averaging of anisotropic (orientation-dependent) interactions. However, an NMR spectrum for a solid sample (or viscous liquid/LC/gel) will produce broad featureless peaks, due to anisotropic interactions (dipolar coupling and chemical shift anisotropy). For this reason, the field of solid-state NMR has developed more slowly than solution-NMR. A major development was the technique of magic-angle spinning (MAS) by Andrew and Lowe,[55–57] which simulates the rapid isotropic motion of liquids by rotating the sample at the so-called magic angle (54.74°) to the external static field. MAS NMR is a powerful tool to acquire high-resolution spectra by averaging anisotropic interactions, that is applicable to a range of samples including solids, semisolids, gels and viscous samples.

There are a wide variety of NMR techniques, including both solution (i.e., static) and MAS NMR experiments, that have been applied to the investigation of the structure and dynamics of ILs/DESs,[58] as well as LCs/ILCs.[59,60] ^{1}H NMR chemical shifts have been used to probe the local environment of anions and cations, and IL-solute interactions.[61] Pulsed field gradient NMR (PFG-NMR), also referred to as diffusion-ordered NMR spectroscopy (DOSY), is used for measuring diffusion coefficients in both neat ILs and aqueous solutions. In ILs, self-diffusion of the cations and anions, typically measured by ^{1}H or ^{19}F PFG-NMR, in combination with other bulk properties such as the viscosity, density and electrical conductivity, provides information on the molecular transport and ionicity (i.e., how ionic they are). In addition to probing ionicity in ILs, PFG-NMR has been used for the

investigation of the self-aggregation behaviour of ILs, primarily those with long alkyl chains, into supramolecular structures such as micelles and bilayers.[62,63] Nuclear spin relaxation measurements provide further insight into the interactions and dynamics in ILs. NMR spin-lattice (R_1) and spin-spin (R_2) relaxation rates combined with measurements of nuclear Overhauser effect (NOE) factors have been used to investigate the reorientation dynamics in neat ILs. In a number of studies by Carper and co-workers, correlation times and activation energies for overall molecular reorientation in addition to segmental reorientations have been derived for a number of ILs from ^{13}C relaxation rates.[64–68] The two-dimensional (2D) ^{1}H-^{1}H NOE spectroscopy (NOESY) experiment, which utilises through-space dipolar couplings, has also been applied to probe intra- and intermolecular interactions within ILs, and IL/solvent interactions.[69]

The above-mentioned techniques have primarily been employed under static conditions, however, MAS NMR has also been been applied to the field of ILs. Rencurosi *et al.* showed that MAS NMR spectroscopy could significantly enhance the resolution of small organic molecules dissolved in ILs using moderate spinning speeds.[70] In addition, it was shown that MAS NMR spectroscopy may be used to directly monitor the progress of an organic reaction in IL solvents.[70] MAS NMR has also been used for the characterisation of peptides dissolved in ionic liquids,[71] and for the characterisation of protein-IL interactions.[72] A number of studies have reported the use of MAS NMR to investigate surface-immobilised ILs. Brenna *et al.* utilised one-dimensional (1D) ^{14}N and 2D ^{1}H and ^{13}C MAS NMR to characterise imidazolium-based ILs immobilised on silica suspended in DMSO, with applications for catalysis.[73] In another study, ^{1}H and ^{29}Si MAS NMR was used to monitor the adsorption of the IL methylimidazolium chloride with a silica surface through changes in chemical shifts.[74] Viau and co-workers investigated drug delivery systems prepared from poly(L-lactic acid) membranes incorporating API-ILs containing the ibuprofenate anion, using a concept similar to immobilisation of ILs on silica to achieve sustainable release kinetics.[75] ^{1}H and ^{1}H-^{13}C cross polarisation (CP) MAS NMR was used to study the API-IL polymer systems in combination with other techniques such as scanning electron microscopy and SAXS. MAS NMR was used to study IL mobility inside the membrane using narrowing of the API-IL signal as evidence of higher molecular mobility, which was dependent on the nature of the IL.

Despite the successful use of MAS NMR in the characterisation of solvent properties of ILs and its proven application for the study of crystalline pharmaceuticals (e.g., for identification of polymorphs), there are very few studies on the characterisation of intermolecular interactions in neat API-ILs/DESs. In one study, Higashi *et al.* applied MAS NMR techniques to study intermolecular interactions between the anti-inflammatory drug, mefenamic acid, and a polymer excipient in a

supersaturated solution.[76] 2D ^{1}H-^{1}H NOESY and radio frequency-driven recoupling (RFDR) MAS experiments were used to characterise hydrophobic and hydrophilic intermolecular interactions in the solution. There is the potential for MAS NMR to be further applied to the study of interactions between components in ILs/DESs, as will be demonstrated in this thesis. Knowledge of such interactions is critical as they may affect membrane-transport and thereby bioavailability of the therapeutic.[26]

NMR spectroscopy has been extensively applied to liquid crystalline materials.[59,60] Many LCs can be aligned with respect to the magnetic field of the spectrometer, enabling the acquisition of high-resolution NMR spectra for static samples. Other complex and/or viscous LCs remain in an unorientated "powder"-like state, with random orientations of LC domains across the sample, and MAS is required to obtain high-resolution spectra. NMR techniques applied to investigate the structure and dynamics of LCs include deuterium (^{2}H) NMR,[77] dipolar NMR,[78] PFG-NMR[79,80] and field-cycling NMR.[81] One of the most interesting properties of LCs, the molecular orientational order, is accessible by measuring any of the anisotropic (i.e., orientation-dependent) nuclear interactions (see Section 2.3 for further details), most commonly ^{2}H quadropolar splittings, or ^{1}H-^{13}C dipolar couplings.[82] The well-defined distance dependence of dipolar couplings means that scaling of dipolar couplings can be primarily attributed to changes in orientation of the internuclear vector. The measurement of ^{1}H-^{13}C dipolar couplings requires the use of two-dimensional separation of dipolar splittings according to chemical shifts. Since the dipolar couplings are local magnetic fields, this class of experiments is referred to as separated local field (SLF) spectroscopy.[83] ^{1}H-^{13}C SLF experiments have been applied to various phases of thermotropic LCs, in addition to lyotropic LCs such as lipid bilayers.[78,84–86] For example, Guo and Fung measured orientational order parameters for eight cyanobiphenyl LCs in the nematic phase by 2D ^{13}C SLF experiments.[87] Hong *et al.* reported segmental order parameters obtained from ^{31}P-^{1}H, ^{13}C-^{1}H, ^{1}H-^{1}H and ^{31}P-^{13}C dipolar couplings for natural abundance and unorientated phosphocholine in the lamellar phase.[88] The couplings were obtained from a variety of MAS NMR experiments, including 2D proton-detected local field (PDLF) spectroscopy.

1.4 Thesis Overview

This thesis details the characterisation of a number of liquid forms of APIs and model compounds including ILs, DESs and ILCs. ^{1}H and ^{13}C MAS NMR are the primary methods utilised and are shown to be a powerful probe of the structure and dynamics in these systems.

Chapters 2 and 3 provide the theoretical and experimental principles con-

cerning NMR, which are necessary to interpret the results of this thesis. Specifically, Chapter 2 presents the quantum mechanical foundations of NMR theory, beginning with the concept of spin angular momentum and the density operator, followed by descriptions of the key interaction Hamiltonians. Chapter 3 covers the basic concepts of a one- and two-dimensional NMR experiment, including signal detection, Fourier transformation, experimental lineshapes, coherence and phase cycling. Additionally, this chapter outlines the specific NMR sequences utilised in this thesis, including heteronuclear and homonuclear correlation experiments for probing interatomic proximities, the measurement of dipolar couplings, and the determination of relaxation times.

The first experimental results of this thesis are presented in Chapter 4, which introduces a simple method for the preparation of ILs, via acid-base neutralisation, and the measurement of a number of important physicochemical properties, including phase transition temperatures, viscosity, conductivity, diffusivity and ionicity. The relationship between structure (i.e., functional group, alkyl chain length, degree of branching, hydrogen bonding ability) and the physicochemical and transport properties is discussed for a series of 16 PILs, with a particular focus on ionicity, which is known to influence the membrane transport of API-PILs.

In Chapter 5, a model DES pharmaceutical, lidocaine ibuprofen, is investigated by MAS NMR. Specific intermolecular hydrogen bonding interactions are identified by two-dimensional ^{1}H-^{1}H NOESY and rotating-frame Overhauser effect spectroscopy (ROESY) MAS NMR experiments, and the hydrogen-bonding dynamics are quantitatively determined by the analysis of chemical exchange via variable temperature (VT) ^{1}H MAS NMR.

Chapters 6, 7 and 8 focus on an IL composed of choline and geranate (CAGE), an antimicrobial and drug delivery agent, and its structural analogues. Chapter 6 provides an introduction to CAGE, which, alongside six analogues, was characterised by differential scanning calorimetry (DSC), SAXS and NMR to investigate the thermal properties, stability, degree of supramolecular order and hydrogen bonding. CAGE and CAGE octanoic acid were found to form thermotropic liquid crystalline phases. In Chapter 7, these LC phases were further investigated by MAS NMR, to obtain site-specific order parameters from the measurement of residual ^{1}H-^{13}C and ^{1}H-^{1}H dipolar couplings. Further insight into the dynamics of the CAGE octanoic acid LC are provided from MAS NMR relaxation measurements in Chapter 8.

Chapter 2

NMR Theory

Nuclear Magnetic Resonance (NMR) spectroscopy is the primary experimental technique utilised in this thesis for the investigation of structure and dynamics in DESs, ILs and LCs. NMR spectroscopy observes resonance transitions between nuclear magnetic energy levels which occur when atomic nuclei are subjected to an external magnetic field. This chapter describes the quantum mechanical theory of nuclear magnetism, including the formalisms used to describe the state of a spin system and their time evolution under the influence of external and internal interactions. The influence of magic-angle spinning (MAS) and molecular motion, and the principles of nuclear spin relaxation and exchange are also discussed. The material in this chapter is based upon the theory presented in *Understanding NMR Spectroscopy* (J. Keeler),[89] *Spin dynamics: basics of nuclear magnetic resonance* (M. H. Levitt),[90] *Solid-State NMR: Basic Principles & Practice* (D. C. Apperley, R. K. Harris and P. Hodgkinson),[91] *Introduction to Solid-Sate NMR Spectroscopy* (M. J. Duer),[92] and *Nuclear Spin Relaxation in Liquids* (J. Kowalewski and L. Maler).[93]

2.1 NMR Fundamentals

2.1.1 Spin Angular Momentum

NMR is a property of the nucleus of an atom, concerned with spin angular momentum, also referred to as *spin*. Nuclear spin is identified by the spin angular momentum quantum number, I. The magnetic moment, $\hat{\mu}$, is related to the spin angular momentum operator by:

$$\hat{\mu} = \gamma \hat{I} \tag{2.1}$$

where γ, the gyromagnetic ratio of the nuclei of interest, is a constant unique to each type of nucleus. Application of an external magnetic field, B_0, creates distinct energy levels arising from the interaction of the magnetic moment with the applied

magnetic field. The energy of each level is:

$$E = -\hat{\mu}B_0 \tag{2.2}$$

By convention, the external magnetic field is aligned along the z-axis. For this reason, z-magnetisation is termed *longitudinal*, whilst the x- and y-components are referred to as *transverse magnetisation*. In terms of quantum mechanical operators, the energy of a nuclear spin in an external magnetic field is described by the Zeeman Hamiltonian operator, $\hat{H}_Z$:

$$\hat{H}_Z = -\hat{\mu}\hat{B}_0 = -\gamma\hbar B_0\hat{I}_z \tag{2.3}$$

where $\hbar$ is the reduced Planck constant ($h/2\pi$), $\hat{\mu}$ is the nuclear magnetic moment operator and $\hat{I}_z$ is the z-component of the nuclear spin angular momentum operator, where:

$$\hat{I}^2 = \hat{I}_x^2 + \hat{I}_y^2 + \hat{I}_z^2 \tag{2.4}$$

$\hat{I}_z$, as well as the x- and y- components of the nuclear spin operator, $\hat{I}_x$ and $\hat{I}_y$, may be represented by matrices, specifically for an isolated spin $I = 1/2$ nucleus:

$$\hat{I}_x = \frac{1}{2}\begin{pmatrix} 0 & 1 \\ 1 & 0 \end{pmatrix}, \hat{I}_y = \frac{1}{2}\begin{pmatrix} 0 & -i \\ i & 0 \end{pmatrix}, \hat{I}_z = \frac{1}{2}\begin{pmatrix} 1 & 0 \\ 0 & -1 \end{pmatrix} \tag{2.5}$$

Equation 2.3 can also be written in terms of the Larmor frequency, $\omega_0 = \gamma B_0$. The factor $\hbar$ has been omitted in order to shift the Hamiltonian from energy to angular frequency units (rad s^{-1}). This convention will be applied from this point forward to all energy operators.

$$\hat{H}_Z = \omega_0\hat{I}_z \tag{2.6}$$

The number of eigenvalues for $\hat{I}_z$ depends on the spin of the nucleus, which is specified by the nuclear spin angular momentum quantum number, I, which may take integer (0, 1, 2, etc.) or half-integer ($1/2$, $3/2$, etc.) values. $\hat{I}_z$ has $(2I + 1)$ eigenfunctions, characterised by the magnetic quantum number, m, which can take integer values between $-I$ and $+I$. Therefore for a spin $1/2$ ($I = 1/2$) nucleus, $\hat{I}_z$ has two eigenfunctions with m equal to $+1/2$ or $-1/2$. These two states are referred to as Zeeman eigenstates, and are commonly described as *spin-up*, denoted $|\alpha\rangle$ (for $m = +1/2$), and *spin-down*, denoted $|\beta\rangle$ (for $m = -1/2$).

$$\begin{aligned} \hat{I}_z|\alpha\rangle &= +\frac{1}{2}|\alpha\rangle \\ \hat{I}_z|\beta\rangle &= -\frac{1}{2}|\beta\rangle \end{aligned} \tag{2.7}$$

By combining these expressions with Equation 2.6, the energy of interaction of the spin with the magnetic field can be described by:

$$\begin{aligned}\hat{H}_z\left|\alpha\right\rangle &= +\frac{1}{2}\omega_0\left|\alpha\right\rangle \\ \hat{H}_z\left|\beta\right\rangle &= -\frac{1}{2}\omega_0\left|\beta\right\rangle\end{aligned} \tag{2.8}$$

showing that the energy difference between the two states is equal to the Larmor frequency, ω_0.

Quantum mechanics does not specify that a spin nuclei must purely exist in either eigenstate. The wavefunction which contains a complete description of the system, for a single spin, can be described as a linear superposition of the eigenfunctions of the Zeeman Hamiltonian.

$$\left|\psi\right\rangle = c_\alpha\left|\alpha\right\rangle + c_\beta\left|\beta\right\rangle \tag{2.9}$$

where c_α and c_β are complex coefficients with $\left|c_\alpha\right|^2$ and $\left|c_\beta\right|^2$ being the probabilities of measuring the corresponding state. In quantum mechanics, the average value of any observable, $\left\langle\hat{A}\right\rangle$, is known as the expectation value, and is described by:

$$\left\langle\hat{A}\right\rangle = \left\langle\psi|\hat{A}|\psi\right\rangle \tag{2.10}$$

The expectation value for the z-component of magnetisation for a single spin may be calculated:

$$\begin{aligned}&\left\langle\hat{I}_z\right\rangle = \left\langle\psi|\hat{I}_z|\psi\right\rangle \\ &= \left[c_\alpha^*\left\langle\alpha\right| + c_\beta^*\left\langle\beta\right|\right]\hat{I}_z\left[c_\alpha\left|\alpha\right\rangle + c_\beta\left|\beta\right\rangle\right] \\ &= c_\alpha c_\alpha^*\left\langle\alpha\right|\hat{I}_z\left|\alpha\right\rangle + c_\alpha^* c_\beta\left\langle\alpha\right|\hat{I}_z\left|\beta\right\rangle + c_\alpha c_\beta^*\left\langle\beta\right|\hat{I}_z\left|\alpha\right\rangle + c_\beta c_\beta^*\left\langle\beta\right|\hat{I}_z\left|\beta\right\rangle\end{aligned} \tag{2.11}$$

Substitution of Equation 2.7 into this expression gives:

$$\begin{aligned}\left\langle\hat{I}_z\right\rangle &= \tfrac{1}{2}c_\alpha c_\alpha^*\left\langle\alpha|\alpha\right\rangle + c_\alpha^* c_\beta\left\langle\alpha|\beta\right\rangle + c_\alpha c_\beta^*\left\langle\beta|\alpha\right\rangle + c_\beta c_\beta^*\left\langle\beta|\beta\right\rangle \\ &= \tfrac{1}{2}\left(c_\alpha c_\alpha^* - c_\beta c_\beta^*\right) \\ &= \tfrac{1}{2}\left|c_\alpha\right|^2 - \tfrac{1}{2}\left|c_\beta\right|^2\end{aligned} \tag{2.12}$$

The expectation values of the transverse spin angular momentum operators may also be expressed in terms of the coefficients c_α and c_β:

$$\begin{aligned}\left\langle\hat{I}_x\right\rangle &= \tfrac{1}{2}\left(c_\alpha c_\beta^* - c_\beta c_\alpha^*\right) \\ \left\langle\hat{I}_y\right\rangle &= \tfrac{1}{2}i\left(c_\alpha c_\beta^* - c_\beta c_\alpha^*\right)\end{aligned} \tag{2.13}$$

The expressions above refer only to a single spin. In a sample, which contains multiple spins orientated in different directions, the sum of the individual magnetic moments is referred to as the *bulk magnetisation*. To determine the bulk magnetisation, M, it is necessary to multiply by γN (where N is the total number of spins) and take the ensemble average, which involves adding the contribution from each spin in the sample and then dividing by the number of spins. The ensemble average is represented by the overbar in the following equations.

$$\begin{aligned} M_x &= \gamma N \overline{\left\langle \hat{I}_x \right\rangle} \\ M_y &= \gamma N \overline{\left\langle \hat{I}_y \right\rangle} \\ M_z &= \gamma N \overline{\left\langle \hat{I}_z \right\rangle} \end{aligned} \tag{2.14}$$

A more convenient approach, is *Density Operator Theory*, which is discussed in the next section.

2.1.2 The Density Operator Formalism

Density Operator Theory is a method for describing the state of a spin system. Its convenience comes from the fact that the ensemble averaging is contained within the density operator, meaning that the bulk magnetisation may be determined directly from the density operator. Recalling the superposition state for a spin $1/2$ nuclei (Equation 2.9), $|\alpha\rangle$ and $|\beta\rangle$ may be represented as vectors:

$$\begin{aligned} |\alpha\rangle &= \begin{pmatrix} 1 \\ 0 \end{pmatrix} \\ |\beta\rangle &= \begin{pmatrix} 0 \\ 1 \end{pmatrix} \end{aligned} \tag{2.15}$$

Substitution of these vectors into Equation 2.9 gives:

$$\begin{aligned} |\psi\rangle &= \begin{pmatrix} c_\alpha \\ c_\beta \end{pmatrix} \\ \langle\psi| &= \begin{pmatrix} c_\alpha^* & c_\beta^* \end{pmatrix} \end{aligned} \tag{2.16}$$

A generalised operator $\hat{A}$, may be represented as a matrix, as shown for the nuclear spin operators in Equation 2.5:

$$\hat{A} = \begin{pmatrix} A_{\alpha\alpha} & A_{\alpha\beta} \\ A_{\beta\alpha} & A_{\beta\beta} \end{pmatrix} \tag{2.17}$$

The expectation value defined in Equation 2.10 may be calculated using Equations 2.16 and 2.17:

$$\begin{aligned}\left\langle \hat{A} \right\rangle &= \left\langle \psi | \hat{A} | \psi \right\rangle \\ &= \begin{pmatrix} c_\alpha^* c_\beta^* \end{pmatrix} \begin{pmatrix} A_{\alpha\alpha} & A_{\alpha\beta} \\ A_{\beta\alpha} & A_{\beta\beta} \end{pmatrix} \begin{pmatrix} c_\alpha \\ c_\beta \end{pmatrix} \\ &= c_\alpha^* c_\alpha A_{\alpha\alpha} + c_\beta^* c_\beta A_{\beta\beta} + c_\alpha^* c_\beta A_{\alpha\beta} + c_\beta^* c_\alpha A_{\beta\alpha}\end{aligned} \tag{2.18}$$

The density operator is defined as:

$$\hat{\rho} = \overline{|\psi\rangle \langle\psi|} \tag{2.19}$$

The overbar indicates an ensemble average and will not be used subsequently. For the single-spin system, the density matrix is:

$$\hat{\rho} = |\psi\rangle \langle\psi| = \begin{pmatrix} c_\alpha \\ c_\beta \end{pmatrix} \begin{pmatrix} c_\alpha^* & c_\beta^* \end{pmatrix} = \begin{pmatrix} c_\alpha c_\alpha^* & c_\alpha c_\beta^* \\ c_\beta c_\alpha^* & c_\beta c_\beta^* \end{pmatrix} \tag{2.20}$$

Taking the product of the density matrix and $\hat{A}$ produces another matrix:

$$\begin{aligned}\hat{\rho}\hat{A} &= \begin{pmatrix} c_\alpha c_\alpha^* & c_\alpha c_\beta^* \\ c_\beta c_\alpha^* & c_\beta c_\beta^* \end{pmatrix} \begin{pmatrix} A_{\alpha\alpha} & A_{\alpha\beta} \\ A_{\beta\alpha} & A_{\beta\beta} \end{pmatrix} \\ &= \begin{pmatrix} c_\alpha c_\alpha^* A_{\alpha\alpha} + c_\alpha c_\beta^* A_{\beta\alpha} & c_\alpha c_\alpha^* A_{\alpha\beta} + c_\alpha c_\beta^* A_{\beta\beta} \\ c_\beta c_\alpha^* A_{\alpha\alpha} + c_\beta c_\beta^* A_{\beta\alpha} & c_\alpha c_\beta^* A_{\alpha\beta} + c_\beta c_\beta^* A_{\beta\beta} \end{pmatrix}\end{aligned} \tag{2.21}$$

The trace of this matrix is:

$$Tr\left(\hat{\rho}\hat{A}\right) = c_\alpha^* c_\alpha A_{\alpha\alpha} + c_\beta^* c_\beta A_{\beta\beta} + c_\alpha^* c_\beta A_{\alpha\beta} + c_\beta^* c_\alpha A_{\beta\alpha} \tag{2.22}$$

This is the same as the expectation value in Equation 2.18. Therefore, it follows that:

$$\left\langle \hat{A} \right\rangle = Tr\left(\hat{\rho}\hat{A}\right) \tag{2.23}$$

Whilst the above description of the density matrix formalism describes only a single spin, it may be used to describe large systems containing many nuclear spins. Since the coefficients c_α and c_β are complex, they may be written in polar notation, a combination of a real coefficient (r_α and r_β), and a phase term (ϕ_α and ϕ_β). Using this notation, the density operator for an individual spin becomes:

$$\hat{\rho} = \begin{pmatrix} r_\alpha r_\alpha & r_\alpha r_\beta e^{i\left(\phi_\alpha - \phi_\beta\right)} \\ r_\alpha r_\beta e^{i\left(\phi_\beta - \phi_\alpha\right)} & r_\beta r_\beta \end{pmatrix} \tag{2.24}$$

In a system of many isolated spins, there will be a random distribution of phase angles, ϕ, leading to the off-diagonal terms averaging to zero in the density matrix:

$$\hat{\rho} = \begin{pmatrix} r_\alpha r_\alpha & 0 \\ 0 & r_\beta r_\beta \end{pmatrix} \tag{2.25}$$

The diagonal terms of the density matrix are described as the *populations* and describe the probabilities of spins existing in the $|\alpha\rangle$ and $|\beta\rangle$ eigenstates. The off-diagonal terms only exist if there is a *phase coherence* between the individual spins, and such a state is therefore termed *coherence*. Coherences are generated by the application of transverse oscillating magnetic fields in the form of radio-frequency (rf) pulses and will be discussed in detail in Section 2.2.2. The power of the density operator approach is the ability to describe and follow the state of a system of multiple coupled spins. A system of two-coupled spins may be described by a wavefunction with eigenstates such as $|\alpha\alpha\rangle$ (both spin-up), and the wavefunction expressed in terms of the corresponding eigenvalues:

$$|\psi\rangle = \begin{pmatrix} c_{\alpha\alpha} \\ c_{\alpha\beta} \\ c_{\beta\alpha} \\ c_{\beta\beta} \end{pmatrix} \tag{2.26}$$

The density matrix for an ensemble of coupled spin $1/2$ pairs is constructed in the same manner as shown for a single spin in equation 2.20:

$$\hat{\rho} = \begin{pmatrix} c_{\alpha\alpha}c^*_{\alpha\alpha} & c_{\alpha\alpha}c^*_{\alpha\beta} & c^*_{\alpha\alpha}c_{\beta\alpha} & c^*_{\alpha\alpha}c_{\beta\beta} \\ c_{\alpha\beta}c^*_{\alpha\alpha} & c_{\alpha\beta}c^*_{\alpha\beta} & c^*_{\alpha\beta}c_{\beta\alpha} & c^*_{\alpha\beta}c_{\beta\beta} \\ c_{\beta\alpha}c^*_{\alpha\alpha} & c_{\beta\alpha}c^*_{\alpha\beta} & c^*_{\beta\alpha}c_{\beta\alpha} & c^*_{\beta\alpha}c_{\beta\beta} \\ c_{\beta\beta}c^*_{\alpha\alpha} & c_{\beta\beta}c^*_{\alpha\beta} & c^*_{\beta\beta}c_{\beta\alpha} & c^*_{\beta\beta}c_{\beta\beta} \end{pmatrix} \tag{2.27}$$

The principal diagonal terms again correspond to the populations of the individual eigenstates whilst the off-diagonal terms are coherences linking these states. The usefulness of the density operator approach is the ability to determine the state of the spin system at any stage of an NMR experiment, provided the Hamiltonians of the relevant interactions are known. The time evolution of the density operator can be derived using the *time-dependent Schrödinger equation*:

$$\begin{aligned} \frac{d}{dt}|\psi(t)\rangle &= \frac{-i}{\hbar}\hat{H}|\psi(t)\rangle \\ \frac{d}{dt}\langle\psi(t)| &= \frac{-i}{\hbar}\langle\psi(t)|\hat{H} \end{aligned} \tag{2.28}$$

From the definition of the density operator (Equation 2.19) it follows that:

$$\begin{aligned}\frac{\delta}{\delta t}\hat{\rho}(t) &= \frac{\delta}{\delta t}\left(|\psi(t)\rangle\langle\psi(t)|\right) \\ &= \left(\frac{\delta}{\delta t}|\psi(t)\rangle\right)\langle\psi(t)| + |\psi(t)\rangle\left(\frac{\delta}{\delta t}\langle\psi(t)|\right) \\ &= -i\hat{H}|\psi\rangle\langle\psi| + i|\psi\rangle\langle\psi|\hat{H} \\ &= -i\left[\hat{H},\hat{\rho}(t)\right]\end{aligned} \tag{2.29}$$

This is known as the *Liouville-Von Neumann equation* of which the solution is:

$$\hat{\rho}(t) = \exp(-i\hat{H}t)\hat{\rho}(0)\exp(i\hat{H}t) \tag{2.30}$$

where the terms, $\exp(-i\hat{H}t)$ and $\exp(i\hat{H}t)$, are known as *propagators*. Using Equation 2.30 with the appropriate Hamiltonian operator, the effects of *rf* pulses and time-evolution periods in NMR pulse sequences may be followed. The Hamiltonians of such interactions are outlined in the Sections 2.2 and 2.3, below. First, an alternative formalism to density operator theory, the product operator formalism, is described.

2.1.3 The Product Operator Formalism

The *product operator formalism* is a simplification of the density operator formalism that provides a straightforward method for following the evolution of the bulk magnetisation during an NMR experiment. In Chapter 3, some of the specific experiments utilised in this thesis are described using product operators.

If $\hat{H}$ and $\hat{\rho}$ are expressed in terms of the angular momentum operators, Equation 2.30 can easily be solved by following a few standard rules based on the known solutions. For example, a $\pi/2$ pulse (see Section 2.2.2) about the x-axis is known to 'rotate' z-magnetisation towards the y-axis. Using arrow notation, connecting the 'old' and 'new' density operators, this may be written in shorthand as:

$$\hat{I}_z \xrightarrow{\frac{\pi}{2}\hat{I}_x} -\hat{I}_y \tag{2.31}$$

Evolution under internal interactions (chemical shift and J-coupling) can also be described using the product operator formalism; for example:

$$\hat{I}_x \xrightarrow{\Omega\hat{I}_z t} \hat{I}_x\cos\Omega t + \hat{I}_y\sin\Omega t \tag{2.32}$$

and

$$\hat{I}_x \xrightarrow{\pi J_{IS}t\hat{I}_z\hat{S}_z} \hat{I}_x\cos\pi J_{IS}t + 2\hat{I}_y\hat{S}_z\sin\pi J_{IS}t \tag{2.33}$$

where $\Omega\hat{I}_z$ is the free precession Hamiltonian, and $\pi J_{IS}t\hat{I}_z\hat{S}_z$ is the Hamiltonian

for the J-coupling between two spins, I and S. Further details on the interaction Hamiltonians are presented in the following sections.

2.2 External Interactions

2.2.1 Zeeman Interaction

The Zeeman interaction is the interaction between a nuclear spin and the external magnetic field, B_0. The Zeeman interaction Hamiltonian, as stated in Equation 2.6 is:

$$\hat{H}_Z = \omega_0 \hat{I}_z \tag{2.34}$$

This may also be described as seen from a reference frame that is rotating at a frequency, ω_{rf}, the *rotating frame*, and is termed the free evolution Hamiltonian:

$$\hat{H}_\Omega = \Omega \hat{I}_z \tag{2.35}$$

where Ω is the relative Larmor frequency or offset frequency, the difference between the Larmor frequency and rotating frame frequency:

$$\Omega = \omega_0 - \omega_{rf} \tag{2.36}$$

To determine the effect of the free evolution Hamiltonian on the density operator, the solution to the Liouville-Von Neumann equation (Equation 2.30) must be applied. The propagators formed from the Hamiltonian may be expressed in matrix form:

$$\exp(\pm i\Omega t \hat{I}_z) = \begin{pmatrix} \exp\left(\pm\frac{1}{2}i\Omega t\right) & 0 \\ 0 & \exp\left(\mp\frac{1}{2}i\Omega t\right) \end{pmatrix} \tag{2.37}$$

For example, the evolution of the density matrix starting at $\hat{\rho} = \hat{I}_x$ is:

$$\begin{aligned} \hat{\rho}(t) &= \begin{pmatrix} \exp\left(-\frac{1}{2}i\Omega t\right) & 0 \\ 0 & \exp\left(\frac{1}{2}i\Omega t\right) \end{pmatrix} \begin{pmatrix} 0 & \frac{1}{2} \\ \frac{1}{2} & 0 \end{pmatrix} \begin{pmatrix} \exp\left(\frac{1}{2}i\Omega t\right) & 0 \\ 0 & \exp\left(-\frac{1}{2}i\Omega t\right) \end{pmatrix} \\ &= \begin{pmatrix} 0 & \frac{1}{2}\exp\left(-i\Omega t\right) \\ \frac{1}{2}\exp\left(i\Omega t\right) & 0 \end{pmatrix} \end{aligned} \tag{2.38}$$

An NMR signal, corresponding to an induced current in a coil, can be represented by the *raising operator*:

$$\hat{I}_+ = \hat{I}_x + i\hat{I}_y = \begin{pmatrix} 0 & 1 \\ 0 & 0 \end{pmatrix} \tag{2.39}$$

From Equation 2.23, the detected NMR signal, under a resonance offset, is given by:

$$\begin{aligned} S(t) &= Tr\left(\hat{\rho}\hat{I_+}\right) \\ &= Tr\left[\begin{pmatrix} 0 & \frac{1}{2}\exp\left(-i\Omega t\right) \\ \frac{1}{2}\exp\left(i\Omega t\right) & 0 \end{pmatrix}\begin{pmatrix} 0 & 1 \\ 0 & 0 \end{pmatrix}\right] \\ &= \frac{1}{2}\left(\cos\left(\Omega t\right) + i\sin\left(\Omega t\right)\right) \end{aligned} \tag{2.40}$$

showing that in the presence of the external magnetic field, transverse magnetisation rotates about the field at the offset frequency (as seen from the rotating frame). The simultaneous detection of the real and imaginary components of the NMR signal is described further in Section 3.1.1.

2.2.2 Radio-Frequency Pulses

In order to generate transverse magnetisation, a radio-frequency (rf) pulse creates a magnetic field in the transverse plane, B_1. The Hamiltonian for a strong rf pulse about the x-axis is:

$$\hat{H}_{rf} = \omega_1 \hat{I}_x \tag{2.41}$$

where ω_1 is the *nutation frequency*, the frequency at which the pulse rotates the magnetisation about the x-axis, described by:

$$\omega_1 = \gamma B_1 \tag{2.42}$$

The propagators formed from the Hamiltonian are:

$$\exp(\pm i\omega_1 t\hat{I}_x) = \begin{pmatrix} \cos\left(\frac{1}{2}\omega_1 t\right) & \pm i\sin\left(\frac{1}{2}\omega_1 t\right) \\ \pm i\sin\left(\frac{1}{2}\omega_1 t\right) & \cos\left(\frac{1}{2}\omega_1 t\right) \end{pmatrix} \tag{2.43}$$

Assuming the system starts at thermal equilibrium ($\hat{\rho} = \hat{I}_z$), the evolution of the density matrix under the influence of the rf pulse may be followed using the Liouville-Von Neumann equation (Equation 2.30):

$$\begin{aligned} \hat{\rho}(t) &= \exp(-i\hat{H}t)\hat{\rho}(0)\exp(i\hat{H}t) \\ &= \begin{pmatrix} \cos\left(\frac{1}{2}\omega_1 t\right) & -i\sin\left(\frac{1}{2}\omega_1 t\right) \\ -i\sin\left(\frac{1}{2}\omega_1 t\right) & \cos\left(\frac{1}{2}\omega_1 t\right) \end{pmatrix}\begin{pmatrix} \frac{1}{2} & 0 \\ 0 & \frac{1}{2} \end{pmatrix}\begin{pmatrix} \cos\left(\frac{1}{2}\omega_1 t\right) & i\sin\left(\frac{1}{2}\omega_1 t\right) \\ i\sin\left(\frac{1}{2}\omega_1 t\right) & \cos\left(\frac{1}{2}\omega_1 t\right) \end{pmatrix} \\ &= \frac{1}{2}\begin{pmatrix} \cos\left(\omega_1 t\right) & i\sin\left(\omega_1 t\right) \\ -i\sin\left(\omega_1 t\right) & -\cos\left(\omega_1 t\right) \end{pmatrix} \\ &= \hat{I}_z\cos(\omega_1 t) - \hat{I}_y\sin(\omega_1 t) \end{aligned} \tag{2.44}$$

The above expression shows that the effect of the *rf* pulse on the equilibrium population state is to generate *coherences* (off-diagonal terms) between the spin eigenstates. In the case of a 90° pulse (where $\omega_1 t = \frac{\pi}{2}$), this term simplifies to:

$$\hat{\rho}(t) = \frac{1}{2}\begin{pmatrix} 0 & i \\ -i & 0 \end{pmatrix} = -\hat{I}_y \tag{2.45}$$

showing that the pulse rotates the z-magnetisation into the $-y$ direction in the transverse plane. A 180° pulse flips the magnetisation to the $-z$ axis. Each NMR experiment can be represented by a schematic diagram showing the pulses (commonly 90° and 180°) and delays, referred to as a *pulse sequence*. Several of these will be illustrated in Chapter 3.

2.3 Internal Interactions

The internal interactions of interest here are the chemical shielding ($\hat{H}_\sigma$), dipolar coupling ($\hat{H}_D$) and J-coupling ($\hat{H}_J$). These interactions may be utilised in experiments to provide molecular-level information on a system, as described in Chapter 3. The quadrupolar interaction ($\hat{H}_Q$) only plays a role for nuclei with $I > 1/2$ and will therefore not be discussed further in this thesis, which focuses on the spin $1/2$ ^{1}H and ^{13}C nuclei. Before introducing the specific forms of the internal interaction Hamiltonians, it is necessary to first describe the axis systems in which they are best described.

2.3.1 Irreducible Spherical Tensors and Frame Transformations

It is most convenient to define the Hamiltonians of internal interactions in their own *Principal Axis System* (PAS) such that the interaction tensor is diagonal. The general form of the Hamiltonian in the PAS is:

$$\begin{aligned} \hat{H}_A^{PAS} &= \hat{I} \cdot \tilde{A}^{PAS} \cdot \hat{S} \\ &= \begin{pmatrix} I_x & I_y & I_z \end{pmatrix} \begin{pmatrix} A_{xx} & 0 & 0 \\ 0 & A_{yy} & 0 \\ 0 & 0 & A_{zz} \end{pmatrix} \begin{pmatrix} S_x \\ S_y \\ S_z \end{pmatrix} \end{aligned} \tag{2.46}$$

The PAS does not usually coincide with the laboratory frame. Since relative orientations differ between interactions, it is necessary to rotate spin interactions from their individual PAS to the laboratory frame of reference to correctly describe the effect of the internal Hamiltonian on the NMR signal. In general, three angles are needed to define a transformation in three-dimensional space, known as *Euler angles*, conventionally denoted α, β and γ, as shown in Figure 2.1.

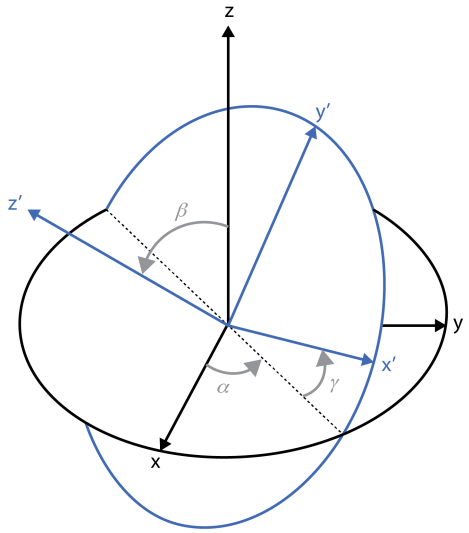

Figure 2.1: The Euler angles used to describe a rotation between two frames of reference. For the transformation of an original axis system (x, y, z; black) to a new axis system (x′, y′, z′; blue), the axes are first rotated about the z-axis by α, followed by a rotation about the new y-axis (y′) through β and then a final rotation through γ about the final z-axis (z′).

By expressing the internal interaction Hamiltonians in terms of a spherical tensor basis, the frame transformations are simplified. The general form of the Hamiltonian becomes:

$$\hat{H}_A = \sum_{j=0}^{2} \sum_{m=-j}^{+j} (-1)^m \hat{T}_{j-m} A_{jm} \tag{2.47}$$

where $\hat{T}_{j-m}$ and A_{j-m} are spherical tensor operators representing the spin and spatial components, respectively, and j describes the rank of the tensors ($j = 0, 1, 2$) and m describes the order of the tensors and can take $2j + 1$ values from $-j$ to j. The general Hamiltonian in the PAS in terms of the spherical tensor operators, A_{j-m} and $\hat{T}_{j-m}$, is:

$$\hat{H}_A^{PAS} = A_{00}^{PAS}\hat{T}_{00} + A_{20}^{PAS}\hat{T}_{20} + A_{22}^{PAS}\hat{T}_{2-2} + A_{2-2}^{PAS}\hat{T}_{22} \tag{2.48}$$

In order to perform a rotation from the PAS to the LAB frame, a spherical tensor component $A_{jm'}^{LAB}$ is given by:

$$A_{jm'}^{LAB} = \sum_{m} A_{jm}^{PAS} D_{mm'}^{j} (\alpha_{PL}, \beta_{PL}, \gamma_{PL}) \tag{2.49}$$

where the Euler angles $(\alpha_{PL}, \beta_{PL}, \gamma_{PL})$ describe the relative orientation of the PAS (P) and laboratory (L) frames and $D_{mm'}^{j} (\alpha_{PL}, \beta_{PL}, \gamma_{PL})$ represents the Wigner

matrix elements:

$$D^{j}_{mm'}(\alpha,\beta,\gamma) = exp(-im'\alpha)d^{j}_{mm'}(\beta)\,exp(-im\gamma) \tag{2.50}$$

where $d^{j}_{mm'}(\beta)$ are the reduced Wigner rotation matrices.

2.3.2 The Secular Approximation

As the spin dynamics is dominated by the Zeeman interaction, the *secular approximation* may be used to simplify the total Hamiltonian by treating all other interactions as a first-order perturbation to the Zeeman Hamiltonian:

$$\hat{H}_{total} = \hat{H}_0 + \hat{H}_1 \tag{2.51}$$

where $\hat{H}_0$ is equal to the Zeeman Hamiltonian, and $\hat{H}_1$ is composed of all remaining interactions. Only components of the interaction Hamiltonian that commute with the Zeeman interaction affect the spin energy levels to first order:

$$\left[\hat{I}_z, \hat{T}_{jm}\right] = m\hat{T}_{jm} \tag{2.52}$$

This condition is satisfied for the *secular* terms, whereby the tensor order $m = 0$. Under the secular approximation, the first-order Hamiltonian in the laboratory frame is given by:

$$\hat{H}^{LAB}_{A} = A^{LAB}_{00}\hat{T}_{00} + A^{LAB}_{20}\hat{T}_{20} \tag{2.53}$$

This assumption is valid in high magnetic fields and is therefore sometimes referred to as the *high-field approximation.*

2.3.3 Chemical Shielding

The chemical shielding interaction arises from the effect of the electronic environment on the nuclei spin. In the strong external field, circulating electrons create a secondary opposing local magnetic field, B_e which shields nuclei from the external field. The magnitude of this secondary field varies between nuclei sites due to the arrangement of electrons within the molecule. As a result, the Larmor frequency varies between nuclei, resulting in an NMR spectrum with peaks at a range of frequencies.

The Hamiltonian describing the chemical shielding interaction, in Cartesian form, is:

$$\hat{H}^{PAS}_{\sigma} = \gamma\hat{I}\cdot\tilde{\sigma}\cdot\hat{B}_0 \tag{2.54}$$

where $\tilde{\sigma}$ is the chemical shielding tensor. Expressed in terms of spherical tensor operators, the Hamiltonian is given by Equation 2.48. Upon rotation to the laboratory

frame the Hamiltonian becomes:

$$\hat{H}_{\sigma}^{LAB} = -\omega_0 \left[\sigma_{iso} + \frac{\sigma_{aniso}}{2}\left(3\cos^2\beta_{PL} - 1 + \eta\sin^2\beta_{PL}\cos 2\alpha_{PL}\right)\hat{I}_z\right] \tag{2.55}$$

where the isotropic and anisotropic chemical shielding, and asymmetry parameter, η, are defined in terms of the shielding tensor in its PAS by:

$$\begin{aligned}
\sigma_{iso} &= \frac{1}{3}(\sigma_{xx}^{PAS} + \sigma_{yy}^{PAS} + \sigma_{zz}^{PAS}) \\
\sigma_{aniso} &= \sigma_{zz}^{PAS} - \sigma_{iso} \\
\eta &= \frac{\sigma_{zz}^{PAS} - \sigma_{iso}}{\sigma_{aniso}}
\end{aligned} \tag{2.56}$$

In practice, rather than reporting the values of the chemical shielding tensor, the field-independent *chemical shift*, δ_{iso}, is reported, relative to a reference compound in parts per million (ppm):

$$\delta_{iso} = \frac{\nu_{sample} - \nu_{ref}}{\nu_{ref}} \times 10^6 \tag{2.57}$$

The corresponding *chemical shift tensor* has elements:

$$\delta_{\alpha\beta} = \frac{\sigma_{\alpha\beta,ref} - \sigma_{\alpha\beta}}{1 - \sigma_{\alpha\beta}} \tag{2.58}$$

where $\sigma_{\alpha\beta}$ is the $\alpha\beta$ element of the shielding tensor in some axis frame, and $\delta_{\alpha\beta}$ is the corresponding element of the chemical shift tensor in the same frame. The principle components of the chemical shift tensor can be represented as the dimensions of an ellipsoid. In analogy to Equation 2.56, the isotropic chemical shift, chemical shift anisotropy and asymmetry are defined as:

$$\begin{aligned}
\delta_{iso} &= \frac{1}{3}(\delta_{xx}^{PAS} + \delta_{yy}^{PAS} + \delta_{zz}^{PAS}) \\
\delta_{aniso} &= \delta_{zz}^{PAS} - \delta_{iso} \\
\eta &= \frac{\delta_{zz}^{PAS} - \delta_{iso}}{\delta_{aniso}}
\end{aligned} \tag{2.59}$$

Equation 2.54 implies that each different molecular orientation, corresponding to a different orientation of the PAS with respect to the external magnetic field, has a different chemical shift associated with it. This orientation dependence is referred to as *chemical shift anisotropy* (CSA). This is illustrated in Figure 2.2a for the case of an orientated sample. In a solid powder sample, the lines from the different molecular orientations overlap to form a continuous lineshape, referred to as a *powder pattern*, which is determined by the principal components of the chemical shift tensor (Figure 2.2b; top spectrum).

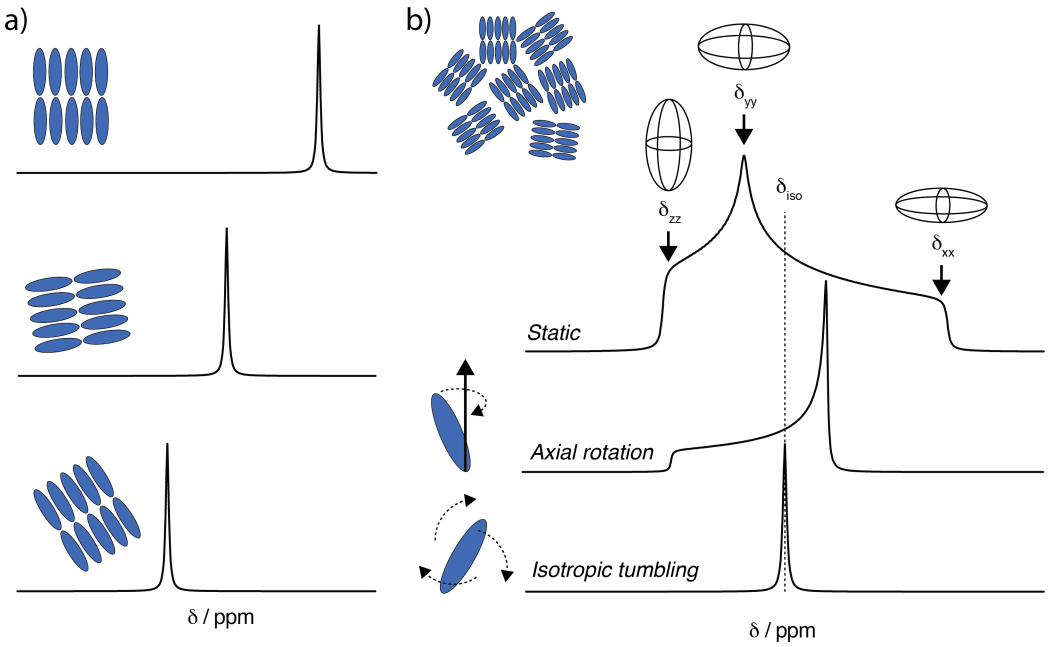

Figure 2.2: (a) Schematic illustration showing the orientation dependence of the chemical shift for an aligned sample. (b) A chemical shift anisotropic powder lineshape ($\eta = 0.5$) under static conditions (top spectrum). The shape of the powder pattern is determined by the principal values of the chemical shift tensor (depicted as an ellipsoid), δ_{xx}, δ_{yy} and δ_{zz}. Fast axial rotation averages two components of the chemical shift tensor to produce an axially symmetric CSA pattern (centre spectrum), whilst isotropic tumbling results in an isotropic lineshape (bottom spectrum).

In an *isotropic liquid*, the molecules undergo molecular tumbling, sampling every possible molecular orientation with equal probability. Provided that the tumbling is fast on the timescale of the NMR experiment, the anisotropic component of the chemical shift is averaged out, resulting in a single, isotropic shift for each electronic environment (Figure 2.2b; bottom spectrum). In *anisotropic liquids* (liquid crystals), and solid or solid-like (e.g. gels) samples, where molecular motions sample only a subset of possible orientations, the CSA is partially averaged to a value that depends on the amplitude of the motion. As an example, a rapid rotation about a single axis resulting in averaging of two components of the chemical shift tensor, is shown in Figure 2.2b (middle spectrum). The effect of CSA in the appearance of an NMR spectrum of solids (or semi-solids, liquid crystals, etc.) can be removed by magic-angle spinning (MAS), which will be discussed in Section 2.3.5.

2.3.4 Dipolar Coupling

Nuclear spins generate a local magnetic field which is felt by surrounding spins. This interaction, termed dipolar coupling, may be visualised as a pair of interacting bar

magnets (Figure 2.3a). The dipolar coupling is mediated through-space, and the strength of the interaction depends on the internuclear distance (proportional to r^{-3}). The dipolar coupling spin Hamilton, in Cartesian coordinates, is given by:

$$\hat{H}_D = -2\hat{I} \cdot \tilde{D} \cdot \hat{S} \tag{2.60}$$

The dipolar-coupling tensor, $\tilde{D}$ contains the principal values $-\frac{d}{2}$, $-\frac{d}{2}$ and $+d$, where the dipolar coupling constant, d (in units of rad s^{-1}), is defined as:

$$d = -\frac{\mu_0 \gamma_1 \gamma_2 \hbar}{4\pi r^3} \tag{2.61}$$

where μ_0 is the permeability of free space.

In order to understand the effect of dipolar coupling on an NMR spectrum, it is necessary to transform from the PAS of the dipolar Hamiltonian, aligned along the internuclear vector (Figure 2.3a), to the laboratory frame, as explained in Section 2.3.1. The dipolar coupling Hamiltonian in spherical tensor form is:

$$\hat{H}_D^{PAS} = A_{20}^{PAS} \hat{T}_{20} \tag{2.62}$$

where the spatial component is given by:

$$A_{20}^{PAS} = \sqrt{6} d_{IS} \tag{2.63}$$

Recalling that due to the secular approximation only $m = 0$ terms remain, when rotated to the laboratory frame, the spatial component of the dipolar Hamiltonian for the static case (i.e. by a rotation R_{PL}) is given by:

$$A_{20}^{L,\text{static}} = \sqrt{6} d_{IS} \frac{1}{2} (3\cos^2 \beta_{PL} - 1) \tag{2.64}$$

The spin component is given by:

$$\hat{T}_{20} = \frac{1}{\sqrt{6}} \left(\hat{I}_z \hat{S}_z - \frac{1}{2} \left[\hat{I}_x \hat{S}_x + \hat{I}_y \hat{S}_y \right] \right) \tag{2.65}$$

As described in Section 2.3.2, the secular approximation is based on energy level differences, and the dipolar coupling Hamiltonian therefore depends on whether the spins are the same nuclear species (*homonuclear dipolar coupling*), or if the spins are of different species (*heteronuclear dipolar coupling*). For this reason, in the case of the heteronuclear dipolar coupling, only the $\hat{I}_z \hat{S}_z$ term in Equation (2.65) is significant. Combination of the spatial and spin components gives the expressions

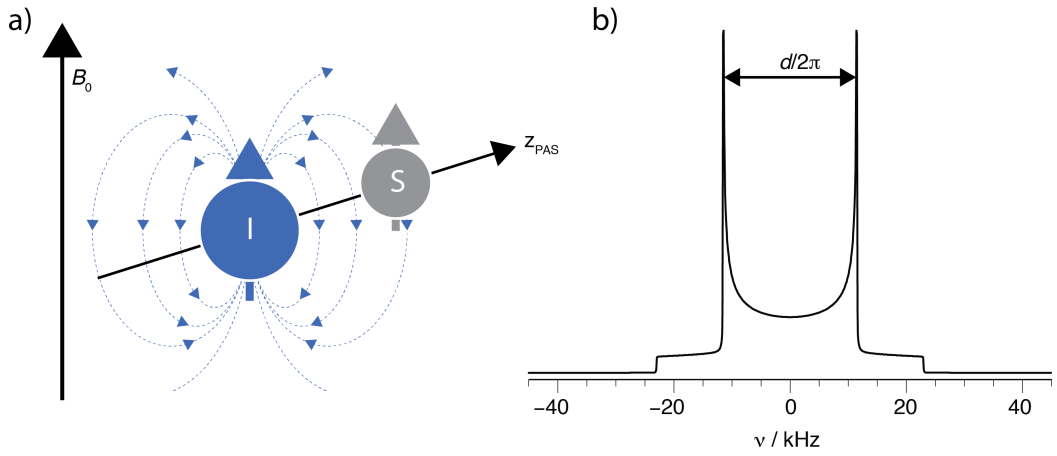

Figure 2.3: (a) Dipolar interaction for two spins, I and S which are close in space. The S spin experiences the magnetic field generated by the I spin. Likewise, the I nuclear spin also experiences the magnetic field generated by the S spin (not shown). The PAS is parallel to a line connecting the centre of the two nuclei. (b) Powder lineshape for a pair of heteronuclear dipolar coupled spin $1/2$ nuclei under static conditions. The spectrum was simulated using SIMPSON for a dipolar coupling, $|d| = 23$ kHz, and convoluted with 40 Hz Lorentzian line-broadening (see Appendix A.2 for SIMPSON input file).

for the homonuclear and heteronuclear dipolar Hamiltonians under static conditions:

$$\hat{H}_D^{L,\text{homo}} = d_{IS}\frac{1}{2}(3\cos^2\beta_{PL} - 1)\left(2\hat{I}_z\hat{S}_z - \left[\hat{I}_x\hat{S}_x + \hat{I}_y\hat{S}_y\right]\right) \tag{2.66}$$

$$\hat{H}_D^{L,\text{hetero}} = d_{IS}\frac{1}{2}(3\cos^2\beta_{PL} - 1)\left(2\hat{I}_z\hat{S}_z\right) \tag{2.67}$$

In the case of heteronuclear dipolar coupling, where only the $\hat{I}_z\hat{S}_z$ term is present, the eigenfunctions of the Hamiltonian are equal to the Zeeman product states, $\alpha\alpha$, $\alpha\beta$, $\beta\alpha$, $\beta\beta$. The resulting static lineshape for a powder sample, known as a *Pake doublet*, is shown in Figure 2.3b. The two maxima correspond to signals from spin pairs orientated perpendicular to the external magnetic field and appear at a distance equal to $d/2\pi$ (in Hz).

The effect of homonuclear dipolar coupling on the NMR spectrum of abundant nuclei like ^{1}H is more complicated, owing to the $\hat{I}_x\hat{S}_x + \hat{I}_y\hat{S}_y$ term. This term is often referred to as the *flip-flop* term, as coupled spins can induce spin state transitions to each other since they precess with similar frequencies. As a result, the eigenfunctions of the homonuclear dipolar Hamiltonian now contain linear combinations of the degenerate Zeeman levels. For a many-spin system, this results in multiple splittings of previously degenerate Zeeman levels, and many transition frequencies, resulting in broad spectral lines. This residual line broadening is not fully removed under MAS.

As for the chemical shift, the dipolar interaction is influenced by molecular

motions. In an *isotropic liquid*, the secular parts of the dipole-dipole couplings average to zero, as seen by evaluating the following integral over all orientations:

$$\int_0^{\pi} (3\cos^2\beta_{PL} - 1)\sin\beta_{PL} d\beta_{PL} = 0 \tag{2.68}$$

In *anisotropic liquids* (liquid crystals), preferential molecular orientations mean that the intramolecular dipolar couplings do not average out completely. The secular dipolar coupling, referred to as the *residual dipolar coupling* (RDC), d_{res}, is equal to:

$$d_{IS,res} = d_{IS} \left\langle 3\cos^2\beta_{PL} - 1 \right\rangle \tag{2.69}$$

where the triangle brackets represent an average over all the orientations sampled by the molecules. A convenient means to describe the degree of order is to take the ratio of the residual dipolar coupling to the coupling in the rigid limit (in the absence of any molecule motions; given by Equation 2.61), squared, defined as the order parameter, S^2:

$$S^2 = \left(\frac{d_{res}}{d_{rigid}} \right)^2 \tag{2.70}$$

Experiments to measure RDCs, and the corresponding order parameters, are discussed in Chapter 3.

2.3.5 Internal Interactions under Magic-Angle Spinning

The anisotropic component of the internal NMR interactions can be removed by physical rotation of the sample at a specific angle relative to the external field (the so-called magic angle). In order to follow the effect of magic-angle spinning (MAS), it is necessary to consider the rotor frame of reference. Therefore, the determination of the interaction Hamiltonian in the laboratory frame requires two successive transformations, first from the PAS to the rotor frame, $R_{PR}(\alpha_{PR}, \beta_{PR}, \gamma_{PR})$, and then from the rotor to the laboratory frame, $R_{RL}(\alpha_{RL}, \beta_{RL}, \gamma_{RL})$. A schematic representation of MAS and the frame transformations is shown in Figure 2.4. Due to the sample rotation, a time dependence is introduced, given by the angle, $\alpha_{RL} = -\omega_r t$, where ω_r is the rotation frequency (in rad s^{-1}, or $\nu_r = \omega_r/2\pi$ in Hz). Applying these rotations (see Section 2.3.1) to the A_{20}^P term of the chemical shielding and dipolar coupling interactions, using the secular approximation, gives:

$$A_{20}^{LAB} = A_{20}^{PAS} \sum_{m'=-2}^{2} D_{0m'}^2(\alpha_{PR}, \beta_{PR}, \gamma_{PR}) d_{0m'}^2(\beta_{RL})\, e^{im'\omega_r t} \tag{2.71}$$

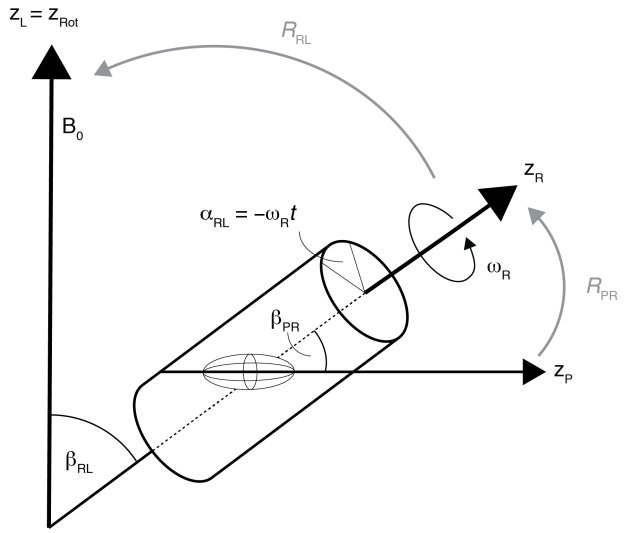

Figure 2.4: Schematic representation of the axis systems and frame transformations used in MAS NMR. Solid black arrows represent the principal axis system (shown for the chemical shielding tensor of a single spin; P), the rotor frame (R), and the laboratory frame (L). The MAS rotor is aligned at an angle of β_{RL} with respect to the external field.

Over a complete rotor period, $\tau_r = 2\pi/\omega_r$, the interaction Hamiltonian is periodic and terms with non-zero values of m$'$ will average to zero:

$$\int_0^{\tau_r} e^{im'\omega_r t} dt = 0 \text{ if } m' \neq 0 \tag{2.72}$$

Equation 2.71 becomes:

$$\left\langle A_{20}^{LAB} \right\rangle_{\tau_r} = A_{20}^{PAS} \frac{1}{4} (3\cos^2\beta_{PR} - 1)(3\cos^2\beta_{RL} - 1) \tag{2.73}$$

By aligning the MAS rotor on an axis of 54.74° to the external field (i.e., the magic angle), Equation 2.73 is averaged to zero over a complete rotation of the sample. When acquisition of the NMR signal is not rotor synchronous, the $m' \neq 0$ terms of Equation 2.71 must also be considered. At the magic angle, evaluation of Equation 2.71 gives:

$$A_{20}^{LAB} = A_{20}^{PAS} (\frac{1}{2} \sin^2\beta_{PR} \cos(2\gamma_{PR} + 2\omega_r t) - \sqrt{2} \sin 2\beta_{PR} \cos(\gamma_{PR} + \omega_r t)) \tag{2.74}$$

An important consequence of the periodic time-dependence of Equation 2.74, is the appearance of spinning sidebands at multiples of the rotation frequency. Figure 2.5 shows simulated CSA and heteronuclear dipolar coupling NMR lineshapes under static and MAS conditions. Under MAS, the broad anisotropic lineshapes are reduced to a sharp centre-band at the isotropic chemical shift and spinning side bands spaced

at multiples of the MAS frequency.

Our discussion so far on the influence of MAS applies to the CSA and heteronuclear dipolar coupling, interactions that are classified as *inhomogeneous*. The Hamiltonians of these interactions introduced in Sections 2.3.3 and 2.3.4 involve only z-spin operators. A different response to MAS arises for the homonuclear dipolar coupling (typically ^{1}H-^{1}H dipolar coupling), a *homogeneous* interaction, where there is an additional time evolution of the state of the spin system owing to the flip-flop term of the Hamiltonian introduced in Section 2.3.4. This prevents complete averaging of the homonuclear dipolar interaction by MAS. As a result, high MAS frequencies are required to achieve high-resolution ^{1}H spectra of solids containing strongly coupled spin networks, and additional methods such as homonuclear decoupling (discussed in Chapter 3) may be required. As discussed in Sections 2.3.3 and 2.3.4, molecular motions lead to partial averaging of the anisotropic interactions, and as such, for highly mobile systems such as liquid crystals, low to moderate MAS frequencies are sufficient to remove the effects of the residual anisotropic interactions and provide high-resolution NMR spectra.

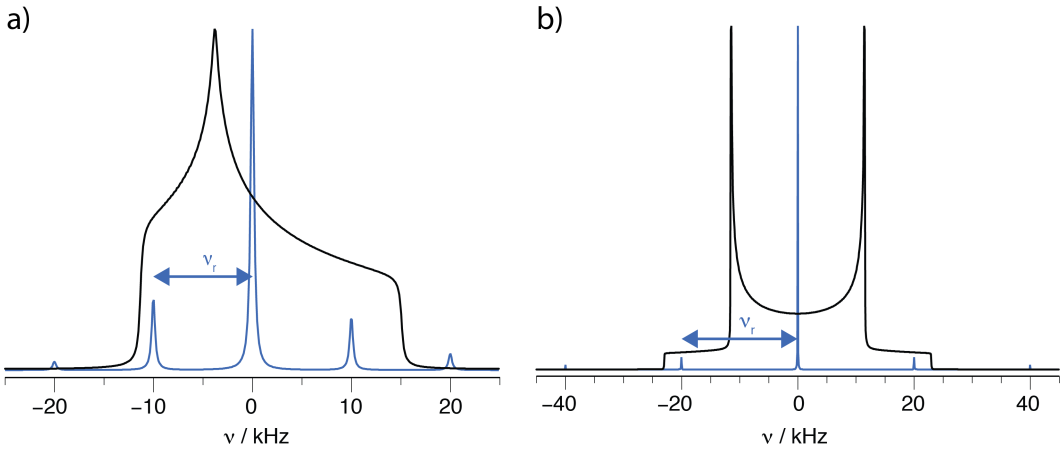

Figure 2.5: (a) Chemical shift anisotropy powder lineshape for an isolated spin $^1/_2$ nucleus under static (black) and MAS ($\nu_r = 10$ kHz) conditions (blue). Spectra were simulated using SIMPSON, with $\delta_{iso} = 0$ ppm, $\delta_{aniso} = 10$ ppm and $\eta = 0.5$, and convoluted with 40 Hz Lorentzian line-broadening. (b) Powder lineshape for a pair of heteronuclear dipolar coupled spin $^1/_2$ nuclei under static (black) and MAS ($\nu_r = 20$ kHz) conditions (blue). Spectra were simulated using SIMPSON for a dipolar coupling, $|d| = 23$ kHz, and were convoluted with 40 Hz Lorentzian line-broadening. In (a, b) the vertical axes of the spectra are normalised. The chemical shift axes are given in kHz, to show that the spinning side-bands under MAS are separated by ν_r. See Appendix A.1 and A.2 for SIMPSON input files for (a) and (b), respectively.

2.3.6 *J*-Coupling

The final internal interaction of relevance to this thesis is J-coupling. J-coupling is a through-bond interaction mediated by bonding electron pairs. As stated by the Pauli Exclusion Principle, the electrons must have opposite spin eigenstates (spin-up and spin-down). Coupling between these electrons and nuclear spins therefore results in splitting of the energy levels. The Hamiltonian for J-coupling between two spins, I and S, is:

$$\hat{H}_D = -2\pi \hat{I} \cdot \tilde{J}_{IS} \cdot \hat{S} \tag{2.75}$$

where $\tilde{J}_{IS}$ is the J-coupling tensor. This tensor contains isotropic and anisotropic components, however, the J anisotropy for light elements such as ^{1}H and ^{13}C is small and can usually be neglected. The isotropic J-coupling is given by the average of the diagonal elements of the J-coupling tensor (and hence it is often referred to as *scalar* coupling):

$$J_{iso} = \frac{1}{3}(J_{xx} + J_{yy} + J_{zz}) \tag{2.76}$$

The isotropic nature of J-coupling means that, unlike dipolar coupling (which is purely anisotropic), the effects of J-coupling are not completely removed by rapid molecular tumbling in isotropic liquids, or by MAS. For light elements, the J-coupling is the smallest of the internal interactions; a one-bond ^{1}H-^{13}C J-coupling is approximately 135 Hz for a C-H distance of 1.09 Å. J-coupling is measurable through a small number of covalent bonds, or in some cases, hydrogen bonds, and can be utilised to identify chemical connectivities. The refocused INEPT (Insensitive Nuclei Enhanced by Polarisation Transfer) experiment which uses the J-coupling as a means of polarisation transfer, is described in Section 3.2.1.

2.4 Relaxation and Exchange

In the previous sections, the effect of dynamics on the anisotropic interactions and the appearance of the NMR spectra were discussed. Motional processes are also the cause of nuclear spin relaxation, and the measurement of NMR relaxation rates is a powerful technique capable of studying motions over a range of timescales. In addition to causing relaxation, motion in the form of exchange can influence the appearance of an NMR spectrum. In this section, the fundamentals of NMR relaxation theory and exchange are presented.

2.4.1 The Origins of Relaxation

After perturbation of a spin system, relaxation takes place, converting the excited state of the spin system back to thermal equilibrium. There are two key relaxation processes: *spin-lattice relaxation* (also known as longitudinal relaxation; described

by R_1), which describes the return of the magnetisation back to the Boltzmann equilibrium state, and *spin-spin relaxation* (also known as transverse relaxation; described by R_2), which is concerned with the decay of coherences.

Relaxation is caused by fluctuating magnetic fields, caused by thermal motion of the molecules. For spin $1/2$ nuclei, it is primarily the dipolar coupling, followed by the CSA (see Sections 2.3.4 and 2.3.3) that are the main contributors to the variations in the local magnetic field. As discussed in Section 2.3.3, the secular dipolar coupling and CSA average to zero in isotropic liquids and are therefore not observed directly in an NMR spectrum. However, nuclear spin relaxation is sensitive to the non-secular parts of the interaction Hamiltonians and can therefore be used for the determination of dynamic and structural information in isotropic liquids (as well as liquid crystal, solids, etc.).

2.4.2 The Correlation and Spectral Density Functions

In order to understand the relationship between molecular motion and nuclear spin relaxation, it is necessary to describe the random motions that cause the fluctuation of the local fields. The time dependence of random molecular motion can be described by the *correlation function*, $G(\tau_c)$. The *correlation time*, τ_c, is defined as the average time taken for a rotation of one radian. The Fourier transform of the correlation function is called the *spectral density*, $J(\omega)$, which describes the amount of motion occurring at a particular frequency, ω. The exact form of the correlation function and the corresponding spectral density function depends on the molecular dynamics of the sample. For the simple case of overall rotational diffusion of a spherical molecule, the correlation function is given by an exponential decay:

$$G(\tau_c) = \exp(-t/\tau_c) \tag{2.77}$$

Fourier transformation gives the Lorentzian spectral density:

$$J(\omega) = \frac{\tau_c}{1 + (\omega\tau_c)^2} \tag{2.78}$$

Figure 2.6 shows plots of this function for various correlation times.

The rigid isotropic reorientation model is too simple to adequately describe the complex dynamics of most real samples. A large number of more complex dynamic models exist, which allow for internal motion of non-rigid molecules. The most frequently used approach, particularly for the study of protein dynamics, is the *model-free* approach of Lipari and Szabo.[94,95] This approach is termed model-free since no assumption is made about the type of physical motion. In the case of a

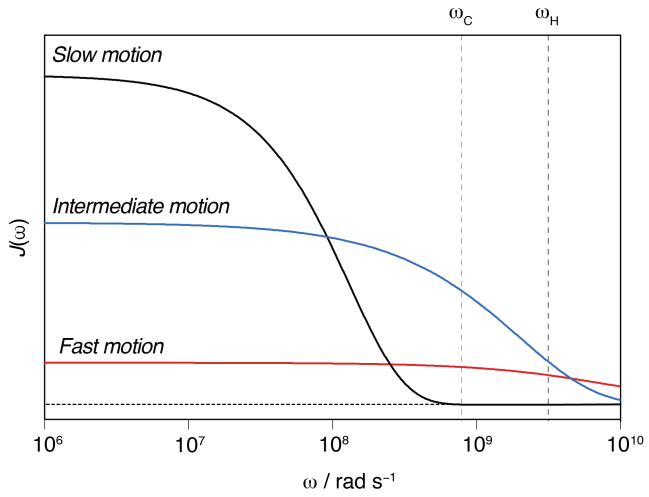

Figure 2.6: Plots of the Lorentzian spectral density function for motion on different timescales. Two frequencies at which $J(\omega)$ contributes to the relaxation rates (see Section 2.4.4), ω_C and ω_H (for $B_0 = 500$ MHz), are shown by dashed lines.

single internal motion, the *simple model-free* (SMF) spectral density is given by:

$$J(\omega) = (1 - S_i^2)\frac{\tau}{1 + (\omega\tau)^2} + S_i^2\frac{\tau_{eff}}{1 + (\omega\tau_{eff})^2}, \frac{1}{\tau} = \frac{1}{\tau_i} + \frac{1}{\tau_{eff}} \tag{2.79}$$

where τ_i is the correlation time for internal motion and τ_{eff} is the effective correlation time for the overall rotational diffusion. S_i^2 is the order parameter for internal motion, which describes the degree of spatial restriction, or amplitude, of the internal motion, and takes values $S_i^2 = 1$ in the absence of internal motion, and $S_i^2 = 0$ for completely unrestricted internal motion.

The spectral densities described above assume overall rotational diffusion takes place, and are therefore referred to as solution spectral densities. In the solid state, where overall rotational diffusion does not take place, the solid-state SMF spectral density is given by:

$$J(\omega) = (1 - S^2)\frac{\tau_{eff}}{1 + (\omega\tau_{eff})^2} \tag{2.80}$$

An improved analysis of relaxation data is often provided by considering motion on multiple time scales. The *extended model-free* (EMF)[96] approach includes two different time scales and associated order parameters, denoted by f and s subscripts for fast and slow motions, respectively:

$$J(\omega) = (1 - S_f^2)\frac{\tau_f}{1 + (\omega\tau_f)^2} + S_f^2(1 - S_s^2)\frac{\tau_s}{1 + (\omega\tau_s)^2} \tag{2.81}$$

2.4.3 Transition Probabilities

The fluctuating magnetic field induces transitions between the spin energy eigenstates. Let us consider a liquid consisting of molecules containing two nuclei with spins I and S which are interacting via the dipolar mechanism described in Section 2.3.4. The system of two spins is characterised by four Zeeman energy levels and by a set of transition probabilities between the levels (Figure 2.7). The dipolar interaction can lead to relaxation-induced transitions between all pairs of energy levels. Differential equations for the rate of change of the population of each level can be derived. The kinetic equation for the population of state $\alpha\alpha$ is:

$$\begin{aligned}\frac{dp_{\alpha\alpha}}{dt} = &-\left(W_I^{(1)} + W_S^{(1)} + W^{(2)}\right)\left(p_{\alpha\alpha} - p_{\alpha\alpha}^0\right) + W^{(2)}\left(p_{\beta\beta} - p_{\beta\beta}^0\right) \\ &+ W_I^{(1)}\left(n_{\beta\alpha} - n_{\beta\alpha}^0\right) + W_S^{(1)}\left(p_{\alpha\beta} - p_{\alpha\beta}^0\right)\end{aligned} \tag{2.82}$$

where $p_{\alpha\alpha}^0$ is the initial population of the state $\alpha\alpha$ and so-forth for the remaining energy levels. Similar kinetic equations can be derived for the other three populations. These equations may be rewritten in terms of the z-magnetisation spin operators introduced in Section 2.1.1, forming the *Solomon equations*[97] for the longitudinal relaxation of a two-spin system:

$$\begin{aligned}\frac{dI_z}{dt} = &-\left(W_I^{(1)} + W_I^{(2)} + W_2 + W_0\right)\left(I_z - I_z^0\right) - \left(W_2 - W_0\right)\left(S_z - S_z^0\right) \\ &- \left(W_I^{(1)} + W_I^{(2)}\right) 2I_zS_z \\ \frac{dS_z}{dt} = &-\left(W_2 - W_0\right)\left(I_z - I_z^0\right) - \left(W_S^{(1)} + W_S^{(2)} + W_2 + W_0\right)\left(S_z - S_z^0\right) \\ &- \left(W_S^{(1)} + W_S^{(2)}\right) 2I_zS_z \\ \frac{d2I_zS_z}{dt} = &-\left(W_I^{(1)} + W_I^{(2)}\right)\left(I_z - I_z^0\right) - \left(W_S^{(1)} + W_S^{(2)}\right)\left(S_z - S_z^0\right) \\ &- \left(W_I^{(1)} + W_I^{(2)} + W_S^{(1)} + W_S^{(2)}\right) 2I_zS_z\end{aligned} \tag{2.83}$$

From Equation 2.83, a number of rate constants in terms of the transition probabilities can be defined. The auto relaxation rates of the I, S, and I_zS_z magnetisation, respectively, are:

$$\begin{aligned}\rho_I &= \left(W_I^{(1)} + W_I^{(2)} + W_2 + W_0\right) \\ \rho_S &= \left(W_S^{(1)} + W_S^{(2)} + W_2 + W_0\right) \\ \rho_{IS} &= \left(W_I^{(1)} + W_I^{(2)} + W_S^{(1)} + W_S^{(2)}\right)\end{aligned} \tag{2.84}$$

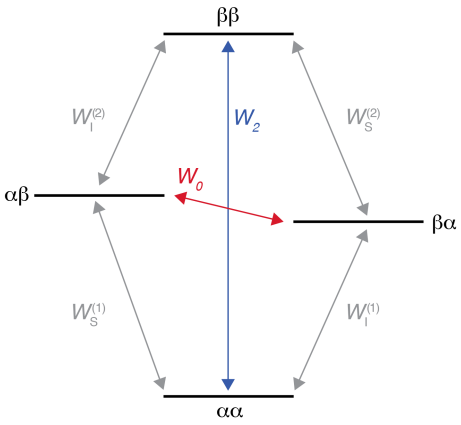

Figure 2.7: Energy level diagram for a two-spin system; the energy levels are labelled with the spin I spin first and the S spin second. The arrows show the possible relaxation induced transitions: four single-quantum transitions (grey), a double-quantum transition (blue), and a zero-quantum transition (red).

The rate at which S magnetisation is transferred to I magnetisation, or vice versa, is called the *cross-relaxation rate*, given by:

$$\sigma_{IS} = W_0 - W_2 \tag{2.85}$$

The transfer of $I_z S_z$ magnetisation into I and S spin magnetisation, respectively, is described by:

$$\begin{aligned} \Delta_I &= \left(W_I^{(1)} - W_I^{(2)}\right) \\ \Delta_S &= \left(W_S^{(1)} - W_S^{(2)}\right) \end{aligned} \tag{2.86}$$

This will only occur if the allowed transitions have different probabilities (i.e. $W_I^{(1)} \neq W_I^{(2)}$ or $W_S^{(1)} \neq W_S^{(2)}$), a situation that arises when there is cross-correlation between different relaxation mechanisms. Using the rate constants defined above, the Solomon equations can be written in the compact matrix form:

$$\frac{d}{dt}\begin{pmatrix} I_z \\ S_z \\ 2I_zS_z \end{pmatrix} = -\begin{pmatrix} \rho_I & \sigma_{IS} & \Delta_I \\ \sigma_{IS} & \rho_S & \Delta_S \\ \Delta_I & \Delta_S & \rho_{IS} \end{pmatrix}\begin{pmatrix} I_z - I_z^0 \\ S_z - S_z^0 \\ 2I_zS_z \end{pmatrix} \tag{2.87}$$

2.4.4 Relaxation Rates in Terms of Spectral Densities

The relaxation rate constants, ρ and σ_{IS}, introduced in the previous section in terms of transition probabilities, may be written in terms of the spectral density function described in Section 2.4.2, linking dynamical information to measurable relaxation rate constants. As discussed in Section 2.4.1, for spin ½ nuclei, the

dominant relaxation mechanism is the dipole-dipole mechanism, followed by the CSA mechanism. This thesis will report the relaxation rates for ^{13}C nuclei, where the dominating dipole-dipole relaxation is caused by the directly bound protons.

The longitudinal auto relaxation rates for the dipole-dipole (DD) and CSA mechanism are given by:

$$\rho^{DD} = R_1^{DD} = n\frac{1}{10}d_{CH}^2\left[J\left(\omega_H - \omega_C\right) + 3J\left(\omega_C\right) + 6J\left(\omega_H + \omega_C\right)\right] \tag{2.88}$$

$$\rho^{CSA} = R_1^{CSA} = \frac{2}{15}(\Delta\sigma)^2\omega_C^2 J\left(\omega_C\right) \tag{2.89}$$

where n is the number of protons, d_{CH} is the CH dipolar coupling constant, given by Equation 2.61, and $\Delta\sigma$ is given by the CSA tensor components according to:

$$\Delta\sigma = \frac{\sigma_{zz}^{PAS} - (\sigma_{xx}^{PAS} + \sigma_{yy}^{PAS})}{2} \tag{2.90}$$

Only the dipolar mechanism is responsible for cross-relaxation, according to:

$$\sigma_{CH} = nd_{CH}^2\left[6J\left(\omega_H + \omega_C\right) - J\left(\omega_H - \omega_C\right)\right] \tag{2.91}$$

An additional relaxation rate that is reported in this thesis is spin-lattice relaxation in the presence of a radio-frequency (rf) field. The characteristic relaxation rate constant is called $R_{1\rho}$, and is commonly called *spin-lattice relaxation in the rotating frame*. $R_{1\rho}$ depends on the spectral density at the frequency of the rf spin-lock pulse, ω_1, and the MAS frequency, ω_r, in addition to the frequencies that contribute to R_1, according to:[98,99]

$$\begin{aligned} R_{1\rho}^{DD} = n\frac{1}{20}d_{CH}^2\big[&\frac{2}{3}J\left(\omega_1 + 2\omega_r\right) + \frac{2}{3}J\left(\omega_1 - 2\omega_r\right) + \frac{4}{3}J\left(\omega_1 + \omega_r\right) \\ &+ \frac{4}{3}J\left(\omega_1 - \omega_r\right) + 3J\left(\omega_C\right) + 6J\left(\omega_H\right) + 6J\left(\omega_C + \omega_H\right) \\ &+ J\left(\omega_C - \omega_H\right)\big] \end{aligned} \tag{2.92}$$

$$\begin{aligned} R_{1\rho}^{CSA} = \frac{1}{45}(\Delta\sigma)^2\omega_C^2\big[&\frac{2}{3}J\left(\omega_1 + 2\omega_r\right) + \frac{2}{3}J\left(\omega_1 - 2\omega_r\right) + \frac{4}{3}J\left(\omega_1 + 2\omega_r\right) \\ &+ \frac{4}{3}J\left(\omega_1 - 2\omega_r\right) + 3J\left(\omega_C\right)\big] \end{aligned} \tag{2.93}$$

2.4.5 Exchange

Exchange processes interchange the environment of nuclei and can affect the appearance of a NMR spectrum. Exchange may be positional (e.g. the rotation of a molecular segment), or involve proton transfer (hydrogen exchange). For simplicity, the case of exchange between two sites (A and B) with distinct chemical shifts is

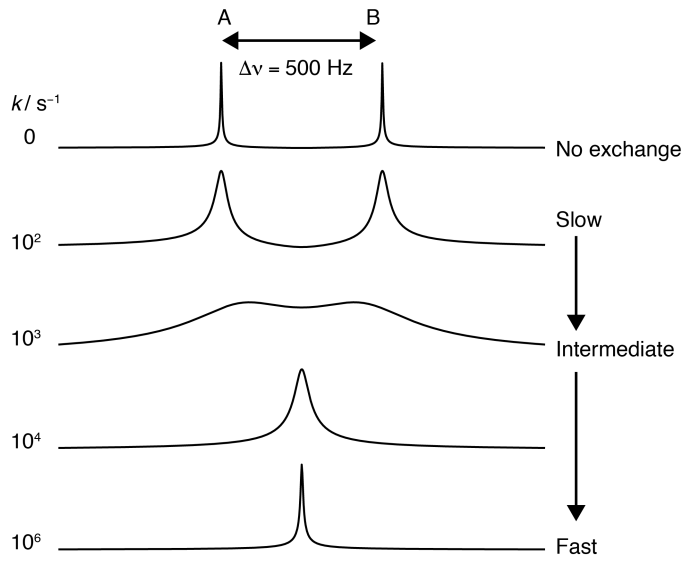

Figure 2.8: Chemical exchange lineshapes for symmetric two-site exchange with $p_A = p_B = 0.5$. The spectra are simulated with $R^0_{2A} = R^0_{2B} = 10$ s^{-1} and $\Delta\nu = 500$ Hz.

considered here, for which an equilibrium can be described by:

$$A \underset{k_b}{\overset{k_f}{\rightleftharpoons}} B \tag{2.94}$$

where k_f and k_b are the forward and reverse rate constants, respectively, and the exchange rate constant is given by:

$$k_{ex} = k_f + k_b \tag{2.95}$$

The observed transverse relaxation rate, R_2^{obs}, contains an exchange contribution, R_{ex}:

$$R_2^{obs} = R_2^0 + R_{ex} \tag{2.96}$$

where R_2^0 is the intrinsic transverse relaxation rate (i.e., in the absence of exchange). The contribution of R_{ex} to the observed linewidth depends upon k_{ex} and $\Delta\nu$. The ratio of $k_{ex}/\Delta\nu$ (both in s^{-1}), where $\Delta\nu$ is the chemical shift difference in Hz between the two sites, determines the exchange regime, as illustrated in Figure 2.8. In the slow exchange regime ($k_{ex} \ll \Delta\nu$), two distinct peaks will be observed at the chemical shift of the individual sites. The linewidth of each state will increase due to depopulation of the state during the detection period which contributes to the exponential decay of the FID and Equation 2.96 can be re-written as:

$$R_2^{obs} = R_2^0 + k \tag{2.97}$$

In the fast exchange regime ($k_{ex} \gg \Delta\nu$), rapid inter-conversion between the two sites results in averaging during the detection period, resulting in a single peak at the population-weighted mean chemical shift and relaxation rate:

$$\delta^{obs} = p_A\delta_A + p_B\delta_B \tag{2.98}$$

$$R_2^{obs} = p_A R_{2,A} + p_B R_{2,B} \tag{2.99}$$

The population of state A is p_A, and $p_B = 1 - p_A$ is the population of state B.

In order to fully study the effects of exchange on NMR spectra, it is necessary to use the McConnell equations.[100] These equations are a modified form of the Bloch equations[53] extended to incorporate exchange and are given by:

$$\frac{d}{dt}\begin{bmatrix} M_A^+(t) \\ M_B^+(t) \end{bmatrix} = \begin{bmatrix} -i\Omega_A - R_{2,A}^0 k_{ex} & p_A k_{ex} \\ p_B k_{ex} & -i\Omega_B - R_{2,B}^0 k_{ex} \end{bmatrix} \begin{bmatrix} M_A^+(0) \\ M_B^+(0) \end{bmatrix} \tag{2.100}$$

where the resonance frequencies for spins in site A and B are Ω_A and Ω_B, respectively, in units of angular frequency (rad s^{-1}). $M_A^+(t)$ and $M_B^+(t)$ are the transverse magnetisation at each site at time t, and $M_A^+(0)$ and $M_B^+(0)$ are the initial magnetisation at $t = 0$ at each site which depend on the populations, p_A and p_B . The transverse relaxation rates of the sites in the absence of exchange are $R_{2,A}^0$ and $R_{2,A}^0$. The solution of Equation 2.100 is given in Appendix A.3.

Chapter 3

NMR Experimental Methods

This chapter describes the experimental techniques used to record NMR spectra for the determination of information on structure and dynamics. Firstly, one- and two-dimensional NMR experiments and lineshapes are considered, and coherence selection by phase cycling is introduced. The specific NMR experiments utilised in this thesis are then described. These include homonuclear ^{1}H-^{1}H and heteronuclear ^{1}H-^{13}C 2D correlation experiments to probe interatomic proximities, and the measurement of dipolar couplings and relaxation rates.

3.1 Pulsed Fourier Transform NMR

3.1.1 Signal Detection and the Fourier Transform

In the most basic NMR experiment, a *rf* pulse is applied to flip the bulk magnetisation from the longitudinal direction into the transverse plane where the precession of the magnetisation is recorded for a time called the *acquisition time*. Both the x- and y-components of the magnetisation are detected simultaneously (Figure 3.1). Each gives rise to a separate signal described by:

$$\begin{aligned} S_x &= S_0 \cos \Omega t \\ S_y &= S_0 \sin \Omega t \end{aligned} \tag{3.1}$$

where S_0 is the maximum signal and Ω is the offset (Equation 2.36), the difference between the Larmor frequency and the rotating frame frequency. Relaxation processes can be considered to lead to an exponential decay of the signal over time. The recorded signal is therefore termed the *free induction decay* (FID). Taking this into

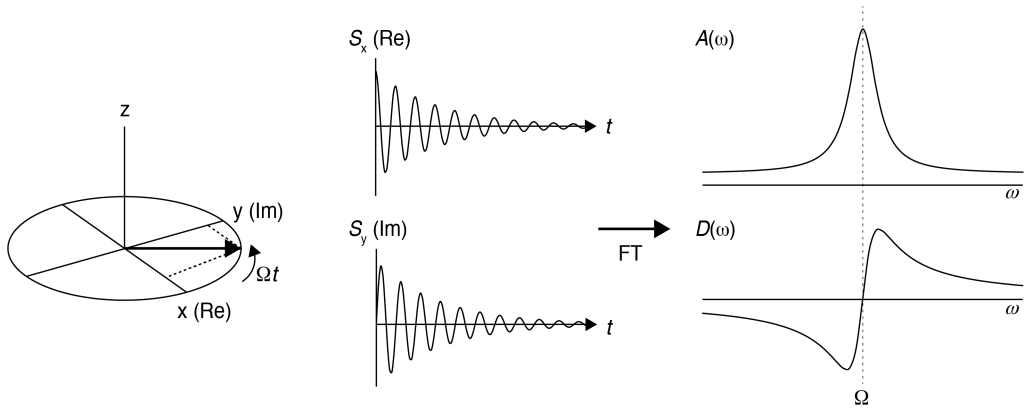

Figure 3.1: Schematic illustration of the real (Re) and imaginary (Im) components of the net magnetisation vector, the complex FID, and the absorptive ($A(\omega)$) and dispersive ($D(\omega)$) Lorentzian lineshapes obtained by Fourier transform.

account the above equations can be modified:

$$\begin{aligned} S_x &= S_0 \cos \Omega t \exp\left(\frac{-t}{T_2}\right) \\ S_y &= S_0 \sin \Omega t \exp\left(\frac{-t}{T_2}\right) \end{aligned} \tag{3.2}$$

where T_2 is the transverse relaxation time. Rather than treating the two components of magnetisation separately, they can be combined into a complex function:

$$\begin{aligned} S(t) &= S_x + iS_y \\ &= S_0 \exp(i\Omega t) \exp\left(\frac{-t}{T_2}\right) \end{aligned} \tag{3.3}$$

Fourier transformation (FT) of the time-domain signal, the FID, gives a complex frequency-domain:

$$\begin{aligned} S(\omega) &= \int_0^{+\infty} S(t) \exp(-i\omega t)\, dt \\ &= \frac{1/T_2}{(1/T_2)^2 + (\omega - \Omega)^2} - i\frac{\omega - \Omega}{(1/T_2)^2 + (\omega - \Omega)^2} \\ &= A(\omega) - iD(\omega) \end{aligned} \tag{3.4}$$

The real and imaginary parts have absorptive ($A(\omega)$) and dispersive ($D(\omega)$) Lorentzian lineshapes respectively (Figure 3.1). The absorptive mode lineshape is preferred as it gives rise to narrower peaks, hence enabling the better resolution of distinct resonances. Phase correction involves adjusting the proportion of the real and imaginary components to achieve the observation of absorptive lineshapes in

NMR spectra.

Two-Dimensional (2D) NMR gives data plotted on two frequency axes rather than one, and can provide information on coherences between nuclei that may not be directly observed. 2D NMR experiments can utilise either through-bond (scalar) or through-space (dipolar) couplings, and may be either homonuclear (e.g. ^{1}H-^{1}H) or heteronuclear (e.g. ^{1}H-^{13}C). A pulse sequence for a generalised 2D NMR experiment is shown in Figure 3.2. During the preparation period, transverse magnetisation is generated, which is allowed to evolve during t_1. The magnetisation is then transferred between coupled nuclei during the mixing time and the FID is acquired during the detection time (t_2). The acquisition is repeated a number of times, incrementing the evolution time (t_1). 2D Fourier transformation yields the 2D spectrum.

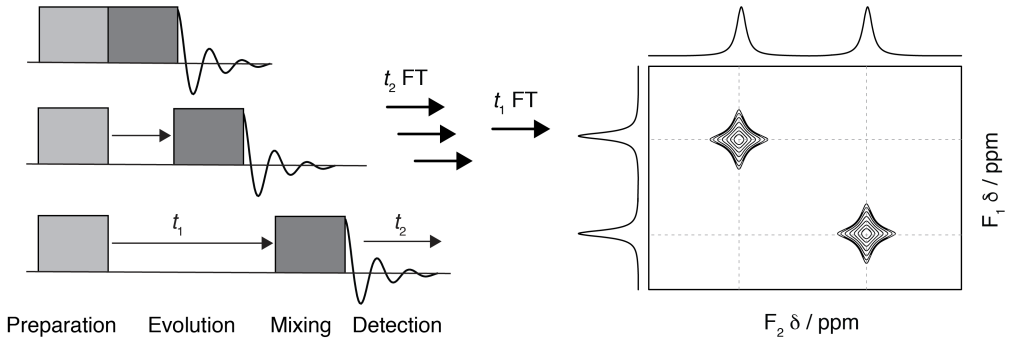

Figure 3.2: General scheme for a 2D NMR experiment. The preparation and mixing periods may be as simple as a single pulse or consist of complex sequences of pulses and delays. Pure absorptive lineshapes are shown in the 2D NMR spectrum.

3.1.2 Coherence and Phase Cycling

In Section 2.2.2 we saw that when an *rf* pulse is applied, different coherences may be excited. The *coherence order* of a density matrix element ρ_{ij} is given by $m_j - m_i$, where m is the magnetic quantum numbers for the i and j basis functions which are mixed in the coherence. $\hat{I}_z$ has a coherence order $p = 0$, whilst the transverse magnetisation operators, $\hat{I}_x$ and $\hat{I}_y$, have coherence orders $p = \pm 1$ (termed *single-quantum* coherences; SQ). For multi-spin systems, higher coherence orders may be generated. For example, in Section 3.2.2, the generation of *double-quantum* ($p = \pm 2$) coherences for a pair of spin $^1/_2$ nuclei will be demonstrated.

A convenient way to describe the desired coherences at each stage in a pulse sequence is to show a coherence transfer pathway beneath the pulse sequence (for example see Figure 3.5). Phase cycling enables the selection of certain coherences and cancelling out of unwanted coherence pathways. This techniques involves the repetition of several experiments with the phases of certain pulses alternated over

the duration of the cycle. Phase cycles may be constructed using two key rules:

1. If a pulse (or group of pulses) changes the coherence order from p_1 to p_2 ($\Delta p = p_2 - p_1$), then shifting the phase of the pulse (or group of pulses) by $\Delta\phi$ results in the coherence acquiring a phase shift of $-\Delta p \times \Delta\phi$.

2. If the phase of a pulse is cycled through a full series of N steps where the phase increment is $360°/N$, then a pathway selected for a particular value of Δp will also result in the selection of pathways corresponding to a change of $\Delta p \pm nN$ where n is an integer.

3.2 NMR Experiments: Interatomic Proximities

3.2.1 Heteronuclear Correlation Experiments: INEPT and CP

The simplest NMR experiment involves direct polarisation (DP) by application of a single 90° pulse (Figure 3.3a). Additionally, for ^{13}C spectra, heteronuclear decoupling is applied during the acquisition time to remove the effects of heteronuclear ^{1}H-^{13}C couplings. Methods of magnetisation transfer from ^{1}H to ^{13}C utilise the higher gyromagnetic ratio of ^{1}H and shorter recycle delay to record ^{13}C NMR spectra with improved sensitivity compared to the DP experiment. Polarisation transfer may be achieved via J-couplings or dipolar couplings, using the refocussed Insensitive Nuclei ENhanced by Polarisation Transfer (INEPT)[101,102] and cross polarisation (CP)[103] experiments, respectively (Figure 3.3b and c). Using these methods of magnetisation transfer, 2D correlation spectra may be obtained to identify interatomic connectivities and spatial proximities (Figure 3.3d). The efficiency of these polarisation transfer mechanisms depends on dynamics (Figure 3.3), as will be described in more detail below.[104]

For magnetisation transfer in solution-state NMR, the refocused INEPT method is commonly used. INEPT is most efficient for mobile molecules in solution, where the homogenous linewidths are smaller than the J-coupling constant. The pulse sequence is shown in Figure 3.3b. The first 90° pulse creates the transverse magnetisation, $-\hat{I}_y$. In the 2D experiment, evolution occurs under the ^{1}H chemical shift during the following t_1 evolution period, whilst the the ^{1}H-^{13}C J-coupling is refocussed by a centered 180° pulse (termed a *spin-echo*). During the following $\tau - \pi - \tau$ spin-echo sequence, the chemical shift evolution on both spins is refocused and the ^{1}H and ^{13}C magnetisation precess under the influence of the heteronuclear J-coupling for 2τ according to (assuming here that $t_1 = 0$ for simplicity):

$$-\hat{I}_y \xrightarrow{2\pi J_{IS}\tau \hat{I}_z \hat{S}_z} -\cos(2\pi J_{IS}\tau)\,\hat{I}_y + \sin(2\pi J_{IS}\tau)\,2\hat{I}_x\hat{S}_z \tag{3.5}$$

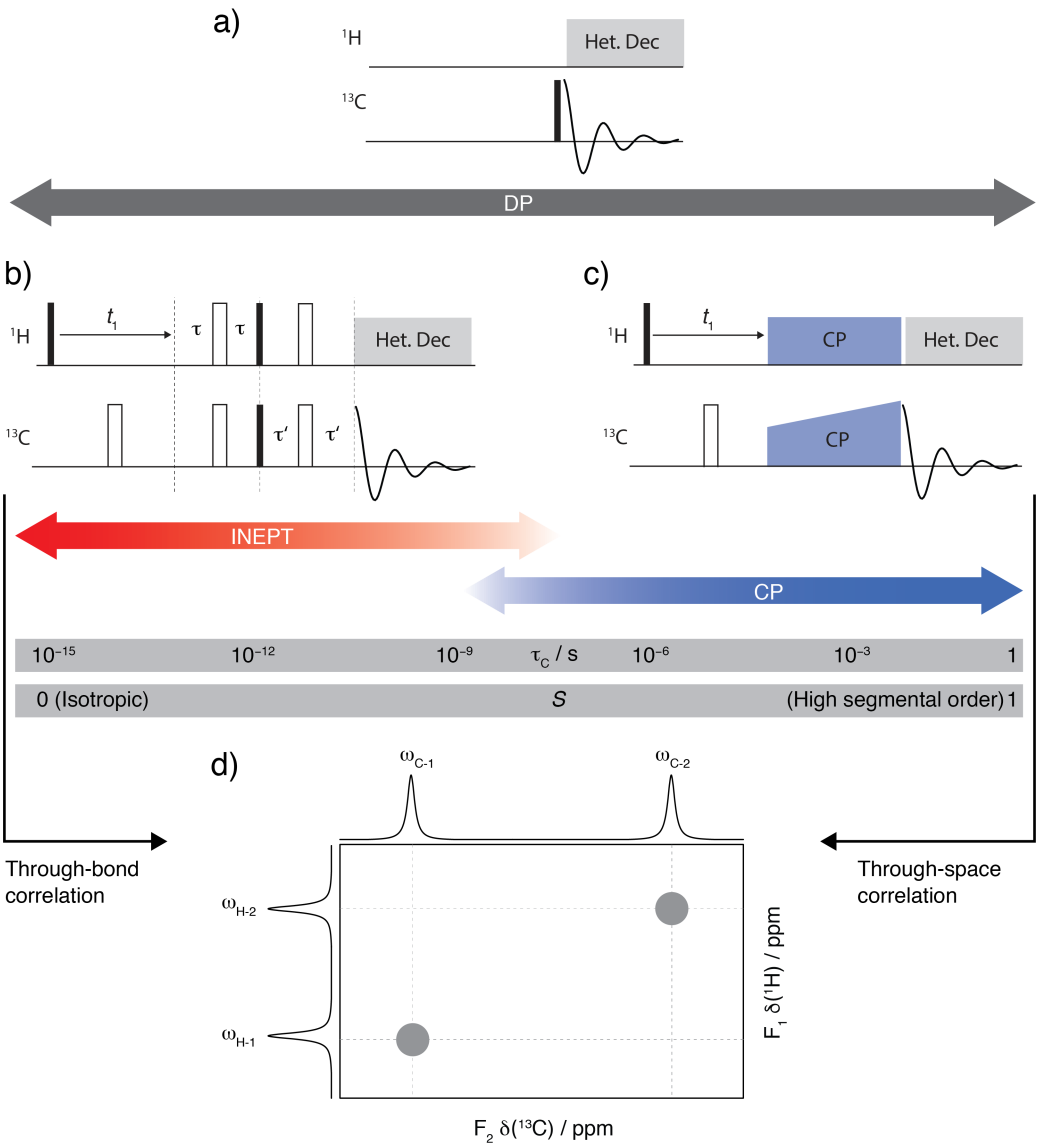

Figure 3.3: (a,b,c) Pulse sequences for (a) DP, (b) refocused INEPT and (c) CP and the dynamical range where the experiments are effective. The pulse sequences in (b) and (c) can be used to acquire 1D ^{13}C spectra by omitting the t_1 evolution period or 2D ^{1}H-^{13}C heteronuclear correlation spectra as illustrated in (d). The 2D heteronuclear correlation spectra shows either through-bond connectivities or through-space proximities, depending on whether magnetisation transfer is achieved through INEPT or CP, respectively, to yield a 2D refocussed-INEPT spectrum, or a 2D CP-HETCOR spectrum.

90° pulses are then applied to both I and S channels, simultaneously, such that:

$$\begin{aligned} &\xrightarrow{\frac{\pi}{2}\hat{I}_y} -\cos\left(2\pi J_{IS}\tau\right)\hat{I}_y - \sin\left(2\pi J_{IS}\tau\right)2\hat{I}_z\hat{S}_z \\ &\xrightarrow{\frac{\pi}{2}\hat{S}_x} -\cos\left(2\pi J_{IS}\tau\right)\hat{I}_y + \sin\left(2\pi J_{IS}\tau\right)2\hat{I}_z\hat{S}_y \end{aligned} \tag{3.6}$$

Another spin echo, $\tau' - \pi - \tau'$ is applied for the refocused INEPT sequence, to convert the anti-phase magnetisation to in-phase $\hat{S}_x$ magnetisation:

$$\sin\left(\pi J_{IS}\tau\right)2\hat{I}_z\hat{S}_y \xrightarrow{2\pi J_{IS}\tau'\hat{I}_z\hat{S}_z} \sin\left(2\pi J_{IS}\tau\right)\sin\left(2\pi J_{IS}\tau'\right)\hat{S}_x \tag{3.7}$$

The second method of polarisation transfer, CP, is routinely used in solid-state NMR and is most effective for rigid or highly ordered samples where the dipolar couplings are not completely averaged by molecular motion. CP involves applying a spin-lock pulse simultaneously on I and S spins (Figure 3.3c), for a contact time of typically a few ms. The nutation frequency, ω_1, is proportional to the B_1 field strength by $\omega_1 = -\gamma B_1$. Adjustment of the spin-lock fields (B_1^I and B_1^S) enable the I and S B_1 fields to be matched, a condition known as the Hartmann-Hahn match:[103]

$$\gamma_I B_1^I = \gamma_S B_1^S \tag{3.8}$$

This equation holds for static samples, however under MAS, where the dipolar interaction is modulated by the rotation, the Hartmann-Hahn condition depends on the spinning frequency:

$$\gamma_I B_1^I - \gamma_S B_1^S = n\omega_r \tag{3.9}$$

where $n = 0, \pm1, \pm2, ...$ and ω_r is the MAS frequency. Under Hartmann-Hahn matching, the I and S spins precess with the same frequency and the heteronuclear dipolar interaction between spins drives the polarisation transfer. CP is more efficient and robust under MAS when a ramped spin-lock pulse (the nutation frequency of the spin-lock pulse is varied) is applied on one of the channels (see Figure 3.3c).[105,106]

3.2.2 Homonuclear Correlation Experiments: NOESY and DQ-SQ NMR

In this section, two homonuclear correlation experiments are described, which both utilise the dipolar coupling to probe proton-proton proximities. As with the INEPT- and CP-based heteroncuclear correlation experiments, these experiments are effective for different dynamical ranges and degrees of anisotropy and provide different information on the systems of interest.

In Section 2.4.3, the Solomon equations describing longitudinal relaxation were introduced. This says that if the S spin deviates from equilibrium there will

be a change to the I spin magnetisation at a rate that is proportional to the cross-relaxation rate, σ_{IS} and the deviation of the S spin from equilibrium. It is the change in intensity of the I spin when the S spin is perturbed which is termed the nuclear Overhauser effect (NOE). There will only be such an effect if σ_{IS} is non-zero, which requires dipolar relaxation via the W_2 and W_0 relaxation pathways (see Figure 2.7). The cross-relaxation rate is strongly dependent on the internuclear distance, making the NOE a powerful probe of fixed intramolecular distances (typically < 5 Å) for structural determination in liquids.

The pulse sequence for the standard 2D nuclear Overhauser effect spectroscopy (NOESY) experiment is shown in Figure 3.4a. It consists of three 90° pulses. The first pulse creates transverse magnetisation, which evolves under the influence of the chemical shift during t_1. The second pulse returns the magnetisation to the z-axis. During the mixing period (τ_m), cross-relaxation between spins causes magnetisation transfer. The third pulse creates transverse magnetisation for detection. The result is a 2D homonuclear correlation spectrum containing cross peaks between protons that are close in space (Figure 3.4b). The sign of the NOE (and the cross-peaks) can be either positive or negative, depending on the relaxation pathway that dominates (recalling from Section 2.4.3 that $\sigma_{IS} = W_2 - W_0$), which in turn is related to molecular motion. For small fast tumbling molecules, $W_2 > W_0$ and the NOEs are positive, whilst for large molecules or viscous solutions, $W_2 < W_0$ and the NOEs are negative.

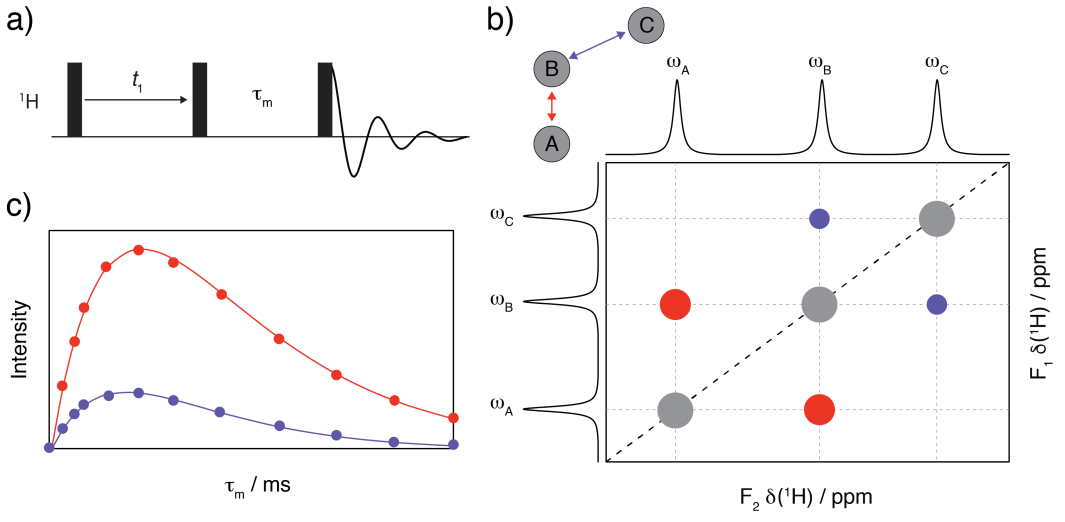

Figure 3.4: (a) Pulse sequence for the 2D NOESY experiment. (b) Schematic illustration of a NOESY spectrum for a 3-spin system and (c) illustrative NOESY build-up curves.

The intensity of the cross-peaks can be plotted as a function of the mixing

time, τ_m, to produce NOESY build-up curves (Figure 3.4c). As τ_m is increased, the cross peaks initially become more intense and then begin to decrease due to spin-lattice relaxation. In the initial build-up region at short mixing times, the cross-relaxation rate can be considered proportional to the initial slope, which, for small molecules with fixed internuclear distances, is proportional to the distance between the spins according to $\sigma_{IS} \propto r_{IS}^{-6}$. This relationship assumes that the frequencies of molecular motions determining the spectral density are higher than the spectrometer frequency, $\omega_0\tau_c \ll 1$ (known as the *extreme narrowing* limit), meaning that the cross-relaxation rate becomes independent of frequency. This may not be the case for ionic liquids that are the focus of this thesis, which typically have a viscosity of up to two orders of magnitude higher than that of water. Furthermore, the interpretation of internuclear NOEs (i.e. between different molecules), where the distances change constantly, is more complex and the cross-relaxation rates become a measure of the probability of close approach of the respective nuclei. While cross-relaxation (the NOE) is responsible for the transfer of magnetisation in liquids, in the solid-state the dominant mechanism responsible for the transportation of magnetisation is spin diffusion, a coherent effect originating from incomplete averaging by MAS of the ^{1}H-^{1}H dipolar interactions.[107,108] In samples on the continuum from liquid to solid, which are presented in this thesis, both the NOE and coherent spin-diffusion are expected to contribute to the NOESY spectra. For these reasons, the interpretation of NOESY experiments for ionic liquids in this thesis is qualitative only.

The second 2D homonuclear correlation experiment used in this thesis is the ^{1}H DQ-^{1}H SQ experiment. The experiment is a powerful probe of proton-proton proximities in the solid-state and in anisotropic liquids, since a DQ coherence can only be created if there is a sufficiently large dipolar coupling. For solids, the experiment probes both intermolecular and intramolecular contacts. In liquid crystals, fast axial rotations about the long molecular axis and translational motion of the molecules results in averaging of the internuclear dipolar couplings to zero, and the DQ-SQ experiment therefore only reports on intramolecular contacts.

The pulse sequence used in this thesis is shown in Figure 3.5a. A dipolar recoupling scheme is employed for the excitation and reconversion of DQ coherence. In this work, the Permutationally Offset Stabilised C7 (POST-C7) sequence for recoupling of the ^{1}H-^{1}H dipolar interaction,[109] given in Figure 3.5a, is used with relatively slow MAS ($\nu_r = 5$ kHz). The selection of DQ coherences (see coherence pathway diagram in Figure 3.5a) is achieved using a 4-step DQ phase cycle by incrementing $\Delta\varphi$ of the reconversion (or excitation) segment in 90° steps ($\Delta\varphi = x, y, -x, -y$) while inverting the receiver every other scan ($\Delta\varphi_{rec} = x, -x, x, -x$). A schematic DQ-SQ spectrum is shown in Figure 3.5b. During the t_1 evolution time, the double-quantum coherence evolves at the sum of the offsets, the double-quantum

frequency ($\Omega_A + \Omega_B$, for two dipolar-coupled spins, A and B). Importantly, unlike the NOESY experiment, the DQ-SQ experiment can identify contacts between like-spins, with *auto-peaks* appearing on the diagonal (Figure 3.5b). Using this experiment, or a normalised 1D version, it is possible to quantify ^{1}H-^{1}H dipolar couplings by measuring DQ build-up curves, as will be described in Section 3.3.2.

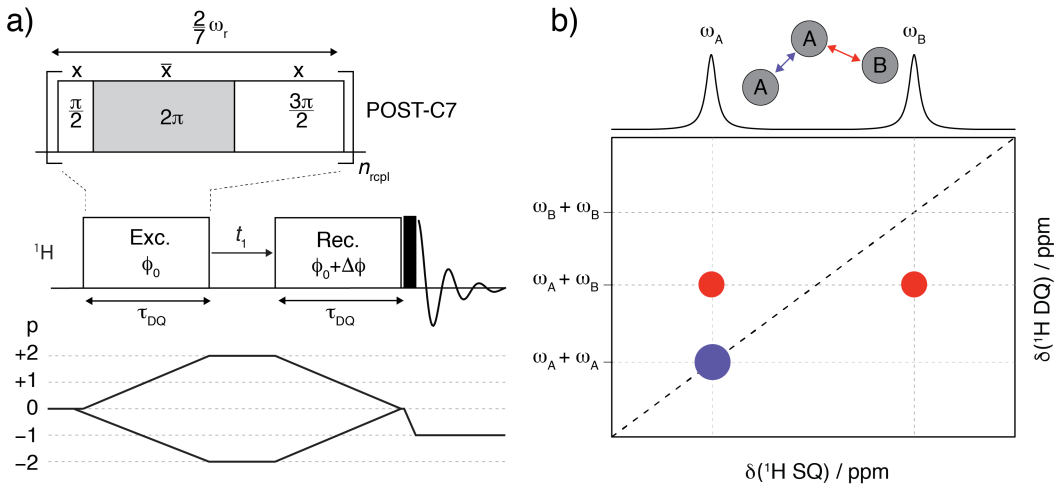

Figure 3.5: (a) Pulse sequence for the ^{1}H DQ-^{1}H SQ correlation experiment using the POST-C7[109] dipolar recoupling sequence. (b) Schematic 2D DQ-SQ correlation spectrum.

3.3 NMR Experiments: Measuring Dipolar Couplings

The measurement of dipolar couplings can provide valuable information on inter-atomic distances in solids. In mobile samples, such as the the liquid crystals studied in this thesis, fast molecular dynamics reduce the dipolar interaction (see Equation 2.70 in Section 2.3.4), and the residual dipolar coupling provides information on the amplitude of motions. In this section, experiments to measure heteronuclear ^{1}H-^{13}C and homonuclear ^{1}H-^{1}H dipolar couplings to obtain the corresponding order parameters, S^2_{CH} and S^2_{HH}, are described.

3.3.1 Heteronuclear Dipolar Couplings: CP Build-up Curves and DIPSHIFT Experiments

Two methods were used to measure ^{1}H-^{13}C heteronuclear dipolar couplings in this thesis: CP build-up curves and the dipolar chemical shift correlation (DIPSHIFT) experiment. Due to the strong distance dependence of the dipolar coupling, the dominant contribution in these experiments can be assumed to come from covalently

bound protons, and the order parameter, S^2_{CH} can therefore be calculated for each resolved ^{13}C site, using equations 2.61 and 2.70 and the C-H bond distance.

^{1}H-^{13}C heteronuclear dipolar couplings may be obtained from CP (see Section 3.2.1) build-up curves, recorded by incrementing the CP contact time (Figure 3.6a), typically from several μs to ms. Strong dipolar couplings yield a rapid polarisation build-up, whilst smaller dipolar couplings display a much slower CP build-up (Figure 3.6b). If there is a dominant dipolar interaction and ^{1}H-^{1}H dipolar coupling are sufficiently removed, the polarisation transfer shows oscillatory behaviour where their frequency of oscillations is directly proportional to the dipolar coupling constant.[110] For systems with strong dipolar couplings (e.g. rigid solid samples, or highly ordered LCs), more advanced versions of the experiment, such as Lee-Goldberg (LG)[111] CP,[112,113] are required, where the proton dipolar interaction is further suppressed by homonuclear decoupling methods.

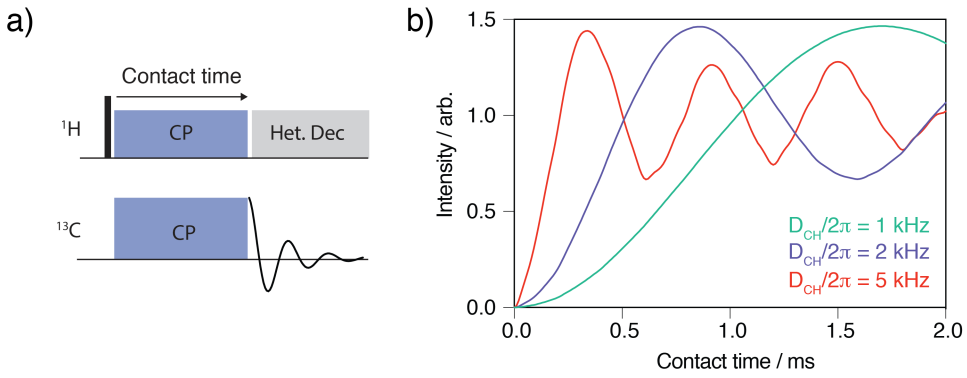

Figure 3.6: (a) Pulse sequence for the measurement of CP build-up curves. (b) Simulated (SIMPSON[114]) CP build-up curves (ν_r = 5 kHz) for a 2-spin system with a dipolar coupling of 500 Hz (green), 2 kHz (purple) or 5 kHz (red). See Appendix B.1 for SIMPSON input file.

The DIPSHIFT experiment is a commonly used separated local field (SLF) experiment that correlates chemical shift and heteronuclear dipolar interaction.[115,116] The specific DIPSHIFT pulse sequence used in this thesis, the T_2-recDIPSHIFT experiment from Cobo *et al.*,[117] is shown in Figure 3.7a. After excitation (either DP, or CP from ^{1}H), the magnetisation evolves during a variable time t_1 under the influence of the heteronuclear ^{1}H-^{13}C dipolar interaction, whilst the ^{1}H homonuclear coupling is suppressed by frequency-switch Lee-Goldberg (FSLG) decoupling. As the C-H dipolar couplings in the liquid crystalline samples studied in this thesis are relatively weak, a recoupled version of the original DIPSHIFT experiment was utilised, where the phase accumulated due to the evolution under the ^{1}H-^{13}C dipolar coupling is amplified by a train of N π pulses (see Figure 3.7a), based on the rotational-echo,

double-resonance (REDOR) experiment for heteronuclear dipolar recoupling under MAS.[118] For the liquid crystalline samples studied in this thesis (Chapter 7), an amplification factor $N = 8$ was used, to measure C-H dipolar couplings in the range 0.5 to 4 kHz. Subsequently, heteronuclear decoupling, such as SPINAL-64[119], is applied for the remainder of the time $N\tau_r$ since excitation, whilst the ^{13}C chemical shift is refocussed. The absence of a ^{13}C π pulse at the $N\tau_r/2$ position, ensures that the signal is recovered during the second half of the t_1 evolution time. DIPSHIFT curves are normalised to the full magnetisation at $t = 0$ (i.e. $S(t_1)/S(0)$). Simulated DIPSHIFT curves are shown in 3.7b for a 2-spin system with varying dipolar coupling. The minimum of the DIPSHIFT curve is lower for higher coupling constants.

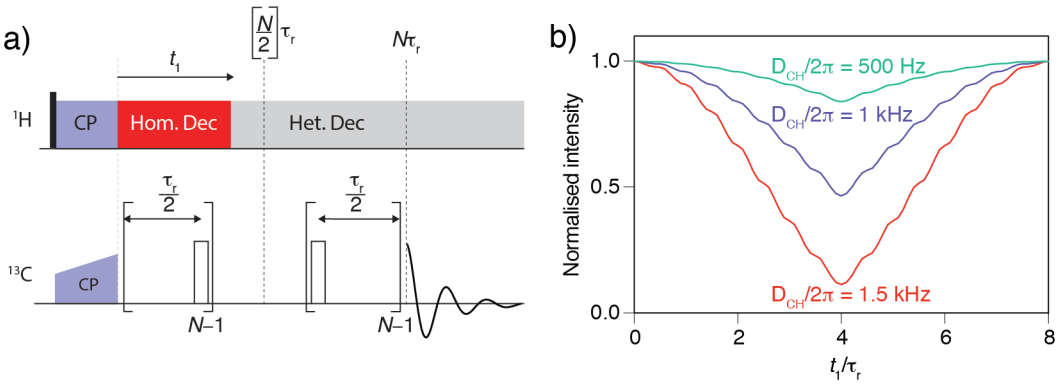

Figure 3.7: (a) Pulse sequence for the T_2-recDIPSHIFT experiment. (b) Simulated (SIMPSON[114]) DIPSHIFT curves ($\nu_r = 5$ kHz) for a 2-spin system with a dipolar coupling of 500 Hz (green), 1 kHz (purple) or 1.5 kHz (red). The DIPSHIFT curves were simulated with 8 rotor periods of recoupling ($N = 8$). See Appendix B.2 for SIMPSON input file.

3.3.2 Homonuclear Dipolar Couplings: ^{1}H DQ Build-up Curves

In Section 3.2.2, the ^{1}H DQ-^{1}H SQ experiment utilised to probe ^{1}H-^{1}H proximities was introduced. The value of the ^{1}H-^{1}H dipolar coupling can be extracted by fitting the intensity build-up behaviour with varying DQ excitation time, τ_{DQ} (see pulse sequence in Figure 3.5a). In this way, relative dipolar couplings may be obtained;[120] however, intensity normalisation is necessary to obtain absolute values of the dipolar coupling.[121,122] For the purpose of describing the normalised DQ experiment, we consider here the simple static case where DQ coherence can be excited with the simple $\frac{\pi}{2} - \tau_{DQ} - \frac{\pi}{2}$ pulse sequence. Using product-operator theory, for a two-spin

system (spins i and j):

$$\begin{aligned}
&\hat{I}_z^i + \hat{I}_z^j \xrightarrow{\frac{\pi}{2}\hat{I}_y} \hat{I}_x^i + \hat{I}_x^j \\
&\qquad \xrightarrow{\tau_{DQ}\hat{H}_{dd}^{ij}} \left(\hat{I}_x^i + \hat{I}_x^j\right)\cos\phi_{DQ} + i\left(2\hat{I}_y^i\hat{I}_z^j + 2\hat{I}_z^i\hat{I}_y^j\right)\sin\phi_{DQ} \\
&\qquad \xrightarrow{\frac{\pi}{2}\hat{I}_y} -\left(\hat{I}_z^i + \hat{I}_z^j\right)\cos\phi_{DQ} - i\left(2\hat{I}_y^i\hat{I}_x^j + 2\hat{I}_x^i\hat{I}_y^j\right)\sin\phi_{DQ}
\end{aligned} \tag{3.10}$$

where the dipolar phase factor, $\phi_{DQ} = \frac{3}{2}d_{eff}^{ij}\tau_{DQ}$ and d_{eff}^{ij} is the effective dipolar coupling constant. The $\sin\phi_{DQ}$ and $\cos\phi_{DQ}$ terms in Equation 3.10 reflect DQ coherence and modulated longitudinal magnetisation, respectively. The application of the same pulse sequence block as for the excitation is applied again, for reconversion of the DQ coherences into z magnetisation:

$$\begin{aligned}
&-\left(\hat{I}_z^i + \hat{I}_z^j\right)\cos\phi_{DQ} - i\left(2\hat{I}_y^i\hat{I}_x^j + 2\hat{I}_x^i\hat{I}_y^j\right)\sin\phi_{DQ} \\
&\xrightarrow{\frac{\pi}{2}\hat{I}_y+\Delta\varphi} \xrightarrow{\tau_{DQ}\hat{H}_{dd}^{ij}} \xrightarrow{\frac{\pi}{2}\hat{I}_y+\Delta\varphi} \left(\hat{I}_z^i + \hat{I}_z^j\right)\left(\cos^2\phi_{DQ} \pm \sin^2\phi_{DQ}\right)
\end{aligned} \tag{3.11}$$

The sign of the $\sin^2\phi_{DQ}$ term in equation 3.11 is decided on by the phase, $\Delta\varphi$. Using the general rules of phase cycling described in Section 3.1.2, it is possible to selectively observe either the $\sin^2\phi_{DQ}$ or $\cos^2\phi_{DQ}$ term. In Section 3.2.2, the selection of DQ coherences (i.e. the $\sin^2\phi_{DQ}$) was described for the 2D ^{1}H DQ-^{1}H SQ experiment, using a 4-step DQ phase cycle by incrementing $\Delta\varphi$ of the reconversion (or excitation) segment in 90° steps while inverting the receiver every other scan. This gives the DQ signal, I_{DQ}. Intensity normalisation is achieved by recording a second analogous reference experiment (I_{ref}), without the selection of DQ coherences (i.e. the $\cos^2\phi_{DQ}$ in equation 3.11 is selected), using the same phases of the DQ excitation and reconversion blocks but by keeping the phase of the receiver constant.[122,123] The sum of the two experimental intensities, referred to as the multiple-quantum sum intensity, $I_{\Sigma MQ}$, is therefore given by $\left(\cos^2\phi_{DQ} + \sin^2\phi_{DQ}\right) = 1$.[122,123] The point-by-point normalised DQ build-up curve is then described by:

$$I_{nDQ} = \frac{I_{DQ}}{I_{\Sigma MQ}} = \frac{\sin^2\phi_{DQ}\cdot R\left(2\tau_{DQ}\right)}{\left(\cos^2\phi_{DQ} + \sin^2\phi_{DQ}\right)\cdot R\left(2\tau_{DQ}\right)} = \sin^2\phi_{DQ} \tag{3.12}$$

where the factor $R(2\tau_{DQ})$ describes the relaxation during the excitation and reconversion periods. It can be seen that the normalisation approach removes the effects of relaxation. It is expected that, in the long-time limit, the normalised intensity, I_{nDQ}, should reach a plateau value of 0.5.[122]

The normalised build-up curve for a single spin-pair follows the oscillatory $\sin^2$ function, which depends on the orientation of the dipolar vector with respect to the magnetic field, β (Figure 3.8a). Therefore, for different orientations of β,

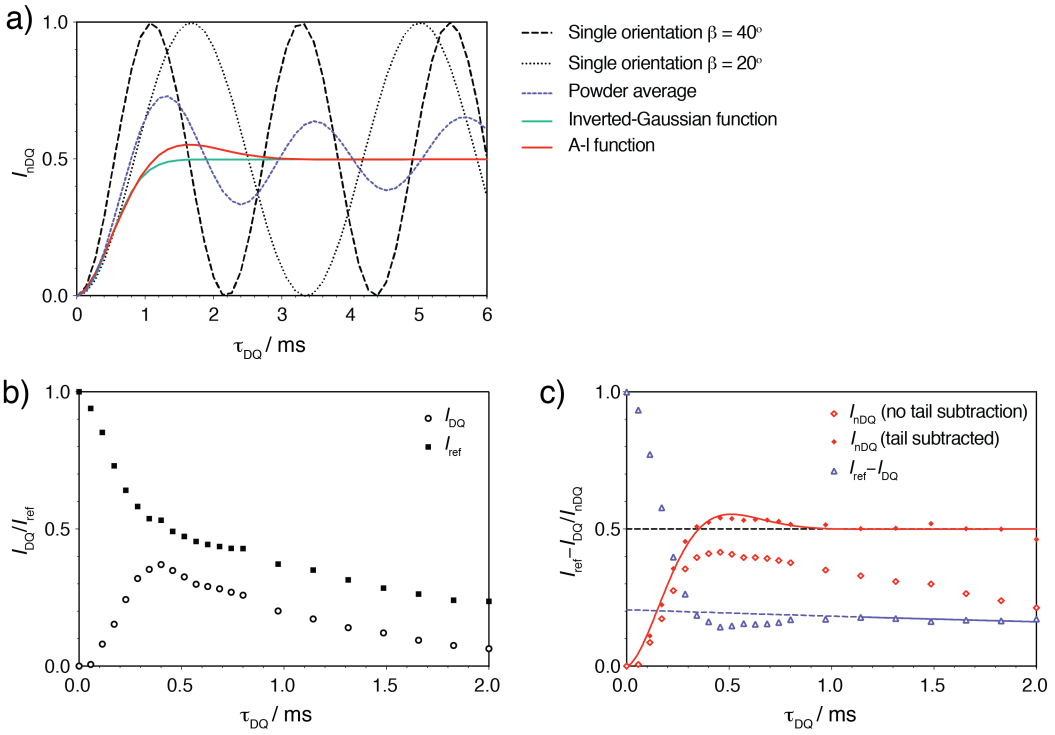

Figure 3.8: (a) Comparison of DQ build-up curves for a spin-pair at single orientations ($\beta = 40°$ and $20°$) and with powder averaging (performed for a set of 320 alpha and beta angles, and 10 gamma angles), simulated using SIMPSON[114] for a dipolar coupling, $d/2\pi = 1$ kHz, and $\nu_r = 15$ kHz, and the empirical inverted-Gaussian and A-l functions (Equations 3.13 and 3.15, respectively, with $d/2\pi = 1$ kHz). (b,c) Example experimental data for a liquid crystalline sample (data presented in Chapter 7). (b) DQ (I_{DQ}) and reference intensity (I_{ref}). (c) Exponential tail fit to $I_{ref} - I_{DQ}$ (solid portion of line shows the fitted tail region) and normalised DQ intensity (I_{nDQ}) with and without tail subtraction. The solid red line is a fit to the A-l build-up function.

the $\sin^2$ function oscillates with different periods. In samples where all orientations of molecules are present, powder averaging over an isotropic distribution of β results in a reduction of the oscillations, as seen in Figure 3.8a. In experimental ^{1}H DQ build-up curves, oscillations are generally not observed due to the effects of multispin interactions and dipolar truncation (see example experimental build-up curve in Figure 3.8b and c). In order to fit experimental build-up curves, an approximate inverted-Gaussian build-up function was derived using the second-moment approximation (Figure 3.8a):[122,124–126]

$$I_{nDQ} = \tfrac{1}{2}\left(1 - \exp\left\{-k d_{res}^2 \tau_{DQ}^2\right\}\right) \tag{3.13}$$

where for the case of a multiple spin system, the residual dipolar coupling represents

an average second-moment-type quantity:[127]

$$d_{res} = \left(\sum\nolimits_{pairs} d^2\right)^{1/2} \tag{3.14}$$

The scaling factor, k, is pulse-sequence specific and is $k_{C7} = 0.86/15 = 0.057$ for POST-C7.[128] Equation 3.13 can only fit the initial build-up region up to $I_{nDQ} = 0.45$. An improved analysis of ^{1}H DQ build-up curves was demonstrated by Chassé *et al.* using the Abragam-like (A-l) build-up function (Figure 3.8a), derived empirically from data on different elastomers:[129]

$$I_{nDQ} = \tfrac{1}{2}\left(1 - \exp\left[-\{0.143 d_{res}\tau_{DQ}\}^{1.5}\right] \times \cos\left[0.221 d_{res}\tau_{DQ}\right]\right) \tag{3.15}$$

Note that the empirical factors in Equation 3.15 have been adjusted to take into account the scaling factor for POST-C7 recoupling, compared to those previously reported for the static case.[129] The A-l function extends the fitting range for DQ build-up curves, enabling fitting of the local maximum, extending above 0.5, which is pronounced in systems with a narrow RDC distribution.[122] For samples with a wide distribution of RDCs, the maximum vanishes, and Equation 3.15 may be combined with a distribution of RDCs.[129]

Experimentally, normalised DQ curves do not always reach the expected value of 0.5 in the long-time limit. This effect has previously been observed for elastomer systems and attributed to isotropically mobile components (short dangling chains and solvent molecules).[122] Such liquid-like components contribute to the reference intensity, but not I_{DQ} (as they lack RDCs), meaning that the normalised intensity, I_{nDQ}, will be lower than expected. Such components form more slowly relaxing long-time tails of I_{ref} which may be fit to an exponential and subtracted to produce a well-behaving normalised build-up curve reaching the 50% intensity plateau (Figure 3.8c):[122,124]

$$I_{nDQ} = \frac{I_{DQ}}{I_{\Sigma MQ} - I_{tail}} \tag{3.16}$$

3.4 Determination of Relaxation Rates

In Section 2.4, the theory behind nuclear spin relaxation was presented. In Chapter 8, a series of relaxation experiments were performed to extract dynamic information: namely R_1, $R_{1\rho}$, and the steady-state NOE. In this section, the methods of measuring these relaxation rates are described.

Saturation recovery was used for measuring ^{13}C R_1 ($= 1/T_1$). The pulse sequence is shown in Figure 3.9a. A series of saturation pulses are first applied to the ^{13}C channel. During the following variable relaxation delay, τ, the spins begin to return to the equilibrium state, resulting in an increased signal over time. A 90°

pulse rotates any z-magnetisation into the xy-plane for detection. ^{1}H decoupling is applied during acquisition. During the variable relaxation time, repeated ^{1}H π pulses remove the effects of cross-correlated relaxation (see Section 2.4.3).[130] For saturation recovery R_1 measurements, the signal recovery can be approximated by a single exponential function:

$$I(\tau) = I_0(1 - e^{-\frac{\tau}{T_1}}) \tag{3.17}$$

where I_0 is the equilibrium magnetisation.

The $R_{1\rho}$ ($= 1/T_{1\rho}$) pulse sequence (Figure 3.9b) begins with a 90° ^{13}C pulse to rotate the magnetisation to the xy-plane, followed by a variable spin-lock pulse (of length τ_{SL}). $R_{1\rho}$ is extracted from the exponential fit according to:

$$I(\tau_{SL}) = I_0(e^{-\frac{\tau_{SL}}{T_{1\rho}}}) \tag{3.18}$$

The presence of motion on the timescale of the spin-lock frequency (microsecond timescale) will influence the measured $R_1\rho$. The process of measuring $R_1\rho$ at different spin-lock powers, is termed *relaxation dispersion* (RD), and may be used to quantify microsecond timescale motions.

The ^{1}H-^{13}C cross-relaxation rate was measured using the steady-state NOE difference experiment (see pulse sequence in Figure 3.9c). This involves recording two spectra: one in which the ^{1}H spins are saturated (I_{sat}), and a reference spectrum (I_{ref}) without ^{1}H saturation, in which all spins are at equilibrium. The ^{1}H irradiation is applied for long enough that a steady-state is achieved (5 s for the experiments in this thesis). The ^{13}C z-magnetisation is altered in this experiment, as a result of cross-relaxation, compared to the reference experiment. The steady-state NOE enhancement factor, η, is given by:

$$\eta = \frac{I_{sat} - I_{ref}}{I_{ref}} \tag{3.19}$$

which is related to the cross-relaxation rate, σ_{CH}, by:

$$\eta = \frac{\sigma_{CH}\gamma_H}{R_1\gamma_C} \tag{3.20}$$

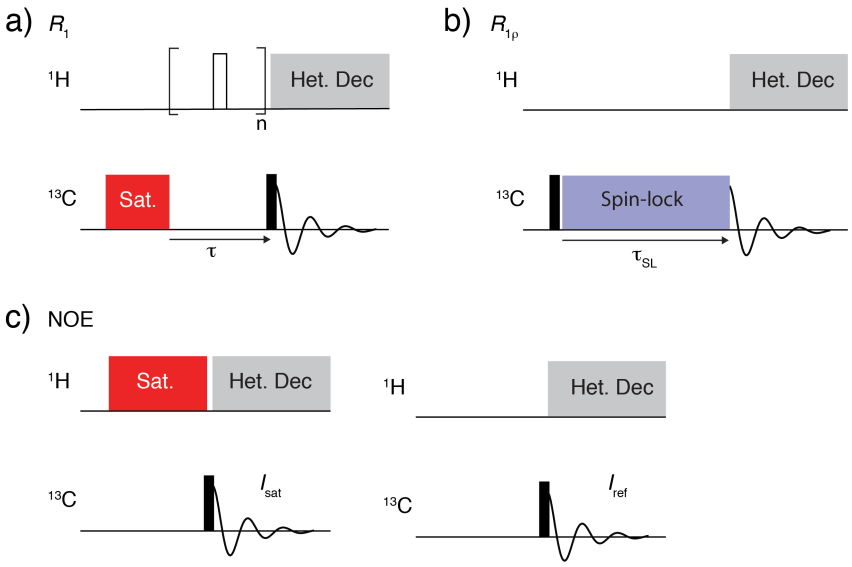

Figure 3.9: Pulse sequences used to measure ^{13}C relaxation rates: (a) R_1 by saturation recovery, (b) $R_1\rho$ and (c) the steady-state NOE.

Chapter 4

Structure Effects on the Ionicity of Protic Ionic Liquids

The work presented in this chapter was conducted under the supervision of Prof. Douglas MacFarlane in the School of Chemistry, Monash University, Australia.

4.1 Abstract

This chapter reports the characterisation of 16 protic ionic liquids (PILs) prepared by neutralisation of primary or tertiary amines with a range of simple carboxylic acids, or salicylic acid. The extent of proton transfer was greater for simple primary amine ILs compared to tertiary amines. For the latter case, proton transfer was increased by providing a better solvation environment for the ions through the addition of a hydroxyl group, either on the tertiary amine, or by formation of PIL/molecular solvent mixtures. The library of PILs were characterised by DSC and a range of transport properties (i.e., viscosity, conductivity and diffusivity) were measured. Using the (fractional) Walden rule, the conductivity and viscosity results were analysed with respect to their deviation from ideal behaviour. The validity of the Walden plot for PILs containing ions of varying sizes was also verified for a number of samples by directly measuring self-diffusion coefficients using pulsed-field gradient spin-echo (PGSE) NMR. Ionicity was found to decrease as the alkyl chain length and degree of branching of both the cations and anions was increased. These results aim to develop a better understanding of the relationship between PIL properties and structure, to help design ILs with optimal properties for applications.

4.2 Introduction

Ionic liquids (ILs), which are salts with melting points below 100 °C, have attracted

interest in a broad range of fields due to their unique characteristics and large potential for tuning and optimising their properties for specific applications.[131] This traditional "salt" definition (i.e. consisting solely of ions) is best fulfilled by the aprotic ionic liquids (AILs) , which consist of well-defined anions and cations. However, there are a number of important sub-classes of ILs, including protic ionic liquids (PILs), solvate ILs and metal complex-based ILs, that are characterised by dynamic equilibria involving neutral species. PILs, the focus of this work, are formed through transfer of a proton from a Brønsted acid (HA) to a Brønsted base (B), according to Equation 4.1.[132]

$$\mathrm{HA} + \mathrm{B} \rightleftharpoons \mathrm{BH}^+ + \mathrm{A}^- \tag{4.1}$$

The properties of PILs are largely dependent on their degree of ionisation, however, the extent to which proton transfer occurs is not yet well understood. The aqueous pK_a values for the acid and base, which determine the equilibrium constant for the proton transfer reaction in dilute aqueous solution, are not directly applicable to neat acid-based mixtures.[133] Yoshizawa *et al.* observed that a $\Delta \mathrm{p}K_a > 10$ was required for complete proton transfer to occur, whilst in aqueous solution, $\Delta \mathrm{p}K_a = 4$ gives 99% proton transfer.[133] The extent of proton transfer will depend on the structure of the acid and base constituents and their solvation ability. Stoimenovski *et al.* demonstrated that simple primary amines were able to deprotonate an indicator acid to a greater extent compared to tertiary amines with similar pK_a values.[134]

Many active pharmaceutical ingredients (APIs) are organic acids or bases that have the ability to form salts. In 2007, Rogers and co-workers described the reformulation of APIs as ILs.[134] Stoimenovski *et al.* reacted pharmaceutically active acids with pharmaceutical/biologically compatible bases to produce PILs.[23] Converting a neutral drug to a salt form can lead to improvements in the drug's properties, such as its solubility, absorption, pharmacodynamics and pharmacokinetics. Whilst there are a number of benefits of IL pharmaceuticals, it is well known that ionic drugs do not readily cross biological membranes and skin. However, it has been shown that some PILs exhibit enhanced membrane permeation, hypothesised to be due to the formation of neutral hydrogen-bonded clusters.[44] Stoimenovski *et al.* proposed that the formation of tetrameric clusters composed of two cations and two anions in primary amine containing PILs were responsible for decreased ionicity and enhanced membrane transport.[23,44] Similar cyclic tetramer hydrogen-bonding arrangements have been observed in molecular liquids such as propanol.[135] Recently, it was confirmed by infrared (IR) spectroscopy that theoretically predicted like-charge, hydrogen-bonded complexes exist in ionic liquids, showing that cooperative hydrogen bonding can compete with repulsive Coulombic forces.[135] Earlier studies by Kohler *et al.* on the interactions of amine and carboxylic acid mixtures also suggested

the presence of hydrogen-bonded clusters.[136,137] For the case of a primary amine, butylamine, and propanoic acid, a complex of approximately four ion pairs with at least partial zwitterionic character was reported. The formation of clusters is present in some ILs but not others, despite similar structure of the cations and/or anions. For example, heptylammonium acetate appears to behave as freely dissociated ions, despite possessing the same functional groups (primary amine and carboxylic acid) as tuammoniumheptane salicylate, a PIL that forms hydrogen-bonded clusters.[23,44] A greater understanding of the factors that drive the formation of such clusters could enable the smart design of cluster-forming IL pharmaceuticals with improved membrane transport properties.

Angell and co-workers described a convenient means to assess the ionicity and the presence of ion correlations, using the Walden plot of log(molar conductivity, Λ_m) versus log(reciprocal viscosity, η^{-1}).[138–140] The Walden rule, originally proposed for dilute electrolyte solutions, predicts a straight line passing through the origin, as expressed by:

$$\log \Lambda_m^0 = \log C + \log \eta^{-1} \tag{4.2}$$

where C is a constant. Typically, a 0.01 M KCl solution is used as a calibration point, and other electrolytes may be placed on the Walden plot for comparison with this 'ideal' behaviour. In a 0.01 M KCl solution it is thought that the ions are well dissociated and approximately equally mobile. Deviations from the ideal line may be quantified by measuring the vertical distance, termed ΔW. A ΔW of 1 indicates that the IL exhibits 10% of the ionic conductivity that it would exhibit if it behaved according to the 0.01 M KCl line. Whilst most ILs fall below the line,[140,141] it is in fact quite surprising that many ILs actually lie as close to the ideal line as they do, given that strong ion correlations are expected to a much greater extent in a pure salt, compared to a dilute aqueous solution. Such correlations may involve ion pairs (cation-anion), like-charge correlations (anion-anion and cation-cation) or larger clusters of multiple anions and cations. Significant research has focused on understanding the position of ILs on the Walden plot.[142] More detailed models based on Walden's rule have been proposed, such as the adjusted Walden plot and the fractional Walden rule, used in this work. By introducing an additional exponent, α, in Equation 4.3, a fractional Walden rule is obtained that allows the slope of the Walden plot to vary.[143]

$$\log \Lambda_m^0 = \log C' + \alpha \log \eta^{-1} \tag{4.3}$$

A more quantitative measure of the ionicity may be obtained from the ionic self-diffusion coefficients, using PGSE NMR. Using the Nernst-Einstein (NE) relation shown in Equation 4.4, the molar conductivity, Λ_{NE}, can be calculated from the

measured diffusion coefficients:

$$\Lambda_{NE} = \frac{F^2}{RT}\left(v_+ z_+ D_+ + v_- z_- D_-\right) \tag{4.4}$$

where F is the Faraday's constant, R is the universal gas constant, T is the temperature, v_+ and v_- are the number of cations and anions per unit formulae, z_+ and z_- and the cation and anion charge and D_+ and D_- are the diffusion coefficients of the cation and anion, respectively. The molar conductivity ratio, $\Lambda_{imp}/\Lambda_{NE}$ compares the conductivity obtained from impedance spectroscopy measurement (Λ_{imp}) to that calculated from NMR diffusivity measurements using the NE relation (Λ_{NE}) and represents the proportion of ions that contribute to ionic conduction from the diffusing species. This may also be described by $\Delta I = \log_{10}(\Lambda_{imp}/\Lambda_{NE})$, analogous to ΔW determined from the Walden plot for comparison.

The proton conduction mechanism, in which charge transport occurs through molecular diffusion, as implied by the Walden and NE equations, is termed the vehicular mechanism. Proton hopping within hydrogen-bonded networks provides an alternative mechanism (the "Grotthuss mechanism", originally proposed for water) of conduction that is independent of the ion diffusion.[144,145] A mixture of Grotthuss-type and vehicular-mechanisms has been suggested to account for the proton conduction of some PILs,[146–148] including those composed of amine and carboxylic acids.[136,137]

The investigated PILs in this paper are based on primary and tertiary amine cations and simple carboxylic acid, or salicylic acid anions and their structures are shown in Figure 1.3. ILs offer advantages in their tunability, which lead to the term 'designer solvents',[20] however due to the complex nature of the possible interionic interactions (i.e., Coulomb forces, dispersive interactions, $\pi - \pi$ stacking, hydrogen bonding, etc.),[149,150] aspects of structure do not easily translate to predictable changes in properties or function. The series of acids and bases in this work were chosen to investigate the influence of structure on the properties of PILs, and differ in their hydrogen bonding ability, alkyl chain length and degree of branching. There is recent interest in the use of IL/molecular solvent mixtures to further tune the properties of ILs.[151] A greater understanding of the interaction of PILs with molecular solvents will benefit many applications. Here, it is shown that the addition of hydrogen bonding solvents to a poorly ionised tertiary amine PIL can increase the degree of proton transfer and alter the transport properties. This work is focused on temperature-dependent transport properties: viscosity, conductivity and diffusivity.

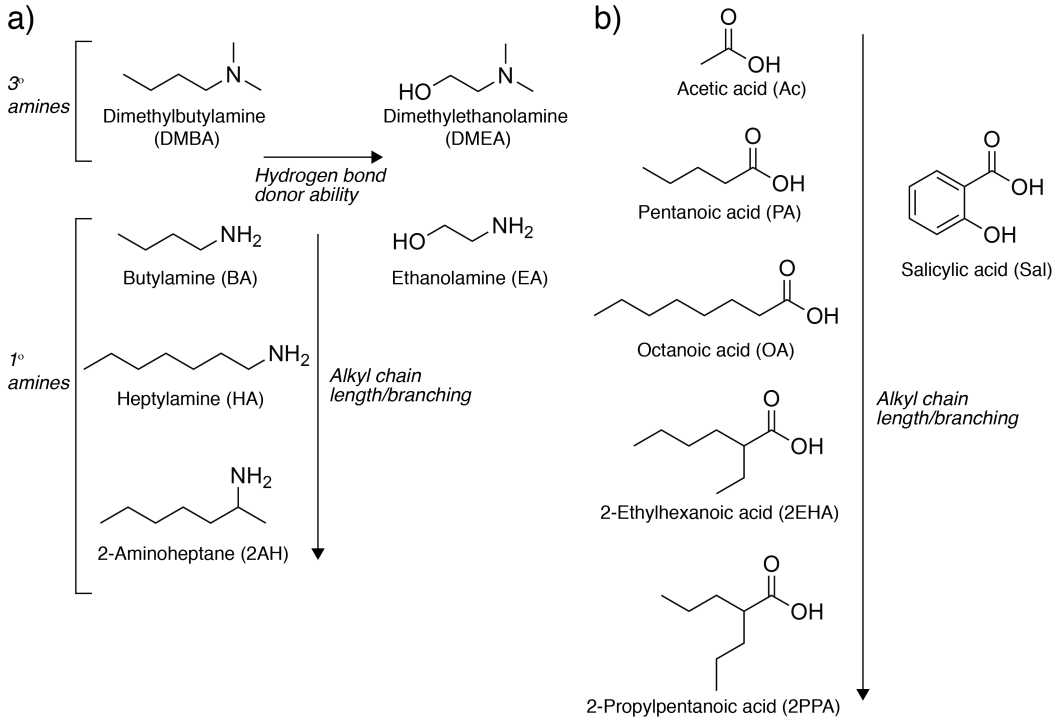

Figure 4.1: Structures of (a) primary amine and tertiary amine bases and (b) acids with varying hydrogen-bonding ability and alkyl chain length and branching used in this chapter.

4.3 Experimental Details

4.3.1 Sample Preparation

All PILs were prepared by mixing equimolar amounts of the constituent acids and bases at room temperature and stirred for 2 h. The PILs were then dried at 40 °C on a Schlenk line ($\sim$ 0.3 torr) for a minimum of 3 h.

4.3.2 Measurement of Thermal and Transport Properties

DSC scans were carried out at a heating/cooling rate of 10 °C min^{-1} using a Perkin Elmer DSC 8000. Transition temperatures are reported using the peak maximum of the thermal transition. The FTIR spectra were obtained using an Agilent FTIR spectrometer. Density measurements were carried out at different temperatures using an Anton Paar DMA5000 density meter. The dynamic viscosities were determined at temperatures matching the density measurements using a rolling ball viscosity meter (Anton Paar Lovis 2000ME). The ionic conductivities were measured by electrochemical impedance spectroscopy. A home-built dip cell consisting of two platinum wires sheathed in glass was immersed in the sample. The complex impedance spectra were measured over a frequency range of 100 MHz to 1 MHz. The temperature

was controlled with a Eurotherm 2204E temperature control unit, a thermocouple and heating block holding the cell compartment. The cell constant was determined using a solution of 0.01 M KCl at 25 °C.

Diffusion coefficients were obtained from ^{1}H PGSE NMR experiments performed on a Bruker Avance III 600 MHz (9.4 T) spectrometer. D_2O in an external capillary was used as the lock solvent. The interval between gradient pulses, Δ, was set to 800 ms, and the length of the gradient pulse, δ, was 2.5 ms. 16 gradient strengths were used ranging from 1.70 to 32.4 T m^{-1}. 16 transients were co-added and a recycle delay of 3 s was used.

4.4 Results and Discussion

4.4.1 Overview and Thermal Properties

16 different protic salts were synthesised by neutralisation of primary or tertiary amines with a range of simple carboxylic acids, or salicylic acid (Sal). Of these, heptylamine acetate and 2-aminoheptane salicylate have been reported previously by Stoimenovski *et al.*[23,44,134] The acids and bases used in this study varied in their chain length, degree of alkyl chain branching, and presence of hydroxyl group. Their structures and abbreviations are shown in Figure 4.1, and the protic salts synthesised in this work are summarised in Table 4.1. Of the 16 compounds synthesised, two formed gels ([2AH][2EHA] and [2AH][2PPA]) and two existed as either supercooled liquids or glassy solids at room temperature ([HA][OA] and [2AH][OA]), whilst the remaining 12 were RT liquids. The two gels were formed by the only PILs synthesised that contained both a branched cation (2AH) and branched anion (2EHA or 2PPA). Ionic liquid gels may be advantageous for certain applications, as not only do they retain the specific properties of ILs, they also gain the functional benefits associated with a solid structure. As these gels were not the focus of this work and measuring the transport properties of such materials is challenging, no further investigation into the samples was performed. Whilst initially forming RT liquids, the octanoate PILs ([HA][OA] and [2AH][OA]) slowly solidified at RT (over a period of several hours), indicating that they had initially formed supercooled liquids.

The phase behaviour was investigated by differential scanning calorimetry (DSC), and their glass transition temperatures (T_g), solid-solid phase transition temperatures (T_{s-s}), and melting points (T_m) are given in Table 4.1, and DSC traces shown in Figure 4.2. Only [DMBA][PA], [HA][PA], [HA][OA] and [2AH][OA] showed crystallisation and melting events. Notably, [HA][PA], [HA][OA] and [2AH][OA] underwent multiple transitions. This complex phase behaviour could be solid-solid phase transitions before melting, characteristic of plastic crystals, where the rotational motion of one or both of the ions in the crystal structure is released or could indicate

Table 4.1: PILs synthesised in this chapter.

	PIL	Abbreviation	RT form	T_g / °C	T_{s-s} / °	T_m / °C
1	Dimethylbutylamine Pentanoate	[DMBA][PA]	Liquid	-[a]	–	–
2	Dimethylethanolamine Pentanoate	[DMEA][PA]	Liquid	-71.6 ± 0.7	–	–
3	Butylamine Pentanoate	[BA][PA]	Liquid	–	–	–
4	Ethanolamine Pentanoate	[EA][PA]	Liquid	-73.7 ± 0.6	–	–
5	Heptylamine Acetate	[HA][Ac]	Liquid	NA[b]	NA[b]	NA[b]
6	Heptylamine Pentanoate	[HA][PA]	Liquid	-88.0 ± 0.3	-16.65 ± 0.01	-5.06 ± 0.4
7	Heptylamine Octanoate	[HA][OA]	Supercooled liquid	–	$3.76 \pm 0.05, 14.91 \pm 0.02$	24.65 ± 0.2
8	Heptylamine 2-Ethylhexanoate	[HA][2EHA]	Liquid	-78 ± 1	–	–
9	Heptylamine 2-Propylpentanoate	[HA][2PPA]	Liquid	-75 ± 3	–	–
10	2-Aminoheptane Pentanoate	[2AH][PA]	Liquid	-80 ± 1	–	–
11	2-Aminoheptane Octanoate	[2AH][OA]	Supercooled liquid	–	-1.64 ± 0.01, -15.6 ± 0.4, 24.8 ± 0.3	31.00.3
12	2-Aminoheptane 2-Ethylhexanoate	[2AH][2EHA]	Gel	–	–	–
13	2-Aminoheptane 2-Propylpentanoate	[2AH][2PPA]	Gel	–	–	–
14	Butylamine Salicylate	[BA][Sal]	Liquid	-60.6 ± 0.26	–	–
15	Heptylamine Salicylate	[HA][Sal]	Liquid	-55 ± 2	–	–
16	2-Aminoheptane Salicylate	[2AH][Sal]	Liquid	-62.5 ± 0.3	–	–

[a] "–" indicates that the transition was not observed by DSC over the temperature range studied.
[b] DSC not measured.

the presence of a mixture of co-existing salt and acid/base components.

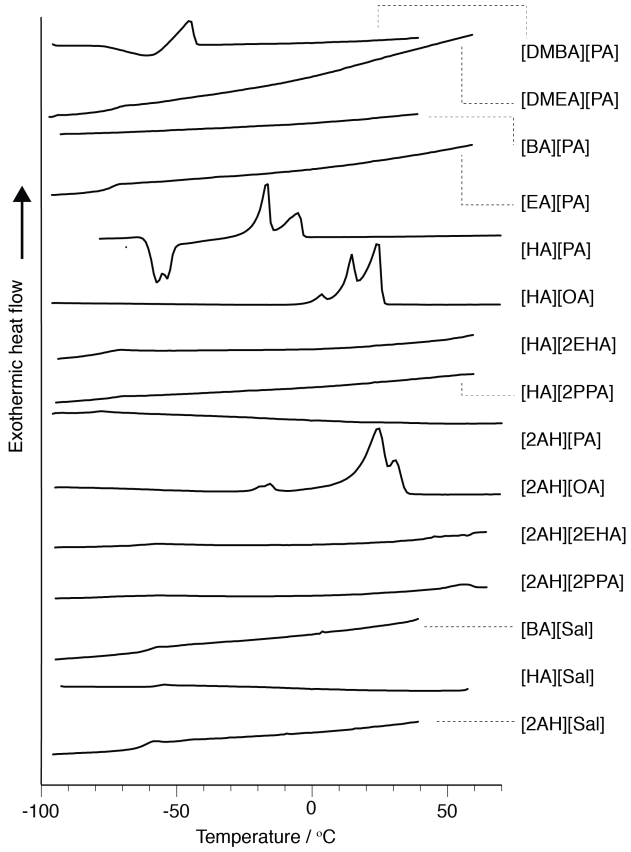

Figure 4.2: DSC thermograms of PILs at a heating rate of 10 °C min^{-1}.

4.4.2 Influence of Hydrogen-Bonding Groups in Primary and Tertiary Amine-Based PILs

The discussion is now turned to the PILs composed of either tertiary or primary amine bases with or without the presence of a hydroxyl group, combined with pentanoic acid (PILs 1-4 in Table 4.1). The pentanoate-based samples were all RT liquids, for both tertiary and primary amine bases with or without a hydroxyl functional group (Table 4.1). The properties of PILs depend largely on their degree of proton transfer. In neat PILs, the solvation environment has a very strong effect on the energy of proton transfer. Stoimenovski *et al.* showed that whilst primary amines tend to produce highly ionised ILs, the simple tertiary amine-based ILs of their study showed a low degree of proton transfer, attributable to the differences in hydrogen bonding environments offered by the amine/ammonium ions.[134,152] They suggested that this trend may be easily disturbed by the presence of other functional groups, especially OH or other hydrogen bonding sites. Indeed, in a later study,

they found that the proton transfer behaviour of ILs containing the tertiary amine cation, 2-pyrrolidinoethanol, (EtOH)pyr, produced a significantly higher degree of proton transfer compared to the simple tertiary amines, presumably as a result of the hydroxyl group.[23] In order to investigate the degree of proton transfer, FTIR spectra of the PILs and the pentanoic acid starting material (Figure 4.3) were recorded. The C=O stretch of pentanoic acid at 1704 cm^{-1} is absent in the primary amine PILs, ([BA][PA]) and [EA][PA]) (Figure 4.3a), which is indicative of complete ionisation. The ionic species may be involved in dynamic hydrogen-bonds of the form $A^{-}\cdots H\text{–}B^{+}$ which can be considered to lie on the proton transfer coordinate,[153] described by the equilibrium in Equation 4.1. A strong peak corresponding to the C=O stretch of the carboxylic acid is present in the spectra of the simple tertiary amine PIL, [DMBA][PA] (Figure 4.3b), indicating poor proton transfer, as expected. This system can therefore be considered an acid-base-IL mixture, with the equilibrium likely involving hydrogen-bonds of the form $A\text{–}H\cdots B$ and, to a smaller extent, $A^{-}\cdots H\text{–}B^{+}$.

For the tertiary amine containing hydroxyl PIL, ([DMEA][PA]), the C=O stretch is still present albeit with reducefd intensity relative to the other peaks, suggesting that, whilst not being complete, a higher degree of proton transfer has occurred compared to the simple tertiary amine PIL. The addition of a hydroxyl group to the amine as a H-bond donor can promote proton transfer by stabilising the carboxylate anion.

Viscosity and conductivity data are presented in Figure 4.4. Both plots show that the investigated PILs have Arrhenius like behaviour. Table 4.2 summarises the Arrhenius fit parameters for viscosity data and conductivity data in Equations 4.5 and 4.6, respectively:

$$\eta = \eta_{\infty} \exp\left(\frac{E_{a,\eta}}{RT}\right) \tag{4.5}$$

$$\kappa = \kappa_{\infty} \exp\left(\frac{-E_{a,\kappa}}{RT}\right) \tag{4.6}$$

where $E_{a,\eta}$ is the apparent activation energy for viscous flow (i.e. the energy barrier that must be overcome for the ions to move past each other), η_{∞} is the maximum dynamic viscosity, $E_{a,\kappa}$ is the apparent activation energy indicating the energy required for an ion to hop into a free hole, κ_{∞} is the maximum electrical conductivity, R is the gas constant, and T is the temperature in Kelvin. Equations 4.5 and 4.6 are not expected to hold over extended temperatures ranges where curvature in the Arrhenius plot would indicate the need to use a VTF form of fitting function, however, the measured data did not show sufficient curvature to warrant the use of the additional fitting parameter.

The primary amine-based pentanoate PILs possess viscosities more than an order of magnitude higher than the tertiary amine-based PIL, consistent with both

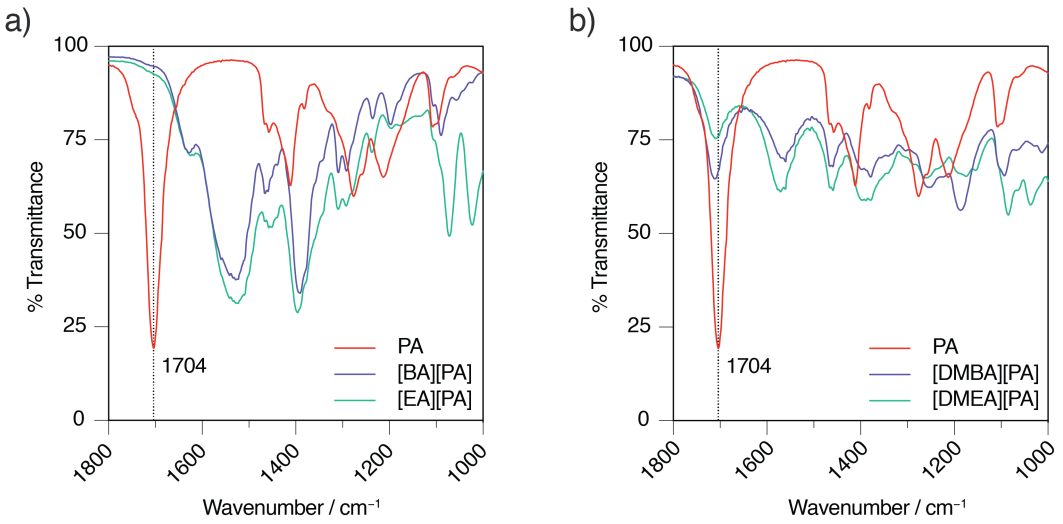

Figure 4.3: FTIR-ATR spectra of (a) pentanoic acid (red), [BA][PA] (purple) and [EA][PA] (green) and (b) pentanoic acid (red), [DMBA][PA] (purple) and [DMEA][PA] (green).

the stronger ionic interactions in the more highly ionised systems and additional hydrogen-bonding possible in the primary amine-based systems, which contain multiple hydrogen-bond donors (Figure 4.4a). Of the primary amine-based PILs, the hydroxyl containing [EA][PA] is more viscous than its simple amine analogue, [BA][PA], which may be attributed to the additional hydrogen bonding involving the hydroxyl group. Similarly, the tertiary amine-based PIL [DMEA][PA] is more viscous than the simple amine [DMBA][PA], as a result of the higher degree of ionisation and additional hydrogen bonding of the hydroxyl group. $E_{a,\eta}$ for [DMBA][PA] is significantly lower at 17.0 kJ mol^{-1}, compared to the other three PILs with apparent activation energies for viscous flow above 30 kJ mol^{-1} (Table 4.2), consistent with a lower energy barrier for viscous flow due to weaker electrostatic interactions. η_∞ was also significantly different for [DBMA][PA], more than two orders of magnitude higher compared to the other PILs (Table 4.2). η_∞ is representative of a structural contribution of the ions to the viscosity, since interactions that contribute to the viscosity are no longer effective at infinite temperature.

The ionic conductivities also show distinct difference between the four PILs (Figure 4.4b), which cannot be attributed to differences in the viscosities alone. The simple tertiary amine-based PIL, [DMBA][PA] shows the lowest conductivity, despite its low viscosity, consistent with a low degree of proton transfer. The hydroxyl functionalised analogue, [DMEA][PA] showed a significant improvement in conductivity, showing higher conductivity than both primary amine-based ILs, despite the lower degree of proton transfer and lower viscosity. As for the tertiary amine PILs, the presence of the hydroxyl group was shown to improve the conductivity

for the primary amine-based PILs, with [EA][PA] showing a higher conductivity compared to the simple primary amine-based [BA][PA], despite being more viscous.

In order to further our understanding of the transport behaviour, the viscosity and conductivity data were combined into Walden plots (Figure 4.5). Fits to the fractional Walden rule (Equation 4.3) are given in Table 4.2. Both the simple amine-based PILs (primary amine [BA][PA]: Figure 4.5a, and tertiary amine [DMBA][PA]: Figure 4.5b) show a significant deviation from the ideal line, although to a much greater extent for [DMBA][PA], consistent with incomplete proton transfer as observed by FTIR. [BA][PA] lies just below the 10% line, despite IR showing complete ionisation. For both the primary and tertiary-based PILs, the presence of the hydroxyl group ([EA][PA]: Figure 4.5a and [DMEA][PA]: Figure 4.5b) results in a significantly closer agreement to the Walden rule compared to the simple amine-based PILs. This is expected for the tertiary amine-based PILs, since the FTIR spectra showed a higher degree of proton transfer for the hydroxyl functionalised PIL. It is less clear why this is the case for the primary amine PILs, where complete ionisation has occurred in either case. This could suggest that the hydroxyl functionalised [EA][PA] displays a lower degree of association (i.e. less tendency to form ion pairs and clusters) compared to the simple amine [BA][PA], despite the additional hydrogen bonding ability. This could be due to increased cation-cation hydrogen bond interactions leading to weaker cation-anion association. The nature of like-ion (cation-cation and anion-anion) correlation affects has also been shown to strongly influence conductivity.[154] Such effects could result from increased cation-cation hydrogen-bond interactions of the ethanolamine ions, i.e. correlated motion, but may also be strongly influenced by the anticorrelated motion of ions. The ethanolamine cation also lacks the extended alkyl chain that is present in butylamine. As will be discussed below, the length of alkyl chains in PILs and the hydrocarbon-hydrocarbon interactions have a significant effect on the ionicity of PILs.

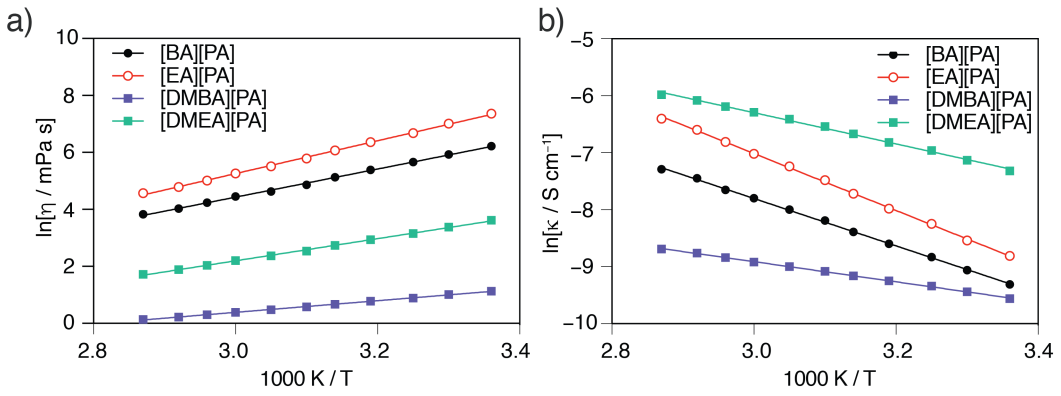

Figure 4.4: Arrhenius plots for pentanoate PILs temperature-dependence (a) viscosity and (b) conductivity data.

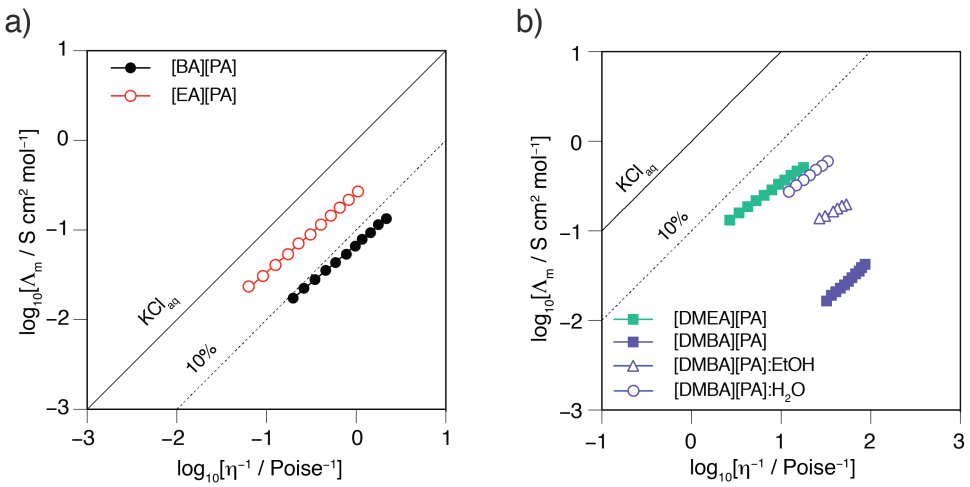

Figure 4.5: Walden plot of temperature-dependent conductivities and viscosities of (a) primary amine and (b) tertiary amine PILs.

The closer to 'ideal' Walden behaviour for the hydroxyl-functionalised PILs could also be accounted for by a secondary Grotthuss-type hopping mechanism for proton transport. A key factor for proton transport via the Grotthuss mechanism is the presence of a hydrogen-bonded network, which is consistent with the increased viscosity observed for the hydroxyl-functionalised PILs. Deviations from the classical Walden rule, where proton conduction is coupled to translational diffusion and the slope, $\alpha = 1$, have previously been attributed to a Grotthuss-type transport mechanism in some PILs, such as lidocaine di-(dihydrogen phosphate), for which $\alpha = 0.53$ was reported.[148] A significantly lower value of $\alpha = 0.723$ for the hydroxyl functionalised [DMEA][PA] compared to [DMBA][PA] ($\alpha = 0.93$) (Table 4.2) was observed, while the primary amine based PILs showed similar values ($\alpha = 0.851$ and 0.877). While these deviations from ideal behaviour could indicate a contribution of a mechanism aside from vehicle transport, $\alpha < 1$ could also reflect temperature-induced changes in the degree of proton transfer or ion association.

Combining ILs and molecular solvents has been shown to be a promising strategy for tuning properties, with a variety of applications reported to benefit from IL/solvent mixtures, so much so that they have recently been referred to as "a 4th Evolution of Ionic Liquids".[151] The properties of IL/solvent mixtures are not always predictable on the basis of simple mixing rules, but instead reflect interactions between the ionic and molecular components. Since the low degree of proton transfer in the tertiary amine ILs is due to poor solvation environment, the tertiary amine-based IL, [DMBA][PA] was combined with stoichiometric quantities of hydrogen-bonding solvents (ethanol or H_2O). For the simple tertiary amine IL,

[DMBA][PA] where poor proton transfer occurred, the addition of a hydrogen bonding solvent (ethanol or H_2O) promoted proton transfer as expected, however proton transfer was still not complete, as indicated by the presence of a carbonyl IR stretch at 1704 cm^{-1} (Figure 4.6a). A significant increase in viscosity was observed on the addition of solvent, consistent with increased proton transfer and/or increased hydrogen bonding and was greater for H_2O compared to ethanol (Figure 4.7b).

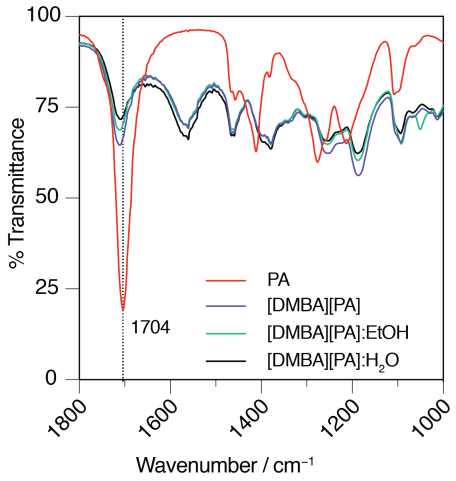

Figure 4.6: FTIR-ATR spectra of (a) pentanoic acid (red), [DMBA][PA] (purple), [DMBA][PA]:EtOH (green) and [DMBA][PA]:H2O (black).

The molar conductivity of both IL/solvent mixtures increased by more than two orders of magnitude, with the H_2O mixture showing the highest conductivity, despite also being the most viscous (Figure 4.7). Walden plots for the IL/molecular solvent mixtures are shown in Figure 4.5b, alongside the tertiary amine-based ILs for comparison. The IL/molecular solvent mixtures appear closer to the 'ideal' line on the Walden plot compared to the pure IL. This is likely a result of increased ionicity due to stabilisation of the carboxylate anion by the hydroxyl proton in the same manner as the hydroxyl group in [DMEA][PA]. The addition of EtOH to [DMBA][PA], however, does not increase the ionicity compared to that of [DMEA][PA], despite both containing the same molar equivalents of the hydroxyl functional group. The difference in the Walden behaviour could be due to the butyl chain present in DMBA but not in DMEA, which will be discussed further below. The H_2O mixture appears closer to the Walden line, almost matching that of the hydroxyl functionalised [DMEA][PA], which may be attributed to the additional hydrogen bond donor ability of H_2O compared to EtOH. The Grotthuss-type proton conduction mechanism may also contribute to a greater extent in the IL/solvent mixtures, where an extended hydrogen-bonded network could result from the addition of the molecular solvents that can provide both hydrogen-acceptor and donor sites. Overall, these results show

that the addition of molecular solvent to ILs displaying poor proton transfer may be a viable strategy in order to improve ionicity

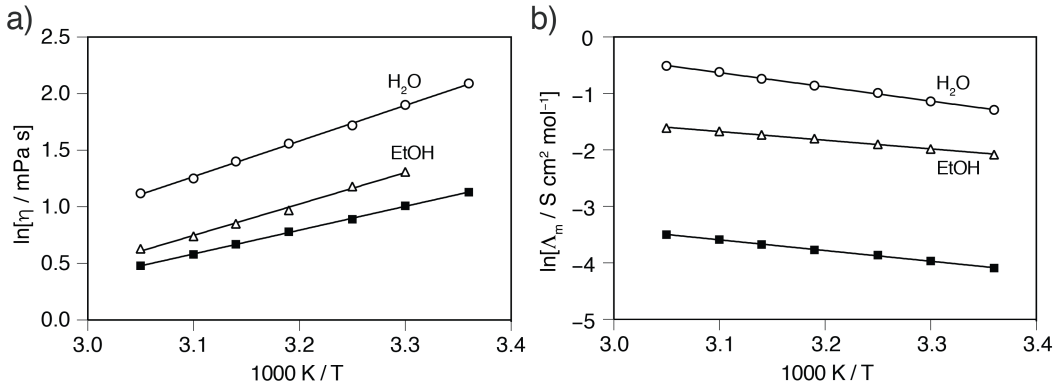

Figure 4.7: (a) Viscosity and (b) molar conductivity data for [DMBA][PA] pure IL (closed squares) and IL/solvent mixtures (open symbols). Note that the molar conductivity is presented in (b) rather than the conductivity as displayed for other ILs, to account for the proportion of ionic and molecular species.

Table 4.2: Arrhenius fit parameters for the viscosity (Equation 4.5) and conductivity (Equation 4.6) data presented in Figure 4.4. and for fractional Walden plots (Equation 4.3) presented in Figure 4.5.

	Viscosity		Conductivity		Walden		
PIL	$10^4 \times \eta_\infty$ / mPa s	$E_{a,\eta}$ / kJ mol^{-1}	κ_∞ / S cm^{-1}	$E_{a,\kappa}$ / kJ mol^{-1}	α	$\log(C'/\text{S cm}^2\ \text{mol}^{-1})$	ΔW (298 K)
[BA][PA]	0.31 ± 0.06	41.0 ± 0.5	$[1.1 \pm 0.1] \times 10^2$	34.6 ± 0.3	0.851 ± 0.007	-1.163 ± 0.002	1.1
[EA][PA]	0.06 ± 0.01	47.9 ± 0.5	$[2.9 \pm 0.4] \times 10^3$	41.5 ± 0.4	0.877 ± 0.006	-0.594 ± 0.004	0.43
[DMBA][PA]	32.0 ± 1.9	17.0 ± 0.2	0.027 ± 0.001	14.7 ± 0.1	0.93 ± 0.01	-3.18 ± 0.03	3.3
[DMEA][PA]	0.8 ± 0.1	32.3 ± 0.4	7 ± 1	22.8 ± 0.4	0.723 ± 0.005	-1.185 ± 0.005	1.3

$R^2 > 0.997$ for all linear fits.

4.4.3 Influence of Alkyl Chain-Length and Branching on the Properties of Primary Amine-Based PILs

In addition to the hydrogen bonding ability and presence of functional groups, the nature of non-polar regions (e.g., alkyl-length and degree of branching) can be expected to strongly influence the properties of PILs. The following discussion is on the PILs composed of either heptylamine (straight chain) or 2-aminoheptane (branched) primary amine bases, combined with five different acids of varying chain length and degree of branching: acetic acid, pentatonic acid, octanoic acid, 2-ethylhexanoic acid, and 2-propylpentanoic acid (PILs 5-13 in Table 4.1). In addition, the influence of the base chain length/degree of branching in three salicylate-based PILs paired with the simple primary amines, butylamine, heptylamine, or 2-aminoheptane (PILs 14-16 in Table 4.1) was investigated.

Temperature-dependent densities, viscosities and conductivities were measured for all of the PILs, excluding the two gels, at temperatures from 298 to 348 K. All of the PILs showed Arrhenius viscosity and conductivity behaviour (Table 4.3). The temperature dependent viscosity of PILs containing a branched ion (either cation or anion), showed a steeper slope, indicating a larger apparent activation energy of viscous flow (Figures 4.8a and 4.8c, Table 3). The conductivities of the different primary amine salicylate PILs differ with the shorter butylammonium IL exhibiting the highest conductivity (Figure 4.8b), even though all the PILs appear to be completely proton transferred. Despite similar viscosities of the pentanoate and octanoate PILs with either heptylamine or 2-aminoheptane (note the crossover of curves at intermediate temperatures), significant differences in conductivities were observed (Figure 4.8c). The branched 2AH containing ILs showed lower conductivities compared to the straight chain HA ILs.

Table 4.3: Arrhenius fit parameters for the viscosity (Equation 4.5) and conductivity (Equation 4.6) data presented in Figure 4.8. and for fractional Walden plots (Equation 4.3) presented in Figure 4.9.

	Viscosity		Conductivity		Walden		
PIL	$10^6 \times \eta_\infty$ / mPa s	$E_{a,\eta}$ / kJ mol^{-1}	κ_∞ / S cm^{-1}	$E_{a,\kappa}$ / kJ mol^{-1}	α	$\log(C'/\text{S cm}^2\ \text{mol}^{-1})$	ΔW (298 K)
[BA][Sal]	0.08 ± 0.04	61 ± 1	$[1.0 \pm 0.4] \times 10^5$	54 ± 1	0.879 ± 0.004	-0.821 ± 0.004	0.65 (303 K)
[HA][Sal]	0.4 ± 0.2	56 ± 1	$[8 \pm 2] \times 10^3$	49.3 ± 0.7	0.897 ± 0.006	-1.162 ± 0.005	1.02
[2AH][Sal]	0.04 ± 0.02	63 ± 1	$[5.4 \pm 0.8] \times 10^2$	44.6 ± 0.4	0.71 ± 0.01	-1.49 ± 0.01	0.96
[HA][Ac]	14 ± 2	43.1 ± 0.4	$[2.6 \pm 0.4] \times 10^2$	35.0 ± 0.4	0.827 ± 0.007	-1.017 ± 0.003	0.90
[HA][PA]	23 ± 3	42.9 ± 0.4	15 ± 2	30.6 ± 0.4	0.734 ± 0.008	-1.146 ± 0.004	0.92
[HA][OA]	9 ± 1	44.8 ± 0.3	2.3 ± 0.7	27.5 ± 0.9	0.63 ± 0.02	-1.149 ± 0.007	1.21
[2AH][PA]	0.032 ± 0.007	61.8 ± 0.6	2.7 ± 0.8	31.7 ± 0.8	0.52 ± 0.01	-2.03 ± 0.01	1.43
[2AH][OA	0.11 ± 0.03	56.9 ± 0.7	0.0021 ± 0.007	21.5 ± 0.8	0.39 ± 0.02	-2.578 ± 0.008	1.93

$R^2 > 0.99$ for all linear fits.

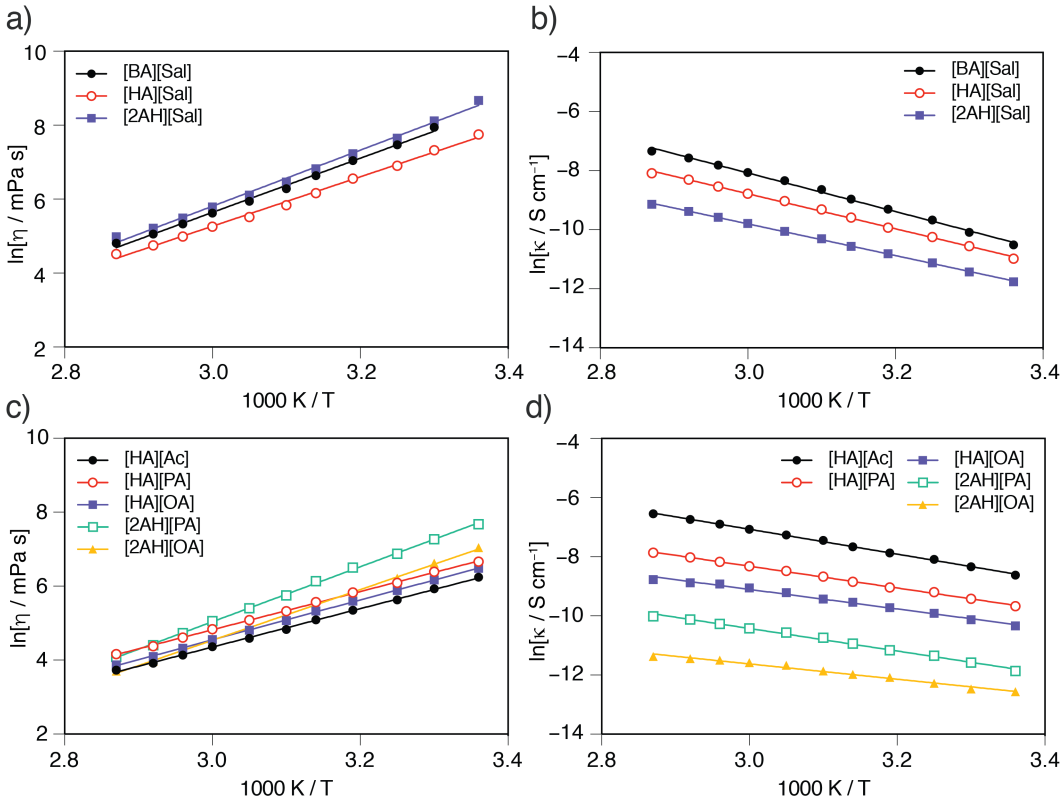

Figure 4.8: Arrhenius plots for salicylate PILs temperature-dependence (a, c) viscosity and (b, d) conductivity and acetate, pentanoate and octanoate PILs temperature-dependence (c) viscosity and (d) conductivity.

As expected, the Walden plot shows a linear temperature dependence for each PIL. [2AH][Sal] falls well below the 'ideal line', as has been previously reported (Figure 4.9a),[23] indicating that the majority of the ions form neutral ion pairs or clusters which are unable to conduct. It was suggested (based on crystal structures of analogous compounds) that the ions organise into a cyclic hydrogen-bonded cluster-like complex consisting of two cations and two anions.[23] Despite also containing a primary amine, [HA][Sal] shows slightly closer to ideal behaviour, whilst [BA][Sal] shows even better agreement with the Walden rule (Figure 4.9a), suggesting that the formation of such clusters is not as common or are not as long-lived as for the 2AH containing PIL, or, additional factors influence the transport behaviour. Understanding the reasons for these differences may enable the design of ILs with a tendency to form strong hydrogen-bonded clusters. This is of particular importance since hydrogen-bonded cluster forming ILs have been shown to transport much more readily through model membranes compared to dissociated PILs.[44]

[HA][Ac] lies close to the 10% line, as previously reported[134] (Figure 4.9b), whilst the PILs with increasing anion chain length show increased deviation from ideal behaviour following the trend octanoate > pentanoate > acetate (Figure 4.9b).

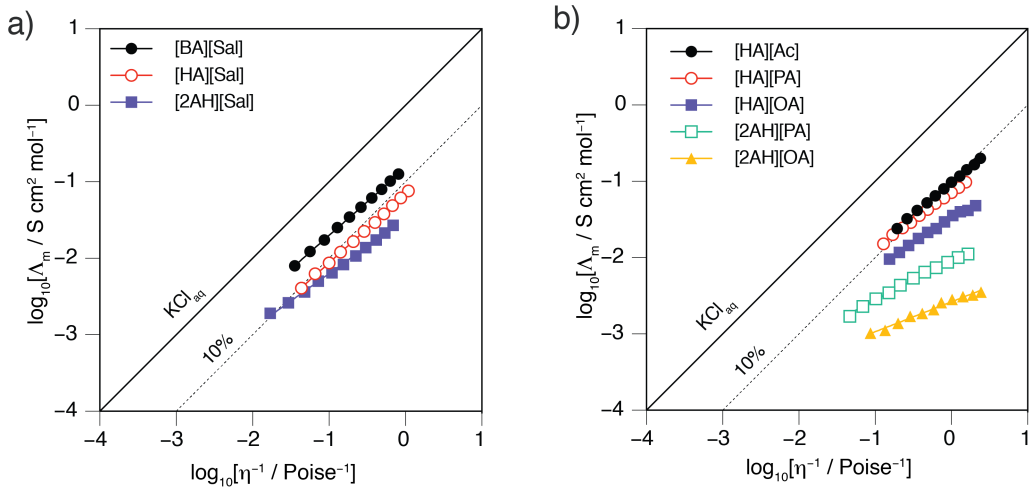

Figure 4.9: Walden plot of temperature-dependence conductivities and viscosities of (a) salicylate PILs with varying primary amine cations and (b) acetate, pentanoate and octanoate PILs.

Increasing the alkyl chain length decreases the molar concentration of the ions, leading to a decrease in the electrostatic attraction between cations and anions, whilst increasing van der Waals interactions of the alkyl chain-ion inductive forces and hydrocarbon-hydrocarbon interactions. Molecular dynamics simulations and X-ray scattering experiments have demonstrated that when the length of alkyl tails increases beyond a critical length, nanophase segregation occurs in numerous ILs, where the charge-rich ionic regions and the charge-poor aliphatic regions cluster into domains.[34,155–157] For the frequently studied imidazolium class of AILs, X-ray diffraction studies showed a characteristic diffraction peak assigned to nonpolar alkyl chain aggregations for those ILs having alkyl chains of four or more carbon atoms. Ueno *et al.* reported that imidazolium ILs with one to two carbon atoms in the alkyl chain of the imidazolium showed similar ionicity, but ionicity began to decrease significantly on going from four to eight carbon atoms, confirming that the attraction between the nonpolar alkyl chain groups impacts on the ionicity of ILs.[158] Griffin *et al.* found that nanophase segregation of alkyl chains in a series of quaternary ammonium ILs reduces the ionicity due to aggregation-induced suppression of dynamics.[159] Nanostructure has also been observed for PILs containing an alkylammonium cation, where there are at least two carbon atoms in the alkyl chain.[160,161] In the pentanoate and octanoate PILs studied here, the van der Waals attraction between the nonpolar alkyl chains and possible segregation into domains could account for the extremely low ionicity observed in the Walden plots. Further studies, such as X-ray diffraction, are required to confirm the presence of nanostructure in the PILs in this work.

As with the salicylate PILs, the branched 2-aminoheptane PILs paired with pentanoate and octanoate, showed poorer ionicity compared to those containing

the straight chain heptylamine. [2AH][PA] and [2AH][OA] also showed a significant deviation from a slope of 1 ($\alpha = 0.52$ and 0.39, respectively), as predicted by the Walden rule. The value of α reflects the difference of apparent activation energies of the ionic conductivity and viscosity and could reflect a temperature induced change in the degree of ion association.

The Walden plot provides a convenient means for comparing ionicity between ILs, however does not take into the effect of differing ion sizes. The effect of ion size can be considered by a corrected Walden plot adjusted using the calculated ionic radius as described by Bonhôte *et al.*[162,163] and Abbott,[164] or by directly measuring the diffusion, most commonly by means of PGSE NMR. The latter method was utilised and diffusion coefficients were measured by PGSE NMR to compare the molar conductivity to experimental diffusivity. Due to experimental difficulties measuring diffusion in highly viscous ILs (a combination of slow diffusion and fast relaxation), PGSE NMR measurements were performed at 40 °C where the samples are significantly less viscous than at RT. The calculated $\Lambda_{imp}/\Lambda_{NE}$ and related $\Delta I = \log_{10}(\Lambda_{imp}/\Lambda_{NE})$ values for several ILs are given in Table 4.4, alongside ΔW obtained from the Walden plots. The excellent correlation between ΔW and ΔI indicate that the Walden plot is a reasonable measure of ionicity, both following the same trends, without requiring the more time-consuming PGSE NMR measurements.

The relative diffusion coefficients of the acidic proton (D_{H+}) compared to those of the non-exchangeable protons of the cation and anion (D_+ and D_-, respectively) can provide information of the mechanism of proton conduction.[147] An enhancement of D_{H+} compared to D_+ may result from intermolecular proton exchange (a Grotthuss-type mechanism), while similar values are expected for the case of vehicular transport. A value of D_{H+}/D_+ 1.5 times higher than the heptylammonium cation was observed for [HA][Ac] (Table 4.4). Watanabe *et al.* proposed a Grotthuss-type proton conduction mechanism in the PIL composed of *N*-methylimidazole and acetic acid involving fast rotation of acetic acid/acetate as a key step.[165] A similar mechanism may contribute in [HA][Ac], accounting for the higher conductivity observed compared to the other PILs. For the remaining PILs, there was either a small enhancement of D_{H+} compared to D_+ ($D_{H+}/D_+ = 1.1$ and 1.2 for [HA][PA] and [2AH][OA], respectively) or no significant difference ($D_{H+}/D_+ = 1.0$ for [2AH][Sal] and [2AH][PA]), consistent with the vehicular mechanism dominating the proton conductivity in these cases.

Table 4.4: Diffusion coefficients from PGSE NMR for PILs. All reported values were recorded at 313 K.

IL	D_+ / m^2 s^{-1}	D_- / m^2 s^{-1}	D_{H+} / m^2 s^{-1}	$\Lambda_{imp}/\Lambda_{NE}$	ΔI^a	ΔW^a
[HA][Ac]	4.4×10^{12}	5.6×10^{12}	6.5×10^{12}	0.15	0.8	1.0
[HA][PA]	4.4×10^{12}	3.9×10^{12}	4.9×10^{12}	0.10	1.0	1.0
[2AH][Sal]	6.3×10^{13}	6.5×10^{13}	6.1×10^{12}	0.11	1.0	1.2
[2AH][PA]	2.6×10^{12}	2.3×10^{12}	2.7×10^{12}	0.020	1.7	1.6
[2AH][OA]	3.2×10^{12}	2.9×10^{12}	3.7×10^{12}	0.007	2.2	2.3

[a]The estimated errors in ΔI and ΔW are ± 0.1.

4.5 Conclusions

A series of PILs were prepared from a range of primary or tertiary amines, and carboxylic acids. Temperature-dependent physicochemical properties such as viscosity, density, and conductivity were measured, and Walden plots constructed to determine the ionicity of the PILs. The ionicities of the studied PILs vary with the systematic variation in the structure of the cations and anions. FTIR and Walden plot studies indicated that the tertiary amine-based PIL exhibited poor proton transfer in comparison to PILs containing primary amines, however improvement of the solvation ability by the addition of a hydroxyl group promoted proton transfer. In general, PILs containing either acids or bases with longer alkyl chain lengths and branched chains showed decreased ionicity. In addition, IL/molecular solvent mixtures were prepared from either water or ethanol, and the tertiary amine-based PIL, [DMBA][PA], which exhibited poor proton transfer in the pure IL form. The addition of the molecular solvent was shown to promote proton transfer, and lead to an increase in viscosity, conductivity and ionicity compared to the pure PIL, demonstrating that IL/molecular solvent mixtures are a promising strategy to tune the transport properties of PILs. PGSE NMR measurements of ionicity showed good correlation between ΔW and ΔI, confirming that the former provides an accessible and realistic reflection of ion association effects.

Chapter 5

Revealing Intermolecular Hydrogen Bonding Structure and Dynamics in a Deep Eutectic Pharmaceutical by MAS NMR Spectroscopy

5.1 Abstract

Liquid forms of pharmaceuticals (ionic liquids and deep eutectic solvents) offer a number of potential advantages over solid-state drugs; a key question is the role of intermolecular hydrogen bonding interactions in enabling membrane transport. Characterisation is challenging since high sample viscosities, typical of liquid pharmaceutical formulations, hamper the use of conventional solution NMR at ambient temperature. Here, the application of magic-angle spinning (MAS) NMR spectroscopy to the deep eutectic pharmaceutical, lidocaine ibuprofen is reported. Using variable temperature MAS NMR, the neat system, at a fixed molar ratio, can be studied over a wide range of temperatures, characterised by changing mobility, using a single experimental setup. Specific intermolecular hydrogen bonding interactions are identified by two-dimensional ^{1}H-^{1}H NOESY and ROESY MAS NMR experiments. Hydrogen-bonding dynamics are quantitatively determined by following the chemical exchange process between the labile protons by means of linewidth analysis of variable temperature ^{1}H MAS NMR spectra.

5.2 Introduction

As the pharmaceutical industry continues to look for novel ways to improve drug design and enhance delivery, ionic liquids (ILs) have become a promising growth area that seeks to overcome some of the limitations that can exist with solid active pharmaceutical ingredients (APIs).[166,167] Specifically, API-ILs have shown an ability to markedly improve characteristics such as solubility and permeability, as well as exhibiting the potential for more tolerable routes of administration (transdermal or oral vs. injection).[16,168–170] In addition to the formation of fully ionised salts, in 2011, Bica *et al.* demonstrated that hydrogen bonding may drive the 'liquefaction' of therapeutics in the form of deep eutectic solvents (DESs), the liquid equivalent of co-crystals.[43] The nature of the interaction between species is hypothesised to impact upon the biological behaviour of APIs. For example, the membrane permeability of dissociated ions in salt form is limited due to a lack of sufficient lipophilicity. However, API-ILs forming hydrogen bonded complexes should behave more like neutral complexes and transport faster through model membranes compared to dissociated ionic drugs.[26,44] It is thus very important to characterise both the structure and dynamics of key hydrogen bonding interactions in API-ILs.

Whilst the elucidation of molecular-level structure in liquids is routinely performed using NMR spectroscopy, conventional solution-state (static) NMR can be hindered by sample viscosity. In these circumstances, slow tumbling can lead to fast transverse relaxation rates and broad spectral lines. ILs and DESs often exhibit high viscosities, typically more than an order of magnitude higher than that of water, and may therefore be difficult to study by NMR in their neat form. Whilst heating viscous liquid samples may address this problem, there are disadvantages such as the disruption of weak intermolecular interactions, or even promoting degradation in heat labile samples. In the case of pharmaceuticals, it is more relevant for characterisation to occur at temperatures typical of patient use. Magic-angle spinning (MAS) NMR enables, in principle, the study of ILs and DESs over a wide range of temperatures and their characterisation in both liquid and solid state in a single set-up. There is a very limited number of previous MAS NMR studies on ILs/DESs; these have focused on solutes dissolved in the IL/DES, or interactions of the IL/DES with other materials or biological molecules, rather than directly probing intermolecular interactions between the molecules of the neat ILs/DESs themselves. Rencurosi *et al.* showed that MAS NMR is an effective tool for the study of solutes dissolved in neat IL solvents, and for monitoring organic reactions in neat ILs.[70] Other applications of MAS NMR associated with ILs include peptide- and protein-IL interactions,[72,171] and the study of surface-immobilised ILs important for catalysis.[73]

This study considers the prototype deep eutectic 'liquid co-crystal'[43,172] formed between the pain relieving compounds lidocaine and ibuprofen,[25,26] denoted

Lid·Ibu (Figure 5.1a). The neutral forms of lidocaine and ibuprofen are solids at room temperature, with melting points (T_m) of $68 - 69$ °C[173] and $75 - 77$ °C,[173] respectively, while the 1:1 combination, Lid·Ibu, is liquid at room temperature, with a glass transition temperature of -27 °C.[26] Wang *et al.* demonstrated via spectroscopic analysis that it is the COO–H···N (tertiary amine) hydrogen bond interaction rather than proton transfer that reduces T_m; Lid·Ibu is a poorly ionised, hydrogen-boned DES,[26] in contrast to a true API-IL (completely ionised) as it has been defined in some publications.[24] The hydrogen bonding between the two APIs has been shown to promote membrane transport; neat Lid·Ibu transported faster through a model silicone membrane compared to the commercial salt forms of the APIs,[26] and transdermal administration of Lid·Ibu to rats resulted in faster and higher systemic absorption of lidocaine, compared to the commercial salt [Lid]Cl.[174] These studies suggest that strong hydrogen bond interactions between lidocaine and ibuprofen in the deep eutectic co-crystal form might be advantageous for transdermal drug delivery.

With the pharmaceutical application of such complexes in mind, the particular focus of this chapter is the identification of intermolecular hydrogen bonding interactions and the quantitative characterisation of dynamic chemical exchange associated with the making and breaking of hydrogen bonding between the two components. This is enabled by the unique possibility afforded by MAS NMR spectroscopy to characterise a single complex, i.e., with a fixed molar ratio, over a wide range of temperatures.

5.3 Experimental Details

5.3.1 Sample Preparation

Lidocaine and ibuprofen were purchased from Sigma-Aldrich (Gillingham, UK) and used as received. Lidocaine ibuprofen was prepared by stirring an equal molar ratio of lidocaine and ibuprofen together in an oil bath at 100 °C for 1 h. The mixture was then stored in a vacuum oven at 50 °C for 24 h after which the sample was stored at room temperature. Lid·Ibu is a pale-yellow liquid at room temperature.

5.3.2 MAS NMR

MAS NMR experiments were performed at ^{1}H Larmor frequencies of $\nu_{0\mathrm{H}} = 500$ (11.7 T), $\nu_{0\mathrm{H}} = 600$ (14.1 T) and $\nu_{0\mathrm{H}} = 850$ (20.0 T) MHz using Bruker Avance III (500 and 850 MHz) and II+ (600 MHz) spectrometers. All experiments were performed using either a 4 mm triple-resonance MAS probe operating in double-resonance mode or using a Bruker 4 mm $\mathrm{E}^{\mathrm{free}}$ probe ($\nu_{0\mathrm{H}} = 500$ MHz). The $\mathrm{E}^{\mathrm{free}}$ probe utilises a low inductance proton RF coil to minimise RF sample heating by reducing the

E-field. In all experiments, the ^{1}H 90° pulse was of duration 2.5 μs (corresponding to a nutation frequency, ν_1 = 100 kHz) except experiments run using the E$^{\text{free}}$ probe, where the ^{1}H 90° pulse length was 3.5 μs (ν_1 = 70 kHz). Except where otherwise stated, a spinning frequency of 10 or 12.5 kHz was used. All reported temperatures are the gas input temperature.

^{1}H one-pulse MAS NMR: 1D ^{1}H spectra were recorded with a recycle delay of 2 s (except Figure 5.3b where the recycle delay was 1 s) and 4 co-added transients. It is noted that the changes observed in the ^{1}H spectra over time (∼2 ppm shift of the carboxylic acid proton) only occurred for Lid·Ibu stored at room temperature in a glass vial and repacked at a later date, whereas only minor shifts (∼0.2 ppm) occurred for the sample stored in the MAS rotor, likely due to lower exposure to humidity.

^{1}H-^{13}C CP MAS and ^{1}H-^{13}C Refocussed INEPT: In order to collect NMR spectra for the lower natural abundance ^{13}C nuclei, scalar or dipolar coupling based methods to transfer magnetisation from ^{1}H to ^{13}C are commonly employed depending on the nature of the sample and the required information. In solution NMR, the INEPT technique using through-bond scalar couplings is used for most heteronuclear correlation experiments. Solid-state NMR of dilute nuclei such as ^{13}C spectra is typically achieved using cross-polarisation (CP) which uses through-space dipolar interactions. A very viscous IL or DES can be considered to lie somewhere on a continuum between liquid and solid. The feasibility of CP or INEPT techniques is likely to depend on its position on this continuum, which dictates dephasing times and the strength of residual dipolar couplings, factors that affect the efficiency of magnetisation transfer for these two methods. This can be clearly seen in the variable temperature ^{1}H-^{13}C refocussed INEPT and CP ^{13}C MAS NMR spectra presented in this chapter.

^{1}H-^{13}C cross polarisation (CP) and refocussed INEPT spectra were acquired at $\nu_{0\text{H}}$ = 500 MHz and ν_{r} = 10 kHz (INEPT) or ν_{r} = 12.5 kHz (CP) MAS frequency. 128 transients were co-added and a recycle delay of 1.5 s was used. Cross-polarisation was achieved using a 70 to 100% ramp[175] on the ^{1}H channel for a contact time of 500 μs. The ^{1}H and ^{13}C nutation frequencies were 60 and 47.5 kHz, respectively. The refocussed INEPT spectra were acquired with a spin-echo ($\tau/2 - \pi - \tau/2$) duration of τ = 2 ms. In ^{13}C detected experiments, SPINAL-64[119] ^{1}H heteronuclear decoupling was applied during acquisition at a nutation frequency of 93 kHz (CP) or 13 kHz (INEPT) and a pulse duration of 5.4 μs (CP) or 38 μs (INEPT).

5.3.3 ^{1}H-^{1}H NOESY and ROESY

NOESY ($\nu_{0\text{H}}$ = 500 MHz) and ROESY ($\nu_{0\text{H}}$ = 500 MHz) spectra were recorded with 8 transients co-added for each of 512 t_1 FIDs, using the States-TPPI[176] method

to restore sign discrimination in the F_1 dimension with a t_1 increment of 80 μs. NOESY mixing times between 3 and 100 ms and a recycle delay of 4 s were used, corresponding to an experimental time of approximately 4.5 hours. A ROESY spectrum was recorded with a mixing time of 10 ms during which a spin lock of ∼20 kHz was applied and a recycle delay of 2 s, corresponding to an experimental time of 2.5 h. NOESY (ν_{0H} = 850 MHz) spectra were recorded with 4 transients co-added for each of 512 t_1 FIDs, using the States-TPPI[176] method to restore sign discrimination in the F_1 dimension with a t_1 increment of 59 μs and a recycle delay of 3 s, corresponding to an experimental time of 3.5 h. An eight-step nested phase cycle was used in the NOESY experiments where the three ^{1}H 90° pulses were cycled through phases (i) x −x, (ii) x x −x −x, and (iii) x x x x −x −x −x −x and the receiver cycled through phases x −x −x x −x x x −x. An eight-step phase cycle was used in the ROESY experiment where the two ^{1}H 90° pulses before and after the spin-lock were cycled through phases x −x −x x y −y −y y and x −x x −x y −y y −y and the receiver cycled through phases x −x −x x y −y −y y.

^{1}H and ^{13}C chemical shifts are referenced to TMS at 0 ppm using L-alanine as a secondary reference (1.1 ppm for the lower ppm ^{1}H resonance and 177.8 ppm for the higher ppm ^{13}C resonance), corresponding to adamantane at 1.85 ppm (^{1}H)[177] and 38.5 ppm (^{13}C).[178] For all ^{1}H VT spectra, the chemical shift axis is referenced such that the methyl (H-11′) chemical shift is unchanged from the value at 298 K (1.15 ppm).

5.4 Results and Discussion

5.4.1 Variable Temperature MAS NMR

^{1}H MAS NMR spectra of neat Lid·Ibu obtained for temperatures between 268 and 328 K are shown in Figure 5.1b. As with conventional liquids, the viscosity of ILs and DES are expected to be strongly temperature dependent, the effect of which is observed in the broadening of the NMR spectra at lower temperatures. At ambient temperature, 10 kHz MAS is sufficient to resolve all proton resonances of Lid·Ibu, apart from overlap in the aromatic region and for the methyl groups (H-1 and H-1′ whilst ensuring that spinning sidebands lie outside the chemical shift range in the ^{1}H spectra (Figure 5.2). Figure 5.1c and d compare ^{13}C spectra recorded using refocussed INEPT or CP, respectively. The INEPT spectra show increased sensitivity at higher temperatures when the sample is 'more liquid', however at room temperature and below there is very little signal, attributable to the rapid dephasing of transverse proton magnetisation in the higher viscosity sample. Whilst CP is efficient at low temperatures in 'solid-like' samples, the efficacy decays upon heating as dipolar couplings are partially averaged by molecular motion. This observation

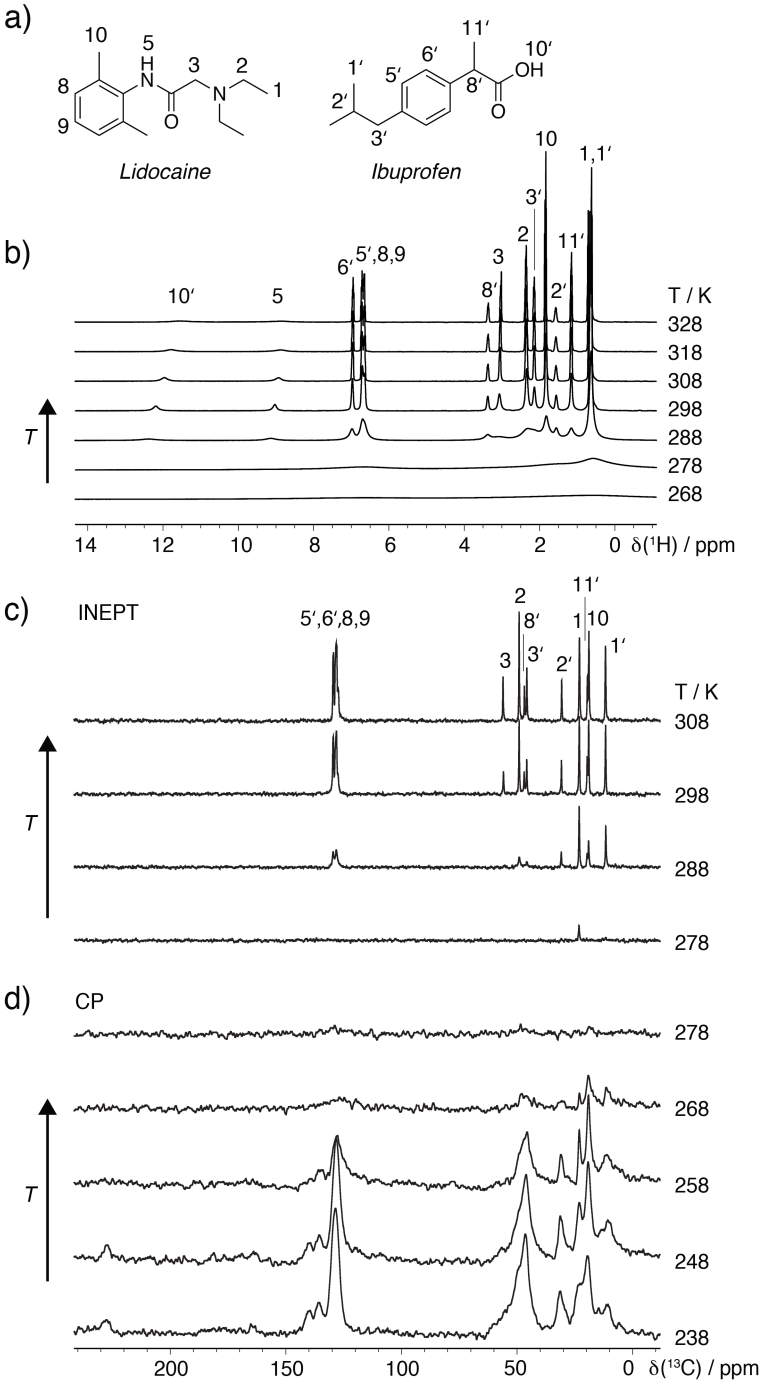

Figure 5.1: Variable-temperature MAS (ν_r = 10 kHz) NMR spectra of Lid·Ibu - see chemical structures of lidocaine and ibuprofen in (a): (b) one-pulse ^{1}H, (c, d) ^{13}C with (c) refocussed INEPT or (d) CP transfer from ^{1}H (ν_{0H} = 500 MHz for all spectra).

matches that of Sarkar *et al.* who reported CP transfers in a high viscosity natural DES (glucose: choline chloride: water in a 1:1:4 ratio) with increasing transfer efficiency upon a decrease in temperature.[179] Overall, the result is a region between liquid and solid phases (between 268 and 288 K for the case of Lid·Ibu) in which the transfer of coherences from the ^{1}H to ^{13}C by either technique is inefficient.

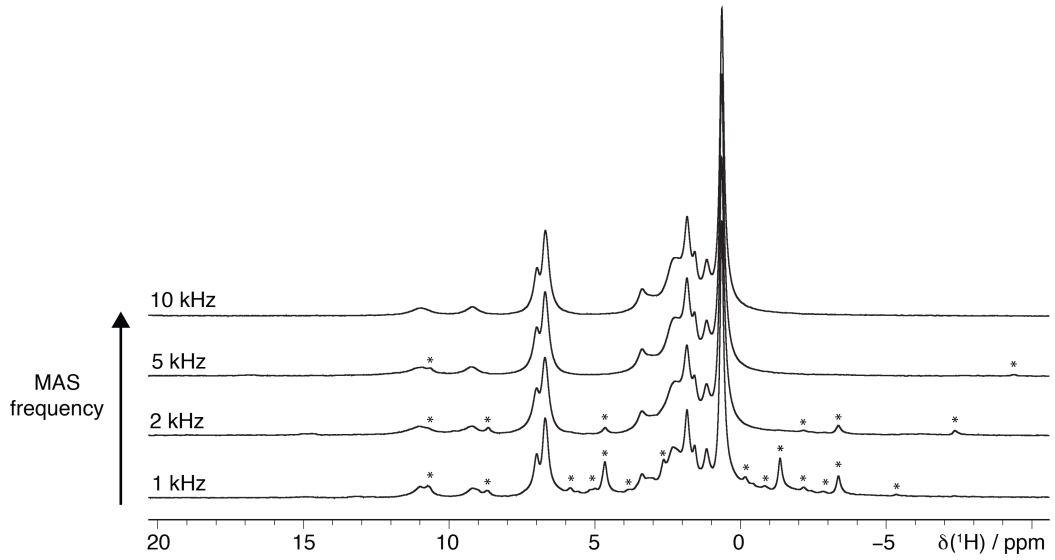

Figure 5.2: The effect of MAS frequency on ^{1}H one-pulse NMR spectra of Lid·Ibu (ν_{0H} = 600 MHz, 298 K input gas temperature). * indicates spinning side bands.

Inspection of the 1D proton spectra as a function of temperature reveal that while the chemical shifts of the CH protons are essentially unchanged, there are changes for the NH and COOH protons which can be attributed to different interactions and chemical exchange processes. Figure 5.3a presents the region between 8.0 and 14 ppm of the variable temperature (VT) 1D proton spectra. The carboxylic acid (H-10′) and amine (H-5) resonances gradually shift to lower ppm values with increasing temperature, with the effect being more prominent for the COOH proton (Figure 5.4a). Such temperature dependent changes in ^{1}H chemical shifts have previously been reported for protons participating in hydrogen bonds for both liquids[180–184] and solids.[185–187]

The carboxylic acid resonance (H-10′) shifted to lower ppm over time (over a period of months) from 12.2 ppm to as low as 10.2 ppm at 298 K (Figure 5.3a and 5.3b). ILs and DESs are generally hygroscopic and readily absorb water from the environment. The shift in the COOH peak can be accounted for by the absorption of a small amount of water in fast exchange with the carboxylic acid proton. In fast chemical exchange between two sites, a single population-weighted average shift ($p_{obs} = p_{COOH}\delta_{COOH} + p_{H_2O}\delta_{H_2O}$) is observed. Less than 1% water (by mass) could result in changes of greater than 2 ppm (Figure 5.3c). This leads to the

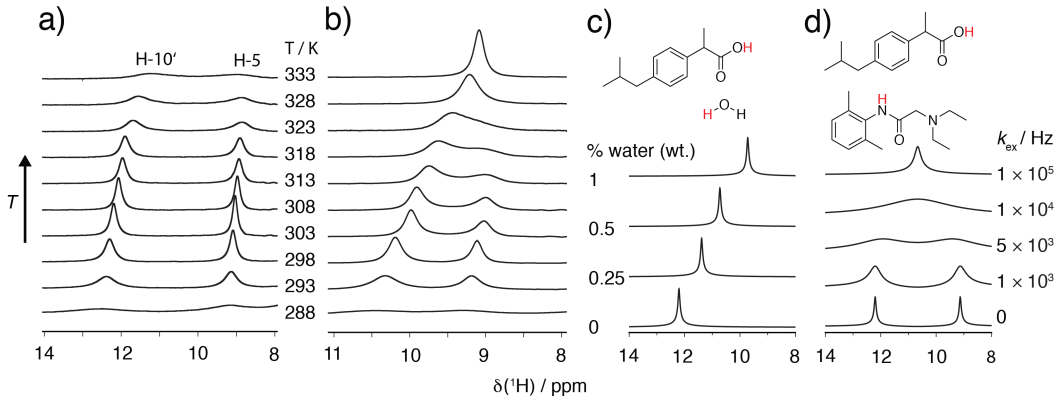

Figure 5.3: (a, b) The effect of temperature on the high-ppm region of ^{1}H MAS NMR spectra (ν_{0H} = 500 MHz, ν_r = 12.5 kHz) of Lid·Ibu in (a) a freshly prepared sample and in (b) a sample stored at room temperature for approximately eight months. (c, d) Numerical simulations (see Equations A.1-A.3 in Appendix A.3 and parameters in Table 5.1) of the effect of chemical exchange for the two processes: fast exchange of the carboxylic acid proton with (c) varying amounts of water, and (d) exchange between the carboxylic acid and amide protons.

Table 5.1: Parameters for numerical simulations of the effect of chemical exchange for the two observed processes: fast exchange of the carboxylic acid proton with varying amounts of water (Figure 5.3c) and exchange between the carboxylic acid and amide protons (Figure 5.3d).

Parameter	Figure 5.3c	Figure 5.3d
B_0 / MHz	500	500
k_{ex} / s^{-1}	1.00 $\times 10^6$	0, 1×10^3, 5×10^3, 1×10^4, 1×10^5
δ_A / ppm	12.2 (COOH)	12.2 (COOH)
δ_B / ppm	4.70 (H_2O)	9.13 (NH)
$R_{2,A}$ / s^{-1}	100	100
$R_{2,B}$ / s^{-1}	100	100
p_A / s^{-1}	0.67, 0.80, 0.89, 1.0	0.5

important point that the absence of a peak at the expected chemical shift of water (approximately 4.7 ppm) does not necessarily indicate that the sample is dry. From the observed change in the COOH chemical shift, the approximate water content can be calculated (assuming the chemical shifts in the absence of exchange, $\delta_{\mathrm{COOH}} = 12.2$ ppm, i.e., the chemical shift at 298 K observed directly after preparation and drying of Lid·Ibu, and $\delta_{\mathrm{H_2O}} = 4.7$ ppm, to be 0.74% wt. H_2O, corresponding to one equivalent of H_2O per 5.5 Lid·Ibu, after a period of eight months of storage at ambient conditions. The presence of water in API-DESs/ILs can be expected to influence the properties. Similarly, the presence of water in crystalline hydrates is known to dramatically alter the physicochemical properties of pharmaceuticals compared to their anhydrous forms.[188,189] The environment of water molecules and the role of hydrogen bonding in solid pharmaceutical hydrates has been characterised by fast (> 60 kHz) ^{1}H MAS solid-state NMR.[190,191] The environment of water in API-ILs/DESs, such as Lid·Ibu, could be characterised by further MAS NMR studies.

A second exchange process between the carboxylic acid and amide proton is evident with significant broadening of the peaks with increasing temperature (Figure 5.3a, b). This is more obvious in the sample with higher water content, where, within the temperature range studied, the peaks first broaden and then merge into a single peak (Figure 5.3b). This is consistent with a two-site chemical exchange process where the appearance of the NMR spectra depends on the relative magnitudes of the rate constant, k_{ex}, and the frequency difference between the two exchanging resonances, $\Delta\nu$ (both in s^{-1}). The two peaks initially broaden and approach one another in the slow ($k_{ex} \ll \Delta\nu$) to intermediate exchange regime ($k_{ex} \sim \Delta\nu$) before merging into a single peak at the point of coalescence (corresponding to $k_{ex} = \pi\Delta\nu/\sqrt{2}$) and then narrowing in the fast exchange limit ($k_{ex} \gg \Delta\nu$) (Figure 5.3d). The exchange may also be mediated by a small population of water; this would be expected to show similar line shapes to a direct exchange process. The changes in chemical shift and linewidth for the exchanging proton peaks are shown graphically in Figure 5.4. In the slow exchange regime, k_{ex} may be obtained from analysis of the linewidths of the exchanging peaks (see Section 2.4.5 in Chapter 2 for further details). At temperatures below 298 K, additional line broadening of all resonances was observed due to slower transverse relaxation with increased sample viscosity and an accurate value of the linewidth in the absence of exchange could not be obtained for the H-10′ or H-5 resonances (Figure 5.4b, e). Since all other peaks not involved in exchange showed comparable linewidths, the linewidth of the well resolved methyl peak H-11′ was therefore taken as a reference to obtain an approximate value of the linewidths in the absence of exchange. The broadening of the exchanging peaks was taken as the difference between the observed linewidth and the width of the reference peak at each temperature. The rate constant of the forward and reverse

reactions, k, is then given by this value multiplied by π. In Figure 5.4c, $\ln k$ (k_f or k_b) versus the inverse temperature is plotted between 303 and 328 K. A linear fit (with R^2 values of 0.99) produced activation energies of 52 ± 2 kJ mol^{-1} and 59 ± 2 kJ mol^{-1} for the forward and reverse reactions, respectively, from the Arrhenius equation, $\ln(k) = \ln(a) - {}^{E_a}/_{RT}$. These values are similar to activation energies of 30-90 kJ mol^{-1} frequently reported for chemical exchange processes studied by NMR.[186,192,193] Over the temperature range studied, the carboxylic acid and amide protons are in slow exchange, with only a small exchange-induced chemical shift of the peaks observed above 318 K (Figure 5.3a, 5.4a). However, in a sample of Lid·Ibu with higher water content, the two peaks are at ppm values significantly closer together and the chemical exchange therefore appears faster on the chemical shift time-scale (Figure 5.3b, 5.4d). The peaks initially broaden with increasing temperature and at ∼325 K coalesce. At higher temperatures, significant narrowing of the peak indicates exchange in the intermediate-fast exchange regime.

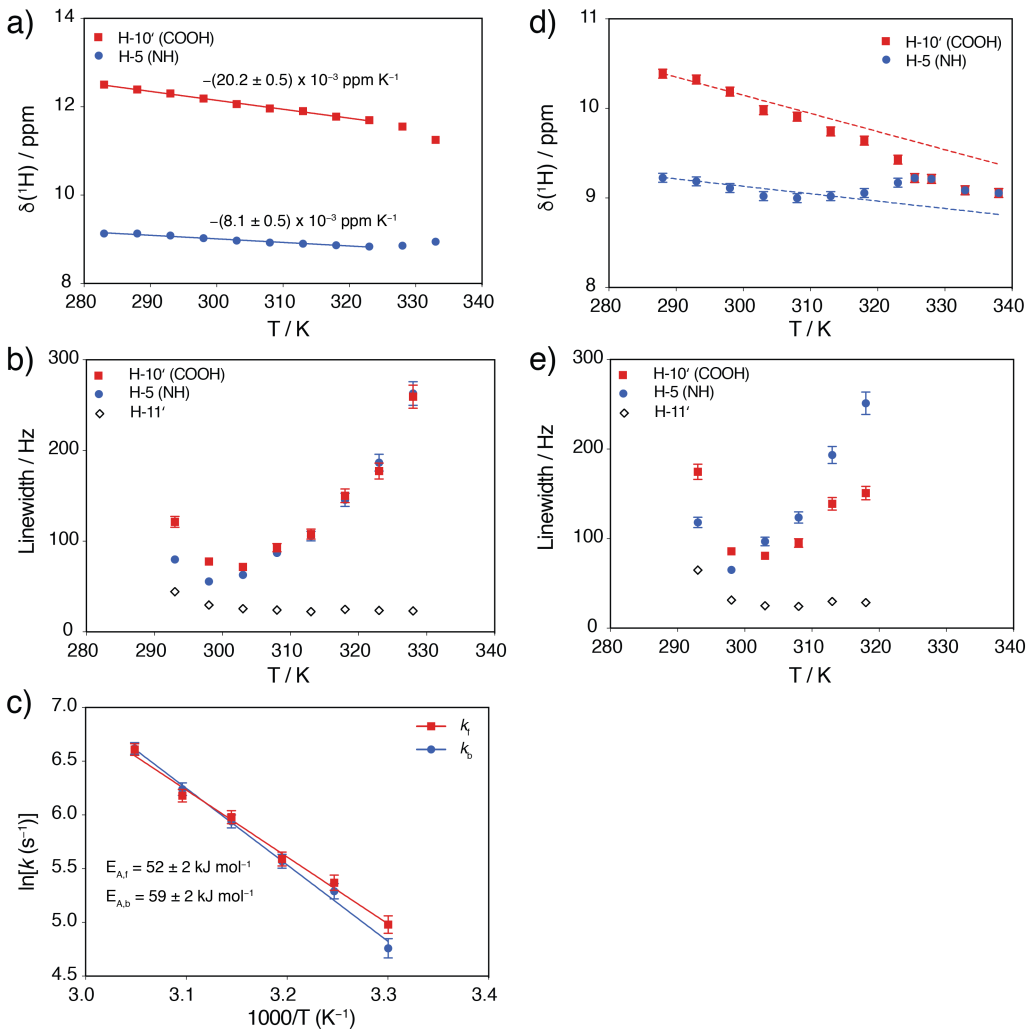

Figure 5.4: Analysis of chemical exchange process between H-10′ and H-5 of Lid·Ibu in (a, b, c) a freshly prepared sample and in (d, e) a sample stored at room temperature for approximately eight months: The effect of temperature on (a,d) the observed chemical shift and (b, e) the linewidth (full width at half maximum height) in ^{1}H one-pulse MAS NMR spectra (Figure 5.3a, b). In (a), the best-fit straight lines in the slow exchange regime obtained from a linear regression analysis used to determine the rate of change of the chemical shift with respect to temperature are shown. The dashed lines in (d) show the same temperature dependence of the chemical shift as in (a) for comparison. (c) Arrhenius plots for the proton exchange process. The rate constants, k_f and k_b, were obtained from the linewidth analysis carried out for the 1D ^{1}H one-pulse VT MAS NMR spectra (Figure 5.3a; see Section 2.4.5 in Chapter 2 for further details). The best-fit straight lines obtained from a linear regression analysis are shown. The estimated error in the measured chemical shift (a, d) and linewidth (b, e) of ±0.05 ppm and 5%, respectively, are not shown if smaller than the symbol height.

5.4.2 ^{1}H-^{1}H NOESY and ROESY MAS NMR

Whilst the ^{1}H NMR chemical shift is a powerful probe of intermolecular interactions, particularly hydrogen bonding, 2D correlation experiments are useful for identifying pairs of nuclei involved in such interactions. In nuclear Overhauser effect spectroscopy (NOESY) experiments, magnetisation is transferred through space during the mixing time, permitting the study of intermolecular interactions. ^{1}H-^{1}H MAS-NOESY experiments have previously been used to detect intramolecular intermolecular hydrogen bonding between solvent molecules and a DES,[194] and between a drug and polymer excipient in supersaturated solution.[76] In addition to MAS-NOESY experiments, a variant where the application of radio frequency-driven recoupling (RFDR)[195] during the NOESY mixing time reintroduces the homonuclear dipolar couplings under MAS, has been described to enhance the coherent ^{1}H-^{1}H dipolar coupling-driven transfer, and has been applied to investigate membrane interactions of peptides and proteins.[196,197] In liquids, cross-relaxation (the NOE) induced by modulation of dipolar couplings by molecular motions is responsible for the transfer of magnetisation between pairs of nuclei spins close in space (typically within $\sim$ 5 Å. In the solid state, the same pulse sequence is often referred to as a spin diffusion experiment because the dominant mechanism responsible for the transportation of magnetisation is spin diffusion, which is not related to molecular motion but rather is a coherent effect originating from an incomplete averaging by MAS of the ^{1}H-^{1}H dipolar interactions.[107,108] Note that the term spin diffusion is used differently in solution NMR and refers to an incoherent multi-step NOE process. To avoid confusion, the two definitions of spin diffusion will be referred to as coherent spin diffusion (solids) and incoherent spin diffusion (liquids). In samples on the continuum from liquid to solid, both the NOE and coherent spin-diffusion are expected to contribute to the NOESY spectra. In the following discussion, the presented NOESY data is interpreted in terms of the NOE effect for Lid·Ibu, i.e., reflecting a state that lies closer to the liquid regime at room temperature and above.

A section of a two-dimensional ^{1}H-^{1}H NOESY MAS spectrum is shown in Figure 5.5a. All NOEs are the same sign as the diagonal as expected for viscous liquids with slow molecular tumbling. Specific interactions between lidocaine and ibuprofen protons were observed particularly from the carboxylic acid proton (H-10′) of ibuprofen. Three strong cross peaks to lidocaine are observed, which can be attributed to strong intermolecular contacts (to protons adjacent to the tertiary nitrogen H-2 and H-3), and/or chemical exchange (to the amide proton H-5). The NOEs to H-2 and H-3 likely result from a hydrogen bond between the carboxylic acid proton and tertiary amine nitrogen as shown in Figure 5.5b. Selected NOE build-up curves for H-10′ are plotted in Figure 5.5c. NOE volumes are shown per proton contributing to the cross peak and normalised to the maximum NOE volume.

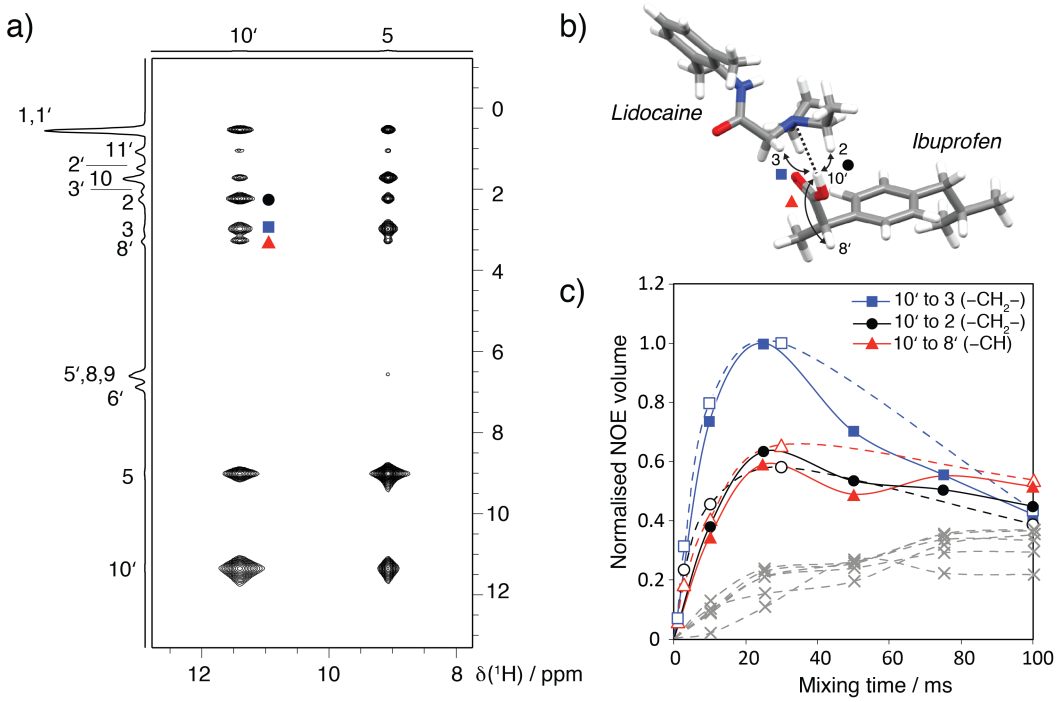

Figure 5.5: ^{1}H-^{1}H NOESY MAS ($\nu_{\mathrm{r}} = 10$ kHz) NMR of Lid·Ibu with input gas at 298 K: (a) An expanded region of a 2D spectrum ($\nu_{0\mathrm{H}} = 600$ MHz) with skyline projections for $\tau_{\mathrm{mix}} = 10$ ms. The base contour level is at 0.03% of the maximum peak intensity. (b) Proposed hydrogen-bonded structure accounting for the strong intermolecular NOEs (H-10′ to H-2 and H-3) as shown by arrows. (c) Comparison of NOE build-up curves at $\nu_{0\mathrm{H}} = 600$ MHz (solid lines, filled symbols) and $\nu_{0\mathrm{H}} = 850$ MHz (dashed lines, open symbols) for the carboxylic acid proton (H-10′) to H-3 (blue squares), H-2 (black circles) and H-8′ (red triangles). Contacts to other protons (excluding the amide proton, H-5) are shown (grey crosses, dashed lines) for comparison. The H-10′ to H-8′ NOE is an intramolecular contact between protons of ibuprofen (see b) and is shown for comparison to the intermolecular contacts between the lidocaine and ibuprofen (H-10′ to H-3 and H-2). To interpret the NOESY spectra, the cross-peak integrals were corrected for the number of equivalent protons contributing to the observed NOE signal by dividing by the product of the number of each proton, $n_A n_B$, and then normalised to the maximum signal for the H-10′ to H-3 cross peak at a mixing time of 10 ms. Lines are included as guides for the eye. The integration error is estimated to be $< 2\%$ and is smaller than the symbol height. The full 2D spectrum is presented in Figure 5.7a.

As expected, an intramolecular NOE is also observed to the adjacent proton (H-8′). Whilst intramolecular NOE signals are known to show an r^{-6} distance dependence, the intermolecular NOE is much more complicated and may vary between the typical r^{-6} short-range behaviour to r^{-1} long-range behaviour depending on the spectrometer frequency.[198] NOE experiments were therefore performed at two frequencies (600 and 850 MHz). Build-up curves of NOEs from the carboxylic acid proton (H-10′) showed the same trends at both magnetic field strengths, (Figure 5.5c) with the strongest NOEs belonging to H-2 and H-3 of lidocaine (intermolecular), followed by intramolecular H-8′, indicating a dominant short-range (r^{-6}) behaviour. Note that the rapid build-up and decay of the NOE indicates the need for short mixing times in viscous samples. Whilst mixing times greater than 200 ms are common for acquiring NOESY spectra of small molecules in solution, at mixing times greater than 50 ms in slow-tumbling neat Lid·Ibu all protons show similar contacts to all other protons due to incoherent spin-diffusion.[199] In previous liquid-state NMR data published on neat Lid·Ibu performed at 70 °C under static conditions, hydrogen-bonding was indirectly evidenced by observing shifts to higher ppm of the protons adjacent to the tertiary nitrogen in lidocaine (H-2, H-3) with increasing ibuprofen content.[26] Under MAS, it was possible to directly detect this hydrogen bond at ambient temperature in a single sample (the 1:1 molar ratio Lid·Ibu). It is noted that at the time of recording the NOESY spectra, the sample had absorbed approximately 0.24% wt. H_2O (based on the observed COOH chemical shift of 11.4 ppm), corresponding to one equivalent of H_2O per 17 Lid·Ibu. While this small amount of water can be expected participate in hydrogen bonding to the lidocaine and ibuprofen, the dominant hydrogen bond interaction is between the two APIs.

Figure 5.6 shows intermolecular NOE build-up curves recorded at two temperatures (298 and 323 K) for the carboxylic acid proton of ibuprofen (H-10′) to the protons adjacent to the tertiary nitrogen (H-2 and H-3, Figure 5.6a) and the amide proton (H-5, Figure 5.6b) of lidocaine. As a sample is heated, it would be expected that reduced NOESY cross peaks would result from faster motion, as the NOE enhancement decreases as it approaches a zero crossing, and may be further reduced by weakening of intermolecular interactions in the sample. In contrast to all other cross peaks to H-10′, which showed decreased intensity at higher temperature (Figure 5.6a), the amide (H-5) to acid cross peak is stronger at 323 K (Figure 5.6b). This behaviour is consistent with the VT 1D spectra (see Figure 5.3) which indicate exchange between the amide and acid protons, and is confirmed by ROESY spectra where the exchange-induced cross peaks appear with opposite intensity compared to cross peaks originating from the NOE mechanism (Figure 5.7). The increased intensity of the H-10′ to H-5 NOESY cross peak at 323 K (Figure 5.6b) is consistent with the increase of the chemical exchange rate as the sample is heated (see previous

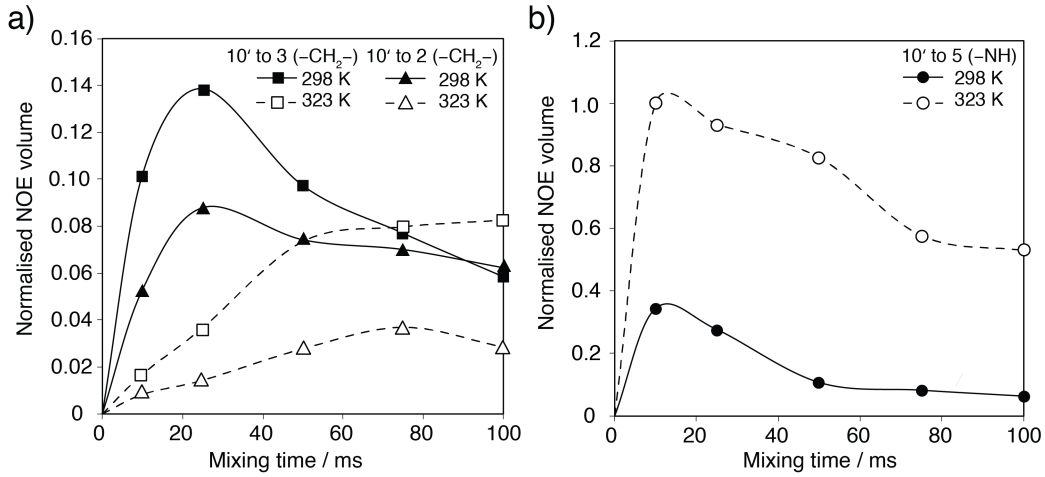

Figure 5.6: (a, b) ^{1}H NOESY MAS (ν_r = 10 kHz) NMR build-up curves (ν_{0H} = 600 MHz) for the carboxylic acid proton (H-10′; 11.4 ppm) of Lid·Ibu to (a) H-3 (squares) and H-2 (triangles) and (b) H-5 (circles) recorded at 298 K (solid lines, filled symbols) and 323 K (dashed lines, open symbols). The integration error is estimated to be $< 2\%$ and is smaller than the symbol height.

discussion of Figure 5.3a and 5.4).

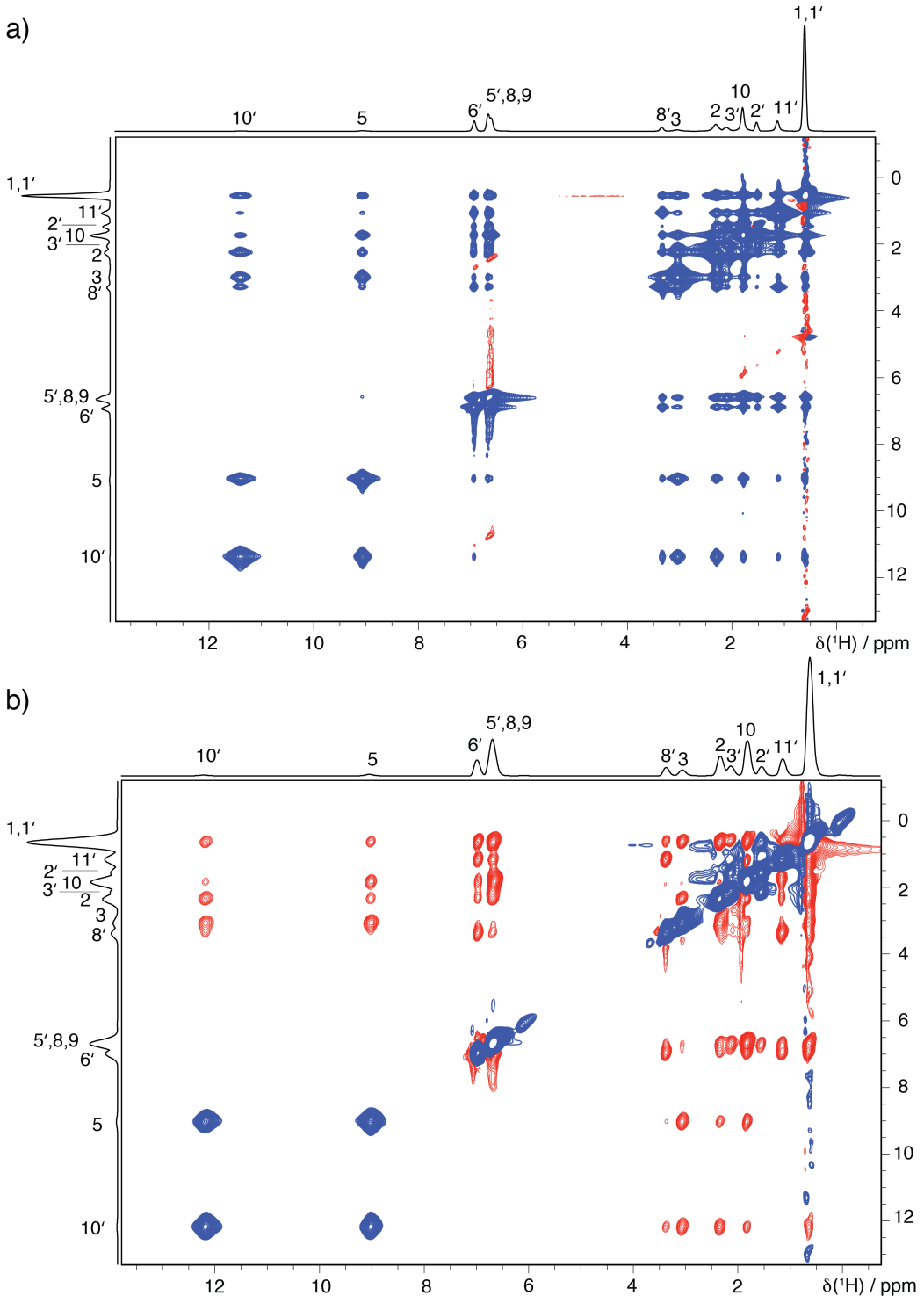

Figure 5.7: (a) A ^{1}H-^{1}H NOESY MAS NMR spectrum (ν_{0H} = 600 MHz, ν_{r} = 10 kHz, 298 K) and (b) a ^{1}H-^{1}H ROESY MAS NMR spectrum (ν_{0H} = 500 MHz, ν_{r} = 10 kHz, 298 K) with skyline projections of neat Lid·Ibu recorded using a mixing time (NOESY) or spin-lock (ROESY) of duration 10 ms. Positively phased peaks are shown in black, and negative peaks are shown in red. The base contour level is at 0.06% (a) and 0.1% (b) of the maximum peak intensity.

5.5 Conclusions

MAS NMR spectroscopy has been applied to probe specific hydrogen interactions and their dynamics, via chemical exchange, in a DES. A key advantage of utilising MAS is the ability to study the system over a wide temperature range. This is to be compared with the solution-state NMR analysis of Wang *et al.* that could only be performed at 70 °C and required an analysis of a series of samples composed of varying molar ratios of lidocaine and ibuprofen to make inferences about the hydrogen bonding interactions.[26]

Using 10 kHz MAS, the resolution of the carboxylic acid and amide protons is sufficient to allow analysis of dynamic chemical exchange processes and yield 2D NOESY and ROESY spectra that allow the direct probing of the important hydrogen bond interactions. When seeking to develop a molecular pharmaceutical for medical application, a detailed understanding of such interactions between the components of ILs/DESs is a pre-requisite for an understanding of the biological behaviour. Specifically, for Lid·Ibu, strong hydrogen bond interactions have been hypothesised to account for promising transport rates of the APIs though model membranes.[26] With growing interest in ILs and DESs as new formulations for improved therapeutics, it is anticipated that MAS NMR will prove to be indispensable for their characterisation, complementing the application of solid-state NMR to conventional solid pharmaceuticals.[200,201]

Chapter 6

Choline and Geranate (CAGE) and Analogue Ionic Liquids

All ionic liquid samples (CAGE and its analogues) in this chapter were synthesised by Dr. Jeraime Griffith, in the research group of Prof. Tom Welton, Department of Chemistry, Imperial College London. SAXS measurements were performed by Dr. Steven Huband, Department of Physics, University of Warwick. Polarising optical micrographs were taken by Mohit Devgan and Dr. Chi Long Chan, in the research group of Dr. Nicholas Brooks, Department of Chemistry, Imperial College London. Mass spectra and analysis were provided by Dr. David Pugh, Department of Chemistry, Imperial College London. The solution NMR experiments of aqueous CAGE were performed with the help of Dr. Peter Gierth at Bruker, Coventry.

6.1 Abstract

Choline and geranic acid (CAGE) is a recently developed ionic liquid (IL) that functions as a broad-spectrum antimicrobial agent, as well as a transdermal and oral delivery agent.[27–29,51,52] Neat CAGE, prepared at a 1:2 ratio: [choline][geranate$_2$(H)], was characterised by DSC, SAXS and NMR, and the behaviour of CAGE in water was investigated by solution NMR. The formation of a partial bilayer liquid crystal (LC) phase in newly synthesised CAGE was identified by SAXS at temperatures below 5 °C, however this phase did not persist over a period of months. Additionally, six variants of CAGE were prepared with one equivalent of geranic acid replaced with an alternative acid, or with alternative cations to choline. The temperature dependence of the COOH/OH ^{1}H chemical shift provides information on the relative strength of hydrogen bonds. CAGE analogues with alternative acids all showed similar temperature coefficients, suggesting that a similar hydrogen bonding strength and arrangement is adopted for each analogue. Furthermore, when

mixed with butyl CAGE, a hydroxyl functionalised model compound was shown to hydrogen bond with geranic acid/geranate. This interaction could play a role in the ability of CAGE to transport drugs across biological barriers. The presence of dynamic hydrogen-bonded complexes was further evidenced by mass spectrometry for the CAGE octanoic acid analogue, which reveals that metathesis occurs between clusters such as [(choline)(geranate)(H)(octanoate)], [(choline)(octanoate)$_2$(H)] and [(choline)(geranate))$_2$(H)]. Additionally, CAGE octanoic acid, was observed to form a stable LC phase at temperatures below ∼20 °C, as observed by SAXS and polarising optical microscopy.

6.2 Introduction

The pharmaceutical industry faces a series of challenges in the delivery of newly developed drug molecules due to their low solubility, poor adsorption and bioavailability, and stability. Oral drug administration is preferred over injection; however, the oral delivery of many drugs is limited by their lipophilicity and is particularly difficult for the delivery of macromolecules such as therapeutic peptides or proteins (e.g. insulin), which are subject to rapid degradation in the digestive tract and poor transport across the epithelium. An alternative route of administration is transdermal delivery, where a drug formulation is applied to the skin; however, the drug must penetrate the stratum corneum, the dense outer layer of the skin that provides a physical barrier against dehydration and pathogens. ILs and deep eutectic solvents (DESs) have been developed for pharmaceutical applications, both as reformulations of active ingredients themselves with improved properties (e.g. lidocaine ibuprofen, as discussed in Chapter 5), and as carriers of pharmaceuticals across the aforementioned barriers.[16,167–170]

The focus of this chapter is on a particular choline-based IL, composed of choline and geranate (CAGE; Figure 6.1), which has been impressively shown to combat a number of the challenges facing the pharmaceutical industry.[27–29,51,52] CAGE first stood out in a screen of a number of ILs and DESs for its excellent antimicrobial activity, transdermal drug delivery properties, and low cytotoxicity to human epithelial cells.[27] The antimicrobial activity of CAGE was assessed against 47 different strains of Gram-negative and Gram-positive bacteria (including drug-resistant strains), fungi, and viruses, with every pathogen being susceptible to CAGE treatment, the majority being neutralised with less than 1% v/v CAGE.[28] CAGE can not only improve the skin penetration of small molecule drugs, but was also found to facilitate the delivery of large proteins into deep skin layers, improving the topical delivery of bovine serum albumin (BSA), ovalbumin (OVA), and insulin, compared to commonly used chemical penetration enhancers.[29] In addition to its

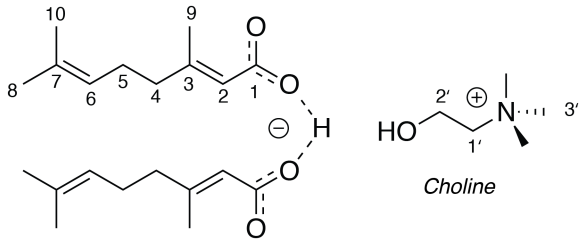

Figure 6.1: Chemical structure of CAGE. The numbering is used for NMR assignments throughout this chapter.

ability to cross the stratum corneum, CAGE has also been shown to navigate the tight epithelial junctions of the intestine, enabling oral delivery of insulin.[52] This is particularly significant since there are currently no commercially available oral formulations of insulin, a medication for type 1 diabetes management administered as an injection. A safe and effective IL-based oral insulin formulation would benefit from higher patient compliance and quality of life of diabetic patients.

The efficacy of ILs as active ingredients themselves, or as drug delivery agents, is expected to depend on their ionic components and composition. In one study on CAGE, the efficacy of transdermal insulin delivery was assessed for variants of CAGE with different ratios of choline and geranic acid (2:1, 1:1, 1:2 and 1:4), with the 1:2 ratio exhibiting the highest delivery efficacy.[51] Similarly, the delivery efficiency of both hydrophilic and hydrophobic drugs were found to strongly depend on the composition of CAGE, with 1:2 CAGE again exhibiting the highest delivery efficiency.[202] As such, CAGE and the analogues presented in this chapter were prepared at this stoichiometry. As discussed in Chapter 5, for lidocaine ibuprofen, the interaction between the components in ILs and DESs may impact the biological activity. Likewise, the intraionic interactions of CAGE have been shown to influence skin transport, however, the mechanistic origin of this requires further investigation.[202] Ibsen *et al.* proposed the mechanism of action of CAGE on the E. coli membrane; the attraction of choline to the negatively charged cell membrane leads to insertion of geranic acid into the lipid bilayer and its consequent disruption.[203] Whilst the interaction between choline and geranate/geranic acid clearly plays a role in the mechanism of action of CAGE (pure geranic acid or 80% choline bicarbonate in water are ineffective alone), stronger interactions between the ionic components may not necessarily be beneficial. Tanner *et al.* found that, of a series of CAGE analogues with various anions or cations, those with fewer interionic interactions (as determined by NOESY NMR) had a higher transdermal transport efficiency.[202]

In this chapter, CAGE was first investigated, and changes in the structure

over time were observed. CAGE was observed, by DSC and SAXS, to initially form a liquid crystalline (LC) phase that has not previously been reported for CAGE. In addition to exploring the structure of neat CAGE, the behaviour of CAGE in water was studied. This has important implications for the use of CAGE, since, whether used as an oral or transdermal delivery agent, CAGE will eventually come into contact with water in physiological media. Subsequently, a number of analogues of CAGE, prepared by replacing either one equivalent of geranic acid with an alternative acid, or substituting choline with an alternative cation differing at the hydroxyl functionality are reported. In order to investigate whether the hydrogen bond strength differed between the CAGE analogues, variable temperature ^{1}H NMR was utilised. One of the CAGE analogues, formed by replacing one equivalent of geranic acid with octanoic acid (CAGE-oct), formed a stable LC phase. SAXS reveals the intermediate-range order of CAGE-oct above the LC-to-isotropic transition, and long-range order of the partial bilayer LC phase at temperatures below 20 °C. The smectic LC texture and LC-to-isotropic phase transition was also viewed via polarising optical microscopy. Additionally, mass spectrometry provides a 'snapshot' of the hydrogen-bonding structures/ionic complexes present in CAGE-oct.

6.3 Experimental Details

6.3.1 Sample Preparation

Choline bicarbonate (80 wt.% solution in water) and octanoic acid were purchased from Sigma and used as received. Geranic acid (85%) was purchased from Sigma but was recrystallised five times from cold HPLC-grade acetone (VWR) before use. CAGE was synthesised following the protocol reported by Zekrewsky *et al.*[28] Briefly, two equivalents of geranic acid, in ethanol, were added to two equivalents of choline bicarbonate (80 wt. % solution) and stirred until CO_2 production ceased. Volatiles were removed in vacuo yielding a colourless oil. This was further dried under high vacuum at 45 °C for 48 hours.

The CAGE analogues were prepared using the same method, replacing either one equivalent of geranic acid with an alternate acid (octanoic acid, levulinic acid or lipoic acid), or replacing choline bicarbonate with 2-methyoxy-N,N,N-trimethylethan-1-ammonium bicarbonate (for ether CAGE) or N,N,N-trimethylbutan-1-ammonium bicarbonate (for butyl CAGE). The butyl CAGE/alcohol mixture was prepared by mixing butyl CAGE and 3,3-dimethylbutan-1-ol in a 1:1 ratio and stirring at RT for 30 min.

For NMR measurements of aqueous CAGE, CAGE was diluted by one part in 50 (by weight) in 0.8 % NaCl in D_2O and mixed on a roller platform for approximately 10 minutes. NMR spectra were either recorded on the emulsion within 4 hours of

preparation, or on the sample after sitting at room temperature for 24 h.

6.3.2 DSC, DLS and SAXS

Differential scanning calorimetry (DSC) scans were carried out at a heating/cooling rate of 10 °C min^{-1} using a Mettler Toledo differential scanning calorimeter. Transition temperatures are reported using the peak maximum of the thermal transition. Nanoparticle size and polydispersity measurements were performed by dynamic light scattering (DLS) on a Zetasizer Nano - ZS (Malvern Instruments) operating at a fixed scattering angle of 173°.

SAXS measurements were made using a Xenocs Xeuss 2.0 equipped with a micro-focus Cu Kα source collimated with Scatterless slits. The scattering was measured using a Pilatus 300k detector with a pixel size of 0.172 mm × 0.172 mm. The distance between the detector and the sample was calibrated using silver behenate ($AgC_{22}H_{43}O_2$), giving a value of 0.339(5) m. The magnitude of the scattering vector (q) is given by $q = 4\pi sin(\theta)/\lambda$, where 2θ is the angle between the incident and scattered X-rays and λ is the wavelength of the incident X-rays. This gave a q range for the detector between 0.023 $Å^{-1}$ and 0.73 $Å^{-1}$ in the horizontal plane. The 2D detection image was integrated as a function of q producing the 1D intensity versus q data. For measurements as a function of temperature, the samples were held between two Kapton windows in a Linkam HFSX 350 furnace. Separate measurements of the Kapton windows and furnace were used for background corrections.

6.3.3 MAS NMR of Neat Samples

MAS NMR experiments were performed at ^{1}H Larmor frequencies of ν_{0H} = 400 (9.4 T), 500 (11.7 T) and 600 (14.1 T) MHz using Bruker Avance III (400 and 500 MHz) and II+ (600 MHz) spectrometers. All experiments were performed using a 4 mm double-resonance MAS probe at a spinning frequency of 5 kHz. In all experiments, the ^{1}H 90° pulses were of duration 2.5 μs (corresponding to a 100 kHz nutation frequency). The temperature was calibrated using methanol, as described in the Bruker Instruments manual, with all stated temperatures being corrected by this procedure. ^{1}H chemical shifts are referenced to TMS at 0 ppm using adamantane as a secondary reference at 1.85 ppm.[177]

6.3.4 NMR of Aqueous CAGE

NMR experiments were carried out on a Bruker Avance III 400 MHz spectrometer. The ^{1}H chemical shifts were referenced to the residual solvent peak. PFG-NMR diffusion experiments were carried out using the pulse-field gradient stimulated echo (PFG-STE) pulse sequence[204] with convection compensation[205,206] to obtain the

diffusion coefficient from the ^{1}H signal. The interval between gradient pulses, Δ, was set to 100 ms, and the length of the gradient pulse, δ, was 1 ms. 16 gradient strengths were used ranging from 2.26 to 44.2 T m^{-1}. 32 transients were co-added and a recycle delay of 6 s was used.

A ROESY spectrum was recorded with 4 transients co-added for each of 128 t_1 FIDs, using the States-TPPI[176] method to restore sign discrimination in the F_1 dimension with a t_1 increment of 286 μs. A mixing time of 300 ms and a recycle delay of 4 s were used.

6.3.5 Polarising Optical Microscopy

Samples were placed into flat glass capillary tubes and supported on a glass slide for imaging using a Nikon Eclipse E600POL microscope with Nikon CFI Achromat 4X,10X and 20x objective lenses. Images were acquired using a QICAM Fast 1394 CCD camera (QImaging). Temperature control was achieved using a Linkam LTS 350 temperature controlled microscope stage with a Linkam TMS 94 temperature controller (Linkam Scientific Instruments), coupled with a liquid nitrogen pump for cooling. Image analysis was carried out using the open source software package ImageJ.

6.3.6 Mass Spectrometry

Mass spectra were obtained by gently warming CAGE-oct until it melted then directly injecting it into a Waters single quadrupole detector at 4.2 kV capillary voltage using electrospray ionisation.

6.4 Results and Discussion

6.4.1 Phase Transitions and Stability of CAGE

CAGE was synthesised by salt metathesis of a 1:2 molar ratio of choline bicarbonate and geranic acid, as previously reported.[28] Over a period of months, CAGE that had been stored at ambient temperature transitioned from clear to yellow (Figure 6.2a and b). The cause of the colour change is not currently known but is being investigated further, however, it is speculated to be due to the partial degradation of geranic acid to products with additional double bonds. In the following section, the two samples in Figure 6.2a and b are referred to as 'freshly prepared' and 'stored' CAGE. CAGE, as with most ILs, is hygroscopic, and has been shown to contain between 0.1-0.6 mole of water (depending on the ion ratio) after storage at ambient conditions for >3 months.[207] Tanner *et al.* reported that no substantial molecular reorganisation was observed in CAGE (1:1 choline/geranate) containing <0.65 mole

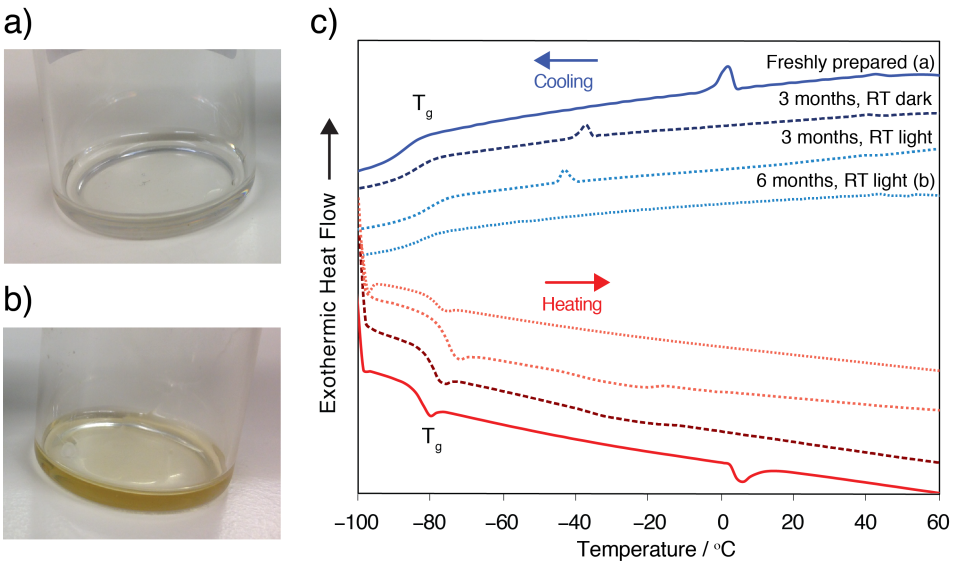

Figure 6.2: (a) Photos of freshly prepared CAGE and (b) CAGE after storage at room temperature for 6 months. (c) First heating and cooling DSC traces for newly synthesised CAGE (solid lines) and CAGE after storage under various conditions (dashed lines); 3 months at room temperature (RT) in dark or light conditions, and for 6 months at RT in light conditions (sample shown in b).

fraction of water and suggested that CAGE could be used without pre-drying with no significant change in the microstructure.[207] Nonetheless, in order to eliminate absorbed water as a cause for the changes observed, the stored CAGE sample was dried under reduced pressure, first on a rotary evaporator for 2 h, then in a vacuum oven at 40 °C for 48 h.

Differential scanning calorimetry (DSC) traces of freshly prepared and stored CAGE are shown in Figure 6.2c. A glass transition, T_g, at −78°C in freshly prepared CAGE and −80°C in stored CAGE, was observed, similarly to the T_g of −77.5°C previously reported by Tanner *et al.*[51] They also reported a cold crystallisation event at 41.7°C, attributed to free geranic acid. A small transition was observed at 44.3°C (peak maximum, onset at 40.7°C) in both freshly prepared and stored CAGE. Whilst no additional phase transitions were observed in stored CAGE (for 6 months at room temperature) up to 60 °C, a thermal transition at 4.0 °C upon heating, and 6.3°C on cooling, is present in freshly prepared CAGE, which was not reported by Tanner *et al.*[51] This transition was observed in three repeated heating and cooling cycles (repeat cycles not shown). After 3 months storage at room temperature, this transition was still observed, however shifted significantly, from 6.3°C to −36.3°C and −41.8°C (on cooling), when the sample was stored in light or dark conditions, respectively. The larger shift in the transition for the sample stored in light, rather than dark conditions, suggests that the degradation responsible for the colour change

and phase behaviour of CAGE, is catalysed by light. On heating the sample, a very broad transition at approximately −17 to −30°C was observed.

In order to investigate the origin of this thermal transition, small-angle X-ray scattering (SAXS) was performed at variable temperatures (Figure 6.3). The first order scattering peak provides information on the ordering, since the layer distance by Bragg's Law is $d = 2\pi/q_{max}$. The SAXS profile of freshly prepared CAGE (Figure 6.3a) shows a sharp narrow first order scattering peak at $q = 0.29$ Å^{-1} (at 20 °C), indicative of a liquid crystalline (LC) phase, at temperatures below 5 °C. Smectic LC phases (or lamellar phases) (Sm) are the most commonly observed phase for ionic liquid crystals (ILCs) and are characterised by the stacking of layers that exhibit some positional and orientational order (Figure 6.3c). The layer formation of smectic ILCs is driven by Coulombic forces and nano-segregation of the charged moieties from the hydrophobic chains:[208] forces that are expected to dominate the intermolecular interactions of CAGE. In contrast, the nematic phase, which displays only orientational order, is rarely observed for ILC systems[209,210] and is unlikely to occur for CAGE owing to the lack of nematic phase favouring features such as $\pi - \pi$ interactions (i.e. aromatic rings).[211] The repeat distance of 22 Å (at 20 °C), roughly the length of two molecules of geranic acid, is analogous to the spacing observed in bilayer membrane systems. The first-order scattering peak shifts to higher q values at higher temperatures, corresponding to a decrease in the repeat distance, and indicating a negative thermal expansion upon heating. At temperatures above 5 °C, the SAXS profile becomes significantly weaker and broader, indicating the loss of the ordered liquid crystalline phase, whilst some intermediate-range structural ordering persists. At temperatures above the LC-to-isotropic transition, the SAXS profile of CAGE closely resembles those observed in ILs based on the 1-alkyl-3-methyl imidazolium cation (Cnmim) of various intermediate alkyl chain lengths ($3 < n < 10$).[157,212] Whilst a micelle-like model for self-assembly in ILs (with alkyl chains longer than a butyl group) was initially suggested to account for the diffraction peak at low-q,[161,212] more recent studies have shown that the diffraction profile may be interpreted as a bicontinuous sponge-like mesoscopic structure,[213–215] resulting from a clustering of polar and non-polar domains (Figure 6.3c). This has further been evidenced by simulations for a number of ILs.[216,217] It is noted that even the commonly referred to 'isotropic state' of many ILs displays some degree of nanoscale structure and charge ordering, although not to the same extent or length scale as for ILCs. Intermediate-range structure has been shown to remain above the Sm-to-isotropic transition temperature in carbohydrate-based LCs, where a low enthalpy/entropy Sm-to-isotropic transition was suggested to be a result of hydrogen-bonded aggregates remaining in the isotropic liquid phase.[218,219]

The stored CAGE sample showed only the single broad first-order scattering

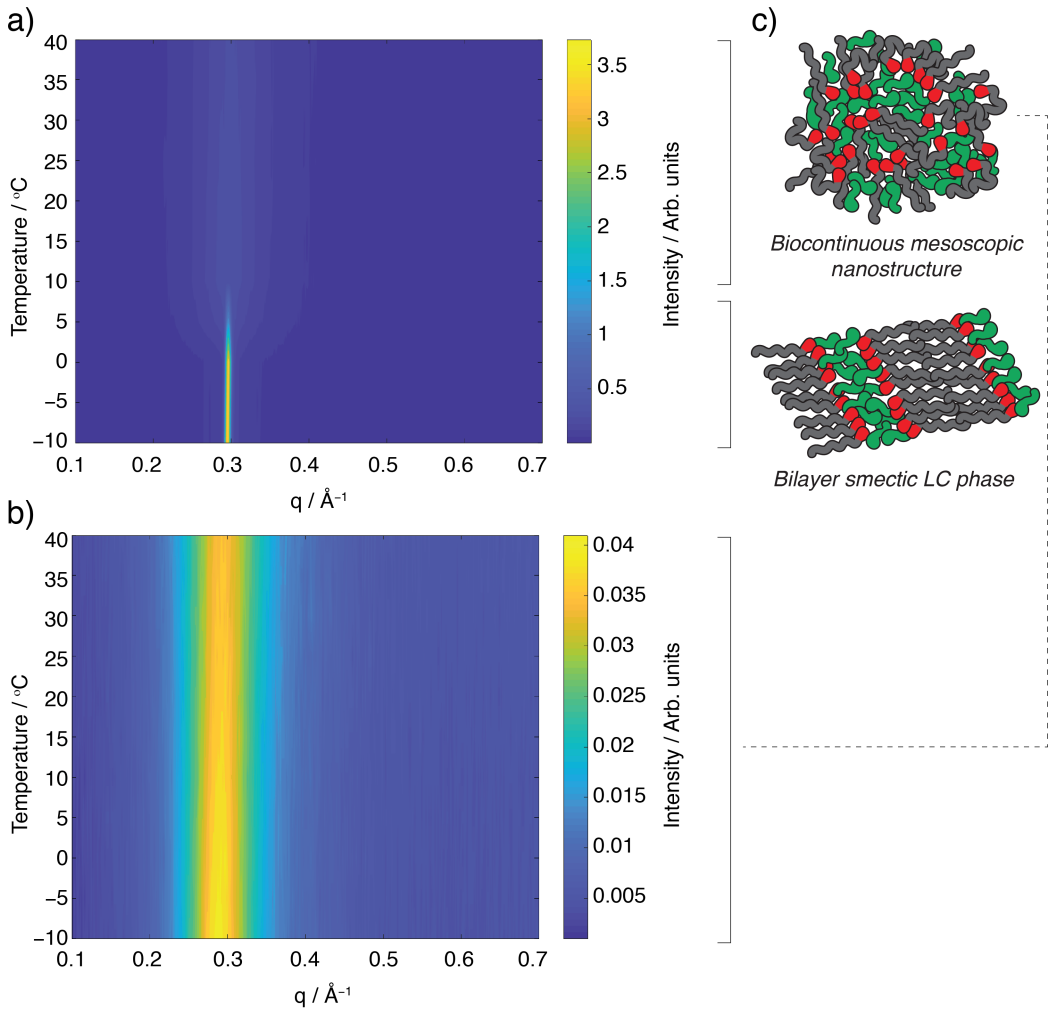

Figure 6.3: (a, b) SAXS contour plot showing the temperature behaviour of the first order scattering peak for (a) newly synthesised CAGE and (b) CAGE after storage for 6 months. (c) Schematic illustration of a bicontinuous mesoscopic nanostructure and a bilayer smectic LC phase.

peak over the temperature range −10 to 40 °C (Figure 6.3b), resembling the profile of freshly prepared CAGE at temperatures above T_c, in agreement with DSC (Figure 6.2c), which showed no thermal transitions in this temperature range. Further studies could investigate the cause for the shift in transition temperature (observed after 3 months) and eventual loss (observed after 6 months) of the liquid crystalline phase of CAGE after prolonged storage. It is hypothesised that either the presence of a small amount of degradation products inhibits the formation of a thermodynamically stable LC phase, or, the LC phase is not stable when the ratio of choline to geranic acid slightly changes from the original 1:2 stoichiometry. ILCs are of considerable interest since they present unique potential applications lacking in ILs and in normal (non-ionic) LCs. Further discussion on this topic and characterisation of the liquid

crystalline phase of CAGE is presented in Chapter 7.

6.4.2 ^{1}H NMR Spectroscopy of Neat CAGE

In order to investigate the molecular structure of neat CAGE (in the isotropic phase), ^{1}H NMR spectroscopy was performed. A 1D one-pulse ^{1}H MAS NMR spectrum is shown in Figure 6.4 (for numbering, see Figure 6.1). A single set of peaks is observed for the geranic acid and geranate, consistent with an equilibrium between the protonated and deprotonated forms. Furthermore, the presence of a single peak for the COOH and OH ^{1}H resonances (at 9.7 ppm) indicates that the acidic proton also undergoes fast chemical exchange (on the timescale of the NMR experiment) with the hydroxyl proton of the choline. Such chemical exchange requires the rapid formation and subsequent breaking of hydrogen bonds between the carboxylic acid, carboxylate, and hydroxyl groups. The presence of hydrogen bonding between the components is further evidenced by the chemical shift of the COOH/OH ^{1}H (which appears at the average of the COOH and OH resonances).

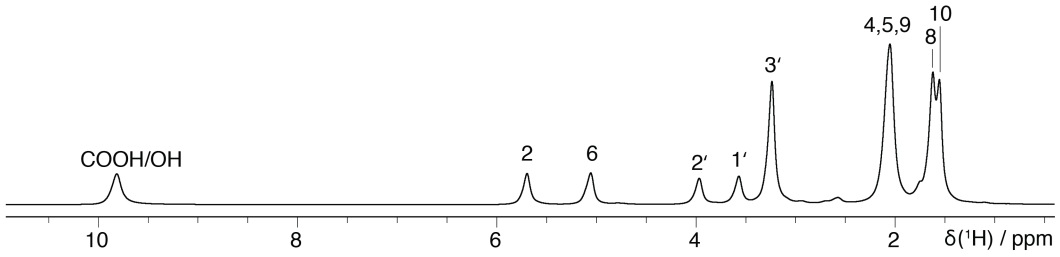

Figure 6.4: A ^{1}H 1D one-pulse MAS NMR spectrum (ν_{0H} = 400 MHz, ν_r = 5 kHz, 295 K) of neat CAGE.

The interaction between the components of CAGE was further investigated using 2D nuclear Overhauser effect spectroscopy (NOESY; Figure 6.5). Tanner *et al.* published a NOESY spectrum of CAGE, however a detailed analysis of the spectrum was not given; they reported only that the strongest cross-peaks were observed between the geranic acid/geranate methyl groups and the methyl groups on the nitrogen of the choline.[51] If this observation was based purely on the intensity alone, then this is not unexpected since the methyl groups contain the largest number of protons and are therefore the most intense peaks in the 1D spectrum. A more useful analysis would result from comparing the relative cross peak intensities normalised to the number of protons. They also did not state the mixing time that was used for their NOESY spectrum. This is important since the relative strength of the NOEs can provide misleading information at longer mixing times, when spin diffusion is significant and indirect contributions to the cross peaks are present. In order to provide a more thorough analysis of the ^{1}H-^{1}H NOEs of CAGE, NOE build-up curves

were recorded (Figure 6.6). A number of factors still make the NOEs difficult to interpret. Firstly, the fast chemical exchange of the COOH and OH resonances means that NOEs arising from these two protons cannot be distinguished. In addition, any ion pairs or clusters are not expected to be long-lived on the timescale of the NOE experiment, which therefore represents an average of the interactions. The normalised NOE build-up curves show that the strongest NOEs for all protons of both the geranate and choline cation are intramolecular (Figure 6.6, blue solid curves), rather than intermolecular contacts between the geranate and choline cation (red dashed curves), as previously suggested.[51] The strongest NOEs are labelled in Figure 6.6 and are as expected considering the closest intramolecular proximities; for example, H-2′ to H-1′, H-3′ to H-2′ and H-8 to H-6 are some of the strongest NOEs between aliphatic protons. The NOEs involving the COOH/OH protons are strongest for H-2 of geranate and H-1′ and H-2′ of the choline cation, and are consistent with the close intramolecular proximities.

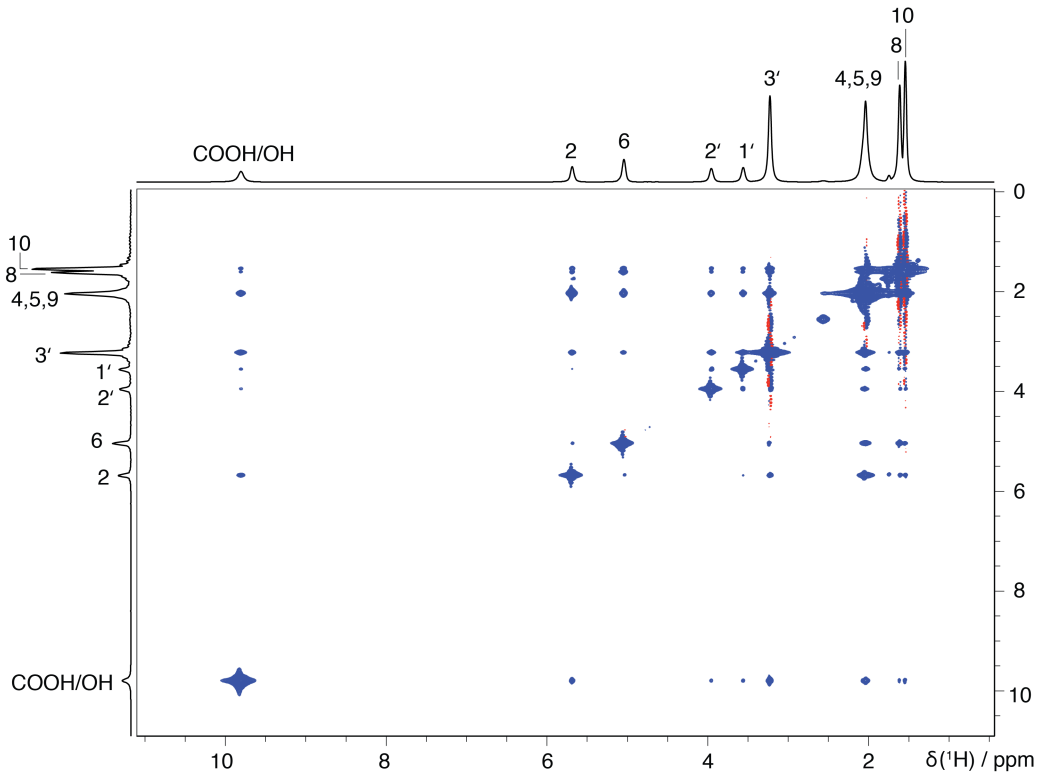

Figure 6.5: A ^{1}H-^{1}H NOESY MAS NMR spectrum (ν_{0H} = 400 MHz, ν_{r} = 5 kHz, 295 K) with skyline projections of neat CAGE recorded using a mixing of duration 50 ms. Positively phased peaks are shown in blue, and negative peaks are shown in red. The base contour level is at 0.25% of the maximum peak intensity.

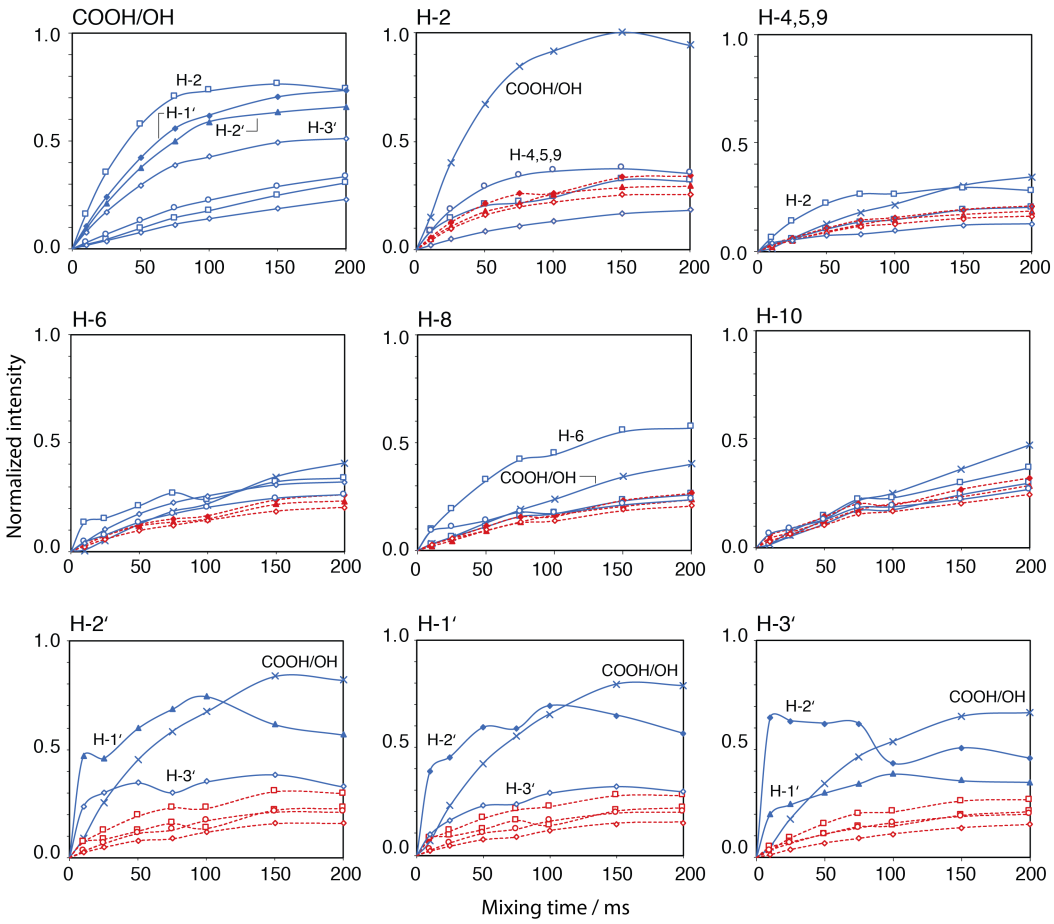

Figure 6.6: ^{1}H NOE build-up curves (ν_{0H} = 500 MHz, ν_r = 5 kHz, 295 K) for neat CAGE showing intramolecular contacts (blue, solid lines) and intermolecular contacts (red, dashed lines). Peak intensities were corrected for the number of equivalent protons by dividing by $n_A n_B$ and then normalised to the maximum NOE volume. Lines are included as guides for the eye.

6.4.3 The Behaviour of CAGE in Water

In addition to studying neat CAGE, knowledge of the behaviour of CAGE in water is critical for its use as a pharmaceutical as it will eventually come into contact with water in physiological media. The behaviour of CAGE in water/NaCl was therefore investigated. NaCl was used at 0.9 wt. %, the concentration typically used for medical purposes, in order to replicate the conditions used for *in vivo* and *ex vivo* assays. On dilution of CAGE in the saline solution, the solution immediately turns a milky white, indicating the formation of an emulsion. It has previously been reported that spontaneous emulsification can occur in systems containing two immiscible liquids with the help of a third component (typically a surfactant).[220] Micron sized droplets were confirmed by dynamic light scattering (DLS) measurements (Figure 6.7) with a mean size of 2.2 ± 3 μm. The emulsion droplets are relatively uniform in size with a polydispersity index, PDI $= 0.22 \pm 0.08$. The CAGE/D_2O/NaCl emulsions are unstable over time with the emulsion droplets vanishing over a period of hours.

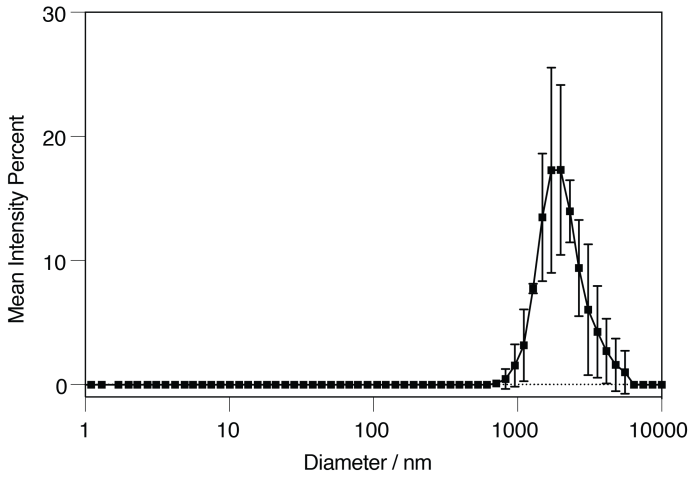

Figure 6.7: Dynamic light scattering (DLS) profile of CAGE in water/NaCl (1 in 50 by wt.), recorded after dissolving CAGE and mixing for 10 min. Error bars show the standard deviation for $n = 3$.

In order to characterise the emulsion, NMR experiments were performed on a freshly prepared dilution (1 in 50 by wt.) of CAGE in D_2O/NaCl. The 1D ^{1}H spectrum of the CAGE/D_2O/NaCl mixture alone provides considerable information about the system (Figure 6.8, bottom spectrum). Firstly, broad peaks indicative of slow molecular tumbling (as expected for emulsion particles) are observed for each component of the DES, indicating that the emulsion droplets are comprised of choline/geranate/geranic acid. Secondly, two sets of peaks are observed for geranate/geranic acid (in an approximately 1:1 ratio), whilst only a single chemical

environment is observed for each proton resonance of choline. The two environments of geranate/geranic acid are observed for all proton resonances including the methyl peaks at the end of the acyl chain (for which the chemical shift would be unaffected by ionisation of the carboxylic acid), indicating that the peaks are not due only to the neutral and acidic forms but rather result from the acid in two separate phases. Since the emulsion was observed to be unstable over time (changing from milky white to clear with droplets of an oily liquid on the surface), a 1D ^{1}H NMR spectrum was recorded of the mixture after it had been sitting at room temperature for 24 h (Figure 6.8). A 1:1 ratio of geranate to choline was observed in solution, confirming that approximately half of the original geranic acid/geranate population, namely the poorly water-soluble geranic acid, had precipitated out of the aqueous solution while leaving the other half geranic acid/geranate fully solubilised, giving raise to the sharp spectrum shown in Figure 6.8 (bottom trace).

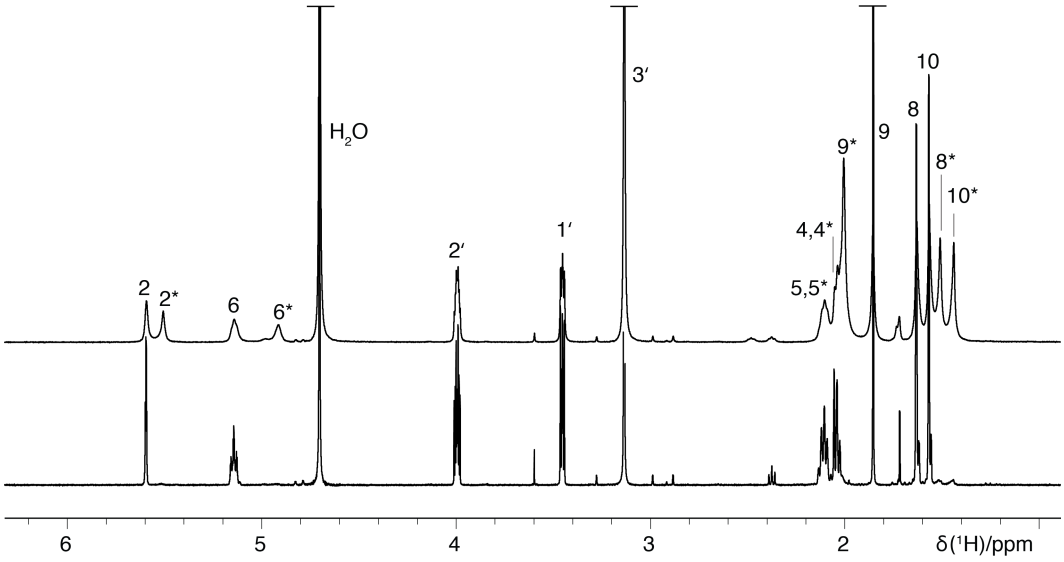

Figure 6.8: ^{1}H 1D NMR spectra (ν_{0H} = 400 MHz) of a freshly prepared CAGE/D_2O/NaCl emulsion (top) and the same sample after sitting for 24 hours (bottom). * indicates the geranic acid in the emulsion droplets (phase II).

To identify the different phases in the emulsion, ^{1}H pulsed-field gradient (PFG) NMR diffusion measurements were performed, with the resulting diffusion-ordered spectroscopy (DOSY) spectrum shown in Figure 6.9. Whilst the two geranate/geranic acid phases clearly have distinct diffusion coefficients, the difference is not as large as would be expected for a freely diffusing molecule compared to a micron size emulsion droplet. Using the Stokes-Einstein equation, approximate sizes for the two geranate/geranic acid phases of 0.58 and 1.5 nm were obtained. The obtained radii are clearly too small for a micron sized droplet and do not appear at first to

correspond to the broad ^{1}H linewidths that indicate much slower diffusion. This discrepancy (both in droplet size by DOSY vs. DLS and linewidth) can be explained by equilibrium between geranate/geranic acid dissolved in the water phase and that in the emulsion droplets. In the case of such exchange between molecules in two phases, the observed (apparent) diffusion coefficient is a population-weighted average of the two diffusion coefficients. ROESY NMR confirms that the geranate/geranic acid exchange between the two phases (Figure 6.10). The broad linewidths of each phase are also consistent with exchange, where, in a similar behaviour to the diffusion coefficients, the apparent transverse relaxation rate is a population-weighted average of the inherent relaxation rate of the resonances in each phase. The diffusion coefficient and ^{1}H linewidths of choline also support molecular exchange between the water and emulsion droplet phases; however, in contrast to geranic acid, the exchange is fast on the NMR timescale resulting in a single set of resonances.

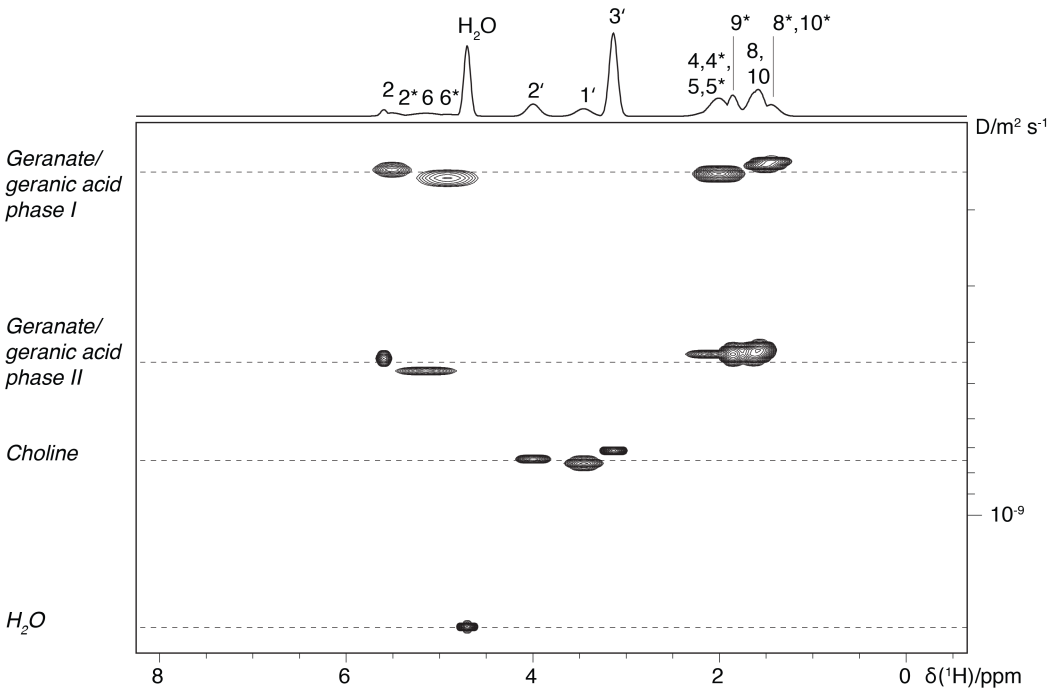

Figure 6.9: A ^{1}H DOSY NMR spectrum (ν_{0H} = 400 MHz) of CAGE/D_2O/NaCl. The spectrum was recorded within one hour of preparation of the emulsion.

It can be concluded that CAGE forms a spontaneous emulsion in water/salt where droplets of the poorly water-soluble geranic acid are stabilised by interactions with choline/geranate. The interactions observed in the neat IL phase (hydrogen bonding and electrostatic interactions) are no longer thermodynamically favoured in the aqueous phase where the ions are preferentially solvated by water and the inorganic salt ions. This results in the neutral geranic acid separating out of solution

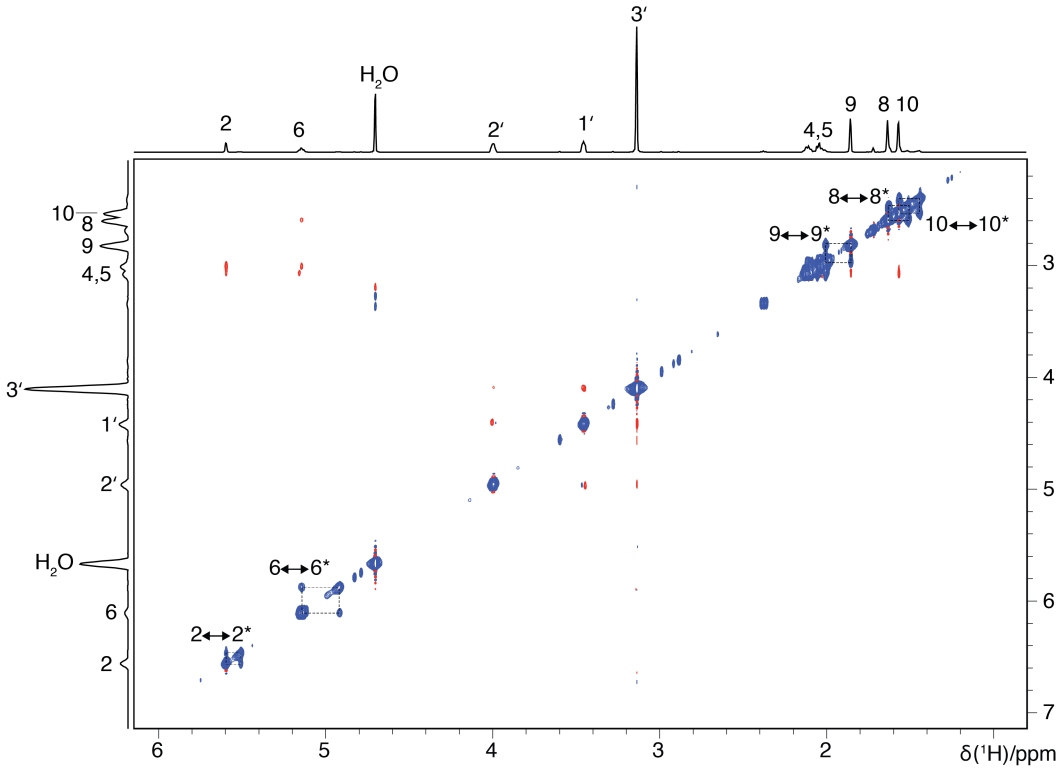

Figure 6.10: A ^{1}H-^{1}H ROESY NMR spectrum (ν_{0H} = 400 MHz) with skyline projections of CAGE/D_2O/NaCl showing molecular exchange between the two geranic acid phases. Positively phased peaks are shown in blue, and negative peaks are shown in red. The base contour level is at 0.05% of the maximum peak intensity.

over time leaving the dissociated water-soluble ions (the choline cation and geranate anion) in the aqueous phase.

6.4.4 Analogues of CAGE

Analogues of CAGE were prepared using various anions or cations (Figure 6.11). A first set of three IL variants was synthesised by replacing one equivalent of geranic acid with alternate organic acids: octanoic acid, levulinic acid, or lipoic acid, to form ILs composed of a 1:1:1 stoichiometric ratio of choline:geranate:alternate acid. Octanoic acid contains the same number of back-bone carbon atoms as geranic acid, but is a straight-chain saturated acid, lacking the methyl side groups and double bonds of geranic acid. Lipoic acid, a compound derived from octanoic acid, features a cyclic disulphide. Levulinic acid is a five-carbon molecule with a ketone functionality. In addition, cationic alternatives to choline were selected that differed in the hydroxyl functionality. The ether, 2-methyoxy-N,N,N-trimethylethan-1-ammonium cation replaces the hydroxyl proton of choline with a methyl group, removing the hydrogen bond donor ability. Both the hydrogen bond donor and acceptor ability is completely

removed in the butyl analogue, N,N,N-trimethylbutan-1-ammonium. These two anionic CAGE analogues are referred to as ether CAGE and butyl CAGE. In order to investigate whether other molecules with hydroxyl functionality could be incorporated into the hydrogen bonded structure of CAGE, a 1:1 mixture of butyl CAGE (lacking the hydroxyl group of choline) and 3,3-dimethylbutan-1-ol (referred to as alcohol) was prepared. All of the CAGE analogues were room temperature liquids, apart from CAGE octanoic acid and CAGE lipoic acid, which were wax-like substances.

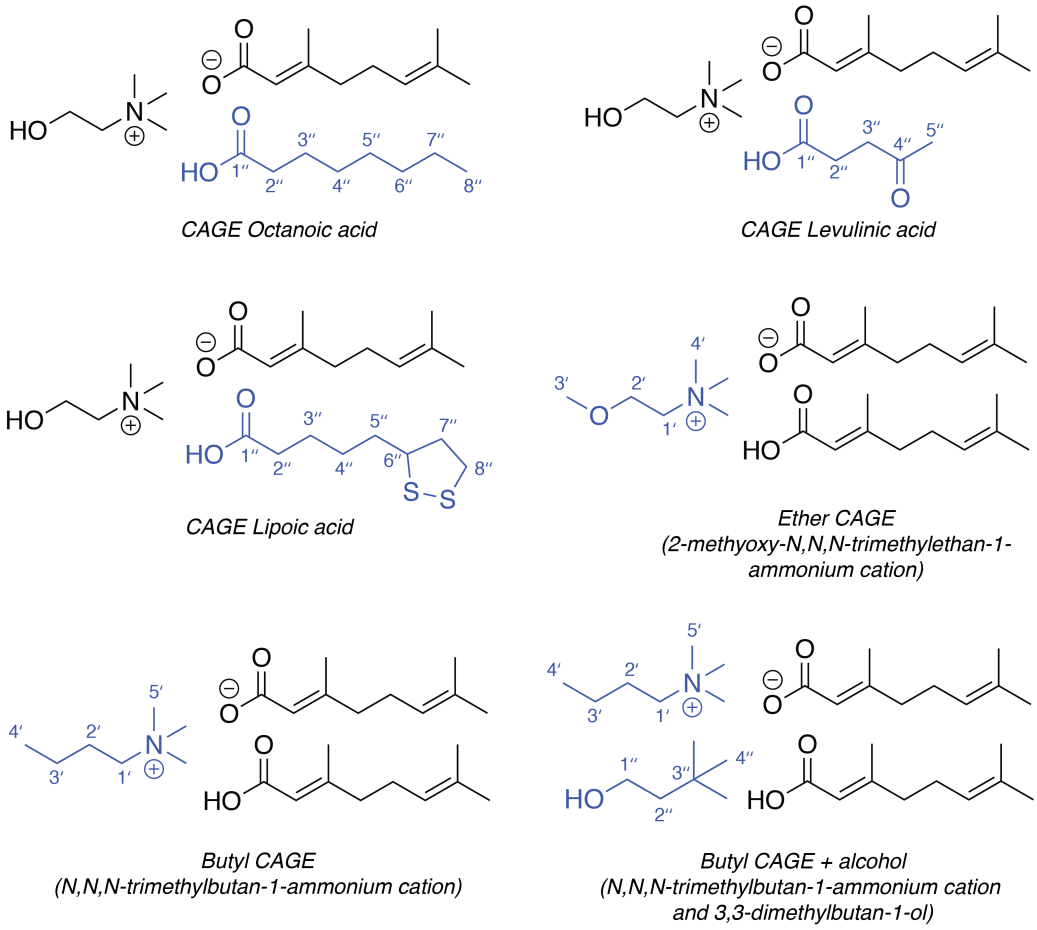

Figure 6.11: Chemical structures of the CAGE analogues used in this study. The molecules used as alternatives to either one molar equivalent of geranic acid, or choline, are shown in blue.

The phase behaviour of the CAGE analogues was investigated by DSC (Figure 6.12). All analogues underwent glass transitions at temperatures between −90 to 70 °C. A sharp transition at 30 °C was observed for CAGE octanoic acid upon heating and at 28 °C on cooling. This transition resembles that of newly synthesised CAGE (at 5 °C), as discussed in Section 6.4.1. The nature of this transition is explored further in Section 6.4.6.

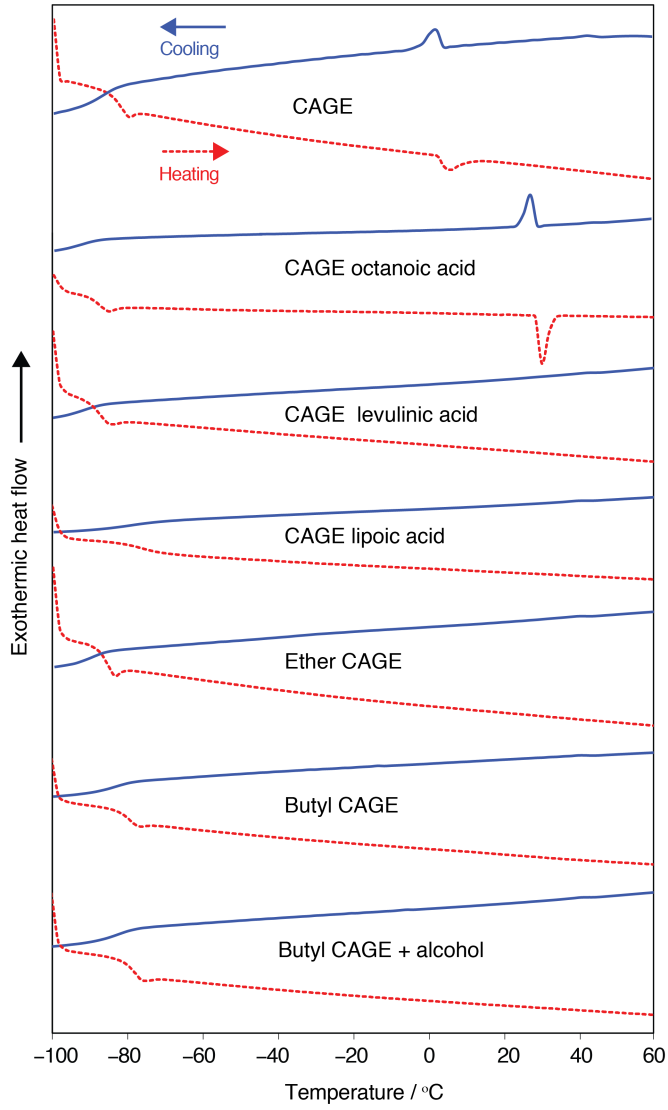

Figure 6.12: Heating (dashed red) and cooling (solid blue) DSC traces for CAGE and its analogues (see Figure 6.11). Note that the DCS traces for CAGE are as presented in Figure 6.2, and repeated here for comparison to the analgoues.

6.4.5 Variable Temperature ^{1}H NMR Spectroscopy of CAGE and its Analogues

The CAGE analogues were further characterised by ^{1}H NMR spectroscopy (Figure 6.13). As with CAGE, a single peak was observed for the COOH and OH ^{1}H resonances for the three cation alternatives of CAGE (Figure 6.13a), indicative of fast chemical exchange on the NMR timescale between the acidic proton and the hydroxyl proton of choline. The exact position of this peak is highly sensitive to ppm concentrations of water in the sample. The COOH ^{1}H resonances appear at higher ppm values for ether CAGE and butyl CAGE since there is no hydroxyl proton (Figure 6.13b). A single COOH/OH ^{1}H resonance is observed for the butyl CAGE/alcohol mixture.

The chemical shift of protons participating in hydrogen bonds is known to be temperature sensitive due to changes in the degree of excitation of the hydrogen-bond-stretching vibrational mode,[180–182,221] and has been shown to correlate with the nature and strength of the hydrogen bond.[221–224] The chemical shift temperature coefficient (TC), determined in the range 268 to 323 K, of $[-7.1 \pm 0.2] \times 10^{-3}$ ppm K^{-1} (Figure 6.14) for CAGE is consistent with intermolecular hydrogen bonding. The hydrogen bonding arrangement involves the carboxylic acid, carboxylate and hydroxyl groups, possibly as hydrogen-bonded clusters, or an extended hydrogen-bonded network and is likely dynamic, where rapid formation and subsequent breaking of hydrogen bonds occurs between the carboxylic acid, carboxylate, and hydroxyl groups. The reported hydrogen bond life-times for ILs are typically on the order of ps.[225–227] The temperature coefficients of the cationic alternatives of CAGE are all similar, suggesting a similar hydrogen bond arrangement (Figure 6.14a and Table 6.1).

The temperature coefficients of the ether and butyl CAGE COOH ^{1}H resonance of $[-8.00 \pm 0.08] \times 10^{-3}$ ppm K^{-1} and $[-8.2 \pm 0.1] \times 10^{-3}$ ppm K^{-1} are slightly higher compared to CAGE. On the addition of the alcohol to butyl CAGE, the temperature coefficient does not significantly change. If the strength of the hydrogen bonding interactions were unchanged, the observed TC would be expected to be the average of the TC of Butyl CAGE and the alcohol of -10.2×10^{-3} ppm K^{-1}. The observed TC of $[-7.97 \pm 0.04] \times 10^{-3}$ ppm K^{-1} is significantly lower than this average, confirming the presence of hydrogen bonding between the alcohol and geranic acid/geranate. It is likely that other hydroxyl functionalised compounds would like-wise form similar hydrogen bonding interactions, which could play a role in the drug delivery of small-molecule pharmaceuticals, many of which contain hydroxyl groups or other hydrogen bonding functional groups.

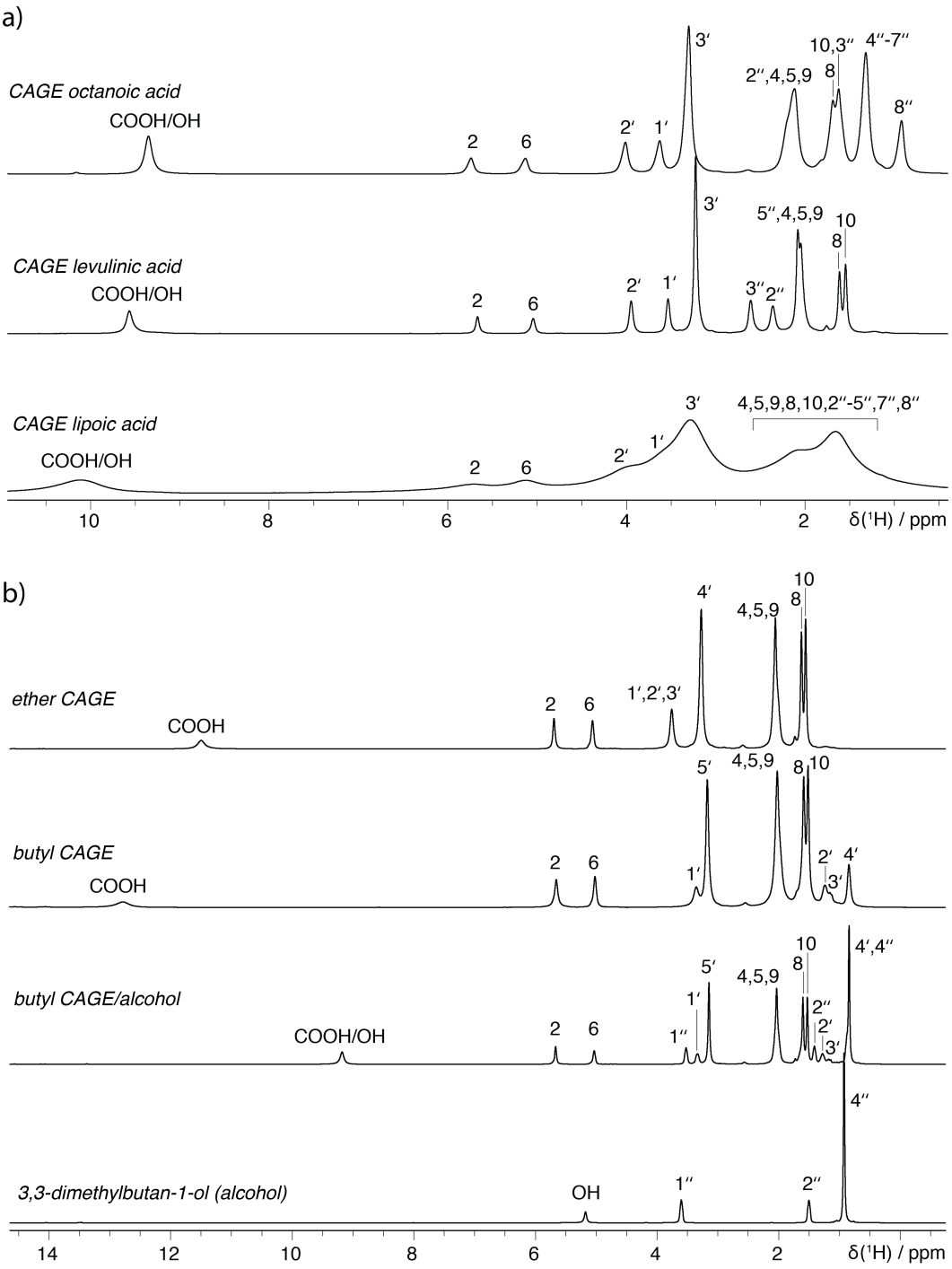

Figure 6.13: ^{1}H 1D MAS NMR spectra (ν_{0H} = 400 MHz, ν_{r} = 5 kHz, 298 K) of the (a) anionic and (b) cationic alternatives of CAGE. For numbering, see Figures 6.1 and 6.11. Note that a larger chemical shift range (up to >14 as compared to 11 ppm is shown in b).

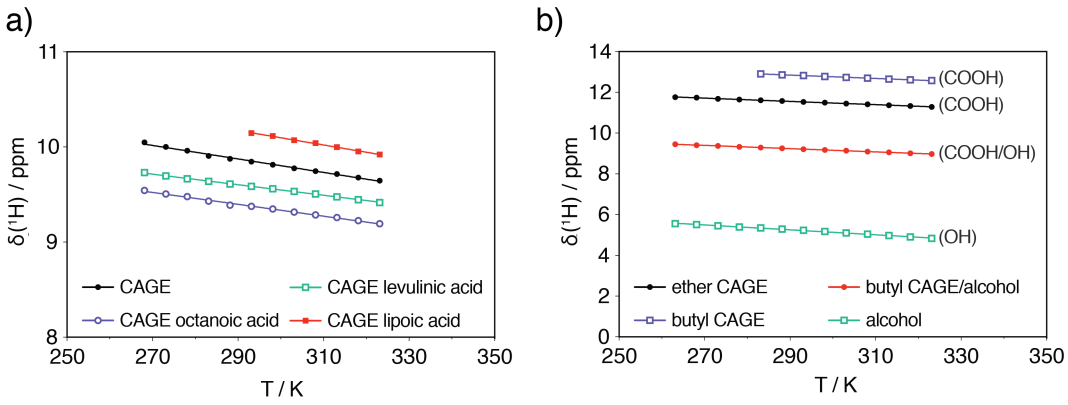

Figure 6.14: Temperature dependence of the COOH/OH ^{1}H resonance for the (a) anionic and (b) cationic alternatives of CAGE. The temperature range is reduced for CAGE levulinic acid (in a) and butyl CAGE (in b) due to insufficient resolution at lower temperatures, and overlap of the COOH resonance with spinning side-bands, respectively.

Table 6.1: Temperature coefficients for the COOH/OH ^{1}H resonances of CAGE and its analogues (see Figure 6.14).

Sample	TC ($\times 10^{-3}$ ppm K^{-1})
CAGE	-7.1 ± 0.2
CAGE octanoic acid	-6.2 ± 0.1
CAGE levulinic acid	-7.6 ± 0.2
CAGE lipoic acid	-5.53 ± 0.05
ether CAGE	-8.00 ± 0.08
butyl CAGE	-8.2 ± 0.1
butyl CAGE/alcohol	-7.97 ± 0.04
alcohol	-12.1 ± 0.2

6.4.6 CAGE Octanoic acid

Of the six investigated analogues, CAGE octanoic acid (CAGE-oct) was observed to undergo a DSC transition similar to the isotropic to LC phase transition of newly synthesised CAGE, albeit at a higher temperature of 30 °C (see Section 6.4.4). Unlike CAGE, this transition was observed after storage at RT for a period greater than 6 months, and this novel stable ILC therefore warrants further investigation. At temperatures below this transition, SAXS of CAGE-oct shows a similar scattering profile as observed for CAGE, with a sharp first-order scattering peak at 0.29 Å^{-1} (at 20 °C), corresponding to a repeat distance of 22 Å, consistent with a bilayer liquid-crystalline phase (Figure 6.15). The LC-to-isotropic phase transition occurs at 20 °C, slightly lower than observed by DSC at 30 °C. This could be due to a number of experimental factors, such as differences in the rate of heating, a possible

temperature gradient and diffusion of the sample along the capillary during the SAXS measurement, or changes to the sample between the DSC and SAXS measurements. At temperatures above the liquid crystal transition, a broad first order scattering peak is observed, similar to CAGE, indicative of some intermediate-range ordering persisting at higher temperatures.

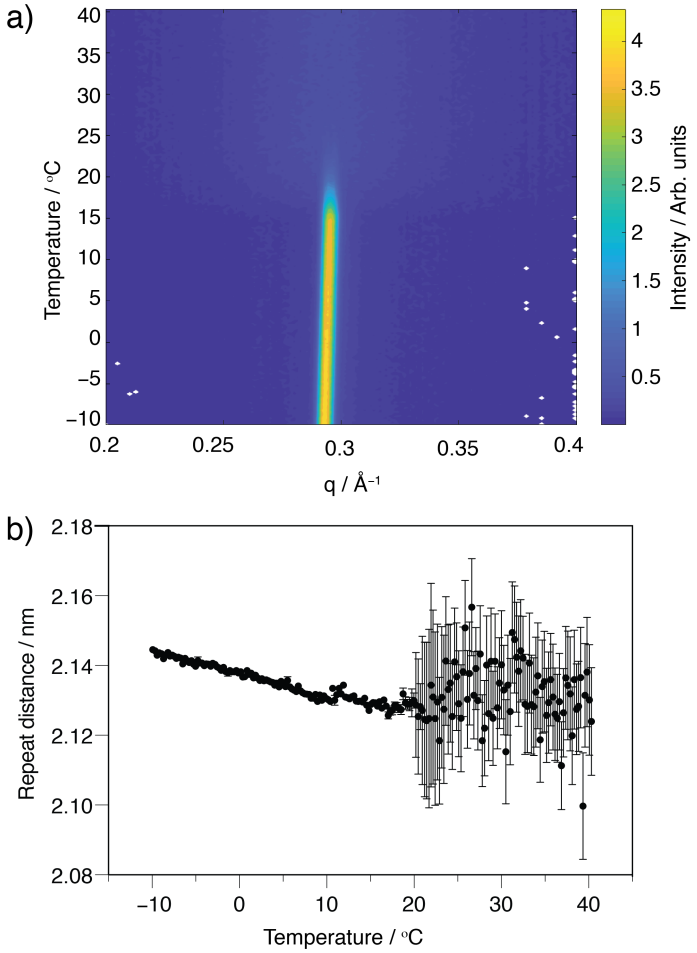

Figure 6.15: (a) SAXS contour plot showing the temperature behaviour of the first order scattering peak for CAGE-oct. (b) Temperature dependence of the repeat distance for CAGE-oct calculated from the first order scattering peak. The large uncertainties in the repeat distance at temperatures above the LC-to-isotropic transition (∼20 °C) are due to the weak broad nature of the scattering peak in the isotropic phase.

Figure 6.16a shows a polarising optical microscopy image of the LC phase of CAGE-oct at 278 K. There appear to be two distinct birefringent areas with larger scale and smaller scale patterning (solid red oval and dashed red oval, respectively). Both of these optical textures are conic fan textures characteristic of a smectic structure[228–232] and the apparently distinct patterns are likely to arise from differences

in nucleation.[233] In addition, there are regions with no birefringence present between LC domains, indicating isotropic liquid regions. The coexistence of an isotropic component with the LC phase is explored further by MAS NMR in Chapter 7. On heating, the LC phase melts to an isotropic phase between 18 and 25 °C (Figure 6.16b); this transition is also seen in the SAXS results described above. On cooling from the isotropic phase, the first birefringence patterns appear between 18 and 20 °C.

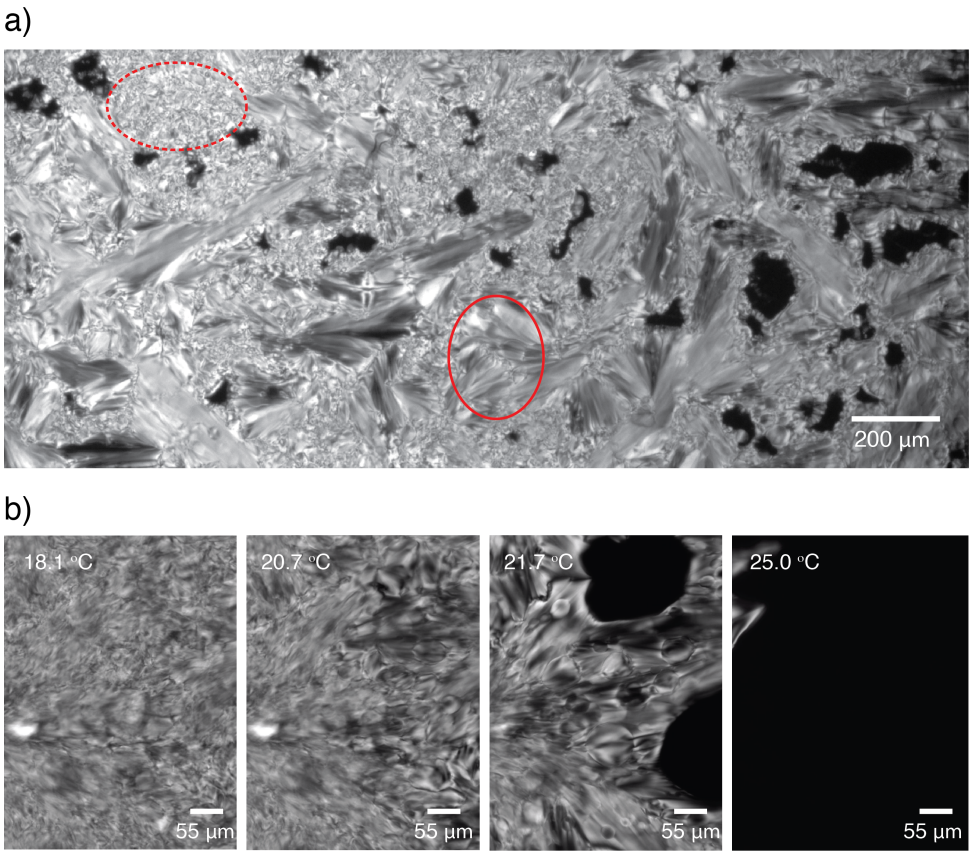

Figure 6.16: (a) Polarising optical micrograph (× 4) of CAGE-oct, showing the LC texture at 5 °C. The red ovals highlight the two distinct birefringent patterns. (b) Polarising optical micrographs (× 20) of CAGE-oct, showing the LC-to-isotropic transition upon heating the sample (from left to right) at 10 °C min^{-1}.

The stability of the CAGE-oct LC compared to CAGE could be related to steric interactions, which are known to affect the stability of LC phases. The smectic phase is more likely to occur when the polar and apolar groups project similar cross-sectional areas on the interlayer planes.[234–236] So, the formation of a stable smectic phase in CAGE octanoic acid, but not in CAGE can be attributed to the shape of the molecules. Octanoic acid, a saturated, unbranched carboxylic acid, should favour the formation of a stable smectic phase, while the unsaturated,

branched geranic acid, which has a larger cross-sectional area, should disfavour the smectic phase. Further characterisation of the long-range structure of the liquid crystalline phase of CAGE octanoic acid is presented in Chapter 7.

In order to further investigate the short-range structure (interactions between ions) of CAGE-oct, mass spectrometry was performed. Careful study of the negative ion mass spectrum of CAGE-oct (see Table 6.2 and Appendix D.1 for the full spectrum) reveals evidence of interactions between choline and carboxylate anions. As expected, both 'free' octanoate and geranate anions are observed under mass spectrometry conditions, but an ion corresponding to CAGE-oct, $[(\text{choline})(\text{geranate})(\text{octanoate})]^-$, is seen at a mass to charge ratio (m/z) 414 (with loss of a proton). This peak is about 70% of the intensity of 'free' octanoate implying that these clusters are significantly more stable than would otherwise be expected from simple electrostatic-based ion clustering, probably due to the hydrogen bonding interactions between the hydroxyl group of choline cation and the carboxylate anions (as evidenced by ^{1}H MAS NMR in Section 6.4.5). Further peaks at m/z 390.4 and 438.4 correspond to $[(\text{choline})(\text{octanoate})_2]^-$ and $[(\text{choline})(\text{geranate})_2]^-$, respectively. The ratio of these three clusters is close to the statistically expected 1:2:1 even though CAGE-oct was synthesised by adding one molar equivalent of 1-octanoic acid to in situ-generated choline geranate, implying anion metathesis is taking place. These peaks are significantly more intense (at least an order of magnitude) than those of the $[(\text{anion})_2(\text{H})]^-$ species, suggesting that there is a strong association of the choline cation with the carboxylate anions. Many larger ion clusters generated by electrostatic ion clustering, for example m/z 661.6 $[(\text{choline})_2(\text{octanoate})_2(\text{geranate})]^-$, were observed at $< 5\%$ of the intensity of 'free' octanoate which is more typical of electrostatic ion clusters, especially those found in the mass spectra of ionic liquids.[237]

Table 6.2: Results of the negative ion mass spectrometry of CAGE-oct (see spectrum in Appendix D.1).

Ion	m/z	%
$[\text{octanoate}]^-$	143.1	100
$[\text{geranate}]^-$	167.2	88
$[\text{H(octanoate)}_2]^-$	287.3	$< 5\%$
$[\text{H(octanoate)(geranate)}]^-$	309.3	$< 5\%$
$[\text{H(geranate)}_2]^-$	333.3	$< 5\%$
$[\text{(choline)(octanoate)}_2]^-$	390.4	50%
$[\text{(choline)(octanoate)(geranate)}]^-$	414.4	73%
$[\text{(choline)(geranate)}_2]^-$	438.4	35%
$[\text{(choline)}_2\text{(octanoate)}_3]^-$	637.6	$< 5\%$
$[\text{(choline)}_2\text{(octanoate)}_2\text{(geranate)}]^-$	661.6	$< 5\%$
$[\text{(choline)}_2\text{(octanoate)(geranate)}_2]^-$	685.6	$< 5\%$
$[\text{(choline)}_2\text{(geranate)}_3]^-$	709.6	$< 5\%$
$[\text{(choline)}_3\text{(octanoate)}_3\text{(geranate)}]^-$	908.8	$< 5\%$
$[\text{(choline)}_3\text{(octanoate)}_2\text{(geranate)}_2]^-$	932.8	$< 5\%$
$[\text{(choline)}_3\text{(octanoate)(geranate)}_3]^-$	956.7	$< 5\%$
$[\text{(choline)}_3\text{(geranate)}_4]^-$	980.8	$< 5\%$

6.5 Conclusions

In this chapter, neat CAGE and a series of structural analogues have been investigated by NMR, DSC and SAXS. The COOH of the geranic acid and OH protons of the choline cation of CAGE undergo fast chemical exchange, on the NMR timescale, requiring the formation and subsequent breaking of hydrogen bonds between the carboxylic acid, carboxylate and hydroxyl groups. Additional evidence of dynamic hydrogen bonding interactions in the CAGE octanoic acid analogue was evidenced by mass spectrometry, with the $[\text{(choline)(geranate)(octanoate)}]^-$, $[\text{(choline)(octanoate)}_2]^-$ and $[\text{(choline)(geranate)}_2]^-$ species observed at intensities significantly higher than expected of electrostatic ion clusters and compared to those for $[\text{(anion)}_2\text{(H)}]^-$ species, suggesting strong association of the choline cation with the anions. The temperature dependence of the COOH/OH ^{1}H chemical shift did not significantly differ between analogues prepared by the replacement of one equivalent of geranic acid with an alternative acid (octanoic acid, levulinic acid or lipoic acid), suggesting that the structure of the acid, for these analogues, does not have a strong impact on the nature and strength of the hydrogen bonding. The addition of a hydroxyl-functionalised small molecule to butyl CAGE, a cationic analogue of CAGE lacking the hydroxyl functionality of choline, was shown to incorporate into the hydrogen bonding between the geranate/geranic acid, showing a similar temperature coefficient to CAGE. Further studies could investigate whether hydroxyl-functionalised active pharmaceutical ingredients can form similar hydrogen

bond interactions with CAGE or CAGE analogues, and the impact of this interaction on drug-delivery efficacy.

CAGE and the octanoic acid analogue, CAGE-oct, formed LC phases at temperatures below ∼5 °C and ∼20 °C, respectively, as evidenced by DSC and SAXS. A smectic texture was observed for the CAGE-oct LC by polarising optical microscopy. At temperatures above the liquid-crystal to isotropic transition, some intermediate-range order was observed, a property typical of ILs with medium to long alkyl chains due to their inherent amphiphilic nature. Further characterisation of the LC phases of CAGE and CAGE-oct by MAS NMR is the focus of Chapter 7. A change in colour of CAGE from clear to yellow over a period of months was accompanied by the loss of the LC phase, while the LC phase of CAGE-oct persisted more than 6 months after synthesis and storage at room temperature.

Additionally, the behaviour of CAGE in water was explored by solution NMR spectroscopy. On addition to water, CAGE was observed to immediately form a spontaneous emulsion. Over a period of hours, the neutral geranic acid separated out of solution, leaving the dissociated choline and geranate ions in the aqueous phase.

Chapter 7

MAS NMR Investigation of Molecular Order in Ionic Liquid Crystals

CAGE and CAGE-octanoic acid were synthesised by Dr. Jeraime Griffith, in the research group of Prof. Tom Welton, Department of Chemistry, Imperial College London, and Dr. David Pugh, Department of Chemistry, Imperial College London.

7.1 Abstract

The molecular order in the thermotropic ILCs, CAGE, and its analogue CAGE-oct (introduced in Chapter 6), was further investigated using MAS NMR. Specifically, site-specific order parameters for the LC phase of CAGE and CAGE-oct were obtained from the measurement of the partially averaged ^{1}H-^{13}C dipolar couplings by cross-polarisation (CP) build-up curves and dipolar-chemical shift correlation (DIPSHIFT) experiments, and ^{1}H-^{1}H dipolar couplings by double-quantum (DQ) build-up curves. The order parameters, S^2_{CH} and S^2_{HH}, are similar for both CAGE and CAGE-oct, lying in the range 0 to 0.005, and are lower compared to those for smectic (i.e., layered) phases of conventional non-ionic liquid crystals, resembling those of lamellar phases formed by lyotropic surfactant-solvent systems. Additionally, the presence of an isotropic component of approximately 23% and 50% was observed to coexist with the LC phase of CAGE and CAGE-oct, respectively, and quantified by both ^{1}H-^{13}C DIPSHIFT and ^{1}H DQ experiments.

7.2 Introduction

As the name suggests, the liquid crystalline state of matter is an intermediate between liquids and solids; there is long range order but the molecules themselves are mobile. Liquid Crystals (LCs) can form under suitable temperature (thermotropic LCs) or concentration (lyotropic LCs) conditions. A subset of LCs, ionic LCs (ILCs) carry charges, and thus combine the characteristics of LCs and ionic liquids[238,239] (ILs). ILCs combine the conductivity, low vapour pressure, and tuneability (the ability to select or modify properties by the appropriate choice of the anion and cation) of ILs, with the anisotropic properties of LCs. This unique combination of properties has generated interest in ILCs,[208,240,241] which may be used in a broad range of fields, with applications including LC displays,[242] as electrolytes in dye-sensitised solar cells,[243–245] as ordered reaction media or templates in synthetic chemistry,[246–248] and for biological applications.[249,250] The majority of ILCs are based on typical organic nitrogen cations (e.g., imidazolium, ammonium and pyridinium) substituted with one or more long alkyl chains and inorganic anions (e.g., halides, $[BF_4]^-$, $[PF_6]^-$), and form smectic (i.e., layered) phases, exhibiting partial positional order, in addition to orientational order.[240] They typically display considerably less orientational order compared to non-ionic thermotropic LCs, instead resembling the lyotropic lamellar phases of surfactant-water systems.[251,252] Advancing our understanding of ILC structure and dynamics at an atomic level will enable and promote the development of novel ILCs as well as further applications for ILCs.

Choline geranate (CAGE; Figure 7.1), introduced in Chapter 6, is a broad-spectrum antimicrobial and a transdermal and oral delivery agent.[27–29,51,52] The most effective formulation of CAGE is composed of choline, geranic acid and the geranate anion in a 1:1:1 ratio ([choline][geranate$_2$(H)]),[51] which has been described as both an IL, and a deep eutectic solvent (DES),[51,52] a eutectic mixture of two or more components (in some cases both neutral and ionic species) that typically interact via strong hydrogen bonding. As discussed in Chapter 6, CAGE was modified, replacing one equivalent of geranic acid with octanoic acid, to form a novel stable thermotropic ILC, CAGE-octanoic acid ([choline][geranate(H)octanoate]); CAGE-oct; Figure 7.1). The LC-to-isotropic phase transition of CAGE-oct occurs close to room temperature ($\sim$293 K; see SAXS and polarising optical microscopy results in Section 6.4.6), which may be exploited as a temperature-induced 'switch' of the anisotropic properties for specific applications.

When considering structure and order in such materials, both the time-scale and length-scale are of importance. In contrast to a so-called 'isotropic' liquid (where there can still be some short-range ordering), LCs exhibit long-range positional and/or orientational order; the molecular positions and relative orientations are correlated over longer distances. Aspects of the structure (e.g., shape of the constituent

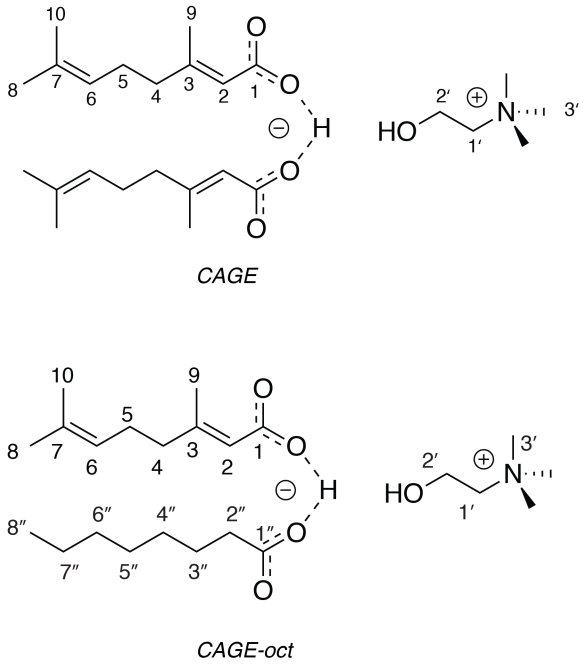

Figure 7.1: Primary structures of CAGE (top) and CAGE-oct (bottom). The numbering shown is used for NMR assignments throughout the text.

molecules and nano-scale segregation of molecular components into distinct regions) determine the formation of LC phases. The segregation of incompatible parts of the molecules (e.g., non-polar aliphatic chains from polar regions), as well as attractive forces (e.g., ionic interactions or hydrogen bonding) drive the formation of long-range positional order in LCs.

SAXS and NMR spectroscopy are complementary techniques to investigate LCs.[253] While SAXS identifies long-range order, NMR yields local atomic-level structure, e.g., about specific intermolecular hydrogen bonding interactions, and is sensitive to molecule/segment/bond orientations. Specifically, the dipolar couplings between spins report on order: the dipolar coupling depends on the timescale and amplitude of molecular motion, because motion averages the couplings. Compared to an isotropic liquid where the molecules undergo rapid tumbling and all orientations are sampled, such that the dipolar couplings are averaged to zero, in anisotropic LC phases, there is a preferential orientation and the dipolar coupling is not completely averaged out. The squared ratio of the partially averaged residual dipolar coupling (RDC, D_{res}), to its unaveraged value (i.e., the value in the rigid limit, D_{rigid}) provides the order parameter, $S^2 = (D_{res}/D_{rigid})^2$. S^2 ranges from 0 for isotropic systems, to 1 for completely rigid systems (see Section 2.3.4 for further details on the dipolar coupling and order parameter).

In solid-state NMR, magic-angle spinning (MAS) averages anisotropic interactions so that high-resolution spectra can be obtained (see Section 2.3.5). Radio-

frequency (rf) pulses can be applied that interfere with the MAS averaging, and thus recouple the interactions, and the strength of the interaction can be measured. One such approach is the much-employed solid-state NMR approach of ^{1}H-^{13}C cross-polarisation (CP), whereby long rf pulses are applied simultaneously with the same nutation frequency (under MAS, this so-called Hartmann-Hahn matching condition is adjusted by a small integer multiple of the spinning frequency) to both the ^{1}H and ^{13}C nuclear spins: ^{1}H-^{13}C heteronuclear dipolar couplings may be obtained from ^{1}H-^{13}C CP build-up curves. If there is a dominant dipolar interaction, the polarisation transfer shows oscillatory behaviour where the frequency of oscillations is directly proportional to the dipolar coupling constant.[110] CP build-up curves or variants such as Lee-Goldburg (LG) CP have been used to obtain RDCs and the related S^2_{CH} order parameters in various dynamic systems, including polymers,[254] and LCs.[255,256]

A complement to probing ^{1}H-^{13}C dipolar coupling is the measurement of ^{1}H-^{1}H homonuclear dipolar couplings, and the related order parameter S^2_{HH}.[121,186,257] [123,258–260] ^{1}H-^{1}H RDCs can be quantified by ^{1}H double quantum (DQ) MAS spectroscopy,[261–265] from which the value of the dipolar coupling constant can be extracted either by fitting the intensity of the build-up behaviour with varying DQ excitation time (τ_{DQ}) or by analysing the spinning sideband pattern in a 2D spectrum recorded with fixed τ_{DQ}. Brown *et al.* utilised ^{1}H-^{1}H residual dipolar couplings to study rotation of the aromatic core in columnar hexabenzocoronene LCs, as well as differential mobility along the alkyl chains in a triphenylene-based mesogen.[186,257] ^{1}H-^{1}H RDCs have also been used to investigate chain dynamics in polymer systems,[121,125,126,266] and for the study of lipid membranes with guest molecules.[267]

Despite the interest in ILCs, and the potential of NMR for probing structure and order, very few NMR studies have been reported on ILC materials. Recently, Di Pietro *et al.*[268] and Dai *et al.*[251,269] reported static NMR studies of ILCs containing imidazolium cations, and inorganic anions ($[NO_3]^-$, Cl^- and $[BF_4]^-$). The MAS NMR techniques used in this chapter have not, thus far been used to investigate ILCs.

In Chapter 6, the short-range (interactions between ions) and long-range structure (the occurrence of the partial bilayer LC phase) of CAGE-oct was investigated by 1D ^{1}H MAS NMR, SAXS, mass spectrometry and polarising optical microscopy. Freshly prepared CAGE was also observed to form a similar smectic phase (as observed by SAXS), however unlike CAGE-oct, this phase was not stable after prolonged storage. This chapter presents a further investigation of the molecular order in these ILCs by 2D MAS NMR. Specifically, residual ^{1}H-^{13}C and ^{1}H-^{1}H dipolar couplings are measured by means of ^{1}H-^{13}C CP and ^{1}H double-quantum (DQ) build-

up curves, so as to obtain order parameters, S^2_{CH} and S^2_{HH}, which quantitatively describe the amplitude of motion of the ions (and molecular segments/bonds) that comprise CAGE and its analogue, CAGE-oct.

7.3 Experimental Details

7.3.1 Sample Preparation

CAGE and CAGE-oct were synthesised as described in Section 6.3.1.

7.3.2 MAS NMR

MAS NMR experiments were performed on a Bruker Avance III spectrometer operating at a ^{1}H Larmor frequency of $\nu_{0\mathrm{H}} = 500$ MHz (11.7 T), using a 3.2 mm double-resonance MAS probe. A spinning frequency, ν_r, of 5 kHz was used. The temperature was calibrated using methanol, as described in the Bruker Instruments manual, with all stated temperatures being corrected by this procedure. The ^{1}H and ^{13}C 90° pulses were of duration 2.5 μs and 5 μs, respectively (corresponding to nutation frequencies, $\nu_{1,\mathrm{H}} = 100$ kHz, and $\nu_{1,\mathrm{C}} = 50$ kHz).

For ^{1}H-^{13}C CP experiments, the ^{1}H and ^{13}C nutation frequencies were approximately 52.5 and 47.5 kHz, respectively. For the 2D HETCOR experiment, CP was achieved using a 70 to 100% ramp[175] on the ^{13}C channel, whereas CP build-up curves were recorded without a ramp to allow for quantitative determination of the dipolar coupling, D_{CH}. For the HETCOR experiment, 32 transients were co-added for each of 384 FIDs, using the States-TPPI[176] method to restore sign discrimination in the F_1 dimension with a t_1 increment of 100 μs, and a recycle delay of 3 s, corresponding to an experimental time of 10.2 hours. CP build-up curves were recorded by incrementing the contact time in 40 μs intervals up to a maximum of 3.6 ms. 256 transients were co-added, with a recycle delay of 3 s, corresponding to an experimental time of 19.2 hours. SPINAL-64[119] heteronuclear decoupling was applied during acquisition at a ^{1}H nutation frequency of 52.5 kHz, corresponding to a pulse duration of 9.0 μs.

DIPSHIFT profiles were recording using both CP and direct polarisation (DP) for the initial excitation procedure. For the ^{1}H-^{13}C CP DIPSHIFT experiment, the ^{1}H and ^{13}C nutation frequencies were 52.5 and 47.5 kHz, respectively. CP was achieved using a 70 to 100% ramp[175] on the ^{13}C channel for a contact time of 5 ms. Eight rotor periods of recoupling ($N = 8$) were used. 192 (CP) or 320 (DP) transients were co-added for 41 t_1 points corresponding to 40 μs t_1 increments up to 1.6 ms ($N\tau_r$) and a recycle delay of 2 s was used. The decoupling schemes for homonuclear and heteronuclear decoupling were FSLG[111,270] and SPINAL-64,[119] respectively, applied at a nutation frequency of 62.5 kHz.

For ^{1}H DQ experiments, the excitation and reconversion of ^{1}H DQ coherences was achieved using the POST-C7 recoupling method[109] at a ^{1}H nutation frequency of 35 kHz. For the ^{1}H DQ-^{1}H SQ experiment, 16 transients were co-added for each of 768 FIDs (with a t_1 increment of 28.6 μs using the States-TPPI[176] method to restore sign discrimination in the F_1 dimension), with a recycle delay of 2 s, corresponding to an experimental time of 6.8 hours. For ^{1}H DQ build-up curves, the DQ filtered (I_{DQ}) and reference (I_{ref}) experiments were recorded in an interleaved fashion. 64 transients were co-added for each of 27 values of τ_{DQ}, ranging from 0 to 4 ms (corresponding to $n_{rcpl} = 70$), with a recycle delay of 3 s corresponding to an experimental time of 2.9 hours. In order to have multiple points for fitting in the initial build-up region for ^{1}H resonances with the larger dipolar coupling constants, the individual elements of POST-C7 were incremented, rather than full POST-C7 cycles (corresponding to n_{rcpl} being a multiple of 7). For experiments with no DQ pre-selection (see pulse sequence in Section 7.4.3 below), DQ selection (more accurately for $4n + 2$ coherence orders, although the DQ coherence order can be assumed to be dominant) was performed using a four-step phase cycle for the reconversion block (0°, 90°, 180°, 270°) while inverting the receiver phase for alternating transients (0°, 180°, 0°, 180°), so as to select $\Delta p = \pm 2$, where p is the coherence order. A reference experiment was recorded in the same manner, however keeping the receiver phase constant. Including CYCLOPS on the final 90° detect pulse to select $\Delta p = \pm 1$, this results in a 16-step phase cycle. For the experiment with DQ pre-selection (see pulse sequence in Section 7.4.3), two independent four-step phase cycles were applied to the two DQ reconversion blocks, resulting in a 64-step phase cycle including CYCLOPS. For the reference experiment, the receiver phase alternation was omitted for only the second DQ reconversion block.

^{1}H and ^{13}C chemical shifts are referenced to TMS at 0 ppm using L-alanine as a secondary reference (1.1 ppm for the lower ppm ^{1}H resonance and 177.8 ppm for the higher ppm ^{13}C resonance), corresponding to adamantane at 1.85 ppm (^{1}H)[177] and 38.5 ppm (^{13}C).[178]

7.3.3 Simulations and Fitting

CP build-up and CP T_2-recDIPSHIFT curves were fit using a simplex minimisation implemented in the opt1.0 package in SIMPSON (v4.2.1).[114,271] Representative SIMPSON input files are included in Appendices E.1 and E.2. Powder averaging was performed for a set of 168 alpha and beta angles, using 10 gamma angles. The simulations used a 2-, 3-, or 4-spin system for fitting of CH, CH_2 and methyl build-up curves and DIPSHIFT profiles, respectively. The rigid-limit proton-carbon and proton-proton distances used to calculate order parameters were obtained from the DFT geometry optimised crystal structure of (2Z,6E)-3,6-dimethylocta-2,6-dien-1-oic

acid (CCDC ref. code CIQBEJ), a structural isomer of geranic acid. Fast methyl rotation was taken into account by multiplication of the rigid-limit dipolar coupling by the order parameter, S^2_{CH}, methyl = 0.111 or S^2_{HH}, methyl = 0.25, which are calculated assuming a tetrahedral C-H geometry ($\theta_{CH} = 109.5°$ and $\theta_{HH} = 90°$), according to $S^2_{\text{methyl}} = {}^1\!/_4(3\cos^2\theta - 1)^2$, where θ is the angle between the internuclear vector and the rotation axis. To investigate the effect of proton-proton couplings on simulated CP build-up curves, the proton-proton dipolar coupling was taken into account by assuming the same order parameter, S^2_{HH}, as S^2_{CH}, apart from methyl groups where the proton-proton dipolar couplings were scaled by $\sqrt{0.25/0.111}$ relative to the proton-dipolar coupling. The scaling factor introduced by FSLG decoupling in the DIPSHIFT experiments was accounted for by division of the obtained dipolar coupling by 0.577. The effects of relaxation were taken into account by the addition of a single exponential relaxation time as a second fitting parameter by multiplication of the numerical simulations by $\exp(\tau/T_{\text{relax}})$.

The 95% confidence intervals for the heteronuclear dipolar coupling were estimated by calculating the residual sum of squares (RSS) between the experimental and simulated build-up curves for a range of different dipolar couplings, where the relaxation parameter was optimised to minimise the RSS in each case. The 95% confidence interval is given as the set of dipolar couplings for which $RSS \leq RSS_{\text{min}}\left[1 + F^{0.05}_{1,n-p}/n - p\,\right]$, where RSS_{min} is the RSS between experimental and simulated curves for the best-fit curve, $F^{\alpha}_{p_1,p_2}$, is the upper α probability point of the F distribution with p_1 and p_2 degrees of freedom, n is the number of experimental points, and p is the number of fitting parameters (see Figure 7.5 for representative error analysis).[272–274] The error in peak intensities was estimated from the experimental noise.

7.4 Results and Discussion: CAGE Octanoic Acid

7.4.1 2D ^{1}H-^{13}C CP Heteronuclear Correlation MAS NMR

A 2D ^{1}H and ^{13}C CP-HETCOR MAS spectrum of CAGE-oct is shown in Figure 7.2. The spectrum was recorded at 273 K, as were all further NMR experiments reported in this chapter; this temperature is below the LC-to-isotropic transition temperature indicated by SAXS and polarising microscopy (see Chapter 6). Under 5 kHz MAS, all of the ^{13}C resonances are resolved. Using a relatively long contact time of 2.5 ms, only a single ^{1}H-^{13}C cross peak was observed for all carbons with a directly bound proton corresponding to the one-bond C-H connectivities. This indicates that the dipolar couplings are highly averaged by molecular motion, implying that CAGE-oct is a dynamic system which is undergoing rapid anion metathesis on the NMR timescale. For comparison, in rigid solids, cross peaks corresponding to

longer-range C-H proximities can already be observed at contact times of only 200 µs.[275]

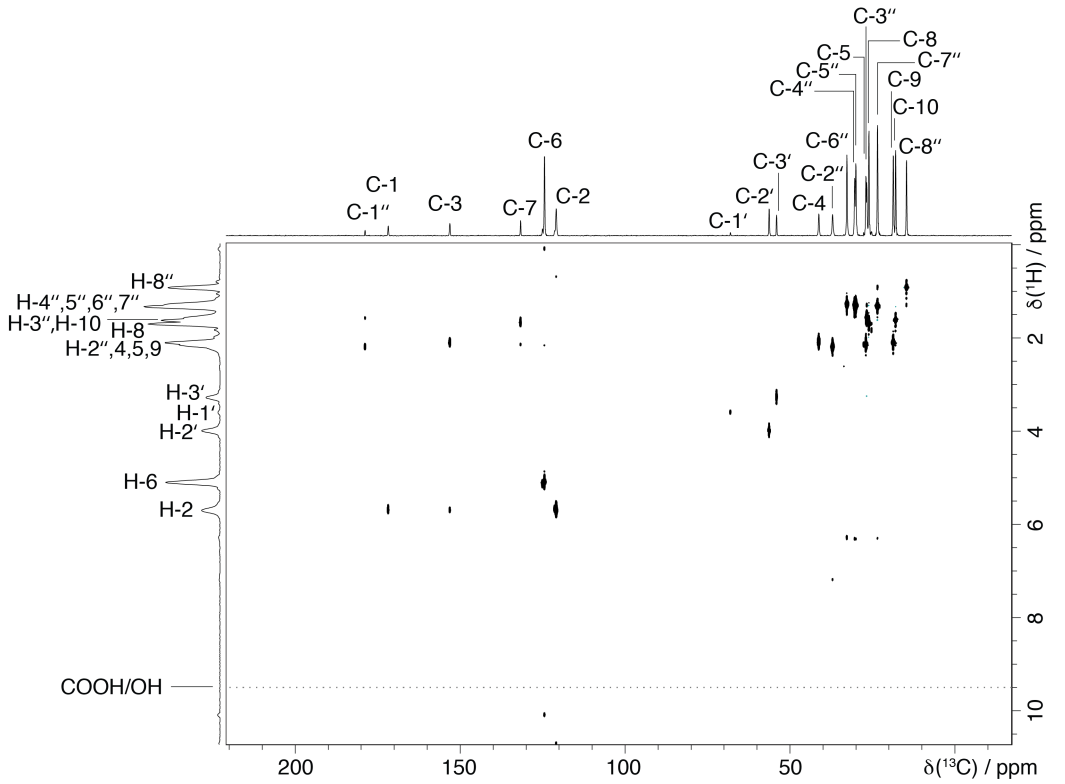

Figure 7.2: A ^{1}H-^{13}C HETCOR MAS NMR spectrum (ν_{0H} = 500 MHz, ν_{r} = 5 kHz) with skyline projections of CAGE-oct, recorded with a CP contact time of 2.5 ms at 273 K. The base contour level is at 3.9% of the maximum peak intensity. Note the absence of the COOH/OH resonance at $\delta(^{1}\mathrm{H})$ = 9.5 ppm (dotted line).

No contacts to the COOH/OH proton were observed despite the carbonyl carbons (C-1 and C-1″) showing a dipolar coupling to the protons of their adjacent carbon (H-2 and H-2″ respectively), which are expected to be located slightly further away than the acidic proton. This suggests that the absence of CP from the COOH/OH proton is due to motion of the exchangeable proton between the ions; i.e., the COOH and OH protons do not stay within close enough proximity of any one carbon for long enough for the observable build-up of ^{1}H-^{13}C CP signal to occur.

7.4.2 ^{1}H-^{13}C MAS NMR: C-H Dipolar Couplings

In order to investigate the molecular dynamics of CAGE-oct in the LC phase, CP build up curves were recorded to quantify the C-H dipolar couplings. The magnitude of the ^{1}H-^{13}C dipolar coupling is dependent on both the distance and orientation of the involved nuclei. For specific chemical moiety, e.g., a covalently bound C-H, there

is a fixed internuclear distance such that the measured dipolar couplings therefore report on the extent of averaging of the dipolar coupling by motions that are fast on the timescale of the NMR experiment (> 100 kHz). CP build up curves were recorded by incrementing the CP contact time up to a maximum of 2 ms (Figure 7.3). Clear oscillatory behaviour was observed for all of the CH and CH_2 groups of the geranate and octanoate with a maximum intensity occurring between 100-600 μs, whilst smoother curves with slower initial build-up and faster relaxation were observed for the methyl groups. Dipolar couplings for all carbons to their directly bonded protons were obtained by iterative least squares fitting to simulated build-up curves (using SIMPSON,[114,271] see Sections 7.3.3 and Appendix E.1) for a 2-, 3- and 4-spin system for CH, CH_2 and CH_3 groups respectively, excluding C-1′ and C-3′ of choline for which the CP intensity was too low to accurately obtain D_{res}.

The proton homonuclear interaction is known to remove oscillatory behaviour in CP build-up curves leading to an exponential CP build-up.[103,276] To investigate the influence of proton-proton dipolar couplings in CAGE-oct, CP build-up curves were simulated for a CH_2 group considering only a C-H dipolar coupling (3.96 kHz, the strongest dipolar coupling observed for C-2″) or also including the dominant proton-proton dipolar coupling between the methylene protons (3.81 kHz, assuming $S^2_{HH} = S^2_{CH}$) as seen in Figure 7.4. At 5 kHz MAS (as was used for experimental build-up curves), the inclusion of the proton-proton dipolar coupling between the methylene protons is shown to dampen the intensity of the oscillations slightly at long contact times but has little effect on the initial build-up and oscillation pattern at contact times up to the value recorded experimentally, of 2 ms. For systems with stronger dipolar couplings (e.g., rigid solid samples, or highly ordered LCs), more advanced versions of the experiment, such as Lee-Goldberg[111] (LG) CP,[112,113] are required, where the proton dipolar interaction is further suppressed by homonuclear decoupling methods. For the current system under study where the dipolar couplings are highly averaged by anisotropic motions to between ∼0-4 kHz, 5 kHz MAS is adequate to produce CP build-up curves with clear initial oscillations, and the use of LGCP is not required to quantify the heteronuclear dipolar coupling. The inclusion of proton-proton dipolar couplings in the fitting procedure (see Section 7.3.3 for details) was found to have no significant effect on the fits (Table 7.1 and Figure 7.4) and therefore only the CH dipolar coupling was included in the fitting. The inclusion of a single exponential relaxation time as a second fitting parameter also did not significantly alter the obtained value of D_{res} for most sites (Table 7.1), however a statistically significant improvement in the fit was obtained for some curves and the relaxation term was therefore included. The resulting best-fit curves are shown by the solid lines in Figure 7.3 and the dipolar couplings, which ranged from 0.88 to 3.96 kHz are given in Table 7.2.

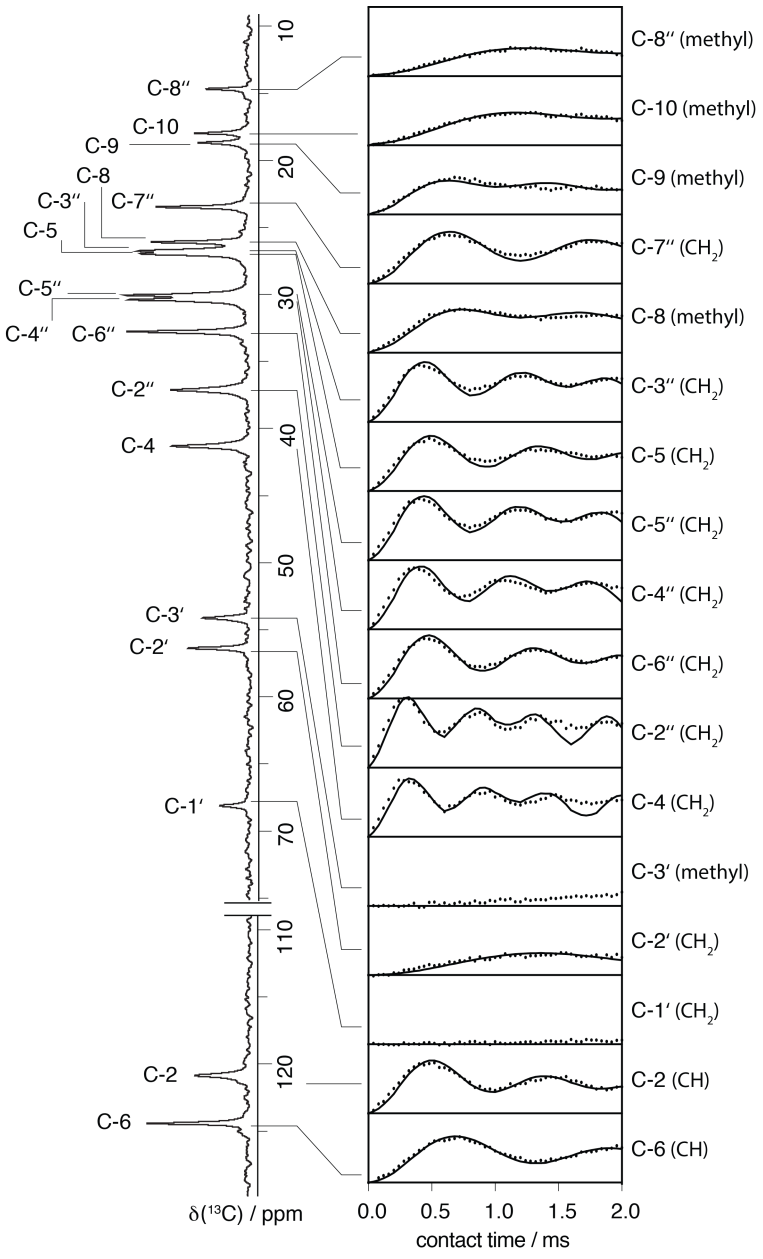

Figure 7.3: ^{1}H-^{13}C CP MAS NMR ($\nu_{0\mathrm{H}} = 500$ MHz, $\nu_{\mathrm{r}} = 5$ kHz) build-up curves for CAGE-oct. The best-fit simulations are depicted as solid lines for dipolar coupling constants, D_{CH}, reported in Table 7.2. The one-dimensional spectrum shown vertically was recorded with a CP contact time of 2.5 ms.

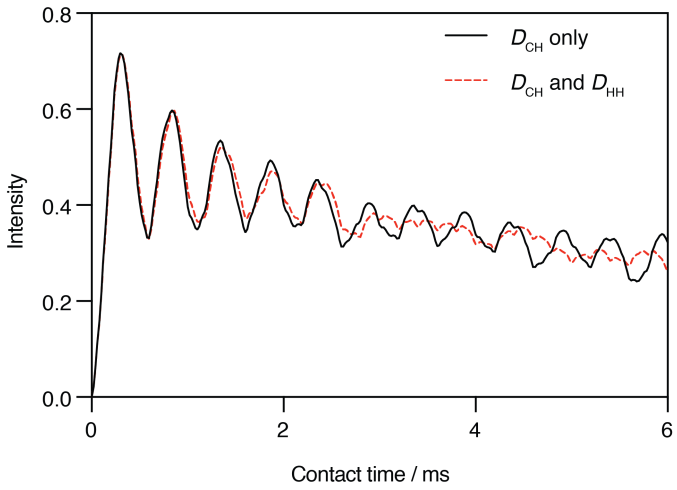

Figure 7.4: Simulated CP build-up curves for a CH_2 spin system with $D_{CH}/2\pi$ = 3.96 kHz, with no proton-proton dipolar couplings (black solid curve) or with $D_{HH}/2\pi$ = 3.81 kHz (red dashed curve).

Table 7.1: Results of fits of the experimental ^{1}H-^{13}C CP build-up curves for CAGE-oct. Fitting details are given in Sections 7.3.3.

		Fitting parameters					
		D_{CH}		D_{CH}, T_{relax}		D_{CH}, D_{HH}, T_{relax}	
Peak	Type	$D_{res}/2\pi^{a}$ / kHz	χ^2_ν	$D_{res}/2\pi^{a,b}$ / kHz	χ^2_ν	$D_{res}/2\pi^{a}$ / kHz	χ^2_ν
C-9	Methyl	1.71 ± 0.06	6.6	1.71 ± 0.06	6.6	1.74 ± 0.06	6.9
C-8	Methyl	1.6 ± 0.1	28	1.6 ± 0.1	28	1.6 ± 0.1	30
C-2″	CH_2	3.96 ± 0.07	41	3.95 ± 0.07	28	4.06 ± 0.07	23
C-4	CH_2	3.66 ± 0.09	33	3.67 ± 0.08	24	3.75 ± 0.08	20
C-2	CH	3.3 ± 0.1	54	3.27 ± 0.06	12	NA	NA
C-4″	CH_2	3.08 ± 0.06	27	3.08 ± 0.06	27	3.13 ± 0.06	23
C-10	Methyl	0.97 ± 0.03	8.2	0.97 ± 0.03	8.2	0.97 ± 0.03	8.2
C-5″	CH_2	2.83 ± 0.06	30	2.83 ± 0.06	29	2.86 ± 0.06	26
C-3″	CH_2	2.74 ± 0.07	28	2.75 ± 0.07	27	2.78 ± 0.07	25
C-8″	Methyl	0.92 ± 0.03	4.3	0.92 ± 0.03	4.3	0.92 ± 0.03	4.3
C-6″	CH_2	2.53 ± 0.04	24	2.53 ± 0.05	23	2.55 ± 0.05	22
C-5	CH_2	2.45 ± 0.07	32	2.45 ± 0.07	32	2.47 ± 0.07	39
C-6	CH	2.37 ± 0.06	17	2.41 ± 0.03	5.9	NA	NA
C-7″	CH_2	1.86 ± 0.03	15	1.86 ± 0.03	15	1.87 ± 0.03	15
C-2′	CH_2	0.88 ± 0.03	7.4	0.88 ± 0.03	7.4	0.88 ± 0.03	7.4
C-1′	CH_2	–[c]	–	–[c]	–	–[c]	–
C-3′	Methyl	–[c]	–	–[c]	–	–[c]	–

[a]Reported errors in D_{CH} give the 95% confidence intervals (see Section 7.3.3 for details, and Figure 7.5 for error analysis for a representative data set).

[b]$D_{res}/2\pi$ values for fits with parameters, D_{CH} and T_{relax}, are reported in Table 7.2 and are repeated here for comparison to the other fitting models.

[c]Too low to extract from the experimental data

Table 7.2: Results of fits of the experimental ^{1}H-^{13}C CP build-up curves (see Figure 7.3, as recorded at 273 K) and CP-T_2-recDIPSHIFT profiles (see Figure 3.7b, as recorded at 273 K) for CAGE-oct. Fitting details are given in Sections 7.3.3.

		CP build-up			CP-T_2-recDIPSHIFT			
Peak	Type	$D_{res}/2\pi^a$ / kHz	S^2_{CH}	χ^2_ν	$D_{res}/2\pi^a$ / kHz	S^2_{CH}	χ^2_ν	% isotropic
C-9	Methyl	1.71 ± 0.06	0.050 ± 0.003	6.6	1.12 ± 0.04	0.022 ± 0.001	1.5	2 ± 3
C-8	Methyl	1.6 ± 0.1	0.043 ± 0.004	28	1.09 ± 0.03	0.0204 ± 0.0008	1.5	32 ± 2
C-2″	CH_2	3.95 ± 0.07	0.0304 ± 0.0007	28	3.8 ± 0.2	0.028 ± 0.002	0.8	25 ± 5
C-4	CH_2	3.67 ± 0.08	0.0261 ± 0.0008	24	3.6 ± 0.2	0.025 ± 0.002	0.4	16 ± 4
C-2	CH	3.27 ± 0.06	0.0210 ± 0.0006	12	2.75 ± 0.06	0.0148 ± 0.0005	0.6	8 ± 2
C-4″	CH_2	3.08 ± 0.06	0.0184 ± 0.0005	27	3.00 ± 0.08	0.0175 ± 0.0007	0.5	21 ± 3
C-10	Methyl	0.97 ± 0.03	0.0161 ± 0.0008	8.2	0.78 ± 0.02	0.0105 ± 0.0004	0.5	45 ± 5
C-5″	CH_2	2.83 ± 0.06	0.0155 ± 0.0004	29	2.86 ± 0.04	0.0159 ± 0.0003	0.7	20 ± 3
C-3″	CH_2	2.75 ± 0.07	0.0147 ± 0.0005	27	2.76 ± 0.06	0.0148 ± 0.0005	0.3	22 ± 4
C-8″	Methyl	0.92 ± 0.03	0.0145 ± 0.0006	4.3	0.73 ± 0.03	0.0092 ± 0.0005	0.6	52 ± 3
C-6″	CH_2	2.53 ± 0.05	0.0125 ± 0.0003	23	2.57 ± 0.09	0.0128 ± 0.0006	1.7	23 ± 4
C-5	CH_2	2.45 ± 0.07	0.0117 ± 0.0005	32	2.40 ± 0.06	0.0112 ± 0.0004	7.0	21 ± 3
C-6	CH	2.41 ± 0.03	0.0114 ± 0.0002	5.9	2.24 ± 0.02	0.0098 ± 0.0001	0.5	23 ± 2
C-7″	CH_2	1.86 ± 0.03	0.0067 ± 0.0002	15	1.90 ± 0.03	0.0070 ± 0.0002	0.3	33 ± 2
C-2′	CH_2	0.88 ± 0.03	0.00150 ± 0.00008	7.4	0.88 ± 0.04	0.0015 ± 0.0001	0.2	69 ± 7
C-1′	CH_2	–[b]	–[b]	–	–[b]	–[b]	–	–
C-3′	Methyl	–[b]	–[b]	–	–[b]	–[b]	–	–

[a]Reported errors in D_{CH} give the 95% confidence intervals (see Section 7.3.3 for details, and Figure 7.5 for error analysis for a representative data set).

[b]Too low to extract from the experimental data

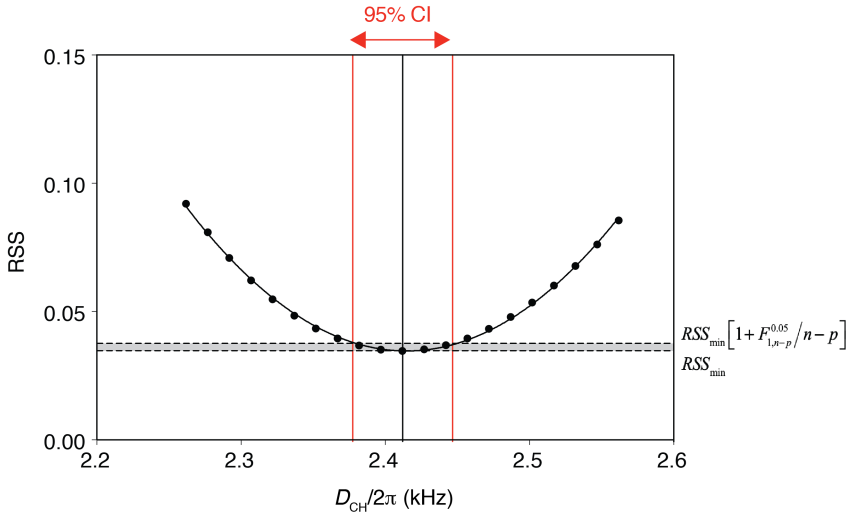

Figure 7.5: Determination of the 95% confidence interval (CI) for the C-H residual dipolar coupling for a representative data set D_{CH} for C-6 determined from CP build-up curves with fit-parameters D_{CH} and T_{relax}). The dipolar coupling was varied on either side of the best-fit dipolar coupling value, and the residual sum of squares (RSS), was calculated (with all remaining fit parameters optimised, i.e., T_{relax} in this case). $RSS = \sum_{i=1}^{n} \left(S_i^{\exp} - S_i^{\mathrm{sim}}\right)^2$, where n is the number of data points, and $S_i^{\exp}$ and S_i^{sim} are the signal intensities for the experimental and simulated build-up curves, respectively. The 95% CI, marked by red solid lines, is estimated as the set of dipolar couplings for which $RSS \leq RSS_{\mathrm{min}} \left[1 + F^{0.05}_{1,n-p}/n - p\right]$ as indicated by dashed lines. The number of data points $n = 51$, and the number of fit parameters $p = 2$ (D_{CH} and T_{relax}). The 95% CI for all C-H dipolar couplings, obtained from CP build-up curves and DIPSHIFT profiles were estimated using the same method.

In addition to the measurement of ^{1}H-^{13}C dipolar couplings by means of CP MAS NMR build-up curves, these were also determined by the dipolar chemical shift correlation (DIPSHIFT) method. As the CH dipolar couplings in CAGE-oct are relatively weak, a recoupled version of the original DIPSHIFT experiment was utilised, where the phase accumulated due to the evolution under the dipolar coupling during t_1 is amplified by a REDOR-like train of π pulses.[116] Further, a variant of the DIPSHIFT experiment reported by Cobo *et al.* was selected, where the evolution time under heteronuclear dipolar coupling is not constant (in contrast to frequently used constant time experiments), and a potential T_2 decay indicative of intermediate time-scale motions is possible.[266] The pulse sequence for the T_2-recDIPSHIFT experiment is shown in Figure 7.6. After excitation (CP or DP), the magnetisation evolves during a variable time t_1 under the influence of the heteronuclear dipolar interaction, whilst the ^{1}H homonuclear coupling is suppressed by FSLG decoupling. DIPSHIFT profiles are shown in Figure 3.7. The resulting DIPSHIFT profiles return to close to the initial maximum intensity at $t_1 = N\tau_r$, indicating that there are

no significant intermediate time-scale motions with rates between 1 to 100 kHz in CAGE-oct.[117,277] This confirms that the treatment of the reduction in the dipolar coupling described by the order parameter as providing information on the amplitude of fast motions is valid.

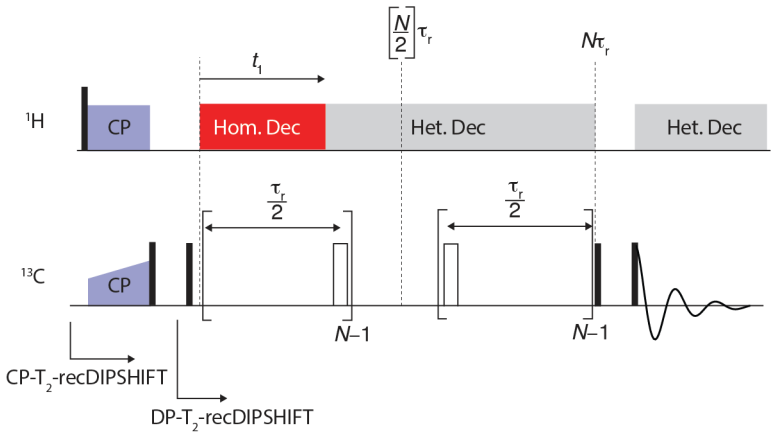

Figure 7.6: T_2-recDIPSHIFT pulse sequence.

DIPSHIFT experiments recorded with DP (Figure 7.7) produced curves that either could not be adequately fit to simulated curves or produced values of the dipolar coupling significantly smaller than those obtained from CP build-up curves. Since the signal $S(t_1)$ is normalised using $S(0)$, any isotropic (i.e. lacking RDCs) component could contribute to $S(0)$ but would not contribute to the phase accumulation due to the evolution under the dipolar coupling during t_1. Excitation of only the components exhibiting RDCs by CP, resulted in DIPSHIFT profiles which produced D_{CH} values in close agreement with those obtained from CP build-up curves (Figure 7.8 and Table 7.2). The amount of isotropic component was estimated by least squares fitting to obtain the scaling factor for $S(0)$ necessary to correct the normalisation procedure for the DP-DIPSHIFT profiles to agree with the best fit simulated CP-DIPSHIFT profiles. The values obtained (Table 7.2) were reasonably consistent between methylene carbons of both geranic and octanoic acid, at $23 \pm 5\%$ isotropic component. The difference between DP- and CP-DIPSHIFT profiles was greater for the terminal methyl groups (C-8, C-10 and C-8″), possibly due to additional isotropic motions of the terminal regions in parts of the sample. This analysis assumes that the difference between DP- and CP-DIPSHIFT profiles was due to completely isotropic components (i.e., $D_{CH} = 0$), rather than less ordered components where the CP had not significantly built up within the CP contact time of 5 ms.

The values of D_{res} obtained from fits of the CP-DIPSHIFT profiles are given in Table 7.2 and the resulting order parameters, S^2_{CH}, are graphically compared to those obtained from CP build-up curves in Figure 7.8. Overall, the two methods

produced values with very good agreement, within error for most of the sites. Notably, the largest discrepancies between the two methods were observed for the methyl groups (C-9, C-8, C-10 and C-8″). The CP build-up curves of the methyl groups (Figure 7.3) did not show clear oscillations as were observed for the CH and CH_2, which could account for slightly less accurate values.

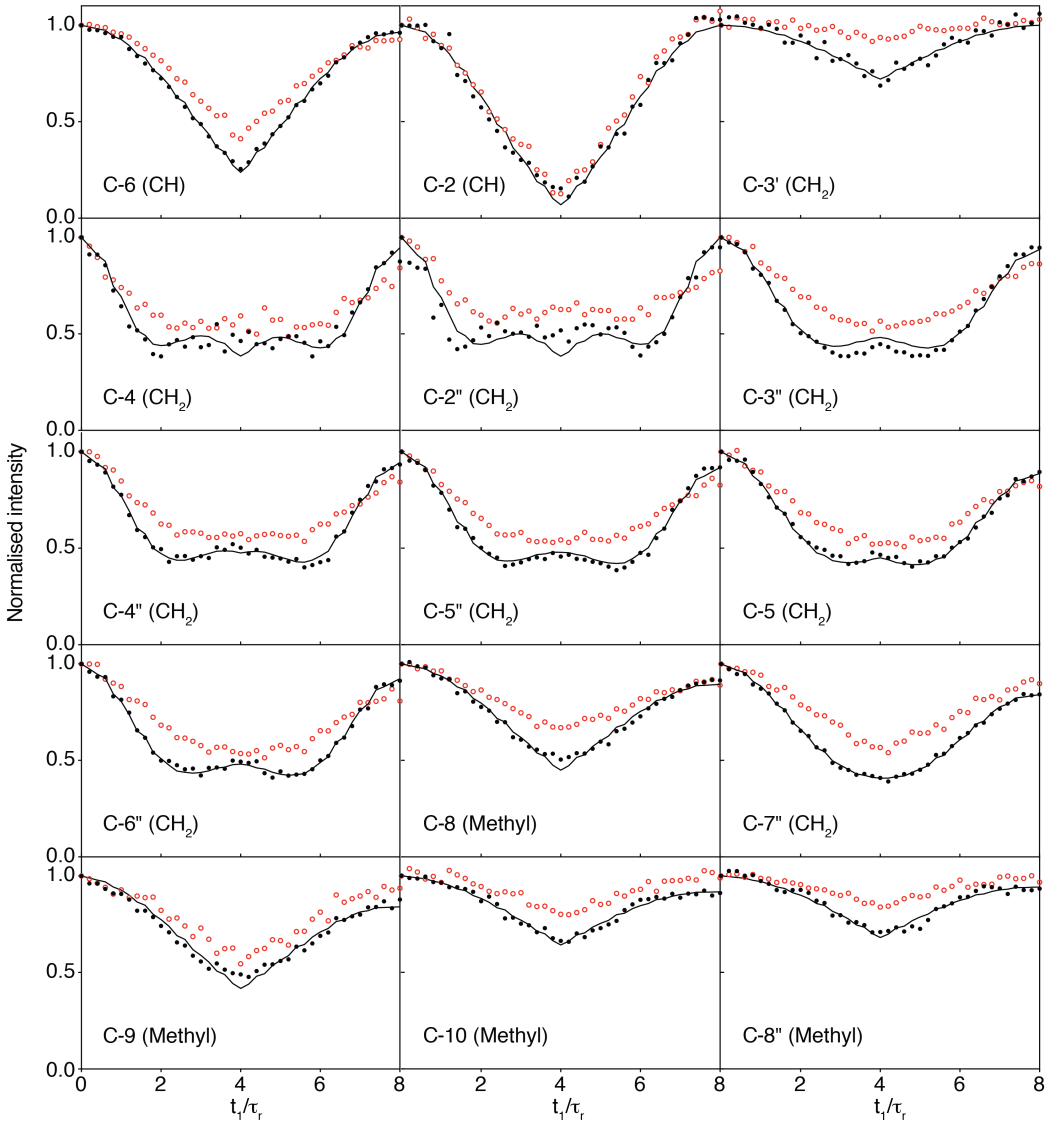

Figure 7.7: DIPSHIFT profiles ($\nu_{0H} = 500$ MHz, $\nu_r = 5$ kHz) for CAGE-oct recorded with DP (red open circles) or ^{1}H-^{13}C CP (black closed circles) and best-fit simulated curves for CP-T_2-recDIPSHIFT (black solid lines). DIPSHIFT profiles were recorded with 8 rotor periods of recoupling ($N = 8$) and FSLG ^{1}H homonuclear decoupling was applied during t_1.

CP-T_2-recDIPSHIFT experiments were also recorded at 253 and 243 K for CAGE-oct in the LC phase to determine if the order parameter, S^2_{CH}, changes with

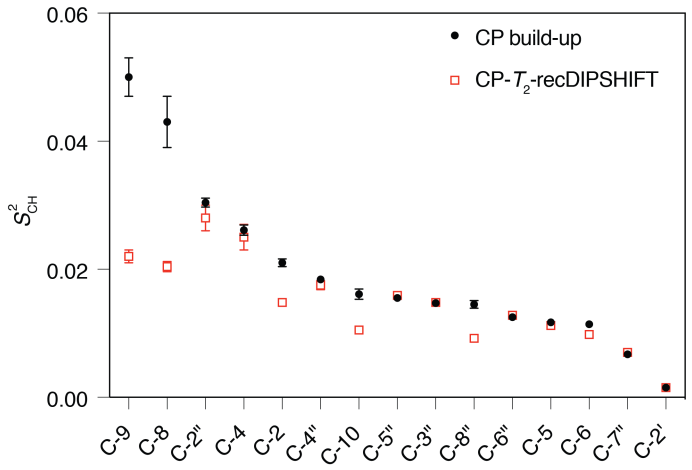

Figure 7.8: Comparison of S^2_{CH} obtained from CP build-up curves (Figure 7.3, Table 7.2) and CP-T2-recDIPSHIFT experiments (Figure 7.7, Table 7.2) at 273 K. The atom order corresponds to decreasing S^2_{CH} as determined from CP build-up curves.

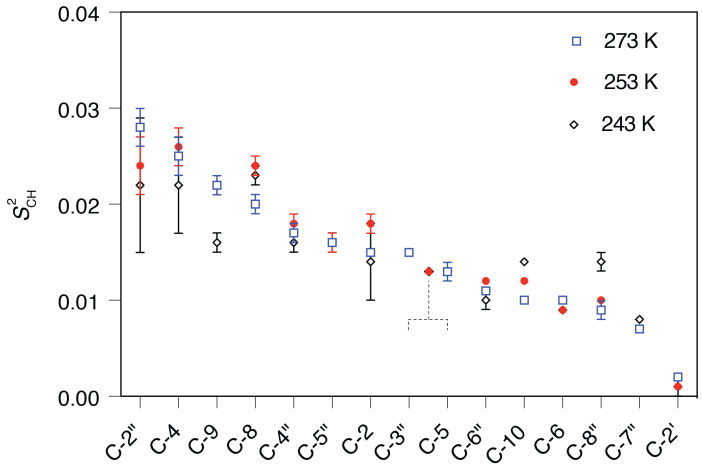

Figure 7.9: The temperature dependence of S^2_{CH} obtained from CP-T_2-recDIPSHIFT experiments. The atom order corresponds to decreasing S^2_{CH}. Order parameters recorded at 273 K are as shown in Figure 7.8 and repeated here for comparison to those at 253 and 243 K. A single value of S^2_{CH} is recorded for C-3″ and C-5 at 253 and 243 K (marked by the dashed line), as these resonances overlap at these temperatures.

temperature (Figure 7.9). Similar order parameters, within error for most sites, were obtained at all temperatures, indicating that the amplitude of motions does not change within this temperature range.

7.4.3 ^{1}H DQ Build-up Curves: H-H Dipolar Couplings

As shown in the previous section, dipolar couplings can be obtained from ^{1}H-^{13}C CP MAS NMR build-up curves, however, this method has some disadvantages due to the low signal-to-noise ratio of carbon detection and inaccuracies in the determination of the smaller coupling constants below 1 kHz. Therefore, the measurement of residual ^{1}H-^{1}H dipolar couplings by DQ MAS NMR was also conducted. This experiment has the advantage of usually good sensitivity due to the high natural abundance and gyromagnetic ratio of protons, and for highly mobile systems such as the LC under study, good resolution is achieved with low MAS frequencies. Small ^{1}H-^{1}H dipolar couplings, as low as 100 Hz, are also accessible from DQ build-up curves.

A 2D ^{1}H DQ-^{1}HSQ MAS NMR spectrum of CAGE-octanoic acid recorded at a MAS frequency of 5 kHz is presented in Figure 7.10. The excitation and reconversion of DQ coherence was achieved using the POST-C7[109] recoupling sequence. The 2D DQ spectrum correlates the single-quantum (SQ) chemical shifts of the constituents of the dipolar coupled spin pair with the chemical shift of the DQ coherence that is equal to the sum of the chemical shifts of the coupled spins. The alkene protons of the geranic acid (H-2 and H-6), the choline methylene protons (H-1′ and H-2′) and H-8″ are resolved and there are three distinct resonances for the remaining aliphatic protons, with overlap of the octanoic acid aliphatic protons (H-4″, 5″, 6″, 7″), protons H-2″, H4, H-5 and H-9 and the terminal methyl protons of geranic acid (H-8, H-10) with H-3″. The COOH/OH proton and the choline methyl proton (H-3′) are absent from the spectrum, indicating that they lack ^{1}H-^{1}H RDCs, consistent with observations of high mobility from ^{1}H-^{13}C CP MAS NMR experiments. The highest intensity peaks are the auto DQ cross-peaks between like-spins (i.e. protons within CH_2 and methyl groups) for all resonances excluding the alkene protons, for which DQ peaks are observed to the aliphatic region (H-2 to H-4 and H-6 to H-8 at 5.7 + 2.1 = 7.8 and 5.1 + 1.7 = 6.8 ppm, respectively).

The partially averaged ^{1}H-^{1}H dipolar couplings report on the amplitude of fast motions of the internuclear vector. The ^{1}H-^{1}H dipolar couplings and corresponding order parameters, S^2_{HH}, also offer complementary insight due to the different angle between the dipolar coupling and rotation axis as compared to ^{1}H-^{13}C. In order to extract the ^{1}H-^{1}H dipolar coupling constants, and the related order parameter, S^2_{HH}, DQ build-up curves were recorded by incrementing the τ_{DQ} of the excitation and reconversion blocks. Whilst relative dipolar couplings are accessible from the build-up of the DQ intensity,[120] intensity normalisation is necessary to obtain absolute values

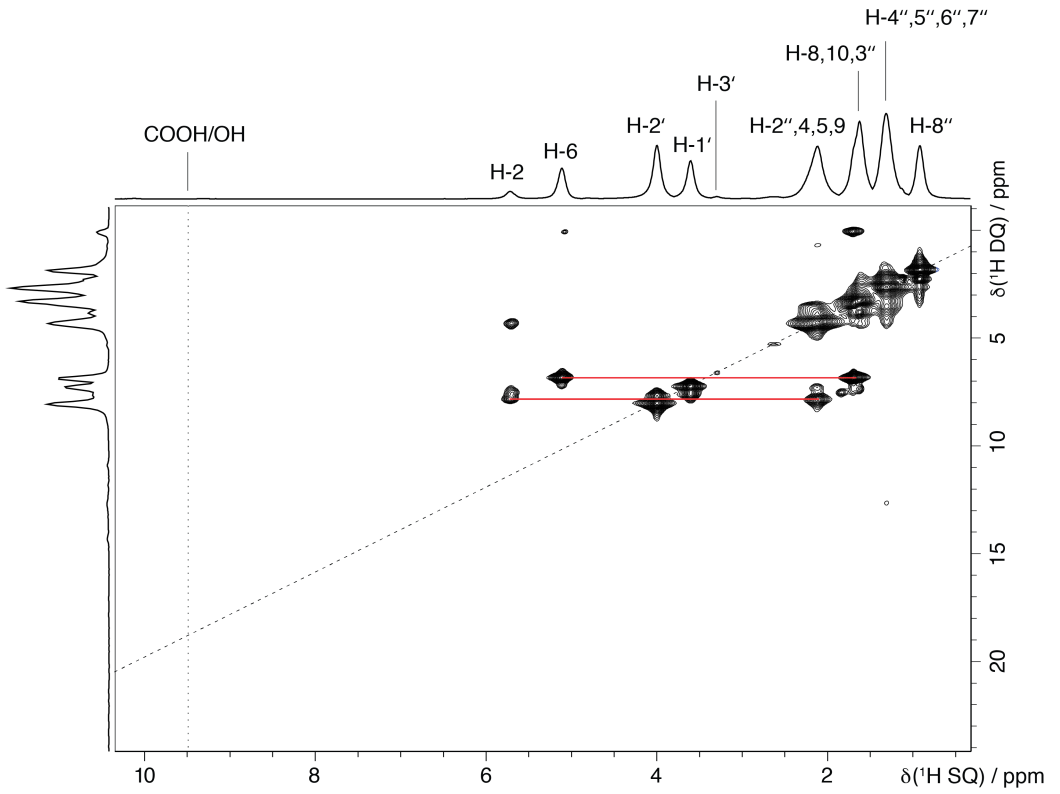

Figure 7.10: A ^{1}H DQ-^{1}H SQ MAS NMR spectrum ($\nu_{0\mathrm{H}} = 500$ MHz, ($\nu_{\mathrm{r}} = 5$ kHz) of CAGE-oct recorded with POST-C7 recoupling for $\tau_{DQ} = 1.2$ ms ($n_{rcpl} = 21$). Note the absence of the COOH/OH resonance at $\delta(^{1}\mathrm{H\ SQ}) = 9.5$ ppm (dotted line). H-H dipolar couplings between the COOH and OH protons, if present, would be observed at the intersection of the dotted line and diagonal (dashed line).

of the dipolar coupling.[121,122] This is achieved by recording a second analogous reference experiment, without the selection of DQ coherences by omitting the receiver phase alternation (for further phase cycling details see Section 7.3.2).[122,123] The sum of the DQ (I_{DQ}) and reference intensities (I_{ref}) is termed the multiple-quantum sum intensity, $I_{\Sigma MQ} = I_{DQ} + I_{ref}$.[122,123] The effect of relaxation is removed from the DQ build up by dividing the DQ intensity by the multiple-quantum sum intensity:

$$I_{nDQ} = \frac{I_{DQ}}{I_{\Sigma MQ}} \tag{7.1}$$

For further details on the normalised ^{1}H DQ build-up experiment, including the pulse sequence and fitting functions utilised to obtain D_{CH}, see Section 3.3.2.

The normalised DQ build-up curves for all ^{1}H peaks of CAGE-oct are shown in Figure 7.11c. The build-up curves do not reach the expected plateau level of 0.5 for any of the protons. This effect has previously been observed for elastomer systems and attributed to isotropically mobile components (short dangling chains

and solvent molecules).[122] Such liquid-like components contribute to the reference intensity, but not I_{DQ} (as they lack RDCs), meaning that the normalised intensity, InDQ, will be lower than expected. In some cases, it has been demonstrated that these components form more slowly relaxing long-time tails of I_{ref} which may be fit to an exponential and subtracted to produce a well-behaving normalised build-up curve reaching the 50% intensity plateau.[122] For CAGE-oct, the long-time relaxing component is similar in both the DQ and reference intensity (Figure 7.11a), and it was therefore not possible to unambiguously subtract an exponential tail from the reference curve. A method to solve this problem is based on the fact that in the long-time limit, where $I_{DQ} = I_{ref}$, the more mobile fraction may be identified and fitted in a plot of $I_{ref} - I_{DQ}$ vs. τ_{DQ} to:[124]

$$I_{ref} - I_{DQ} = B \exp(-\tau_{DQ}/T^*_{2,B}) \tag{7.2}$$

where B is the is the fraction of isotropic component, and $T^*_{2,B}$ is the apparent transverse relaxation time of the isotropic component. The exponential fits are shown in Figure 7.11b. The approximate percentage of isotropic component, determined from the y-intercept (B in Equation 7.2), range from 17 to 32 (Table 7.3), and are consistent with those calculated from the DIPSHIFT experiments (average 23%). Figure 7.11c shows the normalised build-up curves with the long-time exponential tail subtracted from the reference curve in this way, which reach the expected plateau of 0.5. Most of the build-up curves show a pronounced maximum, indicative of a narrow RDC distribution. The build-up curves were fitted to the"Abragam-like" build-up function (Equation 3.15) and the values of D_{res}, which range from 0.5 to 3.7 kHz, are given in Table 7.3.

In order to probe whether the lower than expected plateau (Figure 7.11a) is a result of liquid-like signal contributions (i.e., lacking orientational order), the experimental approach of DQ pre-selection was applied. Saalwächter *et al.* introduced this strategy as a means to suppress such unwanted contributions arising from dangling chain ends and solvent molecules in polymer networks, as an alternative to the exponential tail correction.[122] This strategy involves applying an additional fixed DQ excitation/reconversion block, followed by a z-filter delay, τ_z, preceding the incremented DQ pulse sequence of the original experiment (Figure 7.12a). The first block acts as a DQ pre-selection filter such that only dipolar-coupled components are selected. Application of the pre-selection filter results in an increased intensity of the DQ build-up curve relative to the reference curve (Figure 7.12b, c). The resulting normalised curves reach a maximum value of between 15 to 26% higher than the curves recorded with no DQ pre-selection filter and are significantly closer to reaching the expected plateau of 0.5. Fits to Equation 3.13 give $D_{res}/2\pi$ values comparable to those obtained from fits to data recorded without DQ pre-selection, following tail

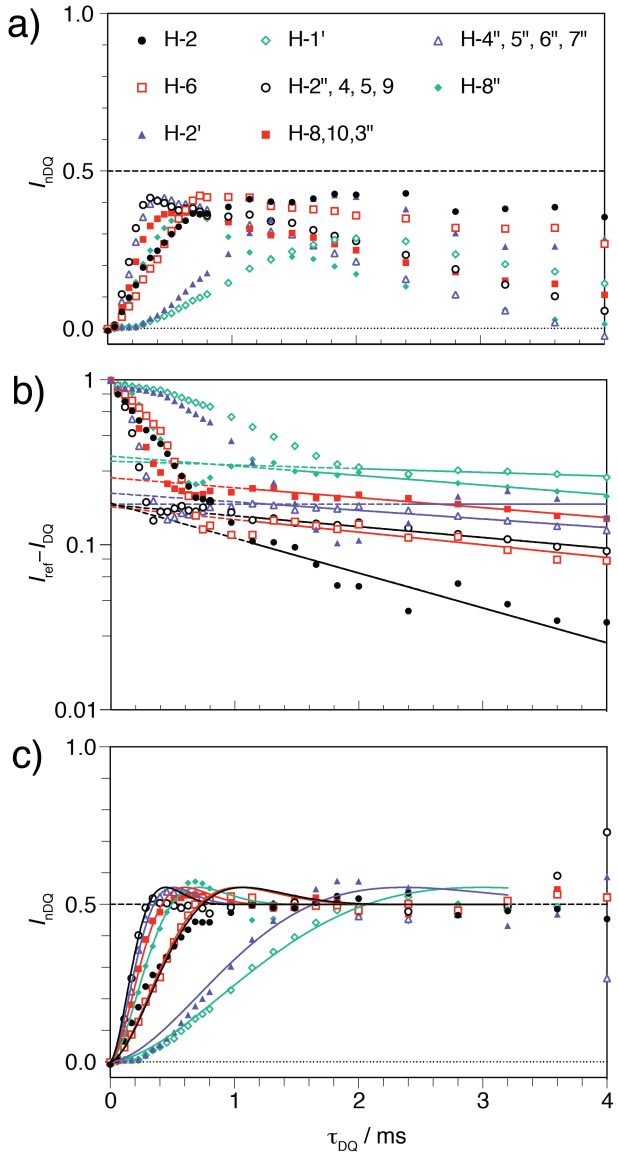

Figure 7.11: (a) Normalised ^{1}H DQ build-up curves for all resolved ^{1}H peaks of CAGE-oct with no tail subtraction. (b) $I_{ref} - I_{DQ}$ for all resolved ^{1}H peaks of CAGE-oct, plotted on a semilogarithmic scale. The lines are fits to $B\exp(-\tau_{DQ}/T^*_{2B})$ (solid portion of lines show the fitted tail region). The resulting exponential tail fits were subtracted from $I_{\Sigma MQ}$ to produce the normalised DQ build-up curves in (c). (c) Normalised ^{1}H DQ build-up curves for all resolved ^{1}H peaks of CAGE-oct with tail subtraction.

subtraction (Table 7.3). The difference between the DQ build-up curves with and without DQ pre-selection suggests that, within the liquid crystalline sample, there are some less ordered components (either unordered regions or individual ions/clusters within the ordered phase) that do not have RDCs or have very small RDCs and justifies the subtraction of the long-time tail from the data recorded with no DQ pre-selection. Isotropic regions were observed to exist in the LC phase of CAGE-oct by polarising optical microscopy, presented in Section 6.4.6. Further evidence of an isotropic component is provided by ^{1}H-^{13}C DIPSHIFT experiments recorded with either direct polarisation or ^{1}H-^{13}C CP, as discussed in Section 7.4.2. The estimated disordered component of approximately 23% from the DIPSHIFT experiments, is in agreement with the observations from ^{1}H DQ build-up experiments, and the presence of isotropic regions observed by polarising optical microscopy (see Chapter 6). The coexistence of liquid disordered/liquid ordered phases has previously been reported in a model membrane system and quantified by ^{1}H-^{13}C dipolar coupling MAS NMR.[278]

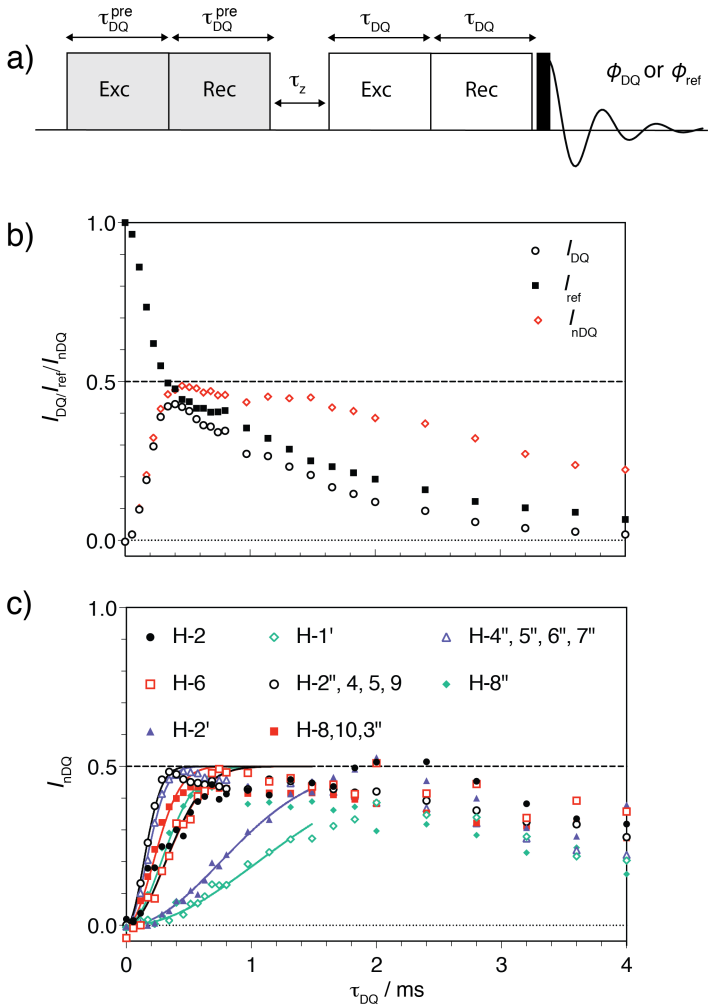

Figure 7.12: (a) Pulse sequences used to measure ^{1}H DQ build-up curves with DQ pre-selection. (b) DQ (I_{DQ}), reference (I_{ref}) and normalised DQ intensity (I_{nDQ}, see Equation 7.1) for a representative peak (H-4″-7″) of CAGE-oct. (c) Normalised ^{1}H DQ build-up curves for all resolved ^{1}H peaks of CAGE-oct, recorded with a pre-selection time $\tau_{DQ}^{pre} = 1.2$ ms ($n_{rcpl} = 21$) and z-filter delay, $\tau_z = 150$ ms. The solid lines are fits to the second-moment-based build-up function (Equation 3.13) up to $\tau_{DQ} = 1.6$ ms.

Table 7.3: Results of fits of the experimental ^{1}H DQ build-up curves for CAGE-oct (Figure 7.11c, recorded at 273 K) to the A-l build-up function (Equation 3.15), and ^{1}H DQ build-curves recorded with DQ pre-selection (Figure 7.12c, recorded at 273 K) to the second-moment-based build-up function (Equation 3.13).

		No DQ pre-selection, tail subtraction			DQ pre-selection
Peak	Dominant coupling	$D_{res}/2\pi$ / kHz	S^2_{HH}	% isotropic[a]	$D_{res}/2\pi$ / kHz
H-2″,4,5,9	CH_2 auto	3.7 ± 0.1	0.030 ± 0.002	17.5 ± 0.5	3.4 ± 0.2
H-4″,5″,6″,7″	CH_2 auto	3.21 ± 0.07	0.0229 ± 0.0007	17 ± 1	2.9 ± 0.1
H-8″	Methyl atuo	2.29 ± 0.06	0.0228 ± 0.0008	20.6 ± 0.6	1.7 ± 0.1
H-2	H-4 (CH to CH_2)	1.53 ± 0.06	0.023 ± 0.001	18 ± 3	1.51 ± 0.09
H-6	H-8 (CH to methyl)	1.58 ± 0.03	0.0207 ± 0.0005	25.5 ± 0.8	1.49 ± 0.05
H-8,10	Methyl atuo	2.72 ± 0.06	0.0164 ± 0.0005	34 ± 1	2.2 ± 0.1
H-2′	CH_2 auto	0.69 ± 0.02	0.00105 ± 0.00004	18 ± 2	0.629 ± 0.009
H-1′	CH_2 auto	0.546 ± 0.009	0.00066 ± 0.00002	32 ± 2	0.45 ± 0.01
H-3′	–[b]	–[b]	–	–	–[b]
COOH/OH	–[b]	–[b]	–	–	–[b]

[a]The % isotropic component is determined from B in Equation 7.2
[b]No build-up of DQ coherence was detected

7.4.4 S^2_{CH} and S^2_{HH} Order Parameters

Order parameters, S^2_{CH} and S^2_{HH}, were calculated as the squared ratio of the motionally averaged dipolar coupling to the rigid limit value and are reported in Table 7.2 and 7.3, respectively. The order parameters are assigned a colour based on their range to show the structural correlation in Figure 7.13. Since the dipolar coupling depends on orientation according to $^1/_2(3\cos^2\theta - 1)$ (see Section 2.3.4), S^2 reports on the amplitude of fast motions (of the ions and molecular segments/bonds). S^2_{CH} ranged from ∼0 to 0.05 while S^2_{HH} ranged from 0 to 0.03 (in comparison to $S^2 = 1$ for a rigid system). These order parameters are significantly lower compared to those of smectic phases of non-ionic LCs, which typically display order parameters of 0.2-0.6[279–281] and are rather similar to those reported for lamellar phases formed by lyotropic mesogen/solvent systems.[88,282,283] Highly disordered alkyl chains corresponding to low orientational order parameters have been found for other ILCs.[251,268,269,284] The differences in order parameters between conventional non-ionic LCs and ILCs such as CAGE-oct can be attributed to differences in the molecular structures and nature of the intermolecular interactions which are the driving forces for mesophase formation. Non-ionic LCs typically contain a rigid (usually aromatic) core and one or more flexible chains, with the LC phase stabilised by dispersion forces.[31] ILCs on the other hand consist of ions, one of which usually contains a long ($n > 8$) alkyl chain, and typically form smectic phases stabilised by electrostatic (Coulombic) interactions within ion-rich layers, and, in some cases (likely the case for CAGE-oct), hydrogen bonding.[285]

Distinct motional amplitudes were observed between the choline cation compared to the anions, and also within the ions. From the trends in these order parameters, conclusions on the structure as well as dynamics can be drawn. Choline showed lower order parameters compared to those of geranate and octanoate, indicating increased mobility. Of the choline carbons, the CH_2 adjacent to the hydroxyl group, C-2′, showed the highest order parameter, $S^2_{CH} = 0.00150$. In comparison, the adjacent CH_2 group, C-1′, and the choline methyl group, C-3′, showed much smaller dipolar couplings, indicating nearly isotropic freedom of motion ($S^2_{CH} \sim 0$) of the choline head group. The ^{1}H-^{1}H RDC for the choline methylene group H-1′ for which the corresponding ^{1}H-^{13}C RDC was too low to accurately determine from the CP build-up curves, was determined to be 546 Hz, corresponding to $S^2_{HH} = 0.00066$. It is noted that the calculated order parameters consider only the dominant dipolar coupling, the auto coupling between the methylene protons, for D_{rigid}, whilst the measured RDC is an averaged value of all couplings. Taking into account the additional weak coupling between the H-1′ and H-2′ protons on adjacent methylene groups, as observed in the 2D ^{1}H DQ-^{1}H SQ NMR spectra would result in only a very slight reduction of S^2_{HH}. The trend in S^2_{HH} for the choline protons, increasing

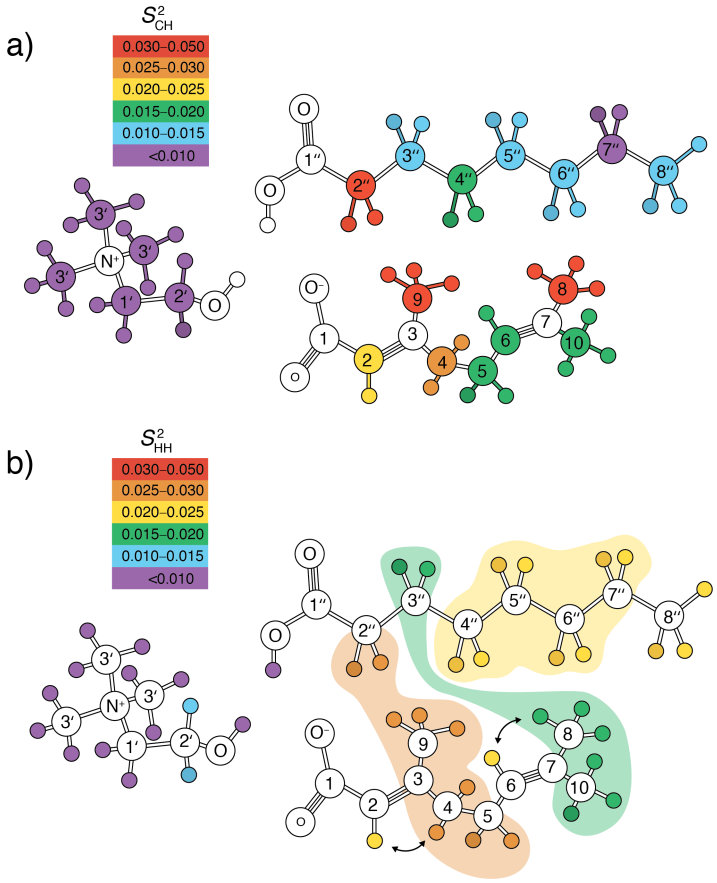

Figure 7.13: Schematic representation of site-specific order parameters, (a) S^2_{CH} and (b) S^2_{HH} for CAGE-oct. In (a), S^2_{CH} is the order parameter for each carbon and its covalently bonded proton(s) determined by CP build-up curves. In (b), S^2_{HH} is the order parameter between protons within individual methylene or methyl groups, apart from H-2 and H-6, for which the dominant dipolar couplings are shown by arrows. The highlighted groups of protons in (b) indicate protons with overlapping peaks in the 1D ^{1}H MAS NMR spectrum, and as such only a single S^2_{HH} was determined for these groups of protons.

from $S^2_{HH} =\sim 0$ (H-3′; no build-up of DQ coherences observed) to 0.00066 (H-1′) and 0.00105 (H-2′) agrees with the conclusions based on the ^{1}H-^{13}C RDCs exhibiting an increasing degree of motion from the hydroxyl group to the -N$(CH_3)_3$ head group. The hydroxyl end of the molecule is likely 'anchored' by hydrogen bonding to the geranate and octanoate. This suggests that hydrogen bonding between all three constituent parts, rather than a purely electrostatic interaction, is critical to understanding the structure of CAGE-oct, consistent with strong evidence of hydrogen bonded [(choline)(geranate)(H)(octanoate)], [(choline)$(octanoate)_2$(H)] and [(choline)$(geranate)_2$)(H)] clusters from mass spectrometry and ^{1}H MAS NMR (see Chapter 6). The choline head group can be envisioned to reorient as it changes hydrogen bonding partners in the dynamic smectic phase. The order parameters are comparable to those obtained for the choline head group in aqueous phospholipid lamellar phases. For example, Hong *et al.* reported S^2_{CH} values for the choline head group of phosphatidylcholine (PC) in the fluid lamellar (L_α) phase of magnitude 2.4×10^{-5} (γ corresponding to C-3′) and 0.0016 (α and β corresponding to C-1′ and C-2′),[88,286] corresponding to purple on the scale in Figure 7.12. Notably, the choline head group is covalently attached via the oxygen in PC, yet the adjacent α proton displays a remarkably similar order parameter to the equivalent C-2′ of the 'free' choline in CAGE-oct ($S^2_{CH} = 0.0015$ for CAGE-oct and 0.0016 for PC), further suggesting strong hydrogen-bonding of the choline cation to geranate/octanoate. It is noted that some studies report the order parameter, S, in contrast to S^2; the values of S reported by Hong *et al.* have been squared, in order to to obtain S^2 for comparison to this study.

The S^2_{CH} of the aliphatic chain protons of geranate and octanoate are generally lower at the terminal end compared to those closest to the carboxylic acid group. S^2_{CH} of the methylene groups of octanoic acid vary between 0.0304 at C-2″ to 0.0067 at C-7″, whilst those of the geranate backbone show similar values and are again slightly higher at the backbone carbons closest to the carboxyl group (C-2 and C-4, compared to C-6 and C-10; Figure 7.13a). The methyl groups branching from the main chain of geranic acid, C-9 and C-8, have the highest S^2_{CH}, which could result from the C-H vectors being more closely aligned with the long molecular axis of geranic acid, which would result in the least averaging due to axial rotation of the molecule about the long axis. The S^2_{HH} for the overlapping octanoic acid alkyl chain protons H-4″-7″ of 0.0229 is close to the highest S^2_{CH} obtained for these carbons ($S^2_{CH} = 0.0184$ for C-4″), as expected since the strongest dipolar couplings will dominate the build-up of DQ coherences. The S^2_{HH} of 0.030 for protons H-2″, 4, 5, and 9 agrees with S^2_{CH} of 0.0304 of C-2″. As for choline, the order parameters of the alkyl chains resemble those of lyotropic phospholipid systems; which range from ∼0.06 to 0.0004 along the acyl tail of PC in the L_α phase (corresponding to red to

purple, on the scale in Figure 7.13).[286] Overall, for CAGE-oct, S^2_{HH} and S^2_{CH} are observed to provide the same information about the dynamics of the system (Figure 7.13).

7.5 Results and Discussion: CAGE

As mentioned in Section 6.4.1, CAGE also showed a LC phase at temperatures below 5 °C. This ordered phase of CAGE was further investigated using the same methods discussed above for CAGE-oct: ^{1}H-^{13}C CP MAS NMR build-up curves, DIPSHIFT and ^{1}H DQ build-up curves.

7.5.1 ^{1}H-^{13}C MAS NMR: C-H Dipolar Couplings

CP build-up curves for CAGE are shown in Figure 7.14, and appear very similar to those of geranic acid/geranate and choline of CAGE-oct. As for CAGE-oct (Figure 7.3), clear oscillations were observed for the CH and CH_2 carbons of geranic acid/geranate, indicative of dominant CH dipolar couplings and sufficient removal of proton-proton dipolar coupling by MAS. A very low CP efficiency for choline indicates almost isotropic reorientation, and as such only D_{CH} and S^2_{CH} of the geranic acid/geranate was obtained. The order parameters, which range from ∼0 to 0.063 are similar to those observed in CAGE-oct.

T_2-recDIPSHIFT profiles for CAGE (Figure 7.15) show significant differences to those for CAGE-oct (Figure 7.7). Firstly, those recorded with direct ^{13}C polarisation, show almost no dephasing during the recoupling time. This suggests that a significant proportion of the sample does not have residual dipolar couplings and is isotropic. Secondly, the DIPSHIFT profiles recorded with initial CP from ^{1}H to 13C, which selects only the ordered proportion of the sample, shows the characteristic dephasing and loss of signal of DIPSHIFT profiles, however the signal is not completely refocussed at $t_1 = N\tau_r$, and only reaches approximately 50% of the initial ($t_1 = 0$) signal intensity. This could be due to a shorter apparent T_2 times in CAGE due to slow motions, or possible intermediate-timescale motions for which destructive interference of the molecular dynamics under MAS rotation has been shown to result in the depashing curve intensity not reaching its initial value.[266] Fits to the CP-T_2-recDIPSHIFT profiles produced D_{CH} and S^2_{CH} values in close agreement to those obtained from the CP build-up curves (Table 7.4), with the exception of the methyl groups.

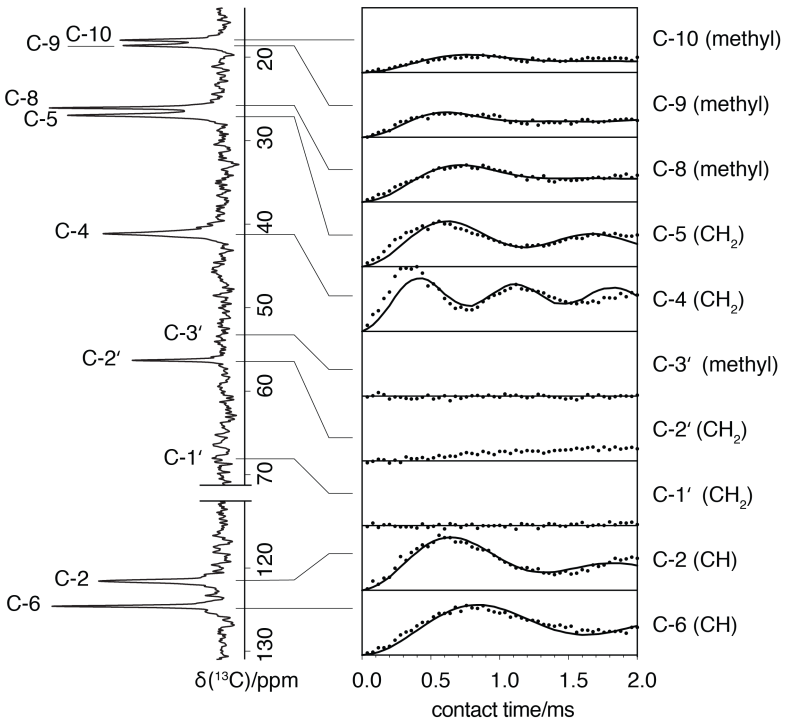

Figure 7.14: ^{1}H-^{13}C CP MAS NMR ($\nu_{0\mathrm{H}} = 500$ MHz, $\nu_{\mathrm{r}} = 5$ kHz) build-up curves for CAGE. The best-fit simulations are depicted as solid lines for dipolar coupling constants, D_{CH}, reported in Table 7.4.

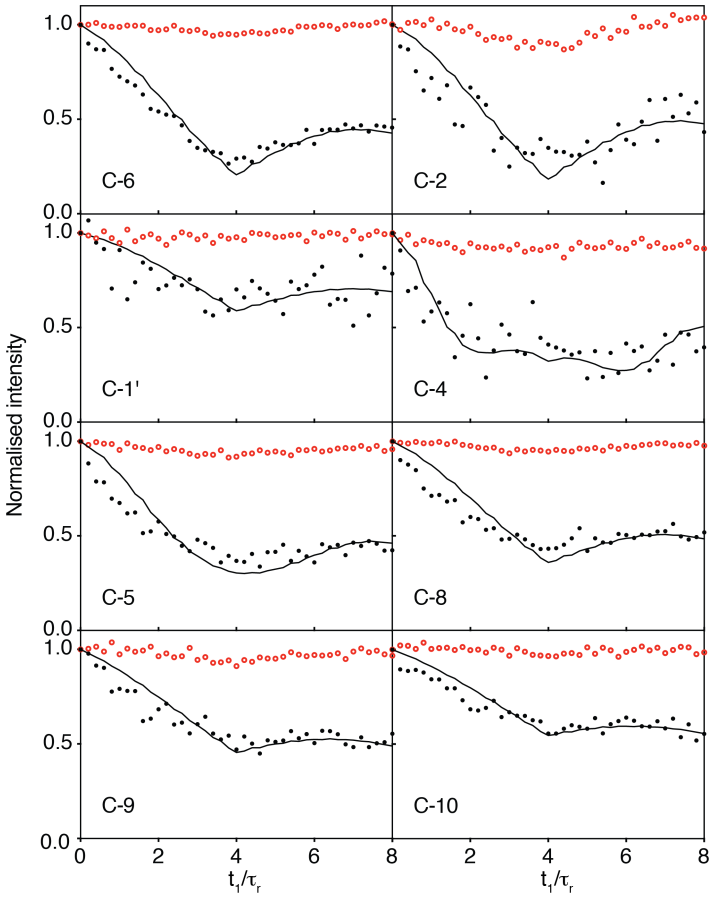

Figure 7.15: DIPSHIFT profiles ($\nu_{0H} = 500$ MHz, $\nu_r = 5$ kHz) for CAGE recorded with DP (red open circles) or ^{1}H-^{13}C CP (black closed circles) and best-fit simulated curves for CP-T2-recDIPSHIFT (black solid lines). DIPSHIFT profiles were recorded with 8 rotor periods of recoupling ($N = 8$) and FSLG ^{1}H homonuclear decoupling was applied during t_1.

Table 7.4: Results of fits of the experimental ^{1}H-^{13}C CP build-up curves and CP-DIPSHIFT profiles for CAGE. Fitting details are given in Sections 7.3.3.

		CP build-up			DIPSHIFT		
Peak	Type	$D_{res}/2\pi$ / kHz	S^2_{CH}	χ^2_ν	$D_{res}/2\pi$ / kHz	S^2_{CH}	χ^2_ν
C-9	Methyl	1.90 ± 0.09	0.063 ± 0.004	1.9	0.81 ± 0.11	0.011 ± 0.002	1.4
C-8	Methyl	1.63± 0.06	0.045 ± 0.002	2.8	1.02 ± 0.13	0.018 ± 0.003	2.0
C-10	Methyl	1.5 ± 0.1	0.040 ± 0.003	2.2	0.69 ± 0.09	0.008 ± 0.001	0.9
C-4	CH_2	2.9 ± 0.1	0.017 ± 0.001	34	3.38 ± 0.51	0.022 ± 0.005	4.2
C-2	CH	2.44 ± 0.06	0.0117 ± 0.0005	7.0	2.18 ± 0.26	0.009 ± 0.002	5.1
C-6	CH	1.96 ± 0.05	0.0076 ± 0.0002	7.0	2.06 ± 0.14	0.0083 ± 0.0008	1.2
C-5	CH_2	1.92 ± 0.06	0.00723 ± 0.00036	9.9	1.81 ± 0.64	0.006 ± 0.003	2.6
C-1′	CH_2	–[a]	–[a]	–	0.92 ± 0.21	0.0016 ± 0.0005	3.9
C-2′	CH_2	–[a]	–[a]	–	–[a]	–[a]	–
C-3′	Methyl	–[a]	–[a]	–	–[a]	–[a]	–

[a]Too low to extract from the experimental data

7.5.2 ^{1}H DQ Build-up Curves: H-H Dipolar Couplings

^{1}H DQ Build-up Curves for CAGE are shown in Figure 7.16. As for CAGE-oct, no DQ coherences where detected for the COOH/OH proton, or the methyl protons of choline (H-3′). The normalised build-up curves for the remaining protons reach a maximum value between 0.15-0.25, significantly lower than the predicted value of 0.5 (Figure 7.16a). As discussed in Section 7.4.3, this is likely due to an isotropic component, which, in agreement with DP-DIPSHIFT experiments, is higher than in CAGE-oct. A rough estimate of the isotropic component obtained from exponential fits to the tail (Equation 7.2) ranged from 43 to 51% (Table 7.5). The normalised curves were corrected to remove the isotropic component by subtraction of an exponential tail (Figure 7.16b), to produce normalised curves that plateau at 0.5 (Figure 7.16c). The curves did not show as pronounced maxima as for CAGE-oct, possible indicating a wider distribution of dipolar couplings, and the initial build-up region was best fit to Equation 3.13, based on the second-moment approximation. The values for D_{HH} and corresponding order parameters, S^2_{HH}, are given in Table 7.5. S^2_{HH}, are between 0.0106 and 0.0168 for geranic acid/geranate, and considerably lower for choline ($\sim$0 and 0.000079).

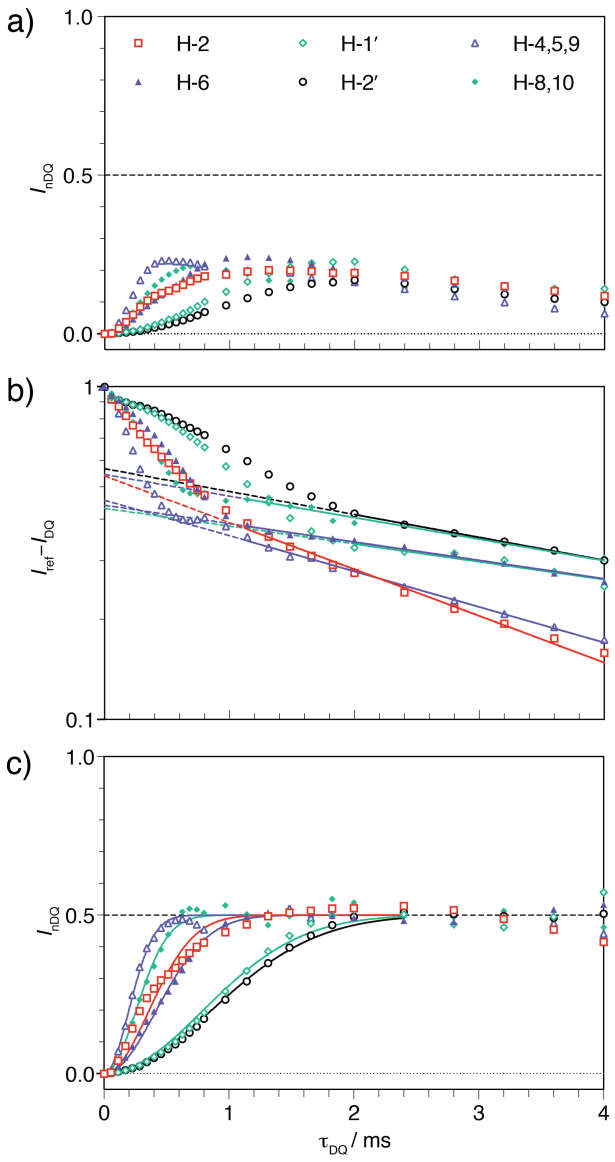

Figure 7.16: (a). Normalised ^{1}H DQ build-up curves for all resolved ^{1}H peaks of CAGE with no tail subtraction. (b) $I_{ref} - I_{DQ}$ for all resolved ^{1}H peaks of CAGE, plotted on a semilogarithmic scale. The lines are fits to $B\exp(-\tau_{DQ}/T_2^*)$ (solid portion of lines show the fitted tail region). The resulting exponential tail fits were subtracted from $I_{\Sigma MQ}$ to produce the normalised DQ build-up curves in (c). (c) Normalised ^{1}H DQ build-up curves for all resolved ^{1}H peaks of CAGE with tail subtraction. The solid lines in are fits to the A-l build-up function (Equation 3.15) up to $\tau_{DQ} = 2.4$ ms.

Table 7.5: Results of fits of the experimental ^{1}H DQ build-up curves for CAGE (Figure 7.16c, recorded at 273 K) to the A-l build-up function (Equation 3.15)

Peak	Dominant coupling	$D_{res}/2\pi$ / kHz	S^2_{HH}	% isotropic$-^a$
H-2	H-4 (CH to CH_2)	1.31 ± 0.04	0.0168 ± 0.0008	48 ± 1
H-8,10	Methyl atuo	1.85 ± 0.05	0.0148 ± 0.0005	51 ± 1
H-4,5,9	CH_2 auto	2.38 ± 0.06	0.0125 ± 0.0004	44.4 ± 0.5
H-6	H-8 (CH to methyl)	1.13 ± 0.01	0.0106 ± 0.0002	46.6 ± 0.8
H-1′	CH_2 auto	0.598 ± 0.009	0.00079 ± 0.00002	43 ± 3
H-2′	CH_2 auto	0.551 ± 0.005	0.00067 ± 0.00001	56.7 ± 0.6
H-3′	$-^b$	$-^b$	–	–
COOH/OH	$-^b$	$-^b$	–	–

[a]The % isotropic component is determined from B in Equation 7.2
[a]No build-up of DQ coherence was detected

7.6 Conclusions

In this chapter, the liquid crystalline phases of CAGE and CAGE-oct were investigated by MAS NMR, which provides information about the mobility and degree of ordering of the individual ions and molecular segments which is not accessible from other techniques such as SAXS. The dynamic order parameters, S^2_{CH} and S^2_{HH}, in the range 0 to 0.05, indicate a highly mobile LC phase for both ILCs, with the obtained ordered parameters being considerably lower than those reported for typical non-ionic LCs, and instead resembling those of aqueous phospholipid bilayer systems. The increased mobility toward the terminal ends of geranate and octanoate (for CAGE-oct) alkyl chains, and the choline -N(CH_3)$_3$ head-group are consistent with hydrogen bonding of the choline cation and anions and indicate that the CAGE and CAGE-oct LCs consist of mobile ionic-rich layers, and regions of fluid alkyl chains. The coexistence of an isotropic component (approximately 23% of the sample for CAGE-oct, and 50% for CAGE) was also detected within the LC phases. This chapter shows that MAS NMR is a highly promising tool for studying the site-specific structure and dynamics of mesogens, utilizing heteronuclear techniques such as the build-up in ^{1}H-^{13}C CP or ^{1}H DQ MAS NMR experiments.

Chapter 8

VT ^{1}H and ^{13}C MAS NMR Relaxation Measurements to Investigate Dynamics in an Ionic Liquid Crystal

8.1 Abstract

The measurement of NMR relaxation rates is a powerful method to obtain information on dynamics. In this chapter, variable temperature (VT) ^{1}H R_1 relaxation rates, in addition to ^{13}C R_1, $R_{1\rho}$ relaxation rates and ^{1}H-^{13}C NOE factors at two magnetic fields, ν_{0H} = 500 and 700 MHz, are reported for CAGE-oct. The ^{13}C relaxation rates were analysed using a number of model-free approaches of increasing complexity, with the aim of characterising the complex dynamics of the LC phase of CAGE-oct. Initial estimates of order parameters, correlation times and activation energies were obtained using the simple model-free (SMF) and extended model-free (EMF) formalisms, which assume motions on one or two time-scales, respectively. An improved fit was found by utilising the SMF approach combined with overall anisotropic molecular tumbling. This allows determination of the parameters describing global anisotropic molecular tumbling, $D_{\perp}$, $D_{||}$, $E_{a,\perp}$ and $E_{a,||}$, and the parameters describing local internal motions, S_i^2, τ_i and $E_{a,i}$. Notable differences in the reorientation dynamics of the choline cation and carboxylate anions are observed. Additionally, the presence of slower motions occurring in the CAGE-oct LC is probed by ^{13}C $R_{1\rho}$ relaxation dispersion (RD) measurements. However, no motions on the μs-ms timescale of significant amplitude are detected at 273 K. These results complement the measurement of RDCs presented in Chapter 7, providing additional information on the dynamics of the CAGE-oct ILC.

8.2 Introduction

In Chapter 7, through the measurement of RDCs and order parameters, it was demonstrated that CAGE-oct is a highly dynamic ILC. The obtained order parameters provide valuable information on the degree of order of the various ions and molecular segments/bonds. However, the order parameters are composed of contributions from motions on different timescales (provided that they are sufficiently fast to reduce the measured dipolar coupling, i.e., on timescales up to the inverse of the interaction strength, in the kHz range). In LCs, such motions are expected to include axial rotation of the molecules around the long molecular axis as well as internal motions (e.g., *trans-gauche* isomerisations). It is not possible to separate the contributions from various motions from the RDCs alone (without making assumptions about the geometry and amplitude of individual motions). The timescale of fast motions cannot be quantified from the RDCs, and slow motions, which do not reduce the dipolar couplings, are not accessible. This chapter aims to fill in these gaps, presenting a further investigation of the complex dynamics of the CAGE-oct LC through the measurement and fitting of NMR relaxation rates.

The measurement of NMR relaxation rates offers access to site-specific details of the dynamics over a wide range of timescales, from ps to ms (see Section 2.4 for further details on the theory of nuclear spin relaxation). Different relaxation measurements are sensitive to particular timescales; for example, R_1 (ps to ns timescale), $R_{1\rho}$ (ns to ms) and $R_{1\rho}$ RD (µs to ms timescale). Various thermally-activated motions dominate certain relaxation rates at different temperatures; variable-temperature (VT) measurements therefore provide additional information. The molecular motions expected for smectic (i.e., layered) LCs are shown in Figure 8.1. In addition to the fast molecular 'spinning' and internal motions mentioned above, slower motions include rotation about the short molecular axis and translational self-diffusion of the molecules within the layers (and between layers). Collective motions may also occur, such as the order director fluctuation, where groups of molecules fluctuate with respect to the average direction of alignment, and layer undulations.

Both solution- and solid-state NMR relaxation studies have proved to be a powerful tool for the investigation of the molecular dynamics in LCs[288–290] and various other types of systems (e.g., ionic liquids,[64–68] polymers,[291] biomembranes[292–295] and proteins[99,296,297]). NMR relaxation studies have been performed on various nuclei, with the most common being ^{1}H, ^{2}H and ^{13}C. The interpretation of ^{1}H relaxation rates is complicated by possible spin diffusion, in addition to contributions of both intra- and intermolecular effects, making quantitative analysis difficult. ^{2}H and ^{13}C NMR overcome these difficulties, with the latter having the advantage of not requiring isotopic labelling. The relaxation of ^{13}C nuclei mainly takes place through the dipolar interaction with the attached protons, with a smaller contribution from the CSA

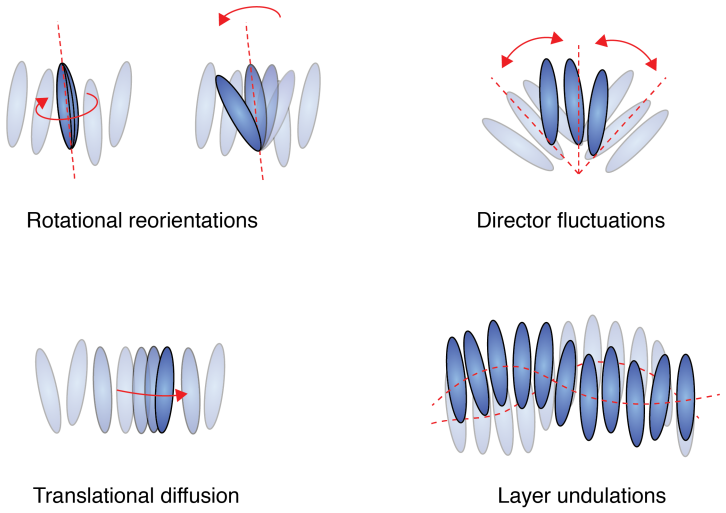

Figure 8.1: Schematic illustration of the main dynamic processes of smectic LCs: overall molecular reorientation around the long molecular axis (i.e. molecular spinning) and overall molecular reorientation about the short molecular axis (i.e., molecular tumbling), director fluctuations, translational self-diffusion and layer undulations. In addition, for molecules with internal degrees of freedom, segmental motions (*trans-gauche* isomerisation) may occur (not shown). Figure adapted from ref.[287]

mechanism (see Section 2.4.4). A few studies have utilised ^{13}C NMR relaxation to investigate LCs. For example, Hayamizu *et. al* reported anisotropic rotational diffusion constants ($D_{||}$ and $D_{\perp}$) from the ^{13}C R_1 relaxation rates of the ring and methyl carbons in the nematic and isotropic liquid phases of the thermotropic LC, 4,4'-dimethyoxyazoxybenzene.[288] ^{13}C R_1 relaxation rates have also been used in conjunction with NOE measurements; for example, Hutton *et. al* reported these VT measurements for the LC, *p*-methyoxybenzylidene-*p*-*n*-butylaniline (MBBA), noting that the ^{13}C relaxation rates are governed by the overall anisotropic rotational diffusion of the molecule, with increased internal motions occurring along the *n*-butyl chain.[289]

This chapter presents a detailed study of relaxation of ^{1}H and ^{13}C nuclei of the thermotropic ILC CAGE-oct. ^{1}H R_1 relaxation rates are first discussed qualitatively, showing clear differences in the dynamics of the choline cation in comparison to the geranate and octanoate anions. ^{13}C R_1 and $R_{1\rho}$ relaxation rates and ^{1}H-^{13}C NOE factors, measured at two magnetic fields, ν_{0H} = 500 and 700 MHz, are then analysed based on two motional models. Relaxation rates are first analysed using the SMF and EMF approaches, which assume motion on one or two time-scales, respectively. While providing initial estimates of activation energies and correlation times, these approaches were not sufficient to describe the complex dynamics of CAGE-oct. The presence of overall anisotropic tumbling was

consequently assumed, combined with the SMF formalism, and found to provide a reasonable fit to all relaxation measurements, providing estimates of the correlation times for the molecular reorientational dynamics and site-specific timescales and order parameters for internal motions. Finally, the presence of slower motions, on the μs-ms timescale, are probed by $R_{1\rho}$ RD measurements.

8.3 Experimental Details

8.3.1 Sample Preparation

CAGE-oct was synthesised as described in Chapter 6, Section 6.3.1.

8.3.2 MAS NMR

MAS NMR experiments were performed on a Bruker Avance III spectrometer operating at a ^{1}H Larmor frequency of ν_{0H} = 500 MHz (11.7 T) and a Bruker Avance III HD spectrometer operating at a ^{1}H Larmor frequency of ν_{0H} = 700 MHz (16.4 T), using 3.2 mm double-resonance MAS probes. A spinning frequency of 10 kHz was used for all experiments, except the ^{1}H R_1 measurements where 5 kHz was used. In all experiments the ^{1}H and ^{13}C 90° pulses were of duration 2.5 and 5 μs, respectively (corresponding to 100 and 50 kHz nutation frequencies). The temperature was calibrated using methanol, as described in the Bruker Instruments manual, with all stated temperatures corrected by this procedure. The temperature was allowed to equilibrate for at least 5 minutes between all experiments.

^{1}H R_1 measurements were performed using an inversion recovery pulse sequence. 4 transients were co-added and a recycle delay of 5 s was used. 16 points were recorded with variable relaxation delays ranging from 158 ms to 5 s. ^{13}C R_1 measurements were made using a saturation recovery pulse sequence. 64 transients were co-added and a recycle delay of 1 s was used. 16 points were recorded with variable relaxation delays ranging from 50 ms to 5 s. A ^{1}H π pulse at 50 kHz was applied every 5 ms during the relaxation time, to reduce any cross-correlated relaxation effects.[130] ^{13}C $R_{1\rho}$ measurements were recorded by direct ^{13}C excitation, followed by a ^{13}C spin-lock with ν_1 = 6 kHz. 32 transients were co-added and a recycle delay of 25 s was used. 12 points were recorded with variable spin-lock times. $R_{1\rho}$ measurements were recorded at three offset frequencies, such that the ^{13}C spin-lock was sufficiently close (< 15 ppm) to on-resonance for all peaks. ^{1}H-^{13}C NOE measurements were performed using the steady-state method. The steady-state NOE was measured after proton saturation for 5 s, and a recycle delay of 25 s was used. In the reference experiment, the recycle delay time was 30 s (equal to the recycle delay plus saturation time). In all ^{13}C experiments, SPINAL-64[119]

heteronuclear decoupling was applied during acquisition at a nutation frequency of 45 kHz, corresponding to a pulse duration of 10.5 µs.

8.3.3 Data Fitting

Spectra were processed with Topspin 4.0, and the relaxation rates were subsequently obtained from fits of the peak intensities against the variable delay, τ, (R_1) or variable spin-lock time, τ_{SL}, ($R_{1\rho}$) performed using Graphpad Prism 8, according to equations 8.1 and 8.2 for R_1 and $R_{1\rho}$ relaxation rates, respectively:

$$I(\tau) = I_0(1 - e^{-\frac{\tau}{T_1}}) \tag{8.1}$$

$$I(\tau_{SL}) = I_0(e^{-\frac{\tau_{SL}}{T_{1\rho}}}) \tag{8.2}$$

The NOE enhancement factor was determined from the intensity of the ^{13}C MAS NMR spectra recorded with ^{1}H saturation, I_{sat}, and the reference experiments, I_{ref}, according to:

$$NOE = \frac{I_{sat} - I_{ref}}{I_{ref}} \tag{8.3}$$

Fitting of the data to the SMF, SMF with anisotropic tumbling, and EMF motional models were performed in Matlab R2019b using the *lsqnonlin* and *MultiStart* algorithms with several random start points in order to find the global minimum. Matlab scripts for fitting to the SMF formalism with overall anisotropic tumbling are given in Appendix F.1. The best-fit parameters were determined by minimising the χ^2 value:

$$\chi^2 = \sum_i \frac{(R_{i,calc} - R_{i,exp})^2}{\sigma^2_{i,exp}} \tag{8.4}$$

where R_i are the relaxation rates or NOE factors, and σ_i are approximate experimental errors. Errors in the R_1 and $R_{1\rho}$ relaxation rates were obtained from the exponential fits, and the error in the NOE factors was estimated to be 10%. Errors in the fit parameters were estimated using Monte Carlo analysis. Briefly, relaxation rates were back-calculated from the best-fit parameters, random noise within experimental error was added to the rates and the resulting rates were fit to the model. 1000 iterations (SMF and EMF analysis) or 500 iterations (SMF with anisotropic tumbling analysis) were performed and the error was set to two times the standard deviation of the results from all runs. In order to evaluate whether the models satisfactorily explain the observed data, reduced χ^2 values were calculated:

$$\chi^2_\nu = \frac{\chi^2_\nu}{\nu} \tag{8.5}$$

where ν is the degrees of freedom, $\nu = n - p$, and n and p are the number of data

points and fit parameters, respectively.

^{13}C R_1 and $R_{1\rho}$ relaxation was assumed to take place via the dipolar mechanism to directly bound protons, in addition to the CSA mechanism for the alkene carbons (see Section 2.4.4 for more details and Equations 2.88-2.93 describing the relaxation rates in terms of spectral densities):

$$R_1 = R_1^{DD} + R_1^{CSA} \tag{8.6}$$

$$R_{1\rho} = R_{1\rho}^{DD} + R_{1\rho}^{CSA} \tag{8.7}$$

The rigid limit CH distances were as used in Chapter 7 (1.102, 1.100 and 1.097 Å for CH, CH_2 and methyl, respectively.) The CSA was assumed to be axially symmetric, with $\Delta\sigma = 108$ ppm for the alkene carbons (C-2 and C-6 of geranic acid), based on the averaged values reported for a number of small molecules containing carbon-carbon double-bonds.[298] Those of the CH_2 and methyl carbons are expected to be considerably smaller ($\Delta\sigma = 16$ and 12 ppm, respectively),[298] and were therefore neglected. To estimate the angles of the various CH bond vectors to the principal axis of the diffusion tensor, the principal axis was assumed to coincide with the principal axes of the moment of inertia tensor for each ion. Octanoate was assumed to be in the all-trans configuration, with the angles obtained from the crystal structure of 1-octanoic acid (CCDC identifier ISENUP) following DFT geometry optimisation using CASTEP[299] Academic Release version 16.1. Geometry optimisation was performed using the Perdew Burke Ernzerhof (PBE) exchange correlation functional,[300] a plane-wave basis set with ultrasoft pseudopotentials and a plane-wave cut-off energy of 700 eV. The angles for choline and geranate were taken as the average angles from five low energy conformers of CAGE (1:1 choline:geranate) in the gas phase, provided by Mikkaila Mckeever-Willis and Particia Hunt (Imperial College London, currently unpublished data).

8.4 Results and Discussion

8.4.1 ^{1}H Spin-lattice Relaxation

Figure 8.2 shows the temperature dependence of the ^{1}H R_1 relaxation rates determined from inversion-recovery experiments for CAGE-oct in the isotropic and LC phases. A clear difference in R_1 is observed for the choline cation and carboxylate anions, with the protons of choline (H-1′, H-2′ and H-3′) relaxing considerably faster at higher temperatures, compared to those of geranate and octanoate. R_1 of the carboxylic acid/hydroxyl proton lies between those of the choline cation and geranate/octanoate, since it undergoes fast proton exchange on the timescale of the experiment, and is therefore observed as the average between the two sites. The

similar ^{1}H R_1 relaxation rates of geranate and octanoate suggest a similar timescale of motion, while the higher R_1 values of choline are consistent with faster overall tumbling, which can be expected based on the smaller size of the choline cation. The differences are also consistent with the motion of the choline cation being less restricted, which agrees with the considerably lower order parameters observed for choline from the measurement of the C-H and H-H residual dipolar couplings (RDCs; see Chapter 7) for CAGE-oct in the LC phase.

No discontinuity is observed in the ^{1}H R_1 relaxation rates at the LC to isotropic transition, suggesting that amplitude and timescale of the motions dominating the ^{1}H R_1 does not drastically change on LC melting. The immediate environment of the ions is not expected to change with the loss of long-range order as SAXS indicated that some intermediate-range order persisted in the isotropic phase (Chapter 7). As the temperature is decreased, the R_1 values merge towards a single value for all protons of CAGE-oct due to the increased efficiency of spin-diffusion at lower temperatures. Both incoherent (driven by multi-step NOE transfer) and coherent (driven by incompletely averaged dipolar couplings) spin-diffusion processes may contribute in the LC phase. As a result, the ^{1}H R_1 values are unable to provide site-specific information on the dynamics of CAGE-oct in the LC phase. Quantitative analysis of ^{1}H relaxation is further complicated by contributions from the modulation of both intermolecular and intramolecular interactions by molecular motions. However, for other nuclei such as ^{13}C, the dominating source of relaxation is due to dipolar coupling to the directly bonded protons. ^{13}C relaxation rates were therefore measured and fit to obtain quantitative information on the dynamics of CAGE-oct in the LC phase, as described in the following sections.

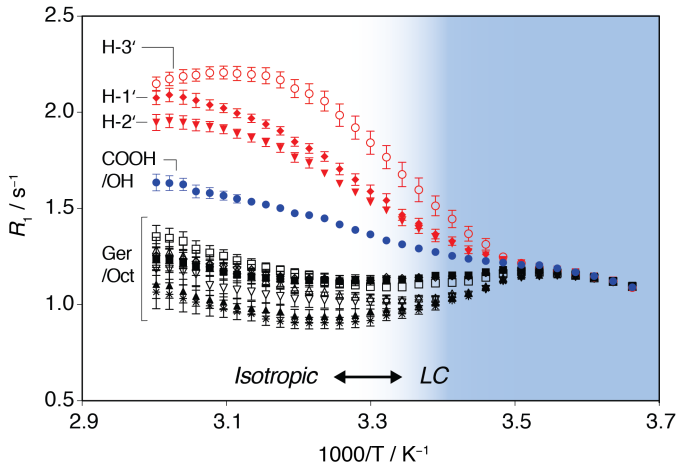

Figure 8.2: The temperature dependence of ^{1}H R_1 relaxation rates (ν_{0H} = 700 MHz, ν_r = 5 kHz) for CAGE-oct in the isotropic (white) and liquid crystalline (blue) phases. Relaxation rates for protons of the choline cation are shown in red, geranate/octanoate in black, and the COOH/OH proton that exchanges between the choline/geranate/octanoate (see Chapter 7) in blue.

8.4.2 Measurement of Variable Temperature ^{13}C R_1 and $R_{1\rho}$ Relaxation Rates and ^{1}H-^{13}C NOE Factors

Different relaxation rates are sensitive to particular timescales of motion: R_1 is dominated by ps-ns timescale motions, whilst $R_{1\rho}$ is sensitive to slower, ns-ms timescale motions. Site-specific ^{13}C R_1 and $R_{1\rho}$, as well as ^{1}H-^{13}C NOE factors, for CAGE-oct were measured at ν_{0H} = 500 MHz and 700 MHz, with ν_r = 10 kHz, and ν_1 = 6 kHz, at sample temperatures from −26 to 52 °C, covering both the LC and isotropic phases (T_m = ∼20 °C; see Chapter 7). The use of 10 kHz MAS provided high resolution, with all peaks being resolved across all temperatures, apart from C-5 and C-3″ which overlapped at temperatures below −8 °C. A single relaxation rate is therefore reported for these two sites at low temperatures and is likely to be less accurate than those of the fully resolved peaks. R_1 measurements were performed by saturation recovery, as shown in Figure 8.3. $R_{1\rho}$ measurements were performed by direct excitation of ^{13}C, followed by a variable delay spin-lock at ν_1 = 6 kHz (Figure 8.4a). Representative data at two temperatures (276 K and 318 K) is shown in Figure 8.4b for all ^{13}C sites of CAGE-oct. The mean relaxation rate constant was obtained by fitting to the initial slope of the decay, where the intensity was greater than 50% of the initial intensity, to a single exponential. Steady-state ^{1}H-^{13}C NOE factors were obtained by NOE difference experiments, by recording two experiments: one with ^{1}H saturation, and a reference experiment with no ^{1}H-^{13}C saturation (see Figure 8.5 for representative spectra).

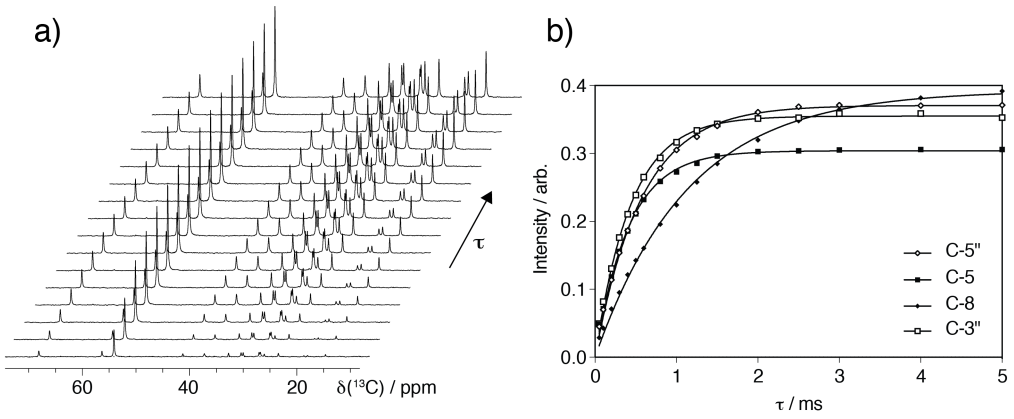

Figure 8.3: Representative data (ν_{0H} = 700 MHz, T = 277 K) for ^{13}C R_1 saturation-recovery measurements for CAGE-oct. a) A portion of the spectra recorded with 16 variable delay times ranging from 50 ms to 5 s. b) Exponential fits of the return of magnetisation to equilibrium, following saturation, for peaks C-5″, C-5, C-8 and C-3″.

The measured R_1 and $R_{1\rho}$ relaxation rates and NOE factors are shown in Figures 8.6, 8.7 and 8.8, respectively. Over the temperature range studied, R_1 for the majority of sites decreases with increasing temperature. This behaviour is typical of small molecules undergoing reorientations, with $\omega\tau_c < 1$. The R_1 curves approach a maximum at $\omega\tau_c \approx 1$, where the correlation time is on the order of $2\pi/\omega \approx 10^{-8}$ s, at spectrometers operating at ^{1}H Larmor frequencies 500 and 700 MHz (ν_{0C} = 126 and 176 MHz, respectively). For most sites, the R_1 maximum is not yet reached at the lowest recorded temperature (−26°C, the limit of our experimental equipment). The exceptions are the CH_2 carbons of the choline (C-1′ and C-2′), and C-2 and C-4 of geranic acid, which show a maximum in R_1, with R_1 increasing with increasing temperature in the low temperature region. There is a general trend of decreasing R_1 along the octanoic acid chain from C-2″ to C-8″, consistent with an increased range of internal motion (and lower order parameter; see Chapter 7) toward the terminal end of the alkyl chain, resulting in an increased contribution of molecular tumbling to R_1. Moreover, C-2″, C-3″ and C-4″ appear to approach a R_1 maximum toward the lowest recorded temperature, indicative of a higher activation energy for the reorientation, compared to the carbons closest to the terminal end of the alkyl chain. The R_1 relaxation rates for choline are higher across all temperatures compared to those of geranic and octanoic acid, consistent with the ^{1}H R_1 relaxation rates which suggest faster overall tumbling of the choline cation, compared to octanoate and geranate. $R_{1\rho}$ decreases with increasing temperature for all peaks over the temperature range studied (Figure 8.7), consistent with an increase in the rate of reorientational motion. Further analysis of the motions causing the relaxation is described in the following sections.

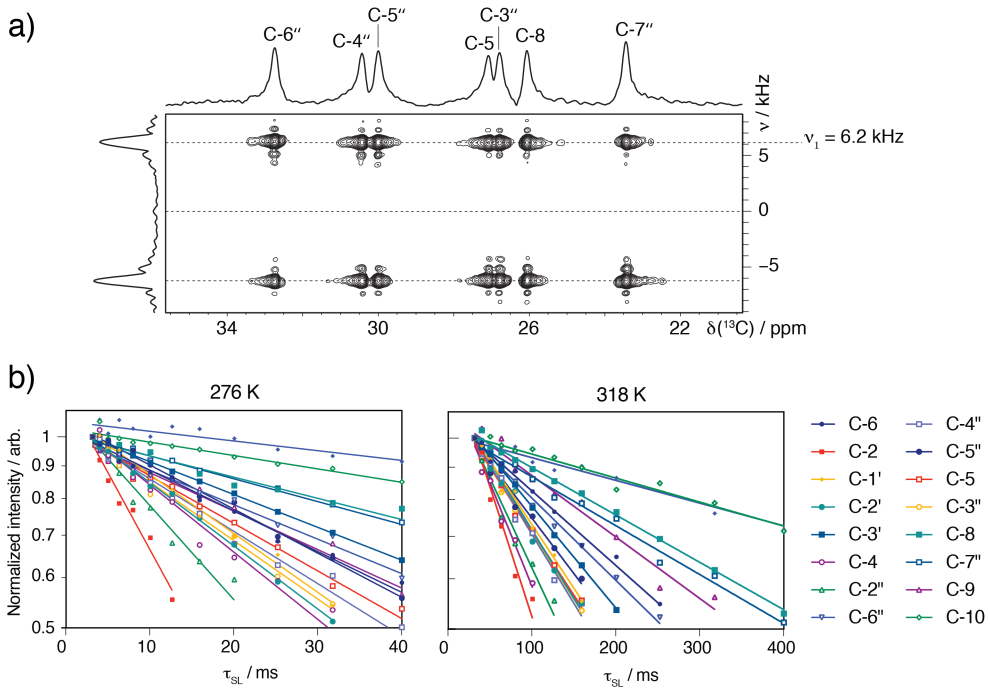

Figure 8.4: Representative data (ν_{0H} = 700 MHz) for ^{13}C $R_{1\rho}$ measurements for CAGE-oct. (a) Measurement of the ^{13}C nutation frequency (T = 277 K) and (b) $R_{1\rho}$ relaxation decay curves as a function of the spin-lock time, τ_{SL}, for all peaks of CAGE-oct at two temperatures (T = 276 K and 318 K). Note the intensity is displayed on a logarithmic scale.

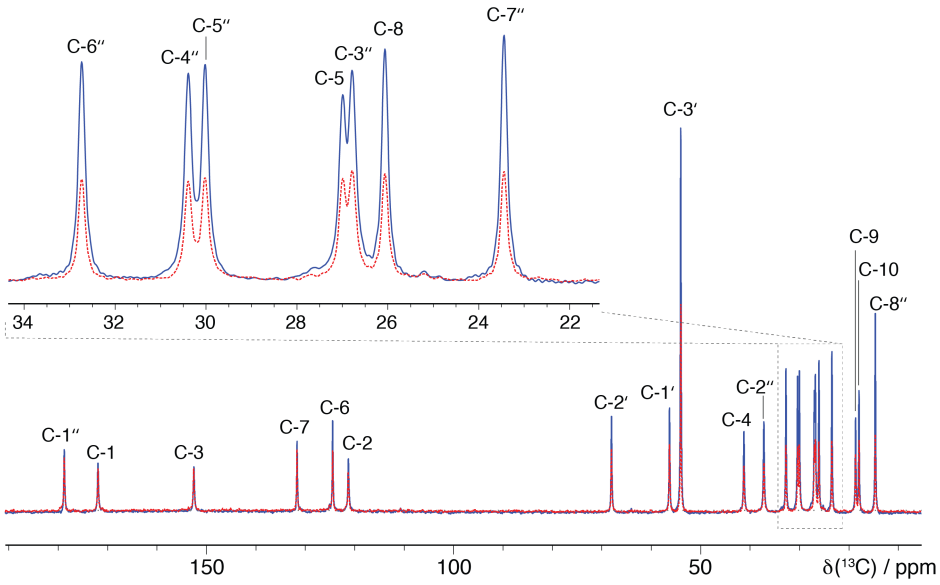

Figure 8.5: Representative data (ν_{0H} = 700 MHz, T = 277 K) for the steady-state ^{1}H-^{13}C NOE difference experiment for CAGE-oct, used to determine the NOE enhancement factors in Figure 8.8. The solid blue spectrum was recorded with ^{1}H saturation for 5 s, and the red dashed spectrum is the reference experiment, recorded with no ^{1}H saturation.

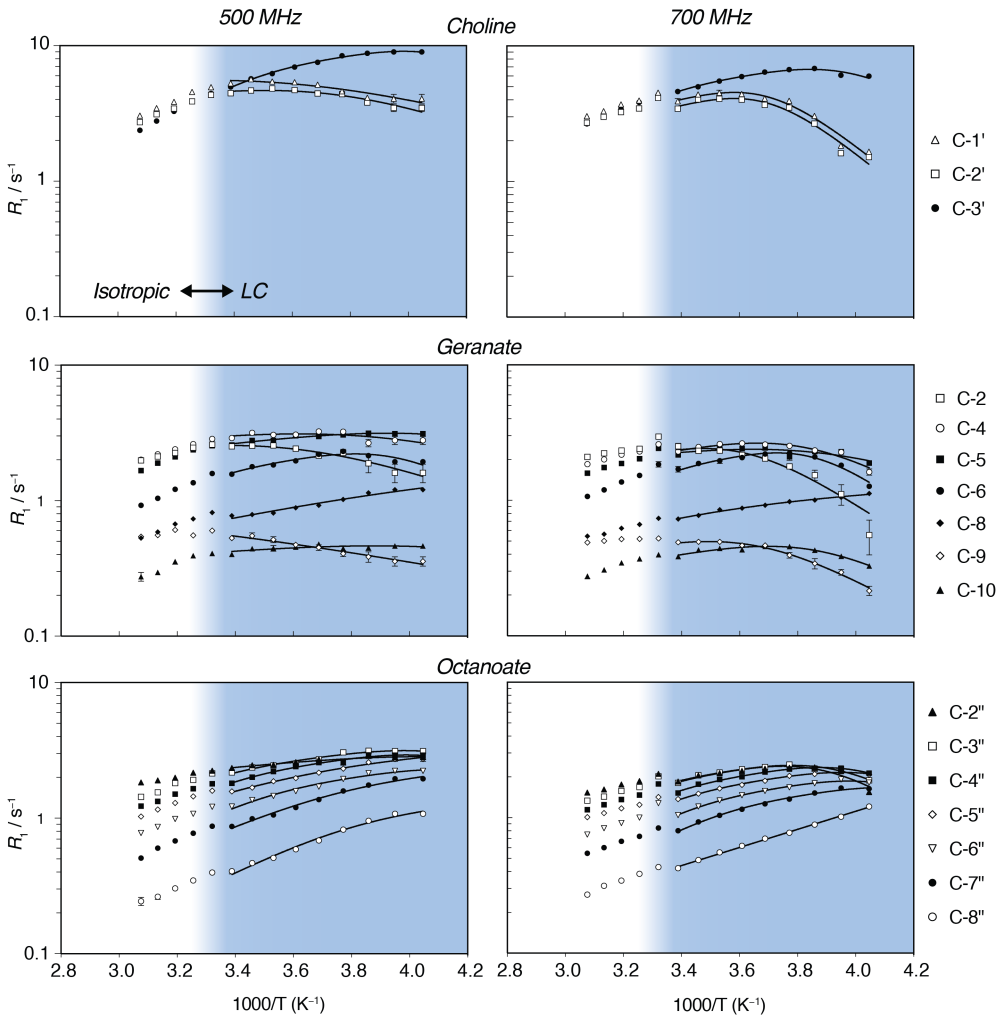

Figure 8.6: The temperature dependence of ^{13}C R_1 relaxation rates ($\nu_r = 10$ kHz) for CAGE-oct in the isotropic (white) and liquid crystalline (blue) phases, recorded at $\nu_{0H} = 500$ MHz (left) and $\nu_{0H} = 700$ MHz (right). Solid lines are fits to the SMF approach (Equation 8.8), assuming an Arrhenius temperature dependence (Equation 8.9).

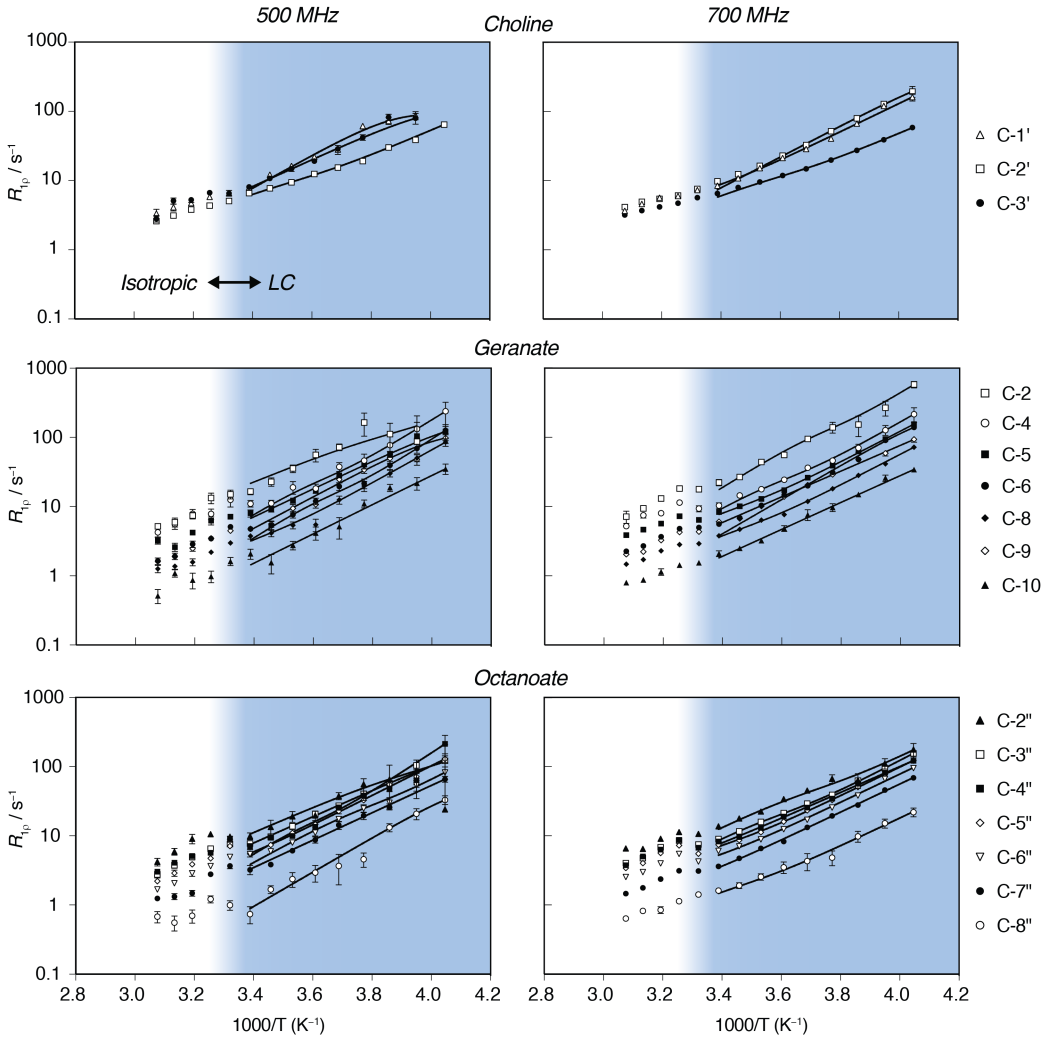

Figure 8.7: The temperature dependence of ^{13}C $R_{1\rho}$ relaxation rates ($\nu_{\mathrm{r}} = 10$ kHz, $\nu_1 = 6$ kHz,) for CAGE-oct in the isotropic (white) and liquid crystalline (blue) phases, recorded at $\nu_{0\mathrm{H}} = 500$ MHz (left) and $\nu_{0\mathrm{H}} = 700$ MHz (right). Solid lines are fits to the SMF approach (Equation 8.8), assuming an Arrhenius temperature dependence (Equation 8.9).

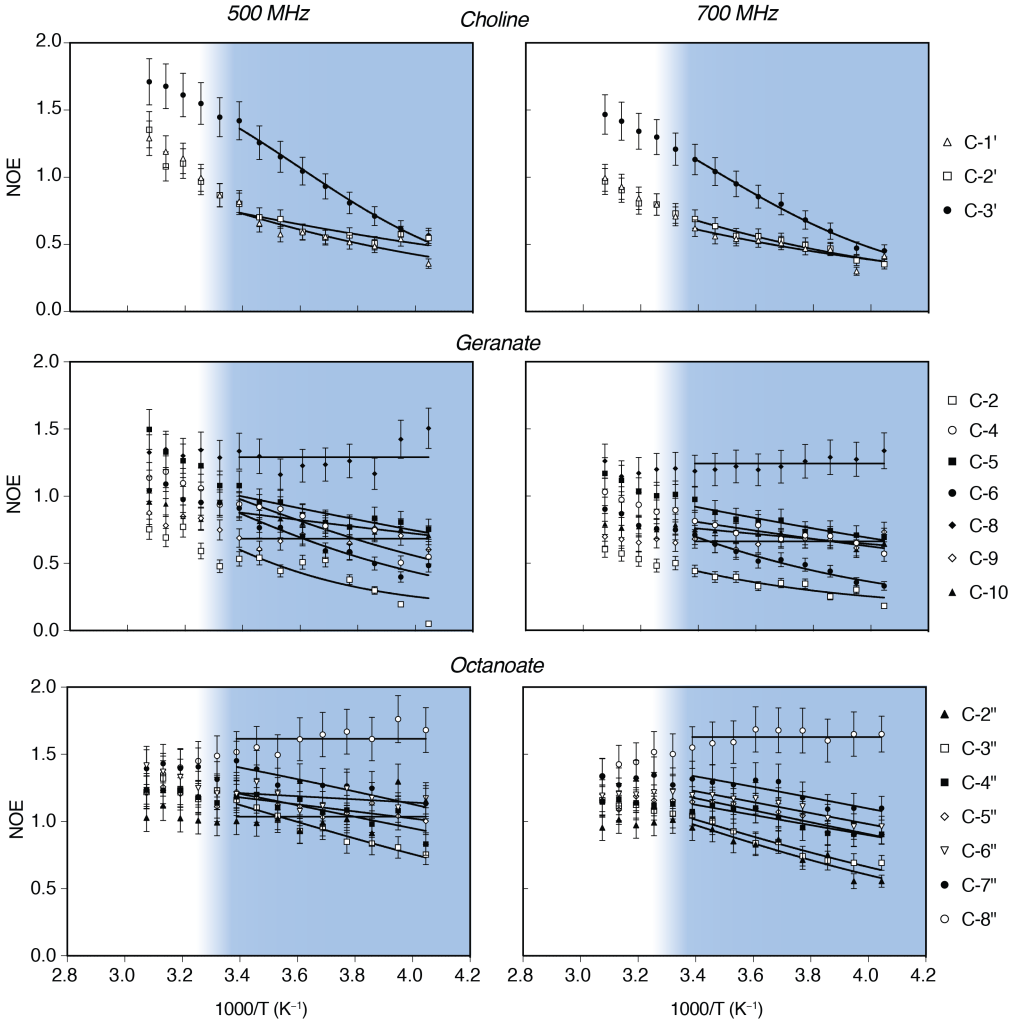

Figure 8.8: The temperature dependence of ^{1}H-^{13}C NOE enhancement for CAGE-oct in the isotropic (white) and liquid crystalline (blue) phases, recorded at $\nu_{0\mathrm{H}} = 500$ MHz (left) and $\nu_{0\mathrm{H}} = 700$ MHz (right). Solid lines are fits to the SMF approach (Equation 8.8), assuming an Arrhenius temperature dependence (Equation 8.9).

8.4.3 Analysis of Relaxation Rates using the SMF and EMF Approaches

As described in Section 2.4.2, different forms of the spectral density can be derived from motional models. In most cases, the spectral densities are approximated by linear combinations of Lorentzian functions.[301] A useful first approximation assumes that the R_1 and $R_{1\rho}$ relaxation rates are each dominated by a single time-scale motion, termed the SMF approach (as given in Equation 2.80):[94,297]

$$J(\omega) = (1 - S^2)\frac{\tau_{eff}}{1 + (\omega\tau_{eff})^2} \tag{8.8}$$

where τ_{eff} is the effective correlation time for the motion. To investigate the influence of motions on ^{13}C relaxation data, the data was fit to the SMF formalism, assuming an Arrhenius temperature dependence, according to:

$$\tau_{eff} = \tau_0 e^{\frac{E_a}{RT}} \tag{8.9}$$

The results of the analysis of the relaxation rates using the SMF formalism, when ^{13}C R_1 and $R_{1\rho}$ are considered separately, are presented in Figure 8.9 and Table 8.1. χ^2_ν between 2-20 for the SMF analysis of R_1 rates indicate that the data is not well described by the SMF approach with a single motion, and that most sites undergo motions on two or more timescales; the SMF analysis reports on only the timescale with the dominating contribution. The $R_{1\rho}$ SMF fits produced lower χ^2_ν values between 1-3 for most sites. The average τ_{eff} obtained from VT R_1 relaxation rates was 0.5 ns (at 273 K) and the activation energy was 20 kJ mol^{-1}. The effective correlation times obtained from SMF fits to VT $R_{1\rho}$ relaxation rates indicated slower motions for all sites. However, there was significant variation between sites and larger errors compared to the R_1 analysis, with τ_{eff} ranging from 10^{-8} to 10^{-6} (average 5×10^{-7} s). The activation energies were similar across all sites, averaging 38 kJ mol^{-1}, which is significantly higher than those of the faster motions that dominate the R_1 relaxation rates (average 20 kJ mol^{-1}).

The effective order parameters, S^2, obtained from R_1 data average 0.66, whilst those from the $R_{1\rho}$ data average 0.81. The order parameters for the geranic acid methyl carbons (C-9, C-8 and C-10) from the R_1 analysis are considerably lower compared to the other sites, which is expected since fast rotation of the methyl group will reduce the contribution of slower motions by the order parameter, $S^2_{methyl} = 0.11$ (for tetrahedral geometry, $\theta = 109.5°$). The generalised order parameters, approximated by the product of the effective order parameters for the motions dominating the R_1 and $R_{1\rho}$ relaxation rates (average 0.54) are far higher than the overall order parameters, S^2_{CH}, obtained from RDCs (average 0.02; see

Chapter 7). This inconsistency further indicates that the assumption of a single timescale motion dominating each relaxation rate is not valid for the CAGE-oct LC.

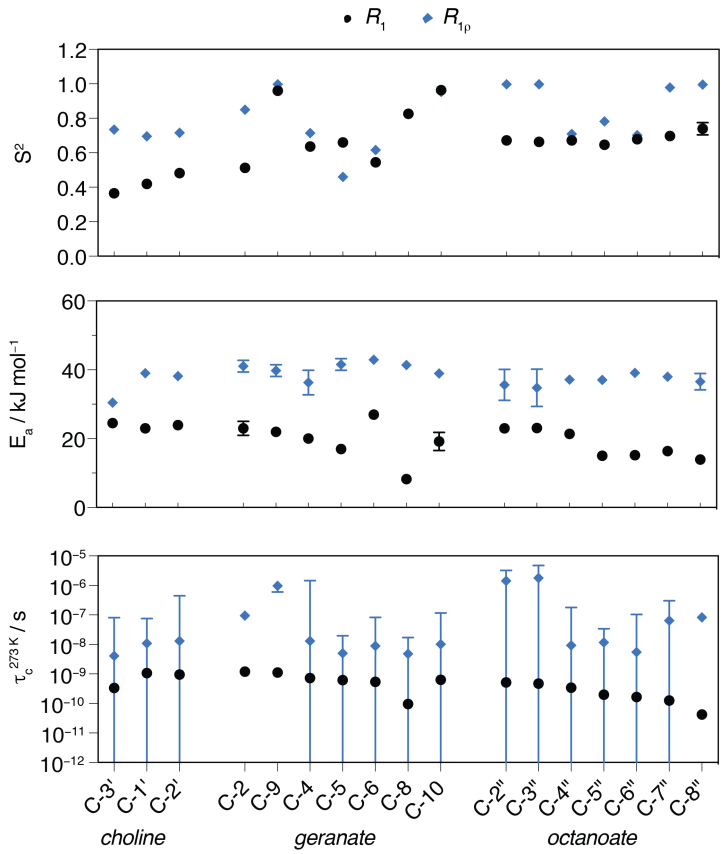

Figure 8.9: The order parameters, activation energies and effective correlation times (at 273 K) for CAGE-oct in the LC phase, from the SMF analysis of the VT R_1 (black circles) and $R_{1\rho}$ (blue diamonds) measurements (Figures 8.6 and 8.7). The data recorded at $\nu_{0\mathrm{H}} = 500$ MHz and $\nu_{0\mathrm{H}} = 700$ MHz were fit simultaneously. Note that some error bars have been clipped at the axis limits. Error bars are not shown if smaller than the symbol height.

Table 8.1: Best-fit parameters for SMF analysis of ^{13}C R_1 and $R_{1\rho}$ relaxation rates for CAGE-oct in the LC phase.

		R_1				$R_{1\rho}$			
		S^2	τ_{eff}[a] / ns	E_a / kJ mol^{-1}	χ^2_ν	S^2	τ_{eff}[a] / ns	E_a / kJ mol^{-1}	χ^2_ν
choline	C-3′	0.366 ± 0.004	0.34 ± 0.01	24.5 ± 0.5	6.2	0.735 ± 0.001	4 ± 77	30.5 ± 0.3	8.0
	C-1′	0.419 ± 0.006	1.07 ± 0.03	23 ± 1	13	0.695 ± 0.004	11 ± 65	39 ± 1	2.5
	C-2′	0.483 ± 0.005	0.96 ± 0.03	23.9 ± 0.9	16	0.7164 ± 0.0005	13 ± 429	38.2 ± 1.5	2.5
geranate	C-2	0.513 ± 0.006	1.20 ± 0.05	23 ± 2	10	0.85 ± 0.02	96 ± 25	41 ± 2	1.1
	C-9	0.961 ± 0.001	1.11 ± 0.05	22 ± 1	19	0.9985 ± 0.0003	$[1.0 \pm 0.4] \times 10^3$	40 ± 2	2.3
	C-4	0.637 ± 0.004	0.73 ± 0.02	20 ± 1	6.0	0.714 ± 0.008	$[0.1 \pm 15] \times 10^2$	37 ± 4	1.2
	C-5	0.661 ± 0.003	0.62 ± 0.01	17 ± 1	3.1	0.461 ± 0.001	5 ± 15	42 ± 2	2.0
	C-6	0.545 ± 0.006	0.55 ± 0.01	27 ± 1	13	0.616 ± 0.007	9 ± 74	42.9 ± 0.8	1.5
	C-8	0.826 ± 0.01	0.10 ± 0.01	8.3 ± 0.4	2.5	0.826 ± 0.001	5 ± 13	41.4 ± 0.6	1.9
	C-10	0.963 ± 0.001	0.64 ± 0.04	19 ± 3	20	0.953 ± 0.001	10 ± 100	39 ± 1	1.1
octanoate	C-2″	0.672 ± 0.003	0.52 ± 0.02	23 ± 1	4.4	0.997 ± 0.002	$[1 \pm 2] \times 10^3$	36 ± 5	1.5
	C-3″	0.663 ± 0.002	0.47 ± 0.01	23.1 ± 0.7	3.9	0.99818 ± 0.00004	$[2 \pm 3] \times 10^3$	35 ± 5	1.6
	C-4″	0.672 ± 0.003	0.35 ± 0.01	21.4 ± 0.9	6.7	0.710 ± 0.009	9 ± 170	37.2 ± 0.9	3.6
	C-5″	0.647 ± 0.02	0.20 ± 0.02	15 ± 1	3.2	0.783 ± 0.002	12 ± 23	37.1 ± 0.7	3.3
	C-6″	0.679 ± 0.01	0.16 ± 0.01	15.2 ± 0.9	2.9	0.702 ± 0.004	5 ± 99	39.1 ± 0.9	1.8
	C-7″	0.698 ± 0.01	0.13 ± 0.01	16.4 ± 0.5	1.6	0.9782 ± 0.0003	65 ± 240	38 ± 1	2.3
	C-8″	0.739 ± 0.04	0.04 ± 0.01	13.9 ± 0.3	2.6	0.9958 ± 0.0003	83 ± 18	37 ± 2	2.2

[a] τ_{eff} is reported at 273 K.

Consequently, the EMF approach,[96] in which motion is modelled assuming the presence of fast and slow motions, is considered (as given in Equation 2.81):

$$J(\omega) = (1 - S_f^2)\frac{\tau_f}{1 + (\omega\tau_f)^2} + S_f^2(1 - S_s^2)\frac{\tau_s}{1 + (\omega\tau_s)^2} \tag{8.10}$$

Each motion is characterised by its own order parameter, correlation time and activation energy: S_f^2, τ_f and $E_{a,f}$ describe the fast motion, while S_s^2, τ_s and $E_{a,s}$ describe the slow motion. The order parameters are related to overall order parameter as $S_{CH}^2 = S_s^2 S_f^2$. The R_1 and $R_{1\rho}$ relaxation rates and NOE factors measured at 500 and 700 MHz magnetic fields were simultaneously fit to the EMF formalism, with the results shown in Figure 8.10 and Table 8.2. The fast motions were treated as local motions for each site, while the motional parameters for the slower motion, τ_s and $E_{a,s}$, were assumed to be global for each molecule. It is expected that the faster motions correspond to internal motions (e.g., *trans-gauche* isomerisations and restricted segmental reorientations), while the slower timescale is expected to correspond to molecular rotational diffusion. The use of an order parameter, S_s^2 specific to each site allows for differences in angle of the C-H bond vector to the axis of reorientation.

The correlation times, activation energies and order parameters for the fast and slow motions were similar to those obtained from the SMF analysis of R_1 and $R_{1\rho}$ relaxation rates, respectively. All components of CAGE-oct were characterised by similar global molecular reorientation with a correlation time, τ_s, on the ns time-scale (15, 17.7 and 22 ns at 273 K for choline, geranate and octanoate, respectively), with activation energies close to 40 kJ mol^{-1}. The local internal motions occurred on timescales ranging from ns to ps (average $\tau_f = 0.31$ ns) with activation energies ranging from 2 to 33 (average 19) kJ mol^{-1}. The order parameters, S_s^2 and S_f^2 were similar, averaging 0.7. The total order parameters, $S_{CH}^2 = S_s^2 S_f^2$, were between 0.3 to 0.7 for most sites (average 0.5). Such high order parameters are inconsistent with the total order parameters, S_{CH}^2, obtained from the RDCs (see Chapter 7), which are very low, ranging from 0.002 to 0.05 (average 0.02). This strongly suggests that the EMF formalism, using motion on two timescales, is unable to capture the complete dynamics that contribute to the NMR relaxation for CAGE-oct. Attempts were made to fit the relaxation data to the EMF formalism by constraining the overall amplitude of motions using the RDCs (i.e. $S_{CH}^2 = S_s^2 S_f^2$). Such an approach has been demonstrated by Haller and Schanda, who showed that while the analysis of relaxation data alone resulted in the systematic overestimation of order parameters in proteins, accurate motional parameters could be obtained by the inclusion of dipolar coupling data.[302] However, for CAGE-oct, the resulting fits were poor ($\chi_\nu^2 > 20$ for all components). The resulting fit parameters are therefore not shown or discussed

further.

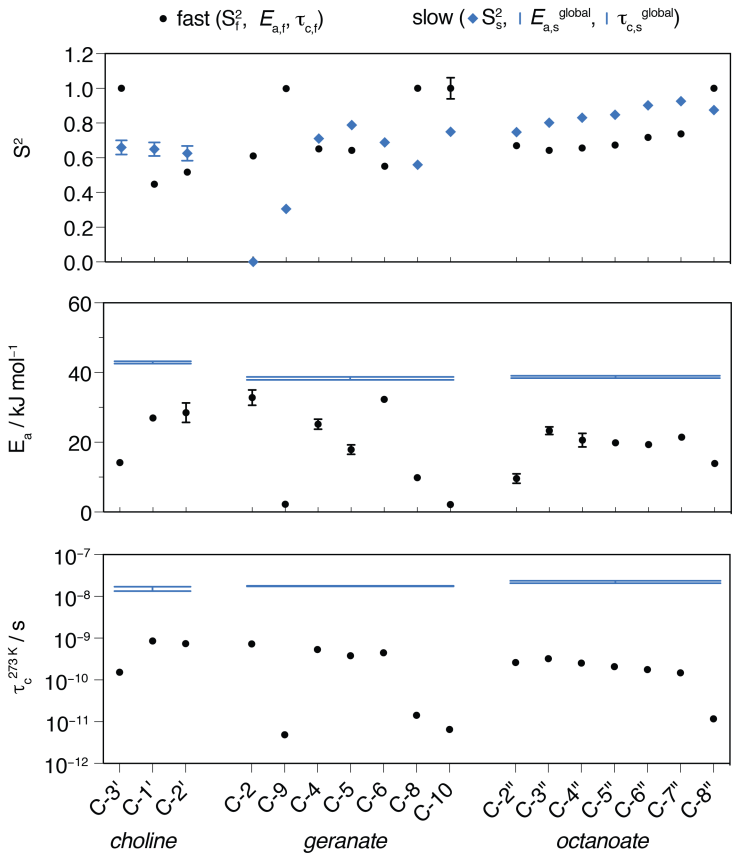

Figure 8.10: The order parameters, activation energies and effective correlation times (at 273 K) for CAGE-oct in the LC phase, from the EMF analysis of the VT R_1, $R_{1\rho}$ relaxation rates and NOE factors. Parameters describe fast motion (black circles) and slow motions (blue diamonds). The data recorded at ν_{0H} = 500 MHz and ν_{0H} = 700 MHz were fit simultaneously. Error bars are not shown if smaller than the symbol height.

Table 8.2: Best-fit parameters for EMF analysis of ^{13}C R_1, $R_{1\rho}$ relaxation rates and ^{1}H-^{13}C NOE factors for CAGE-oct in the LC phase.

		χ^2_ν	S^2_f	τ_f[a] / ns	$E_{a,f}$ / kJ mol^{-1}	S^2_s	τ_s[a,b] / ns	$E_{a,s}$[b] / kJ mol^{-1}
choline		12					15 ± 2	43.0 ± 0.4
	C-3′		1.00	0.153 ± 0.001	14.2 ± 0.3	0.66 ± 0.04		
	C-1′		0.449 ± 0.009	0.86 ± 0.04	27 ± 1	0.66 ± 0.04		
	C-2′		0.52 ± 0.01	0.74 ± 0.05	28.5 ± 2.9	0.63 ± 0.04		
geranate		14					17.7 ± 0.4	38.3 ± 0.5
	C-2		0.611 ± 0.007	0.73 ± 0.03	33 ± 2	0.00		
	C-9		0.999 ± 0.007	$[4.9 \pm 0.1] \times 10^3$	2.3 ± 0.7	0.31 ± 0.02		
	C-4		0.652 ± 0.004	0.54 ± 0.02	25 ± 1	0.71 ± 0.01		
	C-5		0.643 ± 0.005	0.38 ± 0.02	18 ± 1	0.788 ± 0.006		
	C-6		0.551 ± 0.005	0.448 ± 0.009	32.3 ± 0.9	0.69 ± 0.01		
	C-8		1.00	$[14.2 \pm 0.1] \times 10^3$	9.9 ± 0.3	0.56 ± 0.01		
	C-10		1.00 ± 0.06	$[6.5 \pm 0.1] \times 10^3$	2.2 ± 0.4	0.75 ± 0.02		
octanoate		7.2					22 ± 1	38.8 ± 0.4
	C-2″		0.670 ± 0.007	0.26 ± 0.01	10 ± 1	0.75 ± 0.02		
	C-3″		0.643 ± 0.006	0.32 ± 0.02	23 ± 1	0.80 ± 0.01		
	C-4″		0.657 ± 0.008	0.25 ± 0.02	21 ± 2	0.83 ± 0.01		
	C-5″		0.673 ± 0.006	0.210 ± 0.010	20 ± 1	0.849 ± 0.010		
	C-6″		0.719 ± 0.008	0.177 ± 0.009	19.4 ± 0.9	0.903 ± 0.007		
	C-7″		0.738 ± 0.007	0.148 ± 0.007	21.5 ± 0.7	0.926 ± 0.005		
	C-8″		1.00	$[11.70 \pm 0.07] \times 10^3$	13.9 ± 0.2	0.88 ± 0.01		

[a] τ_f and τ_s are reported at 273 K.
[b] τ_s and $E_{a,s}$ were assumed to be global for each molecule, whilst the remaining parameters were local to each site.

8.4.4 Analysis of Relaxation Rates using the SMF Formalism with Overall Anisotropic Molecular Tumbling

The SMF and EMF formalisms utilised in the previous sections consider only restricted motions on one or two time-scales, and are unable to sufficiently account for the complex dynamics of the CAGE-oct LC, particularly the low order parameters obtained from RDCs. From the presence of RDCs (see Chapter 7), it is evident that the components of CAGE-oct do not undergo complete tumbling, i.e., $S^2 > 0$, as was assumed in the solid-state formalisms utilised above. However, the overall order parameters for the CAGE-oct LC are very low (average 0.02). Therefore, in this section, the overall molecular motion of the components of CAGE-oct is approximated by complete anisotropic tumbling (i.e. assuming the overall $S^2 = 0$, as for unrestricted motion).

The solution-state SMF spectral density function for a molecule with axially symmetric rotational Brownian motion superimposed with fast internal motion is given by:[94,303]

$$J(\omega) = \sum_{j=0}^{2} A_j \left[\frac{S_i^2 \tau_j}{1 + (\omega\tau_j)^2} + \frac{\left(1 - S_i^2\right)\tau_j'}{1 + \left(\omega\tau_j'\right)^2} \right] \tag{8.11}$$

where the coefficients A_j depend on the angle of the C-H bond vector to the long molecular axis, θ, according to:

$$\begin{aligned} A_0 &= \tfrac{1}{4}\left(3\cos^2\theta - 1\right)^2 \\ A_1 &= 3\cos^2\theta\sin^2\theta \\ A_2 &= \tfrac{3}{4}\sin^4\theta \end{aligned} \tag{8.12}$$

The correlation time, τ_j^{-1} is defined as $\tau_j^{-1} = \left(6 - j^2\right) D_\perp + j^2 D_{||}$, i.e.:

$$\begin{aligned} \tau_0^{-1} &= 6D_\perp \\ \tau_1^{-1} &= 5D_\perp + D_{||} \\ \tau_2^{-1} &= 2D_\perp + 4D_{||} \end{aligned} \tag{8.13}$$

where $D_\perp$ is the diffusion coefficient for rotation around the long molecular axis, and $D_{||}$ is the diffusion coefficient for rotation about the short molecular axis (i.e., describing the molecular tumbling and spinning motions, respectively.). $\tau_j'^{-1}$ is given by $\tau_j'^{-1} = \tau_i^{-1} + \tau_j^{-1}$, where τ_i is the correlation time for the internal motion, which has an amplitude described by the order parameter, S_i^2. In the derivation of Equation 8.11, it is assumed that the internal motion is uncorrelated to the overall tumbling motion. In the case where $D_\perp = D_{||} (= D_{eff})$, Equation 8.11 reduces to the solution-state EMF equation for overall isotropic motion (Equation 2.79), with

$\tau_{eff} = (6D_{eff})^{-1}$. The motions contributing to the model are illustrated in Figure 8.11 for CAGE-oct.

The parameters describing the overall rotational diffusion ($D_\perp$, $D_{||}$, $E_{a,\perp}$ and $E_{a,||}$) were kept constant for all sites of the same ion, whilst the parameters describing the internal motion (θ, τ_i, $E_{a,i}$ and S_i^2) are local to each site. The correlation times and diffusion coefficients were assumed to show an Arrhenius temperature dependence, according to equation 8.9 and:

$$D = D_0 e^{\frac{-E_a}{RT}} \tag{8.14}$$

The methyl groups were treated by assuming the concurrent fast methyl rotation reduces the internal order parameter by $S^2_{methyl}S^2_i$, where $S^2_{methyl} = 0.11$ (for tetrahedral geometry, $\theta = 109.5°$).

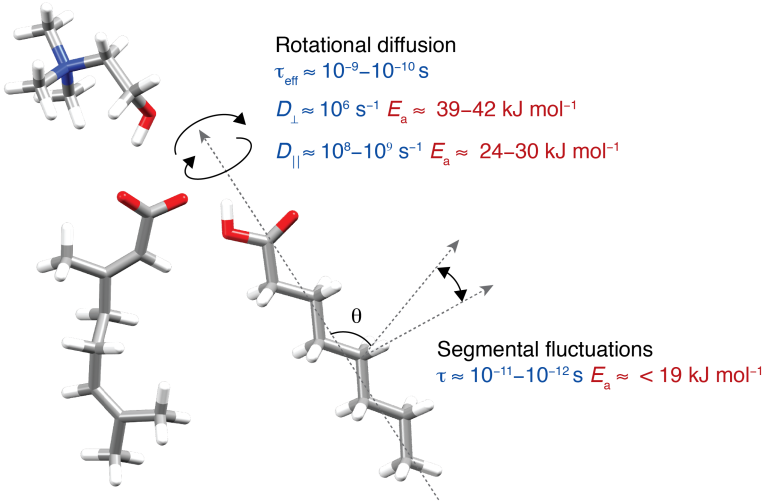

Figure 8.11: Schematic illustration of the dynamics of CAGE-oct in the LC phase. The approximate timescales and activation energies were obtained from fits to the SMF formalism with overall anisotropic tumbling for geranate and octanoate. Correlation times and rotational diffusion coefficients are reported at 273 K.

The SMF model with anisotropic tumbling was able to reasonably account for the experimentally determined R_1 and $R_{1\rho}$ relaxation rates and NOE factors for geranate and octanoate (see representative fits in Figure 8.12), with $\chi^2_\nu = 4.4$ and 4.7, respectively, while χ^2_ν for the choline cation was 13. The best-fit parameters describing the anisotropic rotational diffusion of the components of CAGE-oct (choline, geranate and octanoate) are given in Table 8.3. The best-fit parameters describing the internal motion for each C-H bond vector are given in Table 8.4. The errors in all fit parameters were obtained by Monte Carlo error analysis (see Section 8.3.3 for details), with representative histograms for the fit parameters shown in

Figure 8.13. θ was fixed to the values obtained from geometry optimised structures for choline and octanoate (see Section 8.3.3 for details). In order to obtain satisfactory fits for the geranate ion, θ was included as an additional fit parameter. This will be discussed further below.

Figure 8.12 shows a representative fit for C-4$''$ of octanoate and the contributions of the six Lorentzian components of the spectral density of Equation 8.11. The overall anisotropic rotational diffusion ($D_{||}, D_{\perp} \approx 10^8, 10^6$ s^{-1}, corresponding to τ_0, τ_1 and τ_2 on the order of 10^{-8}, 10^{-9}, and 10^{-10} s, respectively (Equation 8.13)) as well as the faster internal motions ($\tau_{c,i} \approx 10^{-11}$) both contribute significantly to R_1 over the studied temperature range (Figure 8.12a), whilst $R_{1\rho}$ is almost exclusively dominated by the slower overall rotational diffusion (Figure 8.12b). The contribution from the correlation time τ_0 of Equation 8.11, which depends only on the slower diffusion about the short molecular axis according to ${\tau_0}^{-1} = 6D_{\perp}$ (Equation 8.13), is on the order of 10^{-8} s and dominates the $R_{1\rho}$ relaxation rates (Figure 8.12b). This component does not contribute significantly to R_1, while the faster diffusion about the long molecular axis shows a maximum contribution to R_1 at approximately 260 K, and the fast internal motion increasingly contributes at lower temperatures (Figure 8.12a). The contributions of both the fast axial molecular rotation in addition to internal motions to R_1 account for the high χ^2_{ν} values obtained from fitting the R_1 rates assuming a single motion using the SMF approach (Section 8.8), while a single dominating contribution to $R_{1\rho}$ rates is also consistent with the SMF analysis.

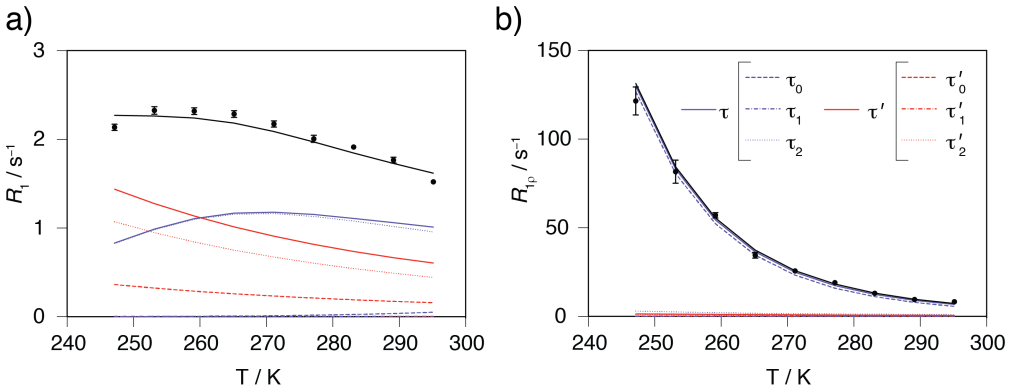

Figure 8.12: Fits of (a) R_1 and (b) $R_{1\rho}$ relaxation rates to a model for global anisotropic tumbling and restricted internal motion for a representative peak, C-4″ of octanoate. The contributions of the six Lorenztian functions of equation 8.11 to the overall relaxation rates are shown. The components defined by the overall anisotropic correlation time, τ_j, are shown in purple, for $j = 0$ (dashed line), $j = 1$ (dashed-dotted line), $j = 2$ (dotted line) and the sum (solid line). The components defined by the correlation time, $\tau_j^{'}$, which are dominated by the fast internal motion, are shown in red, for $j = 0$ (dashed line), $j = 1$ (dashed-dotted line), $j = 2$ (dotted line) and the sum (solid line).

Table 8.3: Fit parameters describing the global anisotropic tumbling of the components of CAGE-oct in the LC phase, obtained from fits of the experimental ^{13}C R_1 and $R_{1\rho}$ relaxation rates and ^{1}H-^{13}C NOE factors to the SMF formalism with overall anisotropic tumbling.

	choline	geranate[a]	octanoate
χ^2_ν	13	4.4	4.7
$E_{a,\perp}$ / kJ mol^{-1}	25.5 ± 0.9	41.3 ± 0.6	39.3 ± 0.3
$D_\perp$[b] / s^{-1}	$[1.50 \pm 0.05] \times 10^7$	$< 5 \times 10^6$	$[3.7 \pm 0.1] \times 10^6$
$E_{a,\|\|}$ / kJ mol^{-1}	57 ± 1	27 ± 3	25.1 ± 0.6
$D_\|\|$[b] / s^{-1}	$[7.0 \pm 0.3] \times 10^7$	$[7 \pm 5] \times 10^8$	$[4.2 \pm 0.1] \times 10^8$
τ_{eff}[b] /s	$[5.0 \pm 0.1] \times 10^{-9}$	$[7 \pm 3] \times 10^{-10}$	$[1.18 \pm 0.03] \times 10^{-9}$
r[b]	4.7 ± 0.3	$< 10^3$	112 ± 2

[a] θ was included as an additional fit parameter for geranate (see Section 8.3.3 for details).
[b] Diffusion coefficients, $D_\perp$ and $D_{||}$, global effective correlation time, τ_{eff}, and anisotropy ratio, r, are reported at 273 K.

Table 8.4: Fit parameters describing the internal motion for all ^{13}C sites of CAGE-oct in the LC phase, obtained from fits of the experimental ^{13}C R_1 and $R_{1\rho}$ relaxation rates and ^{1}H-^{13}C NOE factors to the SMF formalism with overall anisotropic tumbling.

		θ[a] / °	S^2_i	$E_{a,i}$ / kJ mol^{-1}	τ_i[b] / s
choline	C-3′	77	1.000	NA[c]	NA[c]
	C-1′	71	0.567 ± 0.007	59 ± 1	$[2.1 \pm 0.1] \times 10^{-10}$
	C-2′	55	0.597 ± 0.006	71 ± 1	$[1.34 \pm 0.07] \times 10^{-10}$
geranate	C-2	40 ± 19	0.5 ± 0.3	< 16	$< 5 \times 10^{-10}$
	C-9	38 ± 18	0.4 ± 0.3	< 0.02	$[1.8 \pm 0.2] \times 10^{-12}$
	C-4	64 ± 24	0.36 ± 0.08	< 5	$[1.8 \pm 0.7] \times 10^{-11}$
	C-5	46 ± 22	0.25 ± 0.09	10 ± 6	$[3 \pm 1] \times 10^{-11}$
	C-6	63 ± 27	0.4 ± 0.1	11 ± 8	$[3 \pm 2] \times 10^{-11}$
	C-8	69 ± 35	0.4 ± 0.2	13 ± 2	$[7.8 \pm 0.8] \times 10^{-12}$
	C-10	66 ± 27	0.32 ± 0.08	3 ± 5	$[1.7 \pm 0.4] \times 10^{-12}$
octanoate	C-2″	88	0.33 ± 0.01	8 ± 1	$[2.0 \pm 0.2] \times 10^{-11}$
	C-3″	87	0.264 ± 0.007	10 ± 1	$[3.3 \pm 0.1] \times 10^{-11}$
	C-4″	88	0.226 ± 0.006	10.9 ± 0.5	$[2.92 \pm 0.09] \times 10^{-11}$
	C-5″	89	0.202 ± 0.005	14.5 ± 0.6	$[2.40 \pm 0.08] \times 10^{-11}$
	C-6″	89	0.155 ± 0.004	16.9 ± 0.6	$[1.98 \pm 0.06] \times 10^{-11}$
	C-7″	89	0.108 ± 0.003	18.5 ± 0.5	$[1.73 \pm 0.04] \times 10^{-11}$
	C-8″	70	0.17 ± 0.02	16.9 ± 0.5	$[8.3 \pm 0.03] \times 10^{-12}$

[a] θ was fixed to the value obtained from the geometry optimised structures for choline and octanoate, and included as an additional fit parameter for geranate (see Section 8.3.3 for details).
[b] τ_i is reported at 273 K.
[c] $S^2_i = 1$ implies no internal motion.

Rotational diffusion coefficients for the spinning motion ($D_{||}$) of geranate and octanoate were on the order of 10^8 to 10^9 s^{-1} (at 273 K), while those for the tumbling motion ($D_{\perp}$) were 10^6 s^{-1} (Table 8.3). The anisotropy ratio, r, given by the ratio $D_{||}/D_{\perp}$, indicates that the diffusion around the long molecular axis was approximately 112 times faster than the diffusion around the short molecular axis for octanoate, while only the upper limit of $r < 10^3$ could be estimated for geranate within experimental error. $D_{\perp}$ and $D_{||}$ for the choline cation were both on the order 10^7, with a smaller anisotropy ratio of $r = 4.7$. The smaller anisotropy ratio is consistent with the smaller size of the choline cation, and the very low general order parameters, suggesting almost isotropic motion of the choline cation (Chapter 7). The timescales and activation energies describing the spinning motion for CAGE-oct are consistent with those reported for other smectic LCs, whilst the timescale for the tumbling motion on the order of 10^6 is slightly slower. For example, Domenici *et al.* reported rotational diffusion coefficients, determined from deuterium NMR for a number of smectic non-ionic LC phases, on the order of $D_{\perp} \approx 10^7$ to 10^8 s^{-1} and $D_{||} \approx 10^9$ s^{-1}, with the tumbling motion, in general, being one or two orders of magnitude smaller than the spinning motion.[304–307] In the same studies, the reported activation energies, $E_{a,\perp}, E_{a,||}$, were $\approx 30 - 70$ kJ mol^{-1}, similar to the values derived for CAGE-oct of $25 - 60$ kJ mol^{-1} (Table 8.3). The overall tumbling can be described by an effective correlation time, τ_{eff}, defined as $(2D_{||} + 4D_{\perp})^{-1}$, and is given in Table 8.3 at 273 K. τ_{eff} on the order of 10^{-9} to 10^{-10} (at 273 K), are very similar to those obtained from the SMF analysis of R_1 and $R_{1\rho}$ relaxation rates (Figure 8.9), confirming that the SMF approach is able to give a useful first approximation of the timescale of the dominating motion.

In order to investigate further the robustness of fitting the data to SMF formalism with overall anisotropic tumbling, χ^2 surfaces obtained from a grid search of $D_{\perp}$ and $D_{||}$ were investigated for each component of CAGE-oct (Figure 8.14). For the choline cation (Figure 8.14a) and octanoate (Figure 8.14b), a relatively well-defined χ^2 minimum was obtained, whilst the minimum was much shallower for gerante (Figure 8.14c). The data was initially fit with θ fixed to the values obtained from geometry optimised structures, as shown in Figure 8.14a, b and c. The angles were determined by assuming the octanoate was in the all-trans configuration, taken from the geometry optimised crystal structure of octanoic acid, whilst those of choline and geranate were taken as the average of five different low-energy conformers of CAGE (1:1 choline geranate), computed in the gas phase. While θ was consistent between conformers of choline ($\sigma < 0.9°$), the low-energy conformers of the geranate anion showed significant variation, with θ varying by up to 20° between the different conformations. Since the relative contributions of $D_{||}$ and $D_{\perp}$ to the spectral density are very sensitive to small variations in θ, errors in θ could have a large impact on the

fits. For example, for $\theta = 70°$, the coefficient, A_0 in Equation 8.11, largely governing the contribution of the slow tumbling motion ($D_\perp$), given by $A_0 = \frac{1}{4}\left(3\cos^2\theta - 1\right)^2$ (Equation 8.12), is equal to 0.11; for $\theta = 60°$, a 10° difference, $A_0 = 0.02$. As such, with no further geometry information available currently, θ was included as an additional fit parameter for geranate (see χ^2 surface in Figure 8.14d). The obtained fits showed a significant improvement ($\alpha < 0.05$, as determined by the F-test), with $\chi^2_\nu = 4.4$, compared to $\chi^2_\nu = 18$. $D_{||}$ of $\approx 10^9$ was approximately an order of magnitude larger than that obtained from the poor fit with θ fixed, and was much closer to the value obtained for octanoate. Allowing θ to vary in the fitting procedure resulted in a large uncertainty in $D_\perp$, as shown by the wider χ^2 minimum and spread of values obtained from Monte Carlo error analysis (Figure 8.14d).

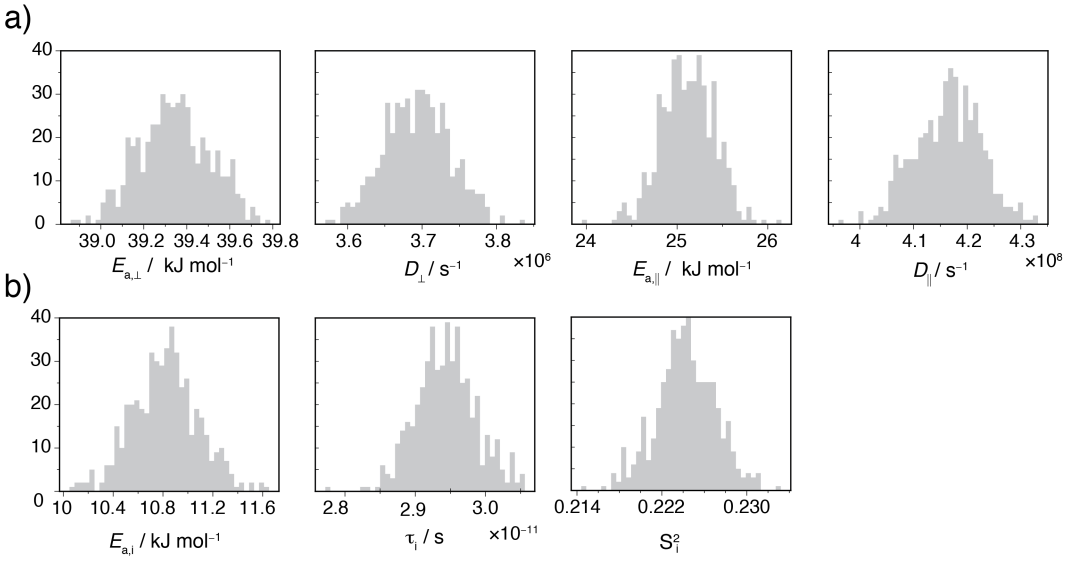

Figure 8.13: Representative histograms of the populations of 500 Monte Carlo fits SMF formalism with overall anisotropic tumbling for octanoate of CAGE-oct in the LC phase for: (a) rotational diffusion around the short and long molecular axis and (b) internal motion for a representative site, C-4″ of octanoate. Diffusion times, $D_\perp$ and $D_{||}$ and the correlation time for internal motion, τ_i, are reported at 273 K.

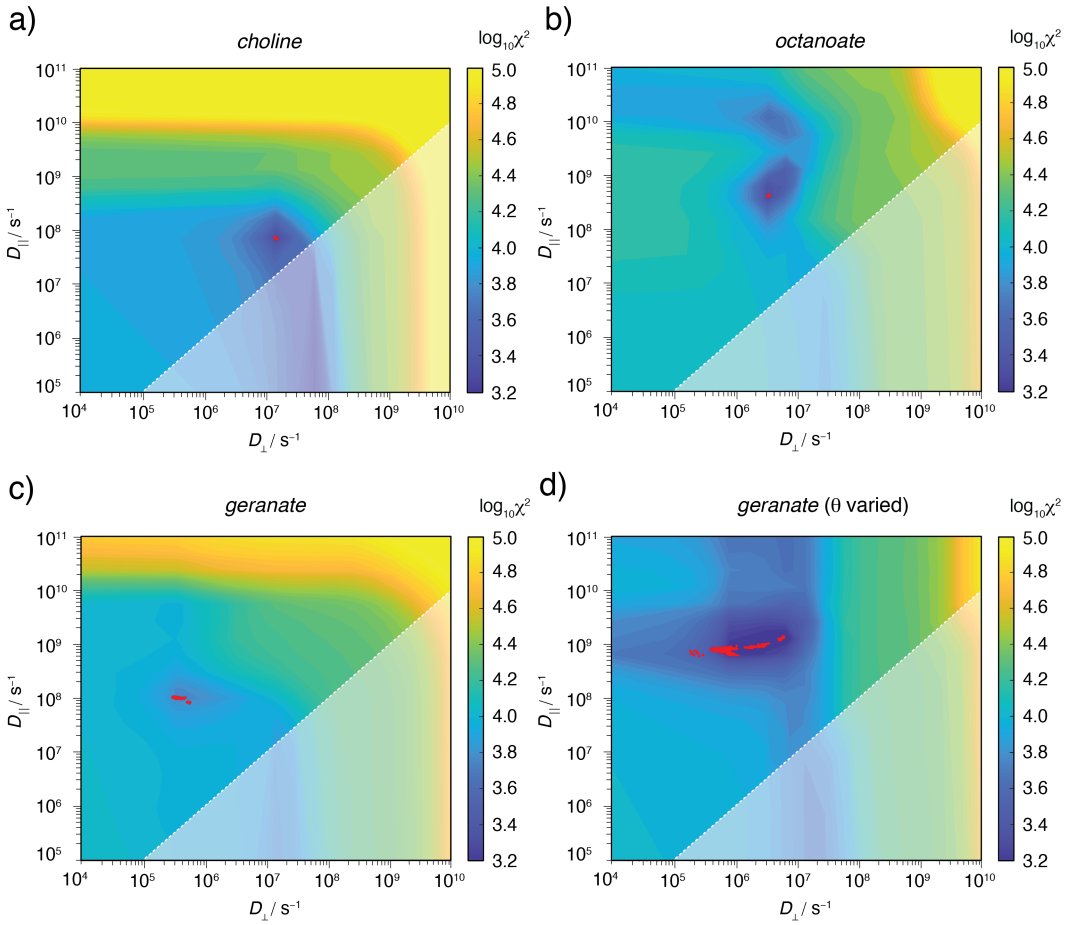

Figure 8.14: χ^2 surfaces of simulated ^{13}C R_1 and $R_{1\rho}$ relaxation rates and ^{1}H-^{13}C NOE factors to the SMF formalism with overall anisotropic tumbling at $\nu_{0H} = 500$ MHz and 700 MHz against the experimental data for varying $D_{||}$ and $D_\perp$ (at 273 K) for the components of CAGE-oct. For each value of $D_{||}$ and $D_\perp$ in the grid, the remaining global parameters ($E_{a,||}$ and $E_{a,\perp}$) and local parameters ($E_{a,i}$, S_i^2 and τ_i (a, b, c) and θ (d only)) were optimised to minimise χ^2. In (a, b, c), θ was fixed to the values obtained from geometry optimised structures (see Section 8.3.3 for details), while in (d), θ was included as an additional fit parameter. The axis limits indicate the fitting bounds for $D_{||}$ and $D_\perp$; the remaining parameters were constrained by the following bounds: $0 < E_{a,||}, E_{a,\perp}, E_{a,i} < 150$ kJ mol^{-1}, $10^{-15} < \tau_i < 10^{-9}$ s and $0 < S_i^2 < 1$. In each plot, the red points show the best fits of 500 Monte Carlo runs, obtained from varying the relaxation rates within the experimental error. The white dashed line in all plots indicates $D_{||} = D_\perp$ (i.e., isotropic rotational diffusion), with the shaded region below the line indicating that the constraint $D_{||} > D_\perp$ (i.e., rotation around the long molecular axis occurs faster than rotation around the short molecular axis) is not satisfied.

The order parameters, S_i^2, for internal motion (Table 8.4) for all sites of CAGE-oct ranged from 0.17 to 0.6 (Table 8.4), with the exception of the -N$(CH_3)_3$ group of choline which gave a high χ^2 value and showed no internal motion ($S_i^2 = 1$), apart from the fast rotation of the methyl group which was included in the fitting. S_i^2 is generally higher toward the carboxylate group for the geranate and octanoate anions, compared to the terminal end of the alkyl chain, consistent with increased range of motion of terminal end, and in agreement with the trends in the order parameters, S_{CH}, measured by RDCs reported in Chapter 7. The correlation times for internal motions, τ_i, ranging from $\approx 10^{-10}$ to 10^{-12} are consistent with those reported for flexible alkyl chains of lipid bilayer systems,[292,308] and n-alkanes of comparable chain length[309,310] The obtained correlation times, however, did not show any clear trends with position. The activation energies for internal motion, $E_{a,i}$ for octanoate, ranged from 8 to 17 kJ mol^{-1}, consistent with the energy barrier for *trans-gauche* isomerisations,[311] and the typical values reported for the internal segmental motions of other liquid crystals and ionic liquids.[64,312] $E_{a,i}$ for geranate showed a wider range for the different CH bonds, from 0 to 16 kJ mol^{-1} with larger uncertainties, whilst those of choline were significantly higher ($E_{a,i} = 59$, 71 kJ mol^{-1} for C-1$'$ and C-2$''$, respectively). The validity of the obtained activation energies could, however, be affected by the assumptions used in the data analysis; it is assumed that the internal motion occurs on a single timescale, and is uncorrelated from the overall tumbling motion. It is likely that the C-H bonds fluctuate with correlation times over a range of timescales, ranging from femtoseconds to nanoseconds, due to vibrational motion, *trans-gauche* isomerisations, and restricted segmental reorientation.

Furthermore, as stated above, in this analysis, the overall order parameter S_{CH}^2 was assumed to be zero, implying unrestricted molecular tumbling. The experimentally determined total order parameters, S_{CH}^2 are between 0.002 and 0.05, indicating that high amplitude, rather than complete, reorientations take place. It is expected that the rotation around the short molecular axis (i.e. the tumbling motion) is restricted in smectic LCs. As such, a more complex spectral density function that considers the molecular reorientations in an anisotropic potential could produce an improved analysis of the CAGE-oct LC. Hindered reorientations around the short molecular axis in CAGE-oct are still observed in this study, with the diffusion around the short molecular axis of geranate and octanoate being one or two orders of magnitude slower than the rotation around the long molecular axis, and displaying significantly higher activation energies ($\approx$25 compared to $\approx$40 kJ mol^{-1}). In addition to interactions such as dispersion forces between neighbouring molecules within the layered structure influencing the rotational diffusion, hydrogen bonding between the hydroxyl and carboxylate groups, as well as ionic interactions contribute to the structure and dynamics of CAGE-oct (as discussed in Chapter 7). Depending

on the timescale of these interactions, they could significantly influence the molecular and segmental reorientations, such that the SMF approach with anisotropic overall tumbling is a poor model for the complex dynamics. The poor fit of the choline cation, compared to geranate and octanoate, could be due to the rotational diffusion of choline being more strongly hindered by hydrogen bonding to the carboxylate anions. Additionally, in smectic LCs, where the molecules/ions are positioned, on average, in layers, translational diffusion within the layers, as well as migration between layers is possible (see Figure 8.1). Translational diffusion across the layers causes changes in orientation, which could also contribute to spin relaxation, and has not been included as an additional relaxation mechanism in this study. Overall, the fact that a consistent description of the overall molecular motion can be obtained for all positions (7 carbons) for both geranate and octanoate supports the motional model.

In the above analysis, collective motions such as order director fluctuations and layer undulations (illustrated in Figure 8.1) have not yet been considered. Such collective motions in LCs typically occur in the intermediate to slow regime (on the order of 10^{-1} to 10^{-7} s).[287] The presence of any motions on timescales slower than those already discussed would have only a small contribution to the relaxation rates, owing to the very small generalised order parameters. In the following section, the possible presence of such motions is probed by RD experiments, which are sensitive to µs-ms timescale motions.

8.4.5 ^{13}C $R_{1\rho}$ Relaxation Dispersion

In order to probe whether slow motions on the µs-ms timescale are present in CAGE-oct, ^{13}C $R_{1\rho}$ RD measurements were conducted. RD measurements investigate the dependence of $R_{1\rho}$ on the frequency of the applied *rf* spin-lock field, ν_1.[100] Under MAS, two different mechanisms can give rise to RD, which may be separated based on the selected *rf* fields. RD at low spin-lock fields, typically $\nu_1 < 10$ kHz, is due to modulation of the isotropic chemical shift. Such modulation contributes to the $R_{1\rho}$ relaxation rate when the timescale of the motion and the *rf* field are similar. With increasing *rf* field, the enhancement of $R_{1\rho}$ is suppressed, resulting in an RD profile that decreases with increasing ν_1. The modulation of anisotropic interactions can also give rise to RD profiles, when the *rf* field is in the vicinity of the near rotary-resonance conditions, $\nu_1 = n\nu_r$ $(n = 1, 2)$ in near-rotary-resonance relaxation dispersion (NERRD) experiments.[313–315] An increase in $R_{1\rho}$ when approaching the rotary-resonance condition is indicative of μs timescale motion. RD and NERRD experiments therefore provide complementary information, probing μs-ms timescale motions by modulation of the isotropic chemical shift and anisotropic interactions, respectively.

To investigate whether such motions are present in the CAGE-oct ILC, $R_{1\rho}$ RD/NERDD experiments were conducted at 273 K, at spin-lock fields ranging from 1 kHz up to close to the MAS frequency at 9.5 kHz (ν_r = 10 kHz) (Figure 8.15). No dispersion is observed for any sites of CAGE-oct at low spin-lock fields, from 1 to ∼6 kHz, indicating that either µs-ms motions are not present, or they do not modulate the isotropic chemical shift. In LCs, layer fluctuations typically occur on the µs timescale, however such motions would not be expected to modulate the isotropic chemical shift and will therefore not be detected by RD measurements. Such motions, which modulate the anisotropic dipolar coupling and CSA interactions, could, however, be observed near the rotary-resonance condition. For all sites, only a very small increase in $R_{1\rho}$ relaxation rates was observed near the rotary-resonance condition of 10 kHz (Figure 8.15). This small, sharp increase in $R_{1\rho}$ is likely due to coherent contributions due the rotary-resonance recoupling, rather than slow motion.

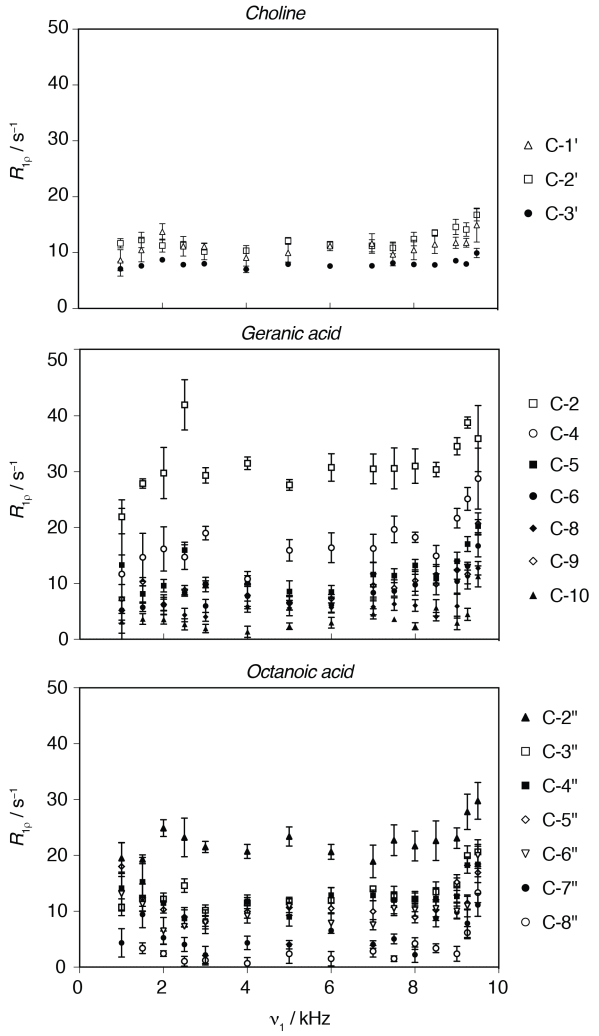

Figure 8.15: $R_{1\rho}$ RD profiles for CAGE-oct ($\nu_{0\mathrm{H}}$ = 700 MHz, ν_{r} = 10 kHz, T = 273 K).

8.5 Conclusions

In this chapter, a comprehensive MAS NMR relaxation study of the ILC, CAGE-oct, was presented. Specifically, site-specific VT relaxation measurements of ^{1}H R_1, ^{13}C R_1, ^{13}C $R_{1\rho}$, ^{1}H-^{13}C NOE, and ^{13}C $R_{1\rho}$ RD were measured. ^{1}H R_1 measurements reveal distinct differences in the dynamics of the choline cation compared to the carboxylate anions, suggesting faster reorientation. ^{13}C R_1 and $R_{1\rho}$ VT relaxation rates measured at two magnetic fields, were first analysed individually using the SMF approach to obtain estimates of the correlation times and activation energies of the dominating motions; however, this approach is unable to account for the complex dynamics of the LC phase. Likewise, considering restricted motions on two times-scales with the EMF approach was unable to describe the complete dynamics

of CAGE-oct. In particular, the results of the analysis using the SMF and EMF formalisms were inconsistent with the low overall order parameters obtained from RDCs. A significantly improved fit was obtained by assuming complete overall anisotropic tumbling and local internal motions. The analysis for geranate and octanoate produced diffusion coefficients on the order of 10^8 to 10^9 s^{-1} for the molecular spinning motion ($D_{||}$), and tumbling motions occurring on timescales two to three orders of magnitude slower ($D_{\perp} \approx 10^6$ s^{-1}). Internal motions on the ps timescale were also detected, with increasing amplitude toward the terminal end of the alkyl chains. $D_{\perp}$ and $D_{||}$ for the choline cation were both of the same order of magnitude (10^7 s^{-1}), indicating closer to isotropic reorientation. The activation energies and orders of magnitude of the correlation times are comparable to those reported for other non-ionic LCs, and ILs. The fast reorientation around the long molecular axis and significant internal motions detected in this study partly account for the low order parameters obtained from RDCs in Chapter 6, while additional motions such as reorientations around the short molecular axis are suggested to result in further averaging of the dipolar couplings. Additionally, ^{13}C $R_{1\rho}$ RD/NERDD measurements were performed, however, these did not detect any slow motions of significant amplitude in CAGE-oct at 273 K.

While the relaxation data presented in this chapter is reasonably well described by the SMF model with anisotropic tumbling, improvements can be envisioned. The validity of the derived parameters is likely to depend on the assumptions used in the analysis. Only the molecular reorientational motions and a single internal motion were considered in this analysis. The assumption of a single internal motion is far too simple to account for the complex internal dynamics that are likely to occur, and the presence of complete overall tumbling is not true for a LC where $S^2_{CH} > 0$. In order to obtain a more accurate description of the complex dynamics of the CAGE-oct LC, additional experimental techniques such as dielectric relaxation and neutron scattering may be required. Additional NMR relaxation experiments could also provide further information. For example, ^2H NMR relaxation measurements and ^1H NMR relaxometry as a function of field strength (typically at frequencies from a few kHz to MHz) have been demonstrated as ideal techniques to quantify slower collective motions that are present in LCs,[316–318] that were not detected by the measurements reported in this chapter. The incorporation of the order parameters obtained from RDCs, reported in Chapter 7, into the relaxation analysis, whilst more complex, could also result in more accurate parameters describing the dynamics of CAGE-oct.

Chapter 9

Summary and Outlook

In this work, multiple nuclear magnetic resonance (NMR) experiments are applied to a number of different ionic liquid (IL), deep eutectic solvent (DES) and ionic liquid crystal (ILC) systems that are of interest for pharmaceutical applications, in order to provide insight into their structure and dynamics. As seen in Chapter 4, the formation of ILs from numerous possible combinations of anions/cations offer the potential to tune particular properties, with small changes in structure (e.g., hydrogen bonding ability, alkyl chain length and degree of branching) shown to influence the bulk properties (proton transfer, ionicity, viscosity and conductivity). Such properties are dependent on the molecular structure of the constituents and nature of the the inter-ionic interactions. The potential of magic angle spinning (MAS) NMR to characterise key interactions at the atomic level is demonstrated in Chapter 5 for the case of a deep eutectic composed of two pain relieving compounds, lidocaine and ibuprofen. Specific intermolecular hydrogen bonding interactions were identified by ^{1}H-^{1}H nuclear Overhauser effect spectroscopy (NOESY) and rotating Overhauser effect spectroscopy (ROESY) MAS NMR experiments and the hydrogen-bonding dynamics were qualitatively determined by following the chemical exchange process between labile protons by means of variable temperature ^{1}H MAS NMR linewidth analysis. Knowledge of such hydrogen bonding interactions in liquid forms of pharmaceuticals (ILs and DESs) is crucial, with hydrogen-bonded complexes, such as Lid·Ibu, exhibiting increased membrane transport compared to commercial salt forms of the APIs. Previous studies utilised solution-state NMR at 70 °C and required analysis of a series of samples composed of varying molar ratios of lidocaine and ibuprofen to make inferences about the hydrogen bonding interactions. The results of Chapter 5 demonstrate the powerful nature of MAS NMR to study viscous systems. It is anticipated that the use of MAS NMR will prove critical in the pursuit of developing ILs and DESs as improved therapeutic agents, complementing the use of solid-state NMR in conventional solid pharmaceuticals.

Chapters 6, 7 and 8 focus on a recently reported IL composed of choline

and geranate (CAGE), which has shown significantly potential, not only as an antimicrobial agent, but also as an efficient oral and transdermal drug delivery system for a number of small-molecule drugs and biomolecules. CAGE was observed, by small-angle X-ray scattering (SAXS) and MAS NMR, to form a liquid crystal (LC) phase, which has not been reported previously in a number of publications on CAGE. Changes in CAGE, including the loss of the LC phase during storage for a period of months, was observed. Further investigation of possible degradation events and phase changes in CAGE is warranted. Solution-state NMR is shown to be useful to characterise the aqueous behaviour of ILs, with ^{1}H-^{1}H NOESY and ROESY NMR experiments utilised, in addition to diffusion ordered spectroscopy (DOSY) experiments, to investigate the phase behaviour and solubility of CAGE in water. Additionally, a series of novel CAGE analogues was reported and characterised by differential scanning calorimetry (DSC) and ^{1}H MAS NMR. Aspects of IL structure, specifically, the role of particular functional groups present in the CAGE analogues, was investigated by VT ^{1}H 1D MAS NMR, utilising the sensitivity of the ^{1}H chemical shift temperature dependence to the strength and nature of hydrogen bond interactions. Further evidence for dynamic hydrogen bonding clusters was provided by mass spectroscopy for the CAGE octanoic acid analogue (CAGE-oct), with the presence of $[(\text{choline})(\text{geranate})(\text{octanoate})]^{-}$, $[(\text{choline})(\text{octanoate})_2]^{-}$ and $[(\text{choline})(\text{geranate})_2]^{-}$ species at intensities significantly higher than expected of electrostatic ion clusters. A stable LC phase was observed for the CAGE-oct analogue by SAXS, and identified as a smectic phase by polarising optical microscopy.

Chapters 7 and 8 focus on dynamics. The power of MAS NMR to obtain site-specific information is further demonstrated in Chapter 7, with excellent resolution under 5 kHz MAS enabling all 21 distinct ^{13}C resonances of the CAGE-oct ILC to be resolved at $\nu_{0H} = 500$ MHz. Two different methods to measure the ^{1}H-^{13}C residual dipolar couplings (RDCs) were demonstrated: cross polarisation (CP) build-up curves and dipolar-coupling chemical-shift correlation (DIPSHIFT) experiments, from which the order parameters were calculated, providing information on the mobility of the individual ions and molecular segments/bonds. The complementary ^{1}H-^{1}H RDCs and the corresponding order parameters were measured by double-quantum (DQ) build-up curves. The obtained order parameters reveal that the choline cation is significantly more dynamic than the carboxylate anions, and show a mobility gradient along the alkyl chains of the geranate and octanoate anions in the LC phase. Furthermore, MAS NMR techniques were used to distinguish components based on mobility; ^{1}H DQ filtering and ^{1}H-^{13}C CP versus ^{13}C direct polarisation (DP) methods were used to detect and quantify an isotropic component coexisting with the LC phases. This is the first study utilising these techniques for the investigation of ILCs.

Chapter 8 presents extensive site-specific variable temperature (VT) relaxation measurements of ^{1}H R_1, ^{13}C R_1, ^{13}C $R_{1\rho}$, ^{1}H-^{13}C NOE, and ^{13}C $R_{1\rho}$ relaxation dispersion (RD) in the CAGE-oct ILC. Relaxation measurements provide additional information on the dynamics to the measurement of RDCs, such as the timescales and activation energies of motions occurring on a wide range of timescales ranging from ms to ps. ^{13}C relaxation rates, which are dominated by the dipolar interaction with directly bound protons, may be analysed using specific motional models; the simple model-free (SMF) approach with overall anisotropic molecular reorientation was selected in this study. While providing a reasonable fit to the experimental data, the obtained parameters are approximate, with the limitations of the model discussed. This investigation is the first use of a combination of VT R_1, $R_{1\rho}$ and NOE factors to study dynamics of an ILC. Notably, ILCs are known to undergo significantly different dynamics compared to conventional non-ionic LCs. The analysis considered only the overall anisotropic molecular reorientations and internal motions, neglecting possible contributions of translational self-diffusion and slower collective motions, which may have smaller contributions to the ^{13}C relaxation rates. Other experimental techniques, such as ^{1}H field-cycling NMR relaxometry, dielectric spectroscopy and electron paramagnetic resonance (EPR) spectroscopy could provide additional information on multiple timescales, to complement the ^{13}C MAS NMR relaxation study presented in this chapter.

Overall, this thesis has demonstrated that NMR spectroscopy represents a viable technique for measuring structure and dynamics of ILs, DESs and ILCs. These are important systems that present the potential to be developed as novel, more effective therapeutic agents that overcome many of the limitations faced by existing medicinal formulations. In order to achieve this, the characterisation of them will be critical, which highlights why the results presented within this thesis are highly impactful and beneficial for advancing this field.

Bibliography

[1] S. K. Mann, T. N. Pham, L. L. McQueen, J. R. Lewandowski, and S. P. Brown. Revealing Intermolecular Hydrogen Bonding Structure and Dynamics in a Deep Eutectic Pharmaceutical by Magic-Angle Spinning NMR Spectroscopy. *Molecular Pharmaceutics*, 17(2):622–631, 2020.

[2] S. K. Mann, M. K. Devgan, W. T. Franks, S. Huband, C. L. Chan, J. Griffith, D. Pugh, N. J. Brooks, T. Welton, T. N. Pham, L. L. McQueen, J. R. Lewandowski, and S. P. Brown. MAS NMR Investigation of Molecular Order in an Ionic Liquid Crystal. *The Journal of Physical Chemistry B*, 2020. *doi: 10.1021/acs.jpcb.0c02328*.

[3] T. Welton. Ionic Liquids: a Brief History. *Biophysical Reviews*, 10(3):691–706, 2018.

[4] P. Walden. Ueber die Molekulargrösse und Elektrische Leitfähigkeit Einiger Geschmolzenen Salze. *Bull Acad Imper Sci (St Petersburg)*, 8(6):405–422, 1914.

[5] K. R. Seddon. Ionic Liquids for Clean Technology. *Journal of Chemical Technology & Biotechnology*, 68(4):351–356, 1997.

[6] J. G. Huddleston, H. D. Willauer, R. P. Swatloski, A. E. Visser, and R. D. Rogers. Room Temperature Ionic Liquids as Novel Media for 'Clean' Liquid-Liquid Extraction. *Chemical Communications*, (16):1765–1766, 1998.

[7] H. Sun, G. Zhu, X. Xu, M. Liao, Y. Li, M. Angell, M. Gu, Y. Zhu, W. H. Hung, J. Li, Y. Kuang, Y. Meng, M.-C. Lin, H. Peng, and H. Dai. A Safe and Non-flammable Sodium Metal Battery Based on an Ionic Liquid Electrolyte. *Nature Communications*, 10(1):3302, 2019.

[8] K. Matsumoto, J. Hwang, S. Kaushik, C. Chen, and R. Hagiwara. Advances in Sodium Secondary Batteries Utilizing Ionic Liquid Electrolytes. *Energy & Environmental Science*, 12(11):3247–3287, 2019.

[9] S. M. Zakeeruddin and M. Grätzel. Solvent-Free Ionic Liquid Electrolytes for Mesoscopic Dye-Sensitized Solar Cells. *Advanced Functional Materials*, 19(14):2187–2202, 2009.

[10] M. Daz, A. Ortiz, and I. Ortiz. Progress in the Use of Ionic Liquids as Electrolyte Membranes in Fuel Cells. *Journal of Membrane Science*, 469:379–396, 2014.

[11] I. M. Gindri, D. A. Siddiqui, C. P. Frizzo, M. A. P. Martins, and D. C. Rodrigues. Ionic Liquid Coatings for Titanium Surfaces: Effect of IL Structure on Coating Profile. *ACS Applied Materials & Interfaces*, 7(49):27421–27431, 2015.

[12] C. Ye, W. Liu, Y. Chen, and L. Yu. Room-Temperature Ionic Liquids: a Novel Versatile Lubricant. *Chemical Communications*, (21):2244–2245, 2001.

[13] U. Kragl, M. Eckstein, and N. Kaftzik. Enzyme Catalysis in Ionic Liquids. *Current Opinion in Biotechnology*, 13(6):565–571, 2002.

[14] R. A. Sheldon, R. M. Lau, M. J. Sorgedrager, F. van Rantwijk, and K. R. Seddon. Biocatalysis in Ionic Liquids. *Green Chemistry*, 4(2):147–151, 2002.

[15] Z. Du, Y. L. Yu, and J. H. Wang. Extraction of Proteins from Biological Fluids by Use of an Ionic Liquid/Aqueous Two-Phase System. *Chemistry - A European Journal*, 13(7):2130–2137, 2007.

[16] K. S. Egorova, E. G. Gordeev, and V. P. Ananikov. Biological Activity of Ionic Liquids and Their Application in Pharmaceutics and Medicine. *Chemical Reviews*, 117(10):7132–7189, 2017.

[17] I. Marrucho, L. Branco, and L. P. N. Rebelo. Ionic Liquids in Pharmaceutical Applications. *Annual Review of Chemical and Biomolecular Engineering*, 5:527–546, 2014.

[18] W. L. Hough, M. Smiglak, H. Rodríguez, R. P. Swatloski, S. K. Spear, D. T. Daly, J. Pernak, J. E. Grisel, R. D. Carliss, and M. D. Soutullo. The Third Evolution of Ionic Liquids: Active Pharmaceutical Ingredients. *New Journal of Chemistry*, 31(8):1429–1436, 2007.

[19] W. L. Hough and R. D. Rogers. Ionic Liquids Then and Now: from Solvents to Materials to Active Pharmaceutical Ingredients. *Bulletin of the Chemical Society of Japan*, 80(12):2262–2269, 2007.

[20] M. Freemantle. Designer Solvents-Ionic Liquids May Boost Clean Technology Development. *Chemical & Engineering News*, 76(13):32–37, 1998.

[21] A. P. Abbott, G. Capper, D. L. Davies, R. K. Rasheed, and V. Tambyrajah. Novel Solvent Properties of Choline Chloride/Urea Mixtures. *Chemical Communications*, (1):70–71, 2003.

[22] Y. H. Choi, J. van Spronsen, Y. Dai, M. Verberne, F. Hollmann, I. W. C. E. Arends, G. Witkamp, and R. Verpoorte. Are Natural Deep Eutectic Solvents the Missing Link in Understanding Cellular Metabolism and Physiology? *Plant Physiology*, 156(4):1701, 2011.

[23] J. Stoimenovski, P. M. Dean, E. I. Izgorodina, and D. R. MacFarlane. Protic Pharmaceutical Ionic Liquids and Solids: Aspects of Protonics. *Faraday Discussions*, 154:335–352, 2012.

[24] H. J. Park and M. R. Prausnitz. Lidocaine-Ibuprofen Ionic Liquid for Dermal Anesthesia. *AIChE Journal*, 61(9):2732–2738, 2015.

[25] K. Bica, H. Rodriguez, G. Gurau, O. Andreea Cojocaru, A. Riisager, R. Fehrmann, and R. D. Rogers. Pharmaceutically Active Ionic Liquids with Solids Handling, Enhanced Thermal Stability, and Fast Release. *Chemical Communications*, 48(44):5422–5424, 2012.

[26] H. Wang, G. Gurau, J. Shamshina, O. A. Cojocaru, J. Janikowski, D. R. MacFarlane, J. H. Davis, and R. D. Rogers. Simultaneous Membrane Transport of Two Active Pharmaceutical Ingredients by Charge Assisted Hydrogen Bond Complex Formation. *Chemical Science*, 5(9):3449–3456, 2014.

[27] M. Zakrewsky, K. S. Lovejoy, T. L. Kern, T. E. Miller, V. Le, A. Nagy, A. M. Goumas, R. S. Iyer, R. E. Del Sesto, A. T. Koppisch, D. T. Fox, and S. Mitragotri. Ionic Liquids as a Class of Materials for Transdermal Delivery and Pathogen Neutralization. *Proceedings of the National Academy of Sciences*, 111(37):13313–13318, 2014.

[28] M. Zakrewsky, A. Banerjee, S. Apte, T. L. Kern, M. R. Jones, R. E. D. Sesto, A. T. Koppisch, D. T. Fox, and S. Mitragotri. Choline and Geranate Deep Eutectic Solvent as a Broad-Spectrum Antiseptic Agent for Preventive and Therapeutic Applications. *Advanced Healthcare Materials*, 5(11):1282–1289, 2016.

[29] A. Banerjee, K. Ibsen, Y. Iwao, M. Zakrewsky, and S. Mitragotri. Transdermal Protein Delivery Using Choline and Geranate (CAGE) Deep Eutectic Solvent. *Advanced Healthcare Materials*, 6(15):1601411, 2017.

[30] E. Smith, A. Abbott, and K. Ryder. Deep Eutectic Solvents (DESs) and Their Applications. *Chemical Reviews*, 114(21):11060–11082, 2014.

[31] K. Goossens, K. Lava, C. W. Bielawski, and K. Binnemans. Ionic Liquid Crystals: Versatile Materials. *Chemical Reviews*, 116(8):4643–4807, 2016.

[32] T. L. Greaves and C. J. Drummond. Solvent Nanostructure, the Solvophobic Effect and Amphiphile Self-Assembly in Ionic Liquids. *Chemical Society Reviews*, 42(3):1096–1120, 2013.

[33] Y. Wang and G. A. Voth. Unique Spatial Heterogeneity in Ionic Liquids. *Journal of the American Chemical Society*, 127(35):12192–12193, 2005.

[34] Y. Wang and G. A. Voth. Tail Aggregation and Domain Diffusion in Ionic Liquids. *The Journal of Physical Chemistry B*, 110(37):18601–18608, 2006.

[35] M. G. Del Pópolo and G. A. Voth. On the Structure and Dynamics of Ionic Liquids. *The Journal of Physical Chemistry B*, 108(5):1744–1752, 2004.

[36] S. M. Urahata and M. C. Ribeiro. Structure of Ionic Liquids of 1-Alkyl-3-methylimidazolium cations: a Systematic Computer Simulation Study. *The Journal of Chemical Physics*, 120(4):1855–1863, 2004.

[37] J. N. Canongia Lopes and A. A. Pdua. Nanostructural organization in ionic liquids. *The Journal of Physical Chemistry B*, 110(7):3330–3335, 2006.

[38] S. Byrn, R. Pfeiffer, M. Ganey, C. Hoiberg, and G. Poochikian. Pharmaceutical Solids: a Strategic Approach to Regulatory Considerations. *Pharmaceutical Research*, 12(7):945–954, 1995.

[39] B. G. Torre and F. Albericio. The Pharmaceutical Industry in 2016. An Analysis of FDA Drug Approvals from a Perspective of the Molecule Type. *Molecules*, 22(3):368, 2017.

[40] P. M. Dean, J. Turanjanin, M. Yoshizawa-Fujita, D. R. MacFarlane, and J. L. Scott. Exploring an Anti-Crystal Engineering Approach to the Preparation of Pharmaceutically Active Ionic Liquids. *Crystal Growth & Design*, 9(2):1137–1145, 2009.

[41] J. L. Shamshina, P. S. Barber, and R. D. Rogers. Ionic Liquids in Drug Delivery. *Expert Opinion on Drug Delivery*, 10(10):1367–1381, 2013.

[42] K. Bica and R. D. Rogers. Confused Ionic Liquid Ions - a "Liquification" and Dosage Strategy for Pharmaceutically Active Salts. *Chemical Communications*, 46(8):1215–1217, 2010.

[43] K. Bica, J. Shamshina, W. L. Hough, D. R. MacFarlane, and R. D. Rogers. Liquid Forms of Pharmaceutical Co-crystals: Exploring the Boundaries of Salt Formation. *Chemical Communications*, 47(8):2267–2269, 2011.

[44] J. Stoimenovski and D. R. MacFarlane. Enhanced Membrane Transport of Pharmaceutically Active Protic Ionic Liquids. *Chemical Communications*, 47(41):11429–11431, 2011.

[45] T. Welton. Room-Temperature Ionic Liquids. Solvents for Synthesis and Catalysis. *Chemical Reviews*, 99(8):2071–2084, 1999.

[46] H. D. Williams, Y. Sahbaz, L. Ford, T.-H. Nguyen, P. J. Scammells, and C. J. Porter. Ionic Liquids Provide Unique Opportunities for Oral Drug Delivery: Structure Optimization and in Vivo Evidence of Utility. *Chemical Communications*, 50(14):1688–1690, 2014.

[47] P. D. McCrary, P. A. Beasley, G. Gurau, A. Narita, P. S. Barber, O. A. Cojocaru, and R. D. Rogers. Drug Specific, Tuning of an Ionic Liquid's Hydrophilic-Lipophilic Balance to Improve Water Solubility of Poorly Soluble Active Pharmaceutical Ingredients. *New Journal of Chemistry*, 37(7):2196–2202, 2013.

[48] S. Shi, T. Yin, X. Tao, and W. Shen. Light Induced Micelle to Vesicle Transition in an Aqueous Solution of a Surface Active Ionic Liquid. *RSC Advances*, 5(92):75806–75809, 2015.

[49] R. Nakamura, M. Tokuda, T. Suzuki, and H. Minami. Preparation of Poly (Ionic Liquid) Hollow Particles with Switchable Permeability. *Langmuir*, 32(10):2331–2337, 2016.

[50] J. Kuchlyan, N. Kundu, and N. Sarkar. Ionic Liquids in Microemulsions: Formulation and Characterization. *Current Opinion in Colloid & Interface Science*, 25:27–38, 2016.

[51] E. E. L. Tanner, K. N. Ibsen, and S. Mitragotri. Transdermal Insulin Delivery Using Choline-Based Ionic Liquids (CAGE). *Journal of Controlled Release*, 286:137–144, 2018.

[52] A. Banerjee, K. Ibsen, T. Brown, R. Chen, C. Agatemor, and S. Mitragotri. Ionic Liquids for Oral Insulin Delivery. *Proceedings of the National Academy of Sciences*, 115(28):7296–7301, 2018.

[53] F. Bloch. Nuclear Induction. *Physical Review*, 70(7-8):460–474, 1946.

[54] E. M. Purcell, H. C. Torrey, and R. V. Pound. Resonance Absorption by Nuclear Magnetic Moments in a Solid. *Physical Review*, 69(1-2):37, 1946.

[55] E. Andrew, A. Bradbury, and R. Eades. Nuclear Magnetic Resonance Spectra from a Crystal Rotated at High Speed. *Nature*, 182(4650):1659–1659, 1958.

[56] E. Andrew, A. Bradbury, and R. Eades. Removal of Dipolar Broadening of Nuclear Magnetic Resonance Spectra of Solids by Specimen Rotation. *Nature*, 183(4678):1802–1803, 1959.

[57] I. Lowe. Free Induction Decays of Rotating Solids. *Physical Review Letters*, 2(7):285, 1959.

[58] K. Damodaran. Chapter 4 - Recent NMR Studies of Ionic Liquids. In *Annual Reports on NMR Spectroscopy*, volume 88, pages 215–244. Academic Press, London, 2016.

[59] R. Y. Dong. *Nuclear Magnetic Resonance of Liquid Crystals*. Springer Science & Business Media, 2012.

[60] V. Domenici. Nuclear Magnetic Resonance: a Powerful Tool to Study Liquid Crystals. *Liquid Crystals Today*, 26(1):2–10, 2017.

[61] N. Dias, K. Shimizu, P. Morgado, E. J. M. Filipe, J. N. Canongia Lopes, and F. Vaca Chávez. Charge Templates in Aromatic Plus Ionic Liquid Systems Revisited: NMR Experiments and Molecular Dynamics Simulations. *The Journal of Physical Chemistry B*, 118(21):5772–5780, 2014.

[62] V. Klimavicius, V. Bacevicius, Z. Gdaniec, and V. Balevicius. Pulsed-Field Gradient ^{1}H NMR Study of Diffusion and Self-Aggregation of Long-Chain Imidazolium-Based Ionic Liquids. *Journal of Molecular Liquids*, 210:223–226, 2015.

[63] M. Figueira-González, V. Francisco, L. García-Río, E. F. Marques, M. Parajó, and P. Rodríguez-Dafonte. Self-Aggregation Properties of Ionic Liquid 1,3-Didecyl-2-methylimidazolium Chloride in Aqueous Solution: From Spheres to Cylinders to Bilayers. *The Journal of Physical Chemistry B*, 117(10):2926–2937, 2013.

[64] J. H. Antony, D. Mertens, A. Dölle, P. Wasserscheid, and W. R. Carper. Molecular Reorientational Dynamics of the Neat Ionic Liquid 1-Butyl-3-methylimidazolium Hexafluorophosphate by Measurement of ^{13}C Nuclear Magnetic Relaxation Data. *ChemPhysChem*, 4(6):588–594, 2003.

[65] W. R. Carper, P. G. Wahlbeck, J. H. Antony, D. Mertens, A. Dölle, and P. Wasserscheid. A Bloembergen-Purcell-Pound ^{13}C NMR Relaxation Study of the Ionic Liquid 1-Butyl-3-methylimidazolium Hexafluorophosphate. *Analytical and Bioanalytical Chemistry*, 378(6):1548–1554, 2004.

[66] J. H. Antony, D. Mertens, T. Breitenstein, A. Dölle, P. Wasserscheid, and W. R. Carper. Molecular Structure, Reorientational Dynamics, and Intermolecular Interactions in the Neat Ionic Liquid 1-Butyl-3-methylimidazolium Hexafluorophosphate. *Pure and Applied Chemistry*, 76(1):255–261, 2004.

[67] N. E. Heimer, J. S. Wilkes, P. G. Wahlbeck, and W. R. Carper. ^{13}C NMR Relaxation Rates in the Ionic Liquid 1-Ethyl-3-methylimidazolium Butanesulfonate. *The Journal of Physical Chemistry A*, 110(3):868–874, 2006.

[68] P. G. Wahlbeck and W. R. Carper. Separation of ^{13}C NMR Relaxation Mechanisms in Viscous Solutions. *Chemical Engineering Communications*, 194(9):1160–1168, 2007.

[69] S. Khatun and E. W. Castner. Ionic Liquid-Solute Interactions Studied by 2D NOE NMR Spectroscopy. *The Journal of Physical Chemistry B*, 119(29):9225–9235, 2015.

[70] A. Rencurosi, L. Lay, G. Russo, D. Prosperi, L. Poletti, and E. Caneva. HRMAS NMR Analysis in Neat Ionic Liquids: a Powerful Tool to Investigate Complex Organic Molecules and Monitor Chemical Reactions. *Green Chemistry*, 9(3):216–218, 2007.

[71] C. Mrestani-Klaus, A. Richardt, C. Wespe, A. Stark, E. Humpfer, and F. Bordusa. Structural Studies on Ionic Liquid/Water/Peptide Systems by HR-MAS NMR Spectroscopy. *ChemPhysChem*, 13(7):1836–1844, 2012.

[72] L. Warner, E. Gjersing, S. E. Follett, K. W. Elliott, S. V. Dzyuba, and K. Varga. The Effects of High Concentrations of Ionic Liquid on GB1 Protein Structure and Dynamics Probed by High-Resolution Magic-Angle-Spinning NMR Spectroscopy. *Biochemistry and Biophysics Reports*, 8:75–80, 2016.

[73] S. Brenna, T. Posset, J. Furrer, and J. Blümel. ^{14}N NMR and Two-Dimensional Suspension ^{1}H and ^{13}C HRMAS NMR Spectroscopy of Ionic Liquids Immobilized on Silica. *Chemistry - A European Journal*, 12(10):2880–2888, 2006.

[74] R. Lungwitz and S. Spange. Structure and Polarity of the Phase Boundary of N-Methylimidazolium Chloride/Silica. *The Journal of Physical Chemistry C*, 112(49):19443–19448, 2008.

[75] C. Jouannin, C. Tourné-Péteilh, V. Darcos, T. Sharkawi, J.-M. Devoisselle, P. Gaveau, P. Dieudonné, A. Vioux, and L. Viau. Drug Delivery Systems Based on Pharmaceutically Active Ionic Liquids and Biocompatible Poly (Lactic Acid). *Journal of Materials Chemistry B*, 2(20):3133–3141, 2014.

[76] K. Higashi, K. Yamamoto, M. K. Pandey, K. H. Mroue, K. Moribe, K. Yamamoto, and A. Ramamoorthy. Insights into Atomic-level Interaction between Mefenamic Acid and Eudragit® EPO in a Supersaturated Solution by High-Resolution Magic-Angle Spinning NMR Spectroscopy. *Molecular Pharmaceutics*, 11(1):351–357, 2014.

[77] R. Y. Dong and X. Shen. Dynamics of a Liquid Crystal by Deuterium NMR: The Analysis of Director Fluctuations and Reorientation of Molecules. *The Journal of Physical Chemistry A*, 101(26):4673–4678, 1997.

[78] K. Schmidt-Rohr, D. Nanz, L. Emsley, and A. Pines. NMR Measurement of Resolved Heteronuclear Dipole Couplings in Liquid Crystals and Lipids. *The Journal of Physical Chemistry*, 98(27):6668–6670, 1994.

[79] G. Lindblom and G. Orädd. NMR Studies of Translational Diffusion in Lyotropic Liquid Crystals and Lipid Membranes. *Progress in Nuclear Magnetic Resonance Spectroscopy*, 26:483–515, 1994.

[80] S. V. Dvinskikh. Nuclear Magnetic Resonance Studies of Translational Diffusion in Thermotropic Ionic Liquid Crystals. *Liquid Crystals*, 2019. *doi: 10.1080/02678292.2019.1647569.*

[81] P. Sebastião, A. Gradiek, L. Pinto, T. Apih, M. Godinho, and M. Vilfan. Fast Field-Cycling NMR Relaxometry Study of Chiral and Nonchiral Nematic Liquid Crystals. *The Journal of Physical Chemistry B*, 115:14348–58, 2011.

[82] J. W. Emsley. NMR Methods of Studying Orientational Order in the Liquid Crystalline and Isotropic Phases of Mesogenic Samples. *Liquid Crystals*, 32(11-12):1515–1524, 2005.

[83] R. K. Hester, J. L. Ackerman, B. L. Neff, and J. S. Waugh. Separated Local Field Spectra in NMR: Determination of Structure of Solids. *Physical Review Letters*, 36(18):1081–1083, 1976.

[84] S. Dvinskikh. Chapter 13 - Characterization of Liquid-crystalline Materials by Separated Local Field Methods. In *Modern Methods in Solid-State NMR*, pages 391–423. Royal Society of Chemistry, Croydon, 2018.

[85] A. Ramamoorthy, Y. Wei, and D.-K. Lee. PISEMA Solid-State NMR Spectroscopy. In *Annual Reports on NMR Spectroscopy*, volume 52, pages 1–52. Academic Press, 2004.

[86] J. D. Gross, D. E. Warschawski, and R. G. Griffin. Dipolar Recoupling in MAS NMR: A Probe for Segmental Order in Lipid Bilayers. *Journal of the American Chemical Society*, 119(4):796–802, 1997.

[87] W. Guo and B. Fung. Determination of the Order Parameters of Liquid Crystals from ^{13}C Chemical Shifts. *The Journal of Chemical Physics*, 95:3917–3923, 1991.

[88] M. Hong, K. Schmidt-Rohr, and D. Nanz. Study of Phospholipid Structure by ^{1}H, ^{13}C, and ^{31}P Dipolar Couplings from Two-Dimensional NMR. *Biophysical Journal*, 69(5):1939–1950, 1995.

[89] J. Keeler. *Understanding NMR Spectroscopy*. John Wiley and Sons, Chichester, U.K, second edition, 2010.

[90] M. H. Levitt. *Spin Dynamics: Basics of Nuclear Magnetic Resonance*. Wiley, Chichester, second edition, 2008.

[91] D. C. Apperley, R. K. Harris, and P. Hodgkinson. *Solid-State NMR: Basic Principles & Practice*. Momentum Press, New York, 2012.

[92] M. J. Duer. *Introduction to Solid-State NMR Spectroscopy*. Blackwell Publishing Ltd, Oxford, 2004.

[93] J. Kowalewski and L. Maler. *Nuclear Spin Relaxation in Liquids*. CRC Press, Boca Raton, second edition, 2018.

[94] G. Lipari and A. Szabo. Model-Free Approach to the Interpretation of Nuclear Magnetic Resonance Relaxation in Macromolecules. 1. Theory and Range of Validity. *Journal of the American Chemical Society*, 104(17):4546–4559, 1982.

[95] G. Lipari and A. Szabo. Model-Free Approach to the Interpretation of Nuclear Magnetic Resonance Relaxation in Macromolecules. 2. Analysis of Experimental Results. *Journal of the American Chemical Society*, 104(17):4559–4570, 1982.

[96] G. M. Clore, A. Szabo, A. Bax, L. E. Kay, P. C. Driscoll, and A. M. Gronenborn. Deviations from the Simple Two-Parameter Model-Free Approach to the Interpretation of Nitrogen-15 Nuclear Magnetic Relaxation of Proteins. *Journal of the American Chemical Society*, 112(12):4989–4991, 1990.

[97] I. Solomon. Relaxation Processes in a System of Two Spins. *Physical Review*, 99:559–565, 1955.

[98] R. Kurbanov, T. Zinkevich, and A. Krushelnitsky. The Nuclear Magnetic Resonance Relaxation Data Analysis in Solids: General $R_1/R_{1\rho}$ Equations and the Model-Free Approach. *The Journal of Chemical Physics*, 135(18):184104, 2011.

[99] J. M. Lamley, C. Öster, R. A. Stevens, and J. R. Lewandowski. Intermolecular Interactions and Protein Dynamics by Solid-State NMR Spectroscopy. *Angewandte Chemie International Edition*, 54(51):15374–15378, 2015.

[100] H. M. McConnell. Reaction Rates by Nuclear Magnetic Resonance. *The Journal of Chemical Physics*, 28(3):430–431, 1958.

[101] G. A. Morris and R. Freeman. Enhancement of Nuclear Magnetic Resonance Signals by Polarization Transfer. *Journal of the American Chemical Society*, 101(3):760–762, 1979.

[102] D. P. Burum and R. R. Ernst. Net Polarization Transfer via a J-Ordered State for Signal Enhancement of Low-Sensitivity Nuclei. *Journal of Magnetic Resonance (1969)*, 39(1):163–168, 1980.

[103] S. R. Hartmann and E. L. Hahn. Nuclear Double Resonance in the Rotating Frame. *Physical Review*, 128(5):2042–2053, 1962.

[104] A. Nowacka, P. C. Mohr, J. Norrman, R. W. Martin, and D. Topgaard. Polarization Transfer Solid-State NMR for Studying Surfactant Phase Behavior. *Langmuir*, 26(22):16848–16856, 2010.

[105] G. Metz, X. L. Wu, and S. O. Smith. Ramped-Amplitude Cross Polarization in Magic-Angle-Spinning NMR. *Journal of Magnetic Resonance, Series A*, 110(2):219–227, 1994.

[106] S. Hediger, B. H. Meier, N. D. Kurur, G. Bodenhausen, and R. R. Ernst. NMR Cross Polarization by Adiabatic Passage Through the Hartmann-Hahn Condition (APHH). *Chemical Physics Letters*, 223(4):283–288, 1994.

[107] A. Kubo and C. A. McDowell. Spectral Spin Diffusion in Polycrystalline Solids under Magic-Angle Spinning. *Journal of the Chemical Society, Faraday Transactions 1: Physical Chemistry in Condensed Phases*, 84(11):3713–3730, 1988.

[108] B. H. Meier. Polarization Transfer and Spin Diffusion in Solid-State NMR. *Advances in Magnetic and Optical Resonance*, 18:1–116, 1994.

[109] M. Hohwy, H. J. Jakobsen, M. Edn, M. H. Levitt, and N. C. Nielsen. Broadband Dipolar Recoupling in the Nuclear Magnetic Resonance of Rotating Solids: A Compensated C7 Pulse Sequence. *The Journal of Chemical Physics*, 108(7):2686–2694, 1998.

[110] L. Müller, A. Kumar, T. Baumann, and R. R. Ernst. Transient Oscillations in NMR Cross-Polarization Experiments in Solids. *Physical Review Letters*, 32(25):1402–1406, 1974.

[111] M. Lee and W. I. Goldburg. Nuclear-Magnetic-Resonance Line Narrowing by a Rotating rf Field. *Physical Review*, 140(4A):A1261–A1271, 1965.

[112] B. J. van Rossum, C. P. de Groot, V. Ladizhansky, S. Vega, and H. J. M. de Groot. A Method for Measuring Heteronuclear (^{1}H-^{13}C) Distances in High Speed MAS NMR. *Journal of the American Chemical Society*, 122(14):3465–3472, 2000.

[113] V. Ladizhansky and S. Vega. Polarization Transfer Dynamics in Lee-Goldburg Cross Polarization Nuclear Magnetic Resonance Experiments on Rotating Solids. *The Journal of Chemical Physics*, 112(16):7158–7168, 2000.

[114] M. Bak, J. T. Rasmussen, and N. C. Nielsen. SIMPSON: A General Simulation Program for Solid-State NMR Spectroscopy. *Journal of Magnetic Resonance*, 147(2):296–330, 2000.

[115] M. G. Munowitz, R. G. Griffin, G. Bodenhausen, and T. H. Huang. Two-Dimensional Rotational Spin-Echo Nuclear Magnetic Resonance in Solids: Correlation of Chemical Shift and Dipolar Interactions. *Journal of the American Chemical Society*, 103(10):2529–2533, 1981.

[116] M. Hong, J. D. Gross, and R. G. Griffin. Site-Resolved Determination of Peptide Torsion Angle ϕ from the Relative Orientations of Backbone N–H and C–H Bonds by Solid-State NMR. *The Journal of Physical Chemistry B*, 101(30):5869–5874, 1997.

[117] M. F. Cobo, A. Achilles, D. Reichert, E. R. deAzevedo, and K. Saalwächter. Recoupled Separated-Local-Field Experiments and Applications to Study Intermediate-Regime Molecular Motions. *Journal of Magnetic Resonance*, 221:85–96, 2012.

[118] T. Gullion and J. Schaefer. Rotational-echo double-resonance NMR. *Journal of Magnetic Resonance (1969)*, 81(1):196–200, 1989.

[119] B. M. Fung, A. K. Khitrin, and K. Ermolaev. An Improved Broadband Decoupling Sequence for Liquid Crystals and Solids. *Journal of Magnetic Resonance*, 142(1):97–101, 2000.

[120] J. P. Bradley, C. Tripon, C. Filip, and S. P. Brown. Determining Relative Proton-Proton Proximities from the Build-Up of Two-Dimensional Correlation Peaks in ^{1}H Double-Quantum MAS NMR: Insight from Multi-Spin Density-Matrix Simulations. *Physical Chemistry Chemical Physics*, 11(32):6941–6952, 2009.

[121] R. Graf, A. Heuer, and H. W. Spiess. Chain-Order Effects in Polymer Melts Probed by ^{1}H Double-Quantum NMR Spectroscopy. *Physical Review Letters*, 80(26):5738–5741, 1998.

[122] K. Saalwächter, P. Ziegler, O. Spyckerelle, B. Haidar, A. Vidal, and J.-U. Sommer. ^{1}H Multiple-Quantum Nuclear Magnetic Resonance Investigations of Molecular Order Distributions in Poly(dimethylsiloxane) Networks: Evidence for a Linear Mixing Law in Bimodal Systems. *The Journal of Chemical Physics*, 119(6):3468–3482, 2003.

[123] K. Saalwächter. Methyl Groups as Local Probes for Polymer Dynamics as Investigated by ^{1}H Double-Quantum Magic-Angle Spinning NMR Spectroscopy. *Chemical Physics Letters*, 362(3):331–340, 2002.

[124] K. Saalwächter. ^{1}H Multiple-Quantum Nuclear Magnetic Resonance Investigations of Molecular Order in Polymer Networks. II. Intensity Decay and Restricted Slow Dynamics. *The Journal of Chemical Physics*, 120(1):454–464, 2004.

[125] K. Saalwächter, B. Herrero, and M. A. López-Manchado. Chain Order and Cross-Link Density of Elastomers As Investigated by Proton Multiple-Quantum NMR. *Macromolecules*, 38(23):9650–9660, 2005.

[126] K. Saalwächter and A. Heuer. Chain Dynamics in Elastomers As Investigated by Proton Multiple-Quantum NMR. *Macromolecules*, 39(9):3291–3303, 2006.

[127] V. E. Zorin, S. P. Brown, and P. Hodgkinson. Quantification of Homonuclear Dipolar Coupling Networks from Magic-Angle Spinning ^{1}H NMR. *Molecular Physics*, 104(2):293–304, 2006.

[128] J. Ren and H. Eckert. DQ-DRENAR: A New NMR Technique to Measure Site-Resolved Magnetic Dipole-Dipole Interactions in Multispin-1/2 Systems: Theory and Validation on Crystalline Phosphates. *The Journal of Chemical Physics*, 138(16):164201, 2013.

[129] W. Chassé, J. L. o. p. Valentín, G. D. Genesky, C. Cohen, and K. Saalwächter. Precise Dipolar Coupling Constant Distribution Analysis in Proton Multiple-Quantum NMR of Elastomers. *The Journal of Chemical Physics*, 134(4):044907, 2011.

[130] L. E. Kay, L. K. Nicholson, F. Delaglio, A. Bax, and D. A. Torchia. Pulse Sequences for Removal of the Effects of Cross Correlation Between Dipolar and Chemical-Shift Anisotropy Relaxation Mechanisms on the Measurement of Heteronuclear T_1 and T_2 Values in Proteins. *Journal of Magnetic Resonance (1969)*, 97(2):359–375, 1992.

[131] N. V. Plechkova and K. R. Seddon. Applications of Ionic Liquids in the Chemical Industry. *Chemical Society Reviews*, 37(1):123–150, 2008.

[132] T. L. Greaves and C. J. Drummond. Protic Ionic Liquids: Properties and Applications. *Chemical Reviews*, 108(1):206–237, 2008.

[133] D. R. MacFarlane, J. M. Pringle, K. M. Johansson, S. A. Forsyth, and M. Forsyth. Lewis Base Ionic Liquids. *Chemical Communications*, (18):1905–1917, 2006.

[134] J. Stoimenovski, E. I. Izgorodina, and D. R. MacFarlane. Ionicity and Proton Transfer in Protic Ionic Liquids. *Physical Chemistry Chemical Physics*, 12(35):10341–10347, 2010.

[135] A. Knorr, P. Stange, K. Fumino, F. Weinhold, and R. Ludwig. Spectroscopic Evidence for Clusters of Like-Charged Ions in Ionic Liquids Stabilized by Cooperative Hydrogen Bonding. *ChemPhysChem*, 17(4):458–462, 2016.

[136] F. Kohler, H. Atrops, H. Kalali, E. Liebermann, E. Wilhelm, F. Ratkovics, and T. Salamon. Molecular Interactions in Mixtures of Carboxylic Acids with Amines. 1. Melting Curves and Viscosities. *The Journal of Physical Chemistry*, 85(17):2520–2524, 1981.

[137] F. Kohler, R. Gopal, G. Goetze, H. Atrops, M. Demeriz, E. Liebermann, E. Wilhelm, F. Ratkovics, and B. Palagyi. Molecular Interactions in Mixtures of Carboxylic Acids with Amines. 2. Volumetric, Conductimetric, and NMR Properties. *The Journal of Physical Chemistry*, 85(17):2524–2529, 1981.

[138] C. A. Angell, N. Byrne, and J.-P. Belieres. Parallel Developments in Aprotic and Protic Ionic Liquids: Physical Chemistry and Applications. *Accounts of Chemical Research*, 40(11):1228–1236, 2007.

[139] W. Xu, E. I. Cooper, and C. A. Angell. Ionic Liquids: Ion Mobilities, Glass Temperatures, and Fragilities. *The Journal of Physical Chemistry B*, 107(25):6170–6178, 2003.

[140] M. Yoshizawa, W. Xu, and C. A. Angell. Ionic Liquids by Proton Transfer: Vapor Pressure, Conductivity, and the Relevance of ΔpK_a from Aqueous Solutions. *Journal of the American Chemical Society*, 125(50):15411–15419, 2003.

[141] C. Zhao, G. Burrell, A. A. J. Torriero, F. Separovic, N. F. Dunlop, D. R. MacFarlane, and A. M. Bond. Electrochemistry of Room Temperature Protic Ionic Liquids. *The Journal of Physical Chemistry B*, 112(23):6923–6936, 2008.

[142] D. R. MacFarlane, M. Forsyth, E. I. Izgorodina, A. P. Abbott, G. Annat, and K. Fraser. On the Concept of Ionicity in Ionic Liquids. *Physical Chemistry Chemical Physics*, 11(25):4962–4967, 2009.

[143] C. Schreiner, S. Zugmann, R. Hartl, and H. J. Gores. Fractional Walden Rule for Ionic Liquids: Examples from Recent Measurements and a Critique of the So-Called Ideal KCl Line for the Walden Plot. *Journal of Chemical & Engineering Data*, 55(5):1784–1788, 2010.

[144] N. Agmon. The Grotthuss Mechanism. *Chemical Physics Letters*, 244(5):456–462, 1995.

[145] K.-D. Kreuer. Proton Conductivity: Materials and Applications. *Chemistry of Materials*, 8(3):610–641, 1996.

[146] M. Anouti, J. Jacquemin, and P. Porion. Transport Properties Investigation of Aqueous Protic Ionic Liquid Solutions through Conductivity, Viscosity, and NMR Self-Diffusion Measurements. *The Journal of Physical Chemistry B*, 116(14):4228–4238, 2012.

[147] A. Noda, M. A. B. H. Susan, K. Kudo, S. Mitsushima, K. Hayamizu, and M. Watanabe. Brønsted Acid-Base Ionic Liquids as Proton-Conducting Nonaqueous Electrolytes. *The Journal of Physical Chemistry B*, 107(17):4024–4033, 2003.

[148] Z. Wojnarowska, Y. Wang, K. J. Paluch, A. P. Sokolov, and M. Paluch. Observation of Highly Decoupled Conductivity in Protic Ionic Conductors. *Physical Chemistry Chemical Physics*, 16(19):9123–9127, 2014.

[149] S. Zahn, F. Uhlig, J. Thar, C. Spickermann, and B. Kirchner. Intermolecular Forces in an Ionic Liquid ([Mmim][Cl]) versus Those in a Typical Salt (NaCl). *Angewandte Chemie International Edition*, 47(19):3639–3641, 2008.

[150] P. A. Hunt, C. R. Ashworth, and R. P. Matthews. Hydrogen Bonding in Ionic Liquids. *Chemical Society Reviews*, 44(5):1257–1288, 2015.

[151] D. R. MacFarlane, A. L. Chong, M. Forsyth, M. Kar, R. Vijayaraghavan, A. Somers, and J. M. Pringle. New Dimensions in Salt-Solvent Mixtures: a 4th Evolution of Ionic Liquids. *Faraday Discussions*, 206:9–28, 2018.

[152] K. M. Johansson, E. I. Izgorodina, M. Forsyth, D. R. MacFarlane, and K. R. Seddon. Protic Ionic Liquids Based on the Dimeric and Oligomeric Anions: $[(AcO)_xH_{x-1}]^-$. *Physical Chemistry Chemical Physics*, 10(20):2972–2978, 2008.

[153] T. Steiner. The Hydrogen Bond in the Solid State. *Angewandte Chemie International Edition*, 41(1):48–76, 2002.

[154] N. M. Vargas-Barbosa and B. Roling. Dynamic Ion Correlations in Solid and Liquid Electrolytes: How Do They Affect Charge and Mass Transport? *ChemElectroChem*, 7(2):367–385, 2020.

[155] R. Hayes, G. G. Warr, and R. Atkin. Structure and Nanostructure in Ionic Liquids. *Chemical Reviews*, 115(13):6357–6426, 2015.

[156] J. N. A. Canongia Lopes and A. A. H. Pádua. Nanostructural Organization in Ionic Liquids. *The Journal of Physical Chemistry B*, 110(7):3330–3335, 2006.

[157] A. Triolo, O. Russina, H.-J. Bleif, and E. Di Cola. Nanoscale Segregation in Room Temperature Ionic Liquids. *The Journal of Physical Chemistry B*, 111(18):4641–4644, 2007.

[158] K. Ueno, H. Tokuda, and M. Watanabe. Ionicity in Ionic Liquids: Correlation with Ionic Structure and Physicochemical Properties. *Physical Chemistry Chemical Physics*, 12(8):1649–1658, 2010.

[159] P. J. Griffin, Y. Wang, A. P. Holt, and A. P. Sokolov. Communication: Influence of Nanophase Segregation on Ion Transport in Room Temperature Ionic Liquids. *The Journal of Chemical Physics*, 144(15):151104, 2016.

[160] R. Atkin and G. G. Warr. The Smallest Amphiphiles: Nanostructure in Protic Room-Temperature Ionic Liquids with Short Alkyl Groups. *The Journal of Physical Chemistry B*, 112(14):4164–4166, 2008.

[161] T. L. Greaves, D. F. Kennedy, S. T. Mudie, and C. J. Drummond. Diversity Observed in the Nanostructure of Protic Ionic Liquids. *The Journal of Physical Chemistry B*, 114(31):10022–10031, 2010.

[162] P. Bonhôte, A.-P. Dias, M. Armand, N. Papageorgiou, K. Kalyanasundaram, and M. Grätzel. Hydrophobic, Highly Conductive Ambient-Temperature Molten Salts. *Inorganic Chemistry*, 37(1):166–166, 1998.

[163] P. Bonhôte, A.-P. Dias, N. Papageorgiou, K. Kalyanasundaram, and M. Grätzel. Hydrophobic, Highly Conductive Ambient-Temperature Molten Salts. *Inorganic Chemistry*, 35(5):1168–1178, 1996.

[164] A. P. Abbott. Model for the Conductivity of Ionic Liquids Based on an Infinite Dilution of Holes. *ChemPhysChem*, 6(12):2502–2505, 2005.

[165] H. Watanabe, T. Umecky, N. Arai, A. Nazet, T. Takamuku, K. R. Harris, Y. Kameda, R. Buchner, and Y. Umebayashi. Possible Proton Conduction Mechanism in Pseudo-Protic Ionic Liquids: A Concept of Specific Proton Conduction. *The Journal of Physical Chemistry B*, 123(29):6244–6252, 2019.

[166] J. L. Shamshina, P. Berton, H. Wang, X. Zhou, G. Gurau, and R. D. Rogers. Chapter 20 - Ionic Liquids in Pharmaceutical Industry. In *Green Techniques for Organic Synthesis and Medicinal Chemistry*. John Wiley and Sons, Hoboken, second edition, 2018.

[167] C. B. Martins Inês, M. C. Oliveira, P. Diogo Hermínio, C. Branco Luís, and M. T. Duarte. MechanoAPI-ILs: Pharmaceutical Ionic Liquids Obtained through Mechanochemical Synthesis. *ChemSusChem*, 10(7):1360–1363, 2017.

[168] W. L. Hough and R. D. Rogers. Ionic Liquids Then and Now: From Solvents to Materials to Active Pharmaceutical Ingredients. *Bulletin of the Chemical Society of Japan*, 80(12):2262–2269, 2007.

[169] Y. Sahbaz, H. D. Williams, T.-H. Nguyen, J. Saunders, L. Ford, S. A. Charman, P. J. Scammells, and C. J. H. Porter. Transformation of Poorly Water-Soluble Drugs into Lipophilic Ionic Liquids Enhances Oral Drug Exposure from Lipid Based Formulations. *Molecular Pharmaceutics*, 12(6):1980–1991, 2015.

[170] J. L. Shamshina, O. A. Cojocaru, S. P. Kelley, K. Bica, S. P. Wallace, G. Gurau, and R. D. Rogers. Acyclovir as an Ionic Liquid Cation or Anion Can Improve Aqueous Solubility. *ACS Omega*, 2(7):3483–3493, 2017.

[171] C. Mrestani-Klaus, A. Richardt, C. Wespe, A. Stark, E. Humpfer, and F. Bordusa. Structural Studies on Ionic Liquid/Water/Peptide Systems by HR-MAS NMR Spectroscopy. *ChemPhysChem*, 13(7):1836–1844, 2012.

[172] A. P. Abbott, D. Boothby, G. Capper, D. L. Davies, and R. K. Rasheed. Deep Eutectic Solvents Formed between Choline Chloride and Carboxylic Acids: Versatile Alternatives to Ionic Liquids. *Journal of the American Chemical Society*, 126(29):9142–9147, 2004.

[173] M. J. O'Neil. *The Merck Index: an Encyclopedia of Chemicals, Drugs, and Biologicals*. Wiley, 14th edition, 2006.

[174] P. Berton, K. R. Di Bona, D. Yancey, S. A. A. Rizvi, M. Gray, G. Gurau, J. L. Shamshina, J. F. Rasco, and R. D. Rogers. Transdermal Bioavailability in Rats of Lidocaine in the Forms of Ionic Liquids, Salts, and Deep Eutectic. *ACS Medicinal Chemistry Letters*, 8(5):498–503, 2017.

[175] G. Metz, M. Ziliox, and S. O. Smith. Towards Quantitative CP-MAS NMR. *Solid State Nuclear Magnetic Resonance*, 7(3):155–160, 1996.

[176] D. Marion, M. Ikura, R. Tschudin, and A. Bax. Rapid Recording of 2D NMR Spectra Without Phase Cycling. Application to the Study of Hydrogen Exchange in Proteins. *Journal of Magnetic Resonance (1969)*, 85(2):393–399, 1989.

[177] S. Hayashi and K. Hayamizu. Chemical Shift Standards in High-Resolution Solid-State NMR (1) ^{13}C, ^{29}Si, and ^{1}H Nuclei. *Bulletin of the Chemical Society of Japan*, 64(2):685–687, 1991.

[178] C. R. Morcombe and K. W. Zilm. Chemical Shift Referencing in MAS Solid State NMR. *Journal of Magnetic Resonance*, 162(2):479–486, 2003.

[179] R. Sarkar, A. Mainz, B. Busi, E. Barbet-Massin, M. Kranz, T. Hofmann, and B. Reif. Immobilization of Soluble Protein Complexes in MAS Solid-State NMR: Sedimentation Versus Viscosity. *Solid State Nuclear Magnetic Resonance*, 76-77:7–14, 2016.

[180] N. Müller and R. C. Reiter. Temperature Dependence of Chemical Shifts of Protons in Hydrogen Bonds. *The Journal of Chemical Physics*, 42(9):3265–3269, 1965.

[181] J. T. Arnold and M. E. Packard. Variations in Absolute Chemical Shift of Nuclear Induction Signals of Hydroxyl Groups of Methyl and Ethyl Alcohol. *The Journal of Chemical Physics*, 19(12):1608–1609, 1951.

[182] U. Liddel and N. F. Ramsey. Temperature Dependent Magnetic Shielding in Ethyl Alcohol. *The Journal of Chemical Physics*, 19(12):1608–1608, 1951.

[183] K. Modig and B. Halle. Proton Magnetic Shielding Tensor in Liquid Water. *Journal of the American Chemical Society*, 124(40):12031–12041, 2002.

[184] Y. Li, Y. Jia, Z. Wang, X. Li, W. Feng, P. Deng, and L. Yuan. An Insight into the Extraction of Transition Metal Ions by Picolinamides Associated with Intramolecular Hydrogen Bonding and Rotational Isomerization. *RSC Advances*, 4(56):29702–29714, 2014.

[185] A. L. Webber, B. Elena, J. M. Griffin, J. R. Yates, T. N. Pham, F. Mauri, C. J. Pickard, A. M. Gil, R. Stein, A. Lesage, L. Emsley, and S. P. Brown. Complete ^{1}H Resonance Assignment of β-Maltose from ^{1}H-^{1}H DQ-SQ CRAMPS and ^{1}H (DQ-DUMBO)-^{13}C SQ Refocused INEPT 2D Solid-State NMR Spectra and First Principles GIPAW Calculations. *Physical Chemistry Chemical Physics*, 12(26):6970–6983, 2010.

[186] S. P. Brown, I. Schnell, J. D. Brand, K. Mullen, and H. W. Spiess. The Competing Effects of $\pi - \pi$ Packing and Hydrogen Bonding in a Hexabenzocoronene Carboxylic Acid Derivative: a ^{1}H Solid-State MAS NMR Investigation. *Physical Chemistry Chemical Physics*, 2(8):1735–1745, 2000.

[187] J. Dumez and C. J. Pickard. Calculation of NMR Chemical Shifts in Organic Solids: Accounting for Motional Effects. *The Journal of Chemical Physics*, 130(10):104701, 2009.

[188] R. K. Khankari and D. J. W. Grant. Pharmaceutical Hydrates. *Thermochimica Acta*, 248:61–79, 1995.

[189] F. Tian, H. Qu, A. Zimmermann, T. Munk, A. C. Jrgensen, and J. Rantanen. Factors Affecting Crystallization of Hydrates. *Journal of Pharmacy and Pharmacology*, 62(11):1534–1546, 2010.

[190] J. T. Damron, K. M. Kersten, M. K. Pandey, K. H. Mroue, J. R. Yarava, Y. Nishiyama, A. J. Matzger, and A. Ramamoorthy. Electrostatic Constraints Assessed by ^{1}H MAS NMR Illuminate Differences in Crystalline Polymorphs. *The Journal of Physical Chemistry Letters*, 8(17):4253–4257, 2017.

[191] J. T. Damron, K. M. Kersten, M. K. Pandey, Y. Nishiyama, A. Matzger, and A. Ramamoorthy. Role of Anomalous Water Constraints in the Efficacy of Pharmaceuticals Probed by ^{1}H Solid-State NMR. *ChemistrySelect*, 2(23):6797–6800, 2017.

[192] L. Zheng, K. W. Fishbein, R. G. Griffin, and J. Herzfeld. Two-Dimensional Solid-State Proton NMR and Proton Exchange. *Journal of the American Chemical Society*, 115(14):6254–6261, 1993.

[193] O. Bodet, S. Goerke, N. G. R. Behl, V. Roeloffs, M. Zaiss, and P. Bachert. Amide Proton Transfer of Carnosine in Aqueous Solution Studied in Vitro by WEX and CEST Experiments. *NMR in Biomedicine*, 28(9):1097–1103, 2015.

[194] Y. Dai, J. van Spronsen, G.-J. Witkamp, R. Verpoorte, and Y. H. Choi. Natural Deep Eutectic Solvents as New Potential Media for Green Technology. *Analytica Chimica Acta*, 766:61–68, 2013.

[195] A. E. Bennett, R. G. Griffin, J. H. Ok, and S. Vega. Chemical Shift Correlation Spectroscopy in Rotating Solids: Radio Frequency-Driven Dipolar Recoupling and Longitudinal Exchange. *The Journal of Chemical Physics*, 96(11):8624–8627, 1992.

[196] M. K. Pandey, S. Vivekanandan, K. Yamamoto, S. Im, L. Waskell, and A. Ramamoorthy. Proton-Detected 2D Radio Frequency Driven Recoupling Solid-State NMR Studies on Micelle-Associated Cytochrome-b5. *Journal of Magnetic Resonance*, 242:169–179, 2014.

[197] A. Ramamoorthy and J. Xu. 2D $^{1}H/^{1}H$ RFDR and NOESY NMR Experiments on a Membrane-Bound Antimicrobial Peptide Under Magic Angle Spinning. *The Journal of Physical Chemistry B*, 117(22):6693–6700, 2013.

[198] S. Gabl, O. Steinhauser, and H. Weingärtner. From Short-Range to Long-Range Intermolecular NOEs in Ionic Liquids: Frequency Does Matter. *Angewandte Chemie*, 125(35):9412–9416, 2013.

[199] N. E. Heimer, R. E. Del Sesto, and W. R. Carper. Evidence for Spin Diffusion in a H,H-NOESY Study of Imidazolium Tetrafluoroborate Ionic Liquids. *Magnetic Resonance in Chemistry*, 42(1):71–75, 2004.

[200] R. K. Harris. Applications of Solid-State NMR to Pharmaceutical Polymorphism and Related Matters. *Journal of Pharmacy and Pharmacology*, 59(2):225–239, 2007.

[201] A. K. Chattah, R. Zhang, K. H. Mroue, L. Y. Pfund, M. R. Longhi, A. Ramamoorthy, and C. Garnero. Investigating Albendazole Desmotropes by Solid-State NMR Spectroscopy. *Molecular Pharmaceutics*, 12(3):731–741, 2015.

[202] E. E. L. Tanner, A. M. Curreri, J. P. R. Balkaran, N. C. Selig-Wober, A. B. Yang, C. Kendig, M. P. Fluhr, N. Kim, and S. Mitragotri. Design Principles of Ionic Liquids for Transdermal Drug Delivery. *Advanced Materials*, 31(27):1901103, 2019.

[203] K. N. Ibsen, H. Ma, A. Banerjee, E. E. L. Tanner, S. Nangia, and S. Mitragotri. Mechanism of Antibacterial Activity of Choline-Based Ionic Liquids (CAGE). *ACS Biomaterials Science & Engineering*, 4(7):2370–2379, 2018.

[204] R. M. Cotts, M. J. R. Hoch, T. Sun, and J. T. Markert. Pulsed Field Gradient Stimulated Echo Methods for Improved NMR Diffusion Measurements in Heterogeneous Systems. *Journal of Magnetic Resonance (1969)*, 83(2):252–266, 1989.

[205] A. Jerschow and N. Müller. Suppression of Convection Artifacts in Stimulated-Echo Diffusion Experiments. Double-Stimulated-Echo Experiments. *Journal of Magnetic Resonance*, 125(2):372–375, 1997.

[206] A. Jerschow and N. Müller. Convection Compensation in Gradient Enhanced Nuclear Magnetic Resonance Spectroscopy. *Journal of Magnetic Resonance*, 132(1):13–18, 1998.

[207] E. E. L. Tanner, K. M. Piston, H. Ma, K. N. Ibsen, S. Nangia, and S. Mitragotri. The Influence of Water on Choline-Based Ionic Liquids. *ACS Biomaterials Science & Engineering*, 5(7):3645–3653, 2019.

[208] A. Alvarez Fernandez and H. P. Kouwer. Key developments in ionic liquid crystals. *International Journal of Molecular Sciences*, 17(5):731, 2016.

[209] K. Binnemans. Ionic Liquid Crystals. *Chemical Reviews*, 105(11):4148–4204, 2005.

[210] G. Saielli. Special Issue Editorial: Ionic Liquid Crystals. *Crystals*, 9(5):274, 2019.

[211] G. Saielli and K. Satoh. A Coarse-Grained Model of Ionic Liquid Crystals: The Effect of Stoichiometry on the Stability of the Ionic Nematic Phase. *Physical Chemistry Chemical Physics*, 21(36):20327–20337, 2019.

[212] A. Triolo, O. Russina, B. Fazio, R. Triolo, and E. Di Cola. Morphology of 1-Alkyl-3-methylimidazolium Hexafluorophosphate Room Temperature Ionic Liquids. *Chemical Physics Letters*, 457(4):362–365, 2008.

[213] O. Russina, F. Lo Celso, M. Di Michiel, S. Passerini, G. B. Appetecchi, F. Castiglione, A. Mele, R. Caminiti, and A. Triolo. Mesoscopic Structural Organization in Triphilic Room Temperature Ionic Liquids. *Faraday Discussions*, 167:499–513, 2013.

[214] A. Triolo, O. Russina, B. Fazio, G. B. Appetecchi, M. Carewska, and S. Passerini. Nanoscale Organization in Piperidinium-Based Room Temperature Ionic Liquids. *The Journal of Chemical Physics*, 130(16):164521, 2009.

[215] R. Olga, T. Alessandro, G. Lorenzo, C. Ruggero, X. Dong, Jr. Larry, G. H., A. B. Richard, L. Q. Edward, P. Natalia, and R. S. Kenneth. Morphology and Intermolecular Dynamics of 1-Alkyl-3-methylimidazolium Bis(trifluoromethane)sulfonylamide Ionic Liquids: Structural and Dynamic Evidence of Nanoscale Segregation. *Journal of Physics: Condensed Matter*, 21(42):424121, 2009.

[216] J. N. A. Canongia Lopes and A. A. H. Pádua. Nanostructural Organization in Ionic Liquids. *The Journal of Physical Chemistry B*, 110(7):3330–3335, 2006.

[217] J. N. Canongia Lopes, M. F. Costa Gomes, and A. A. H. Pádua. Nonpolar, Polar, and Associating Solutes in Ionic Liquids. *The Journal of Physical Chemistry B*, 110(34):16816–16818, 2006.

[218] A. G. Cook, J. L. Wardell, and C. T. Imrie. Carbohydrate Liquid Crystals: Synthesis and Characterisation of the Methyl-6-O-(n-acyl)--d-glucopyranosides. *Chemistry and Physics of Lipids*, 164(2):118–124, 2011.

[219] A. G. Cook, J. L. Wardell, N. J. Brooks, J. M. Seddon, A. MartÍnez-Felipe, and C. T. Imrie. Non-Symmetric Liquid Crystal Dimer Containing a Carbohydrate-Based Moiety. *Carbohydrate Research*, 360:78–83, 2012.

[220] J. C. López-Montilla, P. E. Herrera-Morales, S. Pandey, and D. O. Shah. Spontaneous Emulsification: Mechanisms, Physicochemical Aspects, Modeling, and Applications. *Journal of Dispersion Science and Technology*, 23(1-3):219–268, 2002.

[221] M. Garcia-Viloca, R. Gelabert, À. González-Lafont, M. Moreno, and J. M. Lluch. Temperature Dependence of Proton NMR Chemical Shift As a Criterion To Identify Low-Barrier Hydrogen Bonds. *Journal of the American Chemical Society*, 120(39):10203–10209, 1998.

[222] J. G. Sośnicki and P. E. Hansen. Temperature Coefficient of NH Chemical Shifts of Thioamides and Amides in Relation to Structure. *Journal of Molecular Structure*, 700(1):91–103, 2004.

[223] V. G. Kontogianni, P. Charisiadis, A. Primikyri, C. G. Pappas, V. Exarchou, A. G. Tzakos, and I. P. Gerothanassis. Hydrogen Bonding Probes of Phenol -OH Groups. *Organic & Biomolecular Chemistry*, 11(6):1013–1025, 2013.

[224] P. Che, F. Lu, X. Nie, Y. Huang, Y. Yang, F. Wang, and J. Xu. Hydrogen Bond Distinction and Activation Upon Catalytic Etherification of Hydroxyl Compounds. *Chemical Communications*, 51(6):1077–1080, 2015.

[225] B. Qiao, C. Krekeler, R. Berger, L. Delle Site, and C. Holm. Effect of Anions on Static Orientational Correlations, Hydrogen Bonds, and Dynamics in Ionic Liquids: a Simulational Study. *The Journal of Physical Chemistry B*, 112(6):1743–1751, 2008.

[226] S. Gehrke, M. von Domaros, R. Clark, O. Hollczki, M. Brehm, T. Welton, A. Luzar, and B. Kirchner. Structure and Lifetimes in Ionic Liquids and Their Mixtures. *Faraday Discussions*, 206:219–245, 2018.

[227] I. Skarmoutsos, T. Welton, and P. A. Hunt. The Importance of Timescale for Hydrogen Bonding in Imidazolium Chloride Ionic Liquids. *Physical Chemistry Chemical Physics*, 16(8):3675–3685, 2014.

[228] P. Ovejero, M. J. Mayoral, M. Cano, J. A. Campo, J. V. Heras, P. Fernóndez-Tobar, M. Valién, E. Pinilla, and M. R. Torres. Mesomorphism of Four-Coordinated Four-Chained Metal Complexes Based on Pyrazolylpyridine Derivatives. *Molecular Crystals and Liquid Crystals*, 481(1):34–55, 2008.

[229] M. Marzec, A. Mikułko, S. Wróbel, M. Hanczar, W. Haase, and R. Dabrowski. Influence of Molecular Structure on Phase Diagram and Ferroelectric Behaviour. *Ferroelectrics*, 343(1):181–191, 2006.

[230] X. Li, D. W. Bruce, and M. S. Jean'ne. Dicationic Imidazolium-Based Ionic Liquids and Ionic Liquid Crystals with Variously Positioned Fluoro Substituents. *Journal of Materials Chemistry*, 19(43):8232–8238, 2009.

[231] H. Coles. First Ferrocene-Containing Low Molar Mass Organosiloxane Liquid-Crystalline Materials. *Journal of Materials Chemistry*, 9(5):1085–1090, 1999.

[232] L. Chakraborty, N. Chakraborty, T. D. Choudhury, B. Phani Kumar, A. B. Mandal, and N. V. Rao. Synthesis, Mesomorphic and Photo-Physical Properties of Few d-and f-Block Metals Coordinated to Polar Schiff's Bases. *Liquid Crystals*, 39(5):655–668, 2012.

[233] S. J. Cowling. *Optical Microscopy Studies of Liquid Crystals*. Wiley-VCH Verlag GmbH & Co. KGaA., Weinheim, 2014.

[234] D. J. Abdallah, A. Robertson, H.-F. Hsu, and R. G. Weiss. Smectic Liquid-Crystalline Phases of Quaternary Group VA (Especially Phosphonium) Salts with Three Equivalent Long n-Alkyl Chains. How Do Layered Assemblies Form in Liquid-Crystalline and Crystalline Phases? *Journal of the American Chemical Society*, 122(13):3053–3062, 2000.

[235] H. Chen, D. C. Kwait, Z. S. Gnen, B. T. Weslowski, D. J. Abdallah, and R. G. Weiss. Phase Characterization and Properties of Completely Saturated Quaternary Phosphonium Salts. Ordered, Room-Temperature Ionic Liquids. *Chemistry of Materials*, 14(10):4063–4072, 2002.

[236] J. N. Israelachvili, D. J. Mitchell, and B. W. Ninham. Theory of Self-Assembly of Hydrocarbon Amphiphiles into Micelles and Bilayers. *Journal of the Chemical Society, Faraday Transactions 2: Molecular and Chemical Physics*, 72:1525–1568, 1976.

[237] G. P. Jackson and D. C. Duckworth. Electrospray Mass Spectrometry of Undiluted Ionic Liquids. *Chemical Communications*, (5):522–523, 2004.

[238] P. Wasserscheid and T. Welton. Ionic Liquids in Synthesis. In *Ionic Liquids in Synthesis*. Wiley-VCH, Weinheim, second edition, 2003.

[239] J. S. Wilkes. A Short History of Ionic Liquids From Molten Salts to Neoteric Solvents. *Green Chemistry*, 4(2):73–80, 2002.

[240] K. Goossens, K. Lava, C. W. Bielawski, and K. Binnemans. Ionic Liquid Crystals: Versatile Materials. *Chemical Reviews*, 116(8):4643–4807, 2016.

[241] K. V. Axenov and S. Laschat. Thermotropic Ionic Liquid Crystals. *Materials*, 4(1):206–259, 2011.

[242] M. Schadt. Liquid Crystal Materials and Liquid Crystal Displays. *Annual Review of Materials Science*, 27(1):305–379, 1997.

[243] R. D. Costa, F. Werner, X. Wang, P. Grönninger, S. Feihl, F. T. U. Kohler, P. Wasserscheid, S. Hibler, R. Beranek, K. Meyer, and D. M. Guldi. Beneficial Effects of Liquid Crystalline Phases in Solid-State Dye-Sensitized Solar Cells. *Advanced Energy Materials*, 3(5):657–665, 2013.

[244] N. Yamanaka, R. Kawano, W. Kubo, T. Kitamura, Y. Wada, M. Watanabe, and S. Yanagida. Ionic Liquid Crystal as a Hole Transport Layer of Dye-Sensitized Solar Cells. *Chemical Communications*, (6):740–742, 2005.

[245] N. Yamanaka, R. Kawano, W. Kubo, N. Masaki, T. Kitamura, Y. Wada, M. Watanabe, and S. Yanagida. Dye-Sensitized TiO_2 Solar Cells Using Imidazolium-Type Ionic Liquid Crystal Systems as Effective Electrolytes. *The Journal of Physical Chemistry B*, 111(18):4763–4769, 2007.

[246] C. K. Lee, H. W. Huang, and I. J. B. Lin. Simple Amphiphilic Liquid Crystalline N-alkylimidazolium Salts. A New Solvent System Providing a Partially Ordered Environment. *Chemical Communications*, (19):1911–1912, 2000.

[247] D. W. Bruce, Y. Gao, J. N. CanongiaLopes, K. Shimizu, and J. M. Slattery. Liquid-Crystalline Ionic Liquids as Ordered Reaction Media for the Diels-Alder Reaction. *Chemistry - A European Journal*, 22(45):16113–16123, 2016.

[248] A. Taubert. CuCl Nanoplatelets from an Ionic Liquid-Crystal Precursor. *Angewandte Chemie International Edition*, 43(40):5380–5382, 2004.

[249] M. M. Neidhardt, K. Schmitt, A. Baro, C. Schneider, U. Bilitewski, and S. Laschat. Self-Assembly and Biological Activities of Ionic Liquid Crystals Derived from Aromatic Amino Acids. *Physical Chemistry Chemical Physics*, 20(31):20371–20381, 2018.

[250] W. Dobbs, B. Heinrich, C. Bourgogne, B. Donnio, E. Terazzi, M.-E. Bonnet, F. Stock, P. Erbacher, A.-L. Bolcato-Bellemin, and L. Douce. Mesomorphic Imidazolium Salts: New Vectors for Efficient siRNA Transfection. *Journal of the American Chemical Society*, 131(37):13338–13346, 2009.

[251] J. Dai, B. Kharkov, and S. Dvinskikh. Molecular and Segmental Orientational Order in a Smectic Mesophase of a Thermotropic Ionic Liquid Crystal. *Crystals*, 9:18, 2018.

[252] J.-P. Douliez, A. Ferrarini, and E.-J. Dufourc. On the Relationship Between C-C and C-D Order Parameters and its use for Studying the Conformation of Lipid Acyl Chains in Biomembranes. *The Journal of Chemical Physics*, 109(6):2513–2518, 1998.

[253] L. Calucci and C. A. Veracini. Liquid Crystals and Liquid Crystal Solutions Studied by NMR. In John C. Lindon, editor, *Encyclopedia of Spectroscopy and Spectrometry (Second Edition)*, pages 1349–1356. Academic Press, Oxford, 2010.

[254] M. Hong, X. Yao, K. Jakes, and D. Huster. Investigation of Molecular Motions by Lee-Goldburg Cross-Polarization NMR Spectroscopy. *The Journal of Physical Chemistry B*, 106(29):7355–7364, 2002.

[255] C. S. Nagaraja. Determination of Order Parameters of Liquid Crystals: Use of Dipolar Oscillations Enhanced by Lee-Goldburg Decoupling. *Liquid Crystals*, 26(1):17–21, 1999.

[256] K. V. Ramanathan and N. Sinha. Ordering in Nematic Liquid Crystals from NMR Cross-Polarization Studies. *Pramana*, 61(2):249–262, 2003.

[257] S. P. Brown, I. Schnell, J. D. Brand, K. Müllen, and H. W. Spiess. An Investigation of $\pi - \pi$ Packing in a Columnar Hexabenzocoronene by Fast Magic-Angle Spinning and Double-Quantum ^{1}H Solid-State NMR Spectroscopy. *Journal of the American Chemical Society*, 121(28):6712–6718, 1999.

[258] T. Dollase, R. Graf, A. Heuer, and H. W. Spiess. Local Order and Chain Dynamics in Molten Polymer Blocks Revealed by Proton Double-Quantum NMR. *Macromolecules*, 34(2):298–309, 2001.

[259] K. Saalwchter. An Investigation of Poly(dimethylsiloxane) Chain Dynamics and Order in Its Inclusion Compound with γ-Cyclodextrin by Fast-MAS Solid-State NMR Spectroscopy. *Macromolecular Rapid Communications*, 23(4):286–291, 2002.

[260] M. Schneider, L. Gasper, D. E. Demco, and B. Blümich. Residual Dipolar Couplings by ^{1}H Dipolar-Encoded Longitudinal Magnetization, Double- and Triple-Quantum Nuclear Magnetic Resonance in Cross-Linked Elastomers. *The Journal of Chemical Physics*, 111(1):402–415, 1999.

[261] H. Geen, J. J. Titman, J. Gottwald, and H. W. Spiess. Solid-State Proton Multiple-Quantum NMR Spectroscopy with Fast Magic Angle Spinning. *Chemical Physics Letters*, 227(1):79–86, 1994.

[262] J. Gottwald, D. E. Demco, R. Graf, and H. W. Spiess. High-Resolution Double-Quantum NMR Spectroscopy of Homonuclear Spin Pairs and Proton Connectivities in Solids. *Chemical Physics Letters*, 243(3):314–323, 1995.

[263] S. P. Brown and H. W. Spiess. Advanced Solid-State NMR Methods for the Elucidation of Structure and Dynamics of Molecular, Macromolecular, and Supramolecular Systems. *Chemical Reviews*, 101(12):4125–4156, 2001.

[264] S. P. Brown. Probing Proton-Proton Proximities in the Solid State. *Progress in Nuclear Magnetic Resonance Spectroscopy*, 50(4):199–251, 2007.

[265] S. P. Brown. Applications of High-Resolution ^{1}H Solid-State NMR. *Solid State Nuclear Magnetic Resonance*, 41:1–27, 2012.

[266] M. Fernando Cobo, K. Maliňáková, D. Reichert, K. Saalwächter, and E. Ribeiro deAzevedo. Intermediate Motions and Dipolar Couplings as Studied by Lee-Goldburg Cross-Polarization NMR: Hartmann-Hahn Matching Profiles. *Physical Chemistry Chemical Physics*, 11(32):7036–7047, 2009.

[267] A. Achilles, R. Bärenwald, B.-D. Lechner, S. Werner, H. Ebert, C. Tschierske, A. Blume, K. Bacia, and K. Saalwächter. Self-Assembly of X-Shaped Bolapolyphiles in Lipid Membranes: Solid-State NMR Investigations. *Langmuir*, 32(3):673–682, 2016.

[268] M. E. Di Pietro, T. Margola, G. Celebre, G. De Luca, and G. Saielli. A Combined LX-NMR and Molecular Dynamics Investigation of the Bulk and Local Structure of Ionic Liquid Crystals. *Soft Matter*, 15(22):4486–4497, 2019.

[269] J. Dai, D. Majhi, B. B. Kharkov, and S. V. Dvinskikh. NMR Spectroscopic Study of Orientational Order in Imidazolium-Based Ionic Liquid Crystals. *Crystals*, 9(10):495, 2019.

[270] A. Bielecki, A. C. Kolbert, H. J. M. De Groot, R. G. Griffin, and M. H. Levitt. Frequency-Switched Lee-Goldburg Sequences in Solids. In *Advances in Magnetic and Optical Resonance*, volume 14, pages 111–124. Academic Press, San Diego, 1990.

[271] Z. Tošner, R. Andersen, B. Stevensson, M. Edén, N. C. Nielsen, and T. Vosegaard. Computer-Intensive Simulation of Solid-State NMR Experiments using SIMPSON. *Journal of Magnetic Resonance*, 246:79–93, 2014.

[272] E. M. L. Beale. Confidence Regions in Non-Linear Estimation. *Journal of the Royal Statistical Society: Series B (Methodological)*, 22(1):41–76, 1960.

[273] G. A. F. Seber and C. J. Wild. *Nonlinear Regression*. Wiley-Interscience, New York, 2003.

[274] D. Barrick. *Biomolecular Thermodynamics: From Theory to Application*. CRC Press, Boca Raton, Florida, 2014.

[275] J. P. Bradley, S. P. Velaga, O. N. Antzutkin, and S. P. Brown. Probing Intermolecular Crystal Packing in -Indomethacin by High-Resolution ^{1}H Solid-State NMR Spectroscopy. *Crystal Growth & Design*, 11(8):3463–3471, 2011.

[276] A. Pines, M. G. Gibby, and J. S. Waugh. Proton-Enhanced NMR of Dilute Spins in Solids. *The Journal of Chemical Physics*, 59(2):569–590, 1973.

[277] E. R. deAzevedo, K. Saalwächter, O. Pascui, A. A. de Souza, T. J. Bonagamba, and D. Reichert. Intermediate Motions as Studied by Solid-State Separated Local Field NMR Experiments. *The Journal of Chemical Physics*, 128(10):104505, 2008.

[278] L. Löser, K. Saalwächter, and T. Mendes Ferreira. Liquid-Liquid Phase Coexistence in Lipid Membranes Observed by Natural Abundance ^{1}H-^{13}C Solid-State NMR. *Physical Chemistry Chemical Physics*, 20(15):9751–9754, 2018.

[279] J. H. Han, J. S. Kim, J. K. Park, K. W. Lee, J. I. Jin, E. H. Choi, and C. E. Lee. Nuclear Magnetic Resonance Study of the Smectic-Cholesteric Phase Transition in a Dimesogenic Liquid Crystal. *Current Applied Physics*, 14(10):1356–1359, 2014.

[280] M. E. Di Pietro, G. Celebre, G. De Luca, H. Zimmermann, and G. Cinacchi. Smectic Order Parameters via Liquid Crystal NMR Spectroscopy: Application to a Partial Bilayer Smectic A Phase. *The European Physical Journal E*, 35(10):112, 2012.

[281] J. L. Figueirinhas, C. Cruzi, A. C. Ribeiro, and N. H. Tinh. NMR Study of Molecular Order in a Liquid Crystal with Smectic Ad and Reentrant Nematic Mesophases. A Comparative Study with Models for the SAd Phase. *Molecular Crystals and Liquid Crystals Science and Technology. Section A. Molecular Crystals and Liquid Crystals*, 212(1):263–270, 1992.

[282] B. B. Kharkov, V. I. Chizhik, and S. V. Dvinskikh. Low rf Power High Resolution ^{1}H-^{13}C-^{14}N Separated Local Field Spectroscopy in Lyotropic Mesophases. *Journal of Magnetic Resonance*, 223:73–79, 2012.

[283] T. M. Ferreira, B. Medronho, R. W. Martin, and D. Topgaard. Segmental Order Parameters in a Nonionic Surfactant Lamellar Phase Studied with ^{1}H-^{13}C Solid-State NMR. *Physical Chemistry Chemical Physics*, 10(39):6033–6038, 2008.

[284] M. Veber, C. Jallabert, H. Strzelecka, O. Jullien, and P. Davidson. Non-Symmetrical Dithiolium Salts Mesomorphic Properties. *Liquid Crystals*, 8(6):775–785, 1990.

[285] J. W. Goodby, M. J. Watson, G. Mackenzie, S. M. Kelly, S. Bachir, P. Bault, P. Gode, G. Goethals, P. Martin, G. Ronco, and P. Villa. The Dependence of Mesomorphic Behaviour on the Extent of Hydrogen-Bonding in Sugar Derived Polyols. *Liquid Crystals*, 25(2):139–147, 1998.

[286] M. Hong, K. Schmidt-Rohr, and A. Pines. NMR Measurement of Signs and Magnitudes of C-H Dipolar Couplings in Lecithin. *Journal of the American Chemical Society*, 117(11):3310–3311, 1995.

[287] V. Domenici. The Role of NMR in the Study of Partially Ordered Materials: Perspectives and Challenges. *Pure and Applied Chemistry*, 83(1):67–94, 2010.

[288] K. Hayamizu and O. Yamamoto. ^{13}C Spin-Lattice Relaxation Times in Liquid Crystalline p,p'-Azoxyanisole. *Bulletin of the Chemical Society of Japan*, 50(5):1295–1297, 1977.

[289] H. Hutton, E. Bock, E. Tomchuk, and R. Y. Dong. High Resolution Carbon-13 Spin-Lattice Relaxation Study of the Nematogen p-Methoxybenzylidene-p-n-butylaniline. *The Journal of Chemical Physics*, 68(3):940–944, 1978.

[290] K. Komiya, M. Nanamiya, M. Oshima, and K. Hiraoka. Molecular Dynamics in Smectic and Crystalline Phases Studied by ^{13}C-NMR Spin Lattice Relaxation Time Observation. *Ferroelectrics*, 394(1):16–21, 2010.

[291] M. Geppi, S. Pizzanelli, and C. A. Veracini. Phenyl Ring Dynamics in a Liquid Crystal Polymer through ^{2}H NMR Spectroscopy. *Chemical Physics Letters*, 343(5-6):513–519, 2001.

[292] M. F. Brown. Theory of Spin-Lattice Relaxation in Lipid Bilayers and Biological Membranes. ^{2}H and ^{14}N Quadrupolar Relaxation. *The Journal of Chemical Physics*, 77(3):1576–1599, 1982.

[293] M. F. Brown. Membrane Structure and Dynamics Studied with NMR Spectroscopy. In *Biological Membranes*, pages 175–252. Birkhäuser, Boston, 1996.

[294] M. F. Brown. Theory of Spin-Lattice Relaxation in Lipid Bilayers and Biological Membranes. Dipolar Relaxation. *The Journal of Chemical Physics*, 80(6):2808–2831, 1984.

[295] C. Mayer, K. Müller, K. Weisz, and G. Kothe. Deuteron NMR Relaxation Studies of Phospholipid Membranes. *Liquid Crystals*, 3(6-7):797–806, 1988.

[296] J. R. Lewandowski, J. Sein, H. J. Sass, S. Grzesiek, M. Blackledge, and L. Emsley. Measurement of Site-Specific ^{13}C Spin-Lattice Relaxation in a Crystalline Protein. *Journal of the American Chemical Society*, 132(24):8252–8254, 2010.

[297] V. Chevelkov, A. V. Zhuravleva, Y. Xue, B. Reif, and N. R. Skrynnikov. Combined Analysis of ^{15}N Relaxation Data from Solid- and Solution-State NMR Spectroscopy. *Journal of the American Chemical Society*, 129(42):12594–12595, 2007.

[298] W. S. Veeman. Carbon-13 Chemical Shift Anisotropy. *Progress in Nuclear Magnetic Resonance Spectroscopy*, 16:193–235, 1984.

[299] S. J. Clark, M. D. Segall, C. J. Pickard, P. J. Hasnip, M. I. Probert, K. Refson, and M. C. Payne. First Principles Methods using CASTEP. *Zeitschrift für Kristallographie-Crystalline Materials*, 220(5/6):567–570, 2005.

[300] J. P. Perdew, K. Burke, and M. Ernzerhof. Generalized Gradient Approximation Made Simple. *Physical Review Letters*, 77(18):3865–3868, 1996.

[301] J. Kowalewski and L. Mäler. *Nuclear Spin Relaxation in Liquids: Theory, Experiments, and Applications*. CRC press, Boca Raton, second edition, 2017.

[302] J. D. Haller and P. Schanda. Amplitudes and Time Scales of Picosecond-to-Microsecond Motion in Proteins Studied by Solid-State NMR: a Critical Evaluation of Experimental Approaches and Application to Crystalline Ubiquitin. *Journal of Biomolecular NMR*, 57(3):263–280, 2013.

[303] D. E. Woessner. Nuclear Spin Relaxation in Ellipsoids Undergoing Rotational Brownian Motion. *The Journal of Chemical Physics*, 37(3):647–654, 1962.

[304] V. Domenici, M. Geppi, and C. A. Veracini. A New Approach to the Extraction of Dynamic Information from the Analysis of ^{2}H NMR Relaxation Times in Tilted Chiral Mesophases. *Chemical Physics Letters*, 382(5-6):518–522, 2003.

[305] V. Domenici, J. Czub, M. Geppi, B. Gestblom, S. Urban, and C.-A. Veracini. Dynamics of 4,4'-Di-n-heptylazoxybenzene (HAB) Studied using Dielectric and ^{2}H NMR Relaxation Measurements. *Liquid Crystals*, 31(1):91–99, 2004.

[306] V. Domenici, M. Geppi, C. A. Veracini, R. Blinc, A. Lebar, and B. Zalar. Dynamics of a Ferroelectric Liquid Crystal by Means of ^{2}H NMR Spectroscopy: a Multifrequency Relaxation Study. *ChemPhysChem*, 5(4):559–563, 2004.

[307] V. Domenici, M. Geppi, C. A. Veracini, and R. Y. Dong. Molecular Dynamics of a Ferroelectric Smectogen in its Smectic Phases by Means of ^{2}H NMR Spectroscopy. *Liquid Crystals*, 33(4):479–484, 2006.

[308] M. F. Brown, J. Seelig, and U. Häberlen. Structural Dynamics in Phospholipid Bilayers from Deuterium Spin-Lattice Relaxation Time Measurements. *The Journal of Chemical Physics*, 70(11):5045–5053, 1979.

[309] J. Lyerla Jr, H. McIntyre, and D. Torchia. A ^{13}C Nuclear Magnetic Resonance Study of Alkane Motion. *Macromolecules*, 7(1):11–14, 1974.

[310] Y. K. Levine, N. J. M. Birdsall, A. G. Lee, J. C. Metcalfe, P. Partington, and G. C. K. Roberts. Calculation of Dipolar Nuclear Magnetic Relaxation Times in Molecules with Multiple Internal Rotations. II. Theoretical Results for Anisotropic Over-all Motion of the Molecule, and Comparison with ^{13}C Relaxation Times in n-Alkanes and n-Alkyl Bromides. *The Journal of Chemical Physics*, 60(7):2890–2899, 1974.

[311] G. D. Smith and R. L. Jaffe. Quantum Chemistry Study of Conformational Energies and Rotational Energy Barriers in n-Alkanes. *The Journal of Physical Chemistry*, 100(48):18718–18724, 1996.

[312] M. Imanari, K. Uchida, K. Miyano, H. Seki, and K. Nishikawa. NMR Study on Relationships between Reorientational Dynamics and Phase Behaviour of Room-Temperature Ionic Liquids: 1-Alkyl-3-methylimidazolium Cations. *Physical Chemistry Chemical Physics*, 12(12):2959–2967, 2010.

[313] P. Ma, J. D. Haller, J. Zajakala, P. Macek, A. C. Sivertsen, D. Willbold, J. Boisbouvier, and P. Schanda. Probing Transient Conformational States of Proteins by Solid-State $R_{1\rho}$ Relaxation-Dispersion NMR Spectroscopy. *Angewandte Chemie International Edition*, 53(17):4312–4317, 2014.

[314] C. M. Quinn and A. E. McDermott. Monitoring Conformational Dynamics with Solid-State $R_{1\rho}$ Experiments. *Journal of Biomolecular NMR*, 45(1):5–8, 2009.

[315] C. M. Quinn and A. E. McDermott. Quantifying Conformational Dynamics using Solid-State $R_{1\rho}$ Experiments. *Journal of Magnetic Resonance*, 222:1–7, 2012.

[316] P. J. Sebastião. Chapter 11 - NMR Relaxometry in Liquid Crystals: Molecular Organization and Molecular Dynamics Interrelation. In *Field-cycling NMR Relaxometry: Instrumentation, Model Theories and Applications*, pages 255–302. The Royal Society of Chemistry, Croydon, 2019.

[317] S. Bubici, L. Calucci, G. Ferrante, and M. Geppi. Collective and Molecular Motions of Fluorinated Liquid Crystals by Means of ^{19}F Fast Field-Cycling NMR Relaxometry. *Chemical Physics Letters*, 549:27–31, 2012.

[318] A. Gradišek, T. Apih, V. Domenici, V. Novotna, and P. J. Sebastião. Molecular Dynamics in a Blue Phase Liquid Crystal: a ^{1}H Fast Field-Cycling NMR Relaxometry Study. *Soft Matter*, 9(45):10746–10753, 2013.

[319] A. G. Palmer, C. D. Kroenke, and J. Patrick Loria. Chapter 10 - Nuclear Magnetic Resonance Methods for Quantifying Microsecond-to-Millisecond Motions in Biological Macromolecules. In *Methods in Enzymology*, volume 339, pages 204–238. Academic Press, San Diego, 2001.

Appendix A

NMR Theory

A.1 SIMPSON Input File for Solid-State (Static and MAS) CSA Lineshapes

```
spinsys {
  channels 13C
  nuclei 13C
  shift 1 0p 10p 0.5 0 0 0
}

par {
  # static
  spin_rate        0
  # MAS
  # spin_rate      10000
  variable index   1
  np               512
  proton_frequency 600e6
  start_operator   I1x
  detect_operator  I1p
  method           direct
  crystal_file     ./zcw28656
  # static
  gamma_angles     1
  # MAS
  # gamma_angles   16
  sw               5000
  variable tsw     1e6/sw
  verbose          1101

}

proc pulseq {} {
  global par
```

```
  acq_block {
    delay $par(tsw)
        }
}

proc main {} {
  global par

  set f [fsimpson]
  faddlb $f 40 0
  fft $f
  fsave $f $par(name)_test.spe

}
```

A.2 SIMPSON Input File for Solid-State (Static and MAS) Heteronuclear Dipolar Lineshapes

```
spinsys {
  channels 13C 1H
  nuclei 13C 1H
  dipole 1 2 −23000 0 0 0
}

par {
  # static
  spin_rate        0
  # MAS
  # spin_rate      20000
  variable index   1
  np               1024
  proton_frequency 600e6
  start_operator   I1x
  detect_operator  I1p
  method           direct
  crystal_file     ./zcw28656
  # static
  gamma_angles     1
  # MAS
  # gamma_angles   16
  sw               90000
  variable tsw     1e6/sw
  verbose          1101
}

proc pulseq {} {
  global par
```

```
  acq_block {
    delay $par(tsw)
        }
}

proc main {} {
  global par

  set f [fsimpson]
  faddlb $f 40 0
  fft $f
  fsave $f $par(name)_static.spe
}
```

A.3 Solution of the McConnell Equations for Two-Site Chemical Exchange

The solution of the McConnell equations[100] is:[319]

$$\frac{d}{dt}\begin{bmatrix} M_A^+(t) \\ M_B^+(t) \end{bmatrix} = \begin{bmatrix} a_{AA}(t) & a_{AB}(t) \\ a_{BA}(t) & a_{BB}(t) \end{bmatrix} \begin{bmatrix} M_A^+(0) \\ M_B^+(0) \end{bmatrix} \tag{A.1}$$

whereby (with $\Delta\omega = 2\pi\Delta\nu$):

$$\begin{aligned}
a_{AA}(t) &= \frac{1}{2}\left[\left(1 - \frac{-i\Delta\omega + R_{2,A}^0 - R_{2,B}^0 + k_{ex}(p_A - p_B)}{\lambda_+ - \lambda_-}\right)\exp(-\lambda_- t)\right] \\
&\quad + \left[\left(1 + \frac{-i\Delta\omega + R_{2,A}^0 - R_{2,B}^0 + k_{ex}(p_B - p_A)}{\lambda_+ - \lambda_-}\right)\exp(-\lambda_- t)\right] \\
a_{BB}(t) &= \frac{1}{2}\left[\left(1 + \frac{-i\Delta\omega + R_{2,A}^0 - R_{2,B}^0 + k_{ex}(p_A - p_B)}{\lambda_+ - \lambda_-}\right)\exp(-\lambda_- t)\right] \\
&\quad + \left[\left(1 - \frac{-i\Delta\omega + R_{2,A}^0 - R_{2,B}^0 + k_{ex}(p_B - p_A)}{\lambda_+ - \lambda_-}\right)\exp(-\lambda_- t)\right] \\
a_{AB}(t) &= \frac{k_{ex}p_A}{\lambda_+ - \lambda_-}\left[\exp(-\lambda_- t) - \exp(-\lambda_+ t)\right] \\
a_{BA}(t) &= \frac{k_{ex}p_B}{\lambda_+ - \lambda_-}\left[\exp(-\lambda_- t) - \exp(-\lambda_+ t)\right]
\end{aligned} \tag{A.2}$$

and

$$\lambda_\pm = \frac{1}{2}\begin{pmatrix} -i\Omega_A - i\Omega_B + R_{2,A}^0 + R_{2,B}^0 + k_{ex} \\ \pm\left[\left\{-i\Delta\omega + R_{2,A}^0 + R_{2,B}^0 + k_{ex}(p_B - p_A)\right\}^2 + 4p_A p_B {k_{ex}}^2\right]^{1/2} \end{pmatrix} \tag{A.3}$$

Fourier transformation of $M_A^+(t) + M_B^+(t)$ produces the NMR spectrum.

Appendix B

NMR Experimental Methods

B.1 SIMPSON Input File for CP Build-up Curves

```
spinsys {
  channels 13C 1H
  nuclei 13C 1H 1H
  dipole 1 2 -1000 0 0 0
}

par {
  variable tsw     10
  sw               1E6/tsw
  np               201
  proton_frequency 500e6
  start_operator   I2z
  detect_operator  I1p
  method           direct
  gamma_angles     16
  spin_rate        5000
  verbose          1101
  crystal_file     rep320
  variable theta   54.7356
}

proc pulseq {} {
  global par

  set rfH 52500
  set rfC [expr $rfH + -1*$par(spin_rate)]

  pulseid [expr 0.25e6/$rfH] 0 0 $rfH y

  acq_block {
    pulse $par(tsw) $rfC 0 $rfH 0
```

```
  }
}

proc main {} {
  global par

  set f [fsimpson]
  fsave $f $par(name)_5kHz.fid

}
```

B.2 SIMPSON Input File for DIPSHIFT Profiles

```
spinsys {
  channels 1H 13C
  nuclei 1H 13C
  dipole 1 2 -500 0 0 0
}

par {
  spin_rate        5000
  proton_frequency 500e6
  np               81
  crystal_file     rep168
  gamma_angles     10
  start_operator   I2x
  detect_operator  I2p
  variable rf      50000
  verbose          1101
  variable N       8
  sw               25000
}

proc pulseq {} {
  global par

  set t180 [expr 0.5e6/$par(rf)]
  set tr2 [expr 0.5e6/$par(spin_rate)]

  for {set i 0} {$i < $par(np)} {incr i} {

    set d0 [expr ($par(N)*$i*1.0e6/$par(spin_rate))/($par(np)-1)]
    reset

    if {$d0 < $tr2} {
      delay $d0

    } elseif {$d0 <= [expr $tr2*($par(N)-1)]} {
```

```
      set necho [expr $d0/$tr2]
      for {set p 1} {$p <= floor($necho)} {incr p} {
      delay $tr2
      pulseid $t180 0 0 $par(rf) x
      }
      delay [expr $tr2*($necho-floor($necho))]

    } elseif {$d0 < [expr $tr2*$par(N)+$tr2]} {
      for {set p 1} {$p <= [expr $par(N)-1]} {incr p} {
      delay $tr2
      pulseid $t180 0 0 $par(rf) x
      }
      delay [expr $d0-$tr2*($par(N)-1)]

    } elseif {$d0 < [expr 2*$tr2*($par(N)-1)+$tr2]} {
      for {set p 1} {$p <= [expr $par(N)-1]} {incr p} {
      delay $tr2
      pulseid $t180 0 0 $par(rf) x
      }
      delay $tr2
      set necho [expr ($d0-([expr $tr2*($par(N)-1)+$tr2]))/$tr2]
      for {set p 1} {$p <= floor($necho)} {incr p} {
      delay $tr2
      pulseid $t180 0 0 $par(rf) x
      }
      delay [expr $tr2*($necho-floor($necho))]

    } else {
      for {set p 1} {$p <= [expr $par(N)-1]} {incr p} {
      delay $tr2
      pulseid $t180 0 0 $par(rf) x
      }
      delay $tr2
      for {set p 1} {$p <= [expr $par(N)-1]} {incr p} {
      delay $tr2
      pulseid $t180 0 0 $par(rf) x
      }
      delay [expr $d0-[expr 2*$tr2*($par(N)-1)+$tr2]]
    }
    acq
  }
}

proc main {} {
  global par
  set f [fsimpson]
  fsave $f $par(name)_CH500Hz.fid
}
```

Appendix C

Probing Hydrogen Bonding and Chemical Exchange in a Deep Eutectic Pharmaceutical by MAS NMR Spectroscopy

C.1 Simulation of NMR Spectra for Two-Site Chemical Exchange

The *Python* scripts used in this chapter are presented below.

"Input_variables.py":

```
'''
File for user to define input variables

Parameters may be either a single value or a list

Examples lists:

Vary the spectrometery frequency between 500 and 850 MHz magnets:
freq = [500,600,700,850]

Vary the population of site A between 0.5 and 1:
pA = [0.5,0.6,0.7,0.8,0.9,1]

Vary the chemical shift of site A between 0.5 and 4 ppm:
Appm = [0.5, 1, 2, 4]

Vary the rate constant between 10 and 1e8 s−1:
k = [10,100,1000,1e5,1e8]
```

```
R2A = [10, 25, 50, 75, 100]
'''
####################################
####      Define paramaters      ####
####################################

params = {
  # B0 in MHz, 100 < freq < 1000
  'freq' : 500,
   # fractional population of site A, 0 < pA < 1
  'pA' : [0.1,0.2,0.3,0.4,0.5],
  # chemical shift of site A in ppm
  'Appm' : 10.1,
  # chemical shift of site B in ppm
  'Bppm' : 7.2,
  # exchange rate constant kex in s-1, 0 < kex
  'kHz' : 1e6,
  # transverse relaxation rate of A in absence of exchange
  'R2A' : [10,20,30,40,50],
  # number of signal points
  'N' : 10000,
  # spectral width in Hz
  'sw' : 20000
 }
```

"exchangeSim.py":

```
'''
Simulate NMR spectra for two-site chemical exchange

Enables identification of effects of spectrometer frequency, population
    of exchanging sites,
chemical shift difference, exchange rate, and transverse relaxation rate.

The signal for the free induction decay (FID) is calculated from the
    solution to the Bloch-Mcconnell equations for nuclei spins subject to
     two-site chemical exchange. The NMR spectrum is obtained  from the
    Fourier transform of the FID and plotted. These simulations are
    useful for the interpretation of chemical exchange processes in NMR
    spectroscopy.

Enter parameters in "input_variables.py"

'''
import matplotlib.pyplot as plt
import numpy as np
from scipy.fftpack import fft, fftfreq, fftshift
from scipy.signal import argrelextrema
```

```
import input_variables

class FID():

  def calcparams(self):
    '''
    Recalculates dependent variables from user inputed variables
    '''
    # transverse relaxation rate of B in absence of exchange in s-1
    self.R2B = self.R2A
    # fractional population of site B
    self.pB = 1-self.pA
    # k in s-1
    self.k = self.kHz
    # initial transverse magnetisation
    self.M0 = 1+1j
    # initial transverse magnetisation of A
    self.MA = self.pA*self.M0
    # initial transverse magnetisation of B
    self.MB = self.pB*self.M0
    # chemical shift of A in rad s-1
    self.sA = self.Appm*self.freq*2*np.pi
    # chemical shift of B in rad s-1
    self.sB = self.Bppm*self.freq*2*np.pi
    # chemical shift difference rad s-1
    self.w = self.sA-self.sB
    # sample spacing
    self.s = 1/self.sw
    # sample time points in s
    self.t = np.linspace(0.0, self.N*self.s, self.N)

  def calcM(self):
    '''
    Returns the FID
    '''
    zp = 0.5*(-1j*self.sA-1j*self.sB+self.R2A+self.R2B+self.k+((-1j*self.
        w+self.R2A-self.R2B+self.k*(self.pB-self.pA))**2+4*self.pA*self.
        pB*self.k**2)**0.5)
    zn = 0.5*(-1j*self.sA-1j*self.sB+self.R2A+self.R2B+self.k-((-1j*self.
        w+self.R2A-self.R2B+self.k*(self.pB-self.pA))**2+4*self.pA*self.
        pB*self.k**2)**0.5)
    h = (-1j*self.w+self.R2A-self.R2B+self.k*(self.pB-self.pA))/(zp-zn)
    aAA = 0.5*((1-h)*np.exp(-zn*self.t)+(1+h)*np.exp(-zp*self.t))
    aBB = 0.5*((1+h)*np.exp(-zn*self.t)+(1-h)*np.exp(-zp*self.t))
    aAB = (self.k*self.pA/(zp-zn))*(np.exp(-zn*self.t)-np.exp(-zp*self.t)
        )
    aBA = (self.k*self.pB/(zp-zn))*(np.exp(-zn*self.t)-np.exp(-zp*self.t)
        )
```

```
    return aAA*self.MA+aAB*self.MB+aBA*self.MA+aBB*self.MB

def plot():
  '''
  Plots NMR spectra for varying parameters
  '''
  global x
  global y
  params = input_variables.params
  for v in params:
    if type(params[v]) == list:
      n = len(params[v]) # number of plots
        break
    else:
      n = 1

  f, axarr = plt.subplots(n, sharex=True) # set up subplots
  for i in range(0, n):
    obj = FID
    for v in params:
    if type(params[v]) == list:
      setattr(obj, v, params[v][i])
    else:
      setattr(obj, v, params[v])
    obj.calcparams(obj)
    obj.calcM(obj)
    x=np.fft.fftshift(fftfreq(obj.N,obj.s))/obj.freq
    y=abs(np.fft.fftshift(fft(obj.calcM(obj))))

    # record parameters in text file
    with open('out.txt', 'a') as out_file:
      out_file.write("Plot {} \n \
      Observed chemical shift: {} ppm \n \
      Spectrometer frequency: {} MHz \n \
      Population of site A: {} \n \
      Chemical shift difference: {} ppm \n \
      Exchange rate constant: {} s-1 \n \
      R2 in absence of exchange: {} s-1 \n" \
      .format(i+1, x[argrelextrema(y, np.greater)], obj.freq, obj.pA, obj
          .w/(obj.freq*2*np.pi), obj.kHz, obj.R2A))
    out_file.close

    axarr[i].plot(x, y, 'black')
    axarr[i].set_ylim(ymin=-10)
    axarr[i].axes.get_yaxis().set_visible(False)
    axarr[i].axes.spines['top'].set_visible(False)
    axarr[i].axes.spines['left'].set_visible(False)
    axarr[i].axes.spines['right'].set_visible(False)
```

```
    # Show x axis for bottom plot only
    if i!=n-1:
      axarr[i].axes.get_xaxis().set_visible(False)
      axarr[i].axes.spines['bottom'].set_visible(False)

  plt.gca().invert_xaxis()
  plt.gca().set_xlim(14, 8)
  plt.xlabel('Chemical shift (ppm)')
  f.savefig('./plot.pdf')
  print("Plot saved as 'plot.pdf'")
  print("Plot details saved to 'out.txt'")


def main():
  plot()

if __name__ == "__main__":
  main()
```

Appendix D

Choline and Geranate (CAGE) and Analogue Ionic Liquids

D.1 Negative Ion Mass Spectrum of CAGE-oct

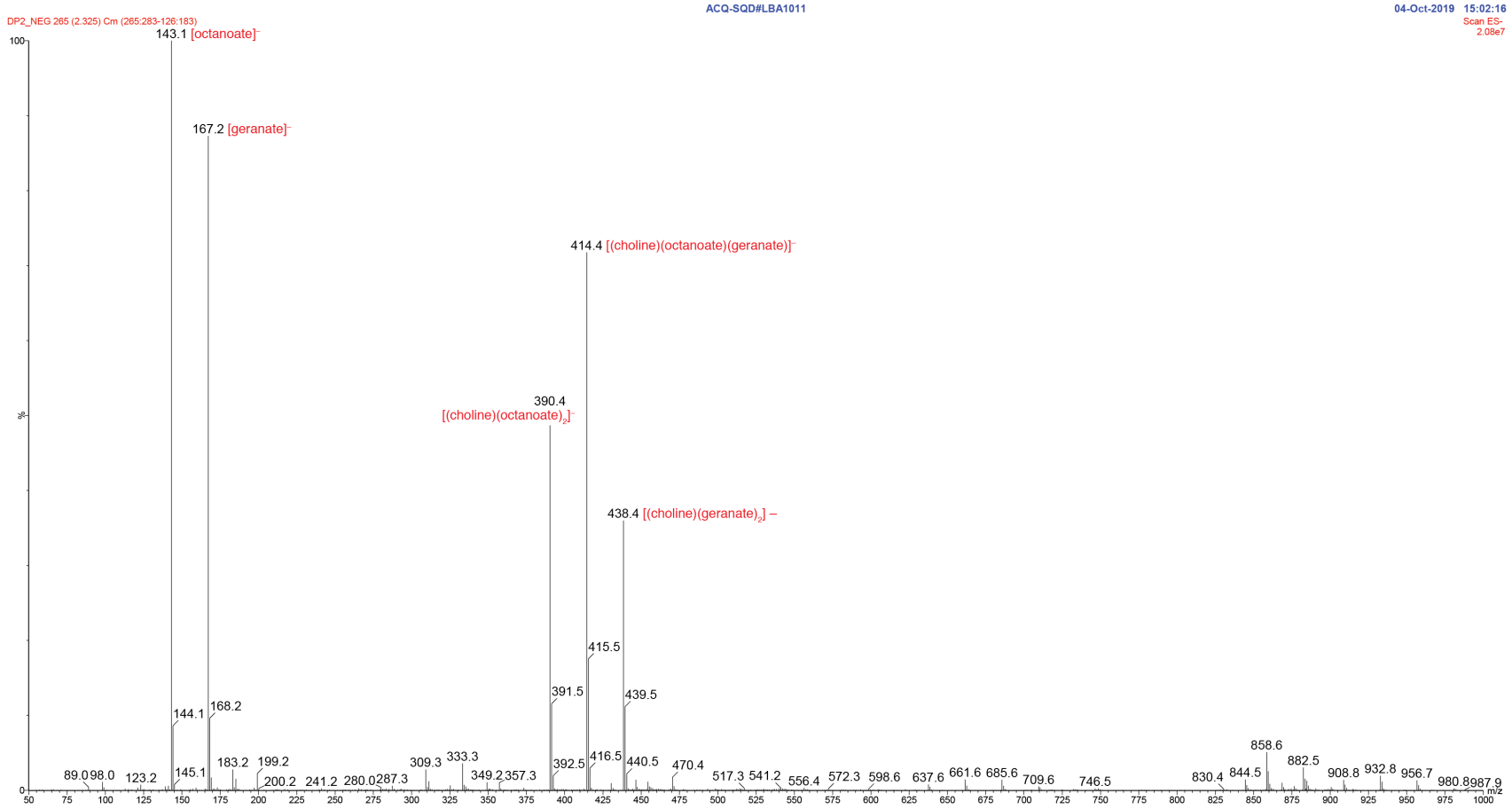

Figure D.1: Negative ion mass spectrum of CAGE-oct.

Appendix E

MAS NMR Investigation of Molecular Order in Ionic Liquid Crystals

E.1 Example SIMPSON Input File for Fitting CP Build-up Curves

```
# CH
spinsys {
  channels 13C 1H
  nuclei 13C 1H
  dipole 1 2 0 0 0 0
}

# CH2
# spinsys {
#  channels     13C 1H
#  nuclei       13C 1H 1H
#  dipole       3 1 0 15.94162346 145.04108269 0
#  dipole       1 2 0 −122.36504473 135.37995988 0
#  dipole       3 2 0 −68.38463525 162.92363959 0
# }

# CH3
# spinsys {
# channels      13C 1H
#  nuclei       13C 1H 1H 1H
#  dipole       1 2 0 52.71954024 47.14496817 0
#  dipole       1 3 0 166.02117095 91.48314947 0
#  dipole       1 4 0 −85.43006463 70.18660966 0
#  dipole       3 2 0 13.70567943 64.03001083 0
```

```
#  dipole       4 2 0 76.36209289 77.70427874 0
#  dipole       4 3 0 131.41221880 103.07354890 0
# }

par {
  variable peak   5

  variable tsw     40
  sw               1E6/40
  np               51
  proton_frequency 500e6
  start_operator   I2z
  detect_operator  I1p
  method           direct
  gamma_angles     10
  spin_rate        5000
  verbose          0
  crystal_file     rep168
}

proc pulseq {} {
  global par

  set rfH 52500
  set rfC [expr $rfH + -1*$par(spin_rate)]

  pulseid [expr 0.25e6/$rfH] 0 0 $rfH y

  acq_block {
    pulse $par(tsw) $rfC 0 $rfH 0
  }
}

proc progress {} {
  global par
  if ![info exists par(progress)] { set par(progress) -1 }
  incr par(progress)
  set str {"*   " \
     " *  " \
     "  * " \
     "   *" \
     "  * " \
     " *  "}
  return [lindex $str [expr $par(progress)%6]]
}

lappend ::auto_path ../../../opt
package require opt
```

```
proc rms {{save 0}} {
  global par

# uncomment for CH2:
# set HH [expr ($opt::dipole12)*22.4/23.3]

# uncomment for CH3:
set HH [expr ($opt::dipole12)*21.7/22.7*0.5/0.3333]

# simulate CP build-up
  set f [fsimpson [list \
# CH
    [list dipole_1_2_aniso $opt::dipole12] \

# uncomment for CH2:
#   [list dipole_1_2_aniso $opt::dipole12] \
#   [list dipole_1_3_aniso $opt::dipole12] \
# uncomment to include CH2 HH coupling:
#   [list dipole_3_2_aniso $HH] \

# uncomment for CH3:
#   [list dipole_1_2_aniso $opt::dipole12] \
#   [list dipole_1_3_aniso $opt::dipole12] \
#   [list dipole_1_4_aniso $opt::dipole12] \
# uncomment to include CH3 HH couplings:
#   [list dipole_2_3_aniso $HH] \
#   [list dipole_2_4_aniso $HH] \
#   [list dipole_3_4_aniso $HH] \
    ]]

# multiple each real point by relaxation term
 for {set i 1} {$i <= $par(np)} {incr i} {
    set t [fx $f $i]
    set re [findex $f $i -re]
    fsetindex $f $i [expr $re*exp(-$t/($opt::t1))] 0
 }

# scale build-up curve
  fautoscale $f $par(exp) -re

  set rms [frealrms $f $par(exp)]
  if {$save == 1} {
    puts [format " \[%s\] %10.3f %10.6f" \
    FINAL $opt::dipole12 $rms]
    # write simulated curve to disc
    fsave $f ../SIMPSON_best_fit_FIDS/$par(name).fid
  } else {
```

```
    puts [format " \[%s\] %10.3f %10.5f %10.6f" \
    [progress] $opt::dipole12 $opt::t1 $rms]
  }
  flush stdout
  funload $f
  return $rms
}

proc main {} {
  global par
  set par(exp) [fload ../../Experimental_fids_max2ms/Peak_$par(peak)_exp.
      fid]

  opt::function rms
  puts " Progress dipole12      t1      rms"
         opt::newpar dipole12 -1000 15
         opt::newpar t1 1 0.2
     opt::minimize 1.0e-6
     rms 1
}
```

E.2 Example SIMPSON Input File for Fitting DIPSHIFT Profiles

```
# CH
spinsys {
  channels 13C 1H
  nuclei 13C 1H
  dipole 1 2 0 0 0 0
}

# CH2
# spinsys {
#  channels     13C 1H
#  nuclei       13C 1H 1H
#  dipole       3 1 0 15.94162346 145.04108269 0
#  dipole       1 2 0 -122.36504473 135.37995988 0
# }

# CH3
# spinsys {
# channels      13C 1H
#  nuclei       13C 1H 1H 1H
#  dipole       1 2 0 52.71954024 47.14496817 0
#  dipole       1 3 0 166.02117095 91.48314947 0
#  dipole       1 4 0 -85.43006463 70.18660966 0
# }
```

```
par {
  variable peak   5

  variable tsw     40
  sw               1E6/40
  np               41
  proton_frequency 500e6
  start_operator   I2x
  detect_operator  I1p
  method           direct
  gamma_angles     10
  spin_rate        5000
  verbose          0
  crystal_file     rep168
  variable N          8
}

proc pulseq {} {
  global par

  set t180 [expr 0.5e6/$par(rf)]
  set tr2 [expr 0.5e6/$par(spin_rate)]

  for {set i 0} {$i < $par(np)} {incr i} {

    set d0 [expr ($par(N)*$i*1.0e6/$par(spin_rate))/($par(np)-1)]
    reset

    if {$d0 < $tr2} {
      delay $d0

    } elseif {$d0 <= [expr $tr2*($par(N)-1)]} {
      set necho [expr $d0/$tr2]
      for {set p 1} {$p <= floor($necho)} {incr p} {
      delay $tr2
      pulseid $t180 0 0 $par(rf) x
      }
      delay [expr $tr2*($necho-floor($necho))]

    } elseif {$d0 < [expr $tr2*$par(N)+$tr2]} {
      for {set p 1} {$p <= [expr $par(N)-1]} {incr p} {
      delay $tr2
      pulseid $t180 0 0 $par(rf) x
      }
      delay [expr $d0-$tr2*($par(N)-1)]

    } elseif {$d0 < [expr 2*$tr2*($par(N)-1)+$tr2]} {
      for {set p 1} {$p <= [expr $par(N)-1]} {incr p} {
```

```
      delay $tr2
      pulseid $t180 0 0 $par(rf) x
      }
      delay $tr2
      set necho [expr ($d0-([expr $tr2*($par(N)-1)+$tr2]))/$tr2]
      for {set p 1} {$p <= floor($necho)} {incr p} {
      delay $tr2
      pulseid $t180 0 0 $par(rf) x
      }
      delay [expr $tr2*($necho-floor($necho))]

    } else {
      for {set p 1} {$p <= [expr $par(N)-1]} {incr p} {
      delay $tr2
      pulseid $t180 0 0 $par(rf) x
      }
      delay $tr2
      for {set p 1} {$p <= [expr $par(N)-1]} {incr p} {
      delay $tr2
      pulseid $t180 0 0 $par(rf) x
      }
      delay [expr $d0-[expr 2*$tr2*($par(N)-1)+$tr2]]
    }
    acq
  }
}

proc progress {} {
  global par
  if ![info exists par(progress)] { set par(progress) -1 }
  incr par(progress)
  set str {"*   " \
      " *  " \
      "  * " \
      "   *" \
      "  * " \
      " *  "}
  return [lindex $str [expr $par(progress)%6]]
}

lappend ::auto_path ../opt
package require opt

proc rms {{save 0}} {
  global par

# simulate DIPSHIFT curve
  set f [fsimpson [list \
```

```
# CH
    [list dipole_1_2_aniso $opt::dipole12] \

# CH2
#   [list dipole_1_2_aniso $opt::dipole12] \
#   [list dipole_1_3_aniso $opt::dipole12] \

# CH3
#   [list dipole_1_2_aniso $opt::dipole12] \
#   [list dipole_1_3_aniso $opt::dipole12] \
#   [list dipole_1_4_aniso $opt::dipole12] \
    ]]

# multiple each real point by relaxation term
 for {set i 1} {$i <= $par(np)} {incr i} {
    set t [fx $f $i]
    set re [findex $f $i -re]
    fsetindex $f $i [expr $re*exp(-$t/($opt::t1))] 0
 }

  set rms [frealrms $f $par(exp)]
  if {$save == 1} {
    puts [format " \[%s\] %10.6f %10.6f %10.6f\015" \
       FINAL $opt::dipole12 $opt::t1 $rms]
      # write simulated curve to disc
      fsave $f ../SIMPSON_FIDS/$par(name)_Peak_$par(peak)_N8_FSLG.fid
  } else {
    puts [format " \[%s\] %10.6f %10.6f %10.6f\015" \
       [progress] $opt::dipole12 $opt::t1 $rms]
  }
  flush stdout
  funload $f
  return $rms
}

proc main {} {
  global par mn
  set par(exp) [fload ../Experimental_fids/Peak_$par(peak)_N8_FSLG_exp.
      fid]

  opt::function rms
  puts " Progress dipole12      t1      rms"
         opt::newpar dipole12 -1000 5
         opt::newpar t1 1 0.2
     opt::minimize 1.0e-6
     rms 1
}
```

Appendix F

VT ^{1}H and ^{13}C MAS NMR Relaxation Measurements to Investigate Dynamics in an Ionic Liquid Crystal

F.1 Fitting NMR Relaxation Data to the SMF Formalism with Overall Anisotropic Tumbling

The *Matlab* scripts used in this chapter are presented below.

Calculation of ^{13}C R_1, $R_{1\rho}$ and ^{1}H-^{13}C NOE factors from the correlation times, activation energies and order parameter:

```
function [R1,R1rho,NOE] = aniso_internal_R1_R1rho(r_CH, csappm, n, flag,
    T, B0, theta, Ds273, Df273, Eas, Eaf, S2i, tci273, Eai)
  %constants
  h = 6.626e-34;
  R = 8.314461;
  gamma_1H  = 2.68e8;
  gamma_13C = 6.73e7;

  % Dipolar coupling and CSA / rad s-1
  d   = 1e-7*(gamma_13C*gamma_1H)*(h/(2*pi))/((r_CH^3));
  csa = csappm*B0*2*pi*gamma_13C/gamma_1H;

  % Larmor frequencies / rad s-1
  omega_1H   = 2.*pi.*B0*1e6;
  omega_13C  = 2.*pi.*B0*1e6.*gamma_13C./gamma_1H;
  omega_sum  = omega_1H+omega_13C;
```

```
omega_diff = omega_1H-omega_13C;
omega_1    = 6000*2*pi;    % rf spin-lock field
omega_r    = 10000*2*pi;   % MAS frequency

% Arrhenius temperature-dependence
% D_| (diffusion about x,y - slow) / s-1
Ds  = Ds273/exp(-Eas*1e3./(R.*273.15))*exp(-Eas*1e3./(R.*T));
% D|| (diffusion about z - fast) / s-1
Df  = Df273/exp(-Eaf*1e3./(R.*273.15))*exp(-Eaf*1e3./(R.*T));
% Correlation time for internal motion / s
tci = tci273/exp(Eai*1e3./(R.*273.15))*exp(Eai*1e3./(R.*T));

% Coefficients
thetarad = theta*pi/180;
A0 = 0.25*(3*cos(thetarad)^2-1)^2;
A1 = 3*cos(thetarad)^2*sin(thetarad)^2;
A2 = 0.75*sin(thetarad)^4;

% Correlation times
tau0  = 1./(6*Ds);
tau1  = 1./(5*Ds+Df);
tau2  = 1./(2*Ds+4*Df);
tau0p = 1./(1./tci+1./tau0);
tau1p = 1./(1./tci+1./tau1);
tau2p = 1./(1./tci+1./tau2);

% S2i for methyls
if n == 3
  S2i = 0.11*S2i;
end

% J aniosotropic-EMF
J=@(omega) A0*(S2i*tau0./(1+(omega.*tau0).^2)...
             +(1-S2i)*tau0p./(1+(omega.*tau0p).^2))...
          +A1*(S2i*tau1./(1+(omega.*tau1).^2)...
              +(1-S2i)*tau1p./(1+(omega.*tau1p).^2))...
          +A2*(S2i*tau2./(1+(omega.*tau2).^2)...
              +(1-S2i)*tau2p./(1+(omega.*tau2p).^2));

% Spectral densities
J0a    = J(omega_1-2*omega_r);
J0b    = J(omega_1-omega_r);
J0c    = J(omega_1+2*omega_r);
J0d    = J(omega_1+omega_r);
J0sum  = 2/3*J0a+4/3*J0b+2/3*J0c+4/3*J0d;
J1H    = J(omega_1H);
J13C   = J(omega_13C);
Jsum   = J(omega_sum);
```

```
  Jdiff  = J(omega_diff);

  % Relaxation rates and NOE factor
  R1DD  = 1/10*n*d^2*(6*Jsum+Jdiff+3*J13C);
  R1CSA = flag*2/15*csa^2*J13C;
  R1    = R1DD+R1CSA;

  R1rhoDD  = 1/20*n*d^2*(J0sum+3*J13C+6*J1H+6*Jsum+Jdiff);
  R1rhoCSA = flag*1/45*csa^2*(J0sum+3*J13C);
  R1rho    = R1rhoDD+R1rhoCSA;

  RNOE = 1/10*n*d^2*(6*Jsum-Jdiff);
  NOE  = (RNOE./R1).*(gamma_1H/gamma_13C);
end
```

Fitting of the ^{13}C R_1, $R_{1\rho}$ and ^{1}H-^{13}C NOE factors:

```
function [params,res,jac,chi2] = global_fitmin_aniso_internal(T,B01,B02,
    mol)

  % inital values and bounds: log10(Ds273), log10(Df273), Eas, Eaf, S2i,
      log10(tci273), Eai
  p0 = [0, 0, 50, 40 zeros(1,length(mol))+0.5 zeros(1,length(mol)) zeros
      (1,length(mol))+10];
  lb  = [4, 5, 0, 0 zeros(1,length(mol)) zeros(1,length(mol))-15 zeros(1,
      length(mol))];
  ub = [10, 11, 150, 150 zeros(1,length(mol))+1  zeros(1,length(mol))-9
      zeros(1,length(mol))+150];

  % run minimisation from multiple start points to find global minimum
  rng default % For reproducibility
  opts = optimoptions('lsqnonlin','FunctionTolerance',1e-3,'StepTolerance
      ',1e-3);
  problem = createOptimProblem('lsqnonlin','objective',@fun,'x0',p0,'lb',
      lb,'ub',ub,'options',opts);
  ms = MultiStart('UseParallel',true,'StartPointsToRun','bounds','Display
      ','iter','FunctionTolerance',1e-3,'XTolerance',1e-3)
  [params,chi2,flg,output] = run(ms,problem,100);

  % run minimisation from best-fit values
  opts = optimoptions('lsqnonlin','Display','iter','FunctionTolerance',1e
      -3,'StepTolerance',1e-3,'MaxFunctionEvaluations',1e4,'MaxIterations
      ',1e4)
  [params,chi2,res,~,~,jac] = lsqnonlin(@fun,params,lb,ub,opts);

   function [output] = fun(p)
      output = [];
      % fit parameters: global overall anisotropic motion
```

```
      Ds273 = 10^(p(1));
      Df273 = 10^(p(2));
      Eas = p(3);
      Eaf = p(4);

      % fit parameters: local internal motion for each site
      for i = 1:length(mol)
        mol(i).S2i = p(i+4);
        mol(i).tc273 = 10^(p(i+length(mol)+4));
        mol(i).Eai = p(i+2*length(mol)+4);

       % Relaxation rates and NOE factors at 500 and 700 MHz
       [R1_500, R1rho_500, NOE_500] = aniso_internal_R1_R1rho(mol(i).r_CH
           ,mol(i).csa,mol(i).n,mol(i).flag,T,B01,mol(i).theta,Ds273,
           Df273,Eas,Eaf,mol(i).S2i,mol(i).tc273,mol(i).Eai);
        R1_700, R1rho_700, NOE_700] = aniso_internal_R1_R1rho(mol(i).r_CH
            ,mol(i).csa,mol(i).n,mol(i).flag,T,B02,mol(i).theta,Ds273,
            Df273,Eas,Eaf,mol(i).S2i,mol(i).tc273,mol(i).Eai);

       output = [output;
       (R1_500-mol(i).R1exp_500(:,1))./(mol(i).R1exp_500(:,2));
       (R1_700-mol(i).R1exp_700(:,1))./(mol(i).R1exp_700(:,2));
       (R1rho_500-mol(i).R1rhoexp_500(:,1))./(mol(i).R1rhoexp_500(:,2));
       (R1rho_700-mol(i).R1rhoexp_700(:,1))./(mol(i).R1rhoexp_700(:,2));
       (NOE_500-mol(i).NOEexp_500(:,1))./0.1.*(mol(i).NOEexp_500(:,1));
       (NOE_700-mol(i).NOEexp_700(:,1))./0.1.*(mol(i).NOEexp_700(:,1))];
      end
      output = rmmissing(output);
   end
end
```